

UNIVERSITY OF CALIFORNIA,
IRVINE

Multi-Physics Computational Grains (MPCGs): Newly-Developed Accurate and Efficient
Numerical Methods for Micromechanical Modeling of Multifunctional Materials and
Composites

DISSERTATION

submitted in partial satisfaction of the requirements
for the degree of

DOCTOR OF PHILOSOPHY

in Mechanical and Aerospace Engineering

by

Peter L. Bishay

Dissertation Committee:
Distinguished Professor Satya N. Atluri, Chair
Associate Professor Lorenzo Valdevit
Assistant Professor Timothy J. Rupert

2014

UMI Number: 3612553

All rights reserved

INFORMATION TO ALL USERS

The quality of this reproduction is dependent upon the quality of the copy submitted.

In the unlikely event that the author did not send a complete manuscript and there are missing pages, these will be noted. Also, if material had to be removed, a note will indicate the deletion.



UMI 3612553

Published by ProQuest LLC (2014). Copyright in the Dissertation held by the Author.

Microform Edition © ProQuest LLC.

All rights reserved. This work is protected against unauthorized copying under Title 17, United States Code



ProQuest LLC.
789 East Eisenhower Parkway
P.O. Box 1346
Ann Arbor, MI 48106 - 1346

© 2014 Peter L. Bishay

DEDICATION

To

my dear wife, Marianne,

for her endless support and unconditional love,

and our new baby, Daniella,

for the happiness she is bringing to our lives

TABLE OF CONTENTS

TABLE OF CONTENTS.....	iii
LIST OF FIGURES.....	vi
LIST OF TABLES	xii
ACKNOWLEDGMENTS.....	xiii
CURRICULUM VITAE	xiv
ABSTRACT OF THE DISSERTATION	xx
INTRODUCTION	1
Chapter 1 : Basic Concepts and Governing Equations	17
1.1 Introduction	17
1.2 Brief description of Piezoelectricity	17
1.3 Brief description of Piezomagnetism	19
1.4 Governing equations for magneto-electro-elastic (MEE) composites.....	21
1.4.1 Matrix boundary conditions.....	25
1.4.2 Impermeable void boundary conditions.....	27
1.4.3 Inclusion boundary conditions.....	27
1.5 Plane-stress and plane-strain assumptions	29
1.6 Brief description of ferroelectricity.....	33
1.7 Constitutive equations for ferroelectric materials	38
1.7.1 Material properties for the different domain types	41
1.8 Heterogeneous materials and Micromechanics	45
1.9 On using Representative Volume Element (RVE) to predict the effective material properties of piezo-composites	49
1.10 Special models to determine the effective material properties of piezoelectric composites....	51
1.11 References of chapter 1	54
Chapter 2 : Lekhnitskii formalism for coupled/uncoupled electro-elastic and magneto-elastic materials	58
2.1 Introduction	58
2.2 Basic formulation	58
2.3 Basic Solution Set.....	68
2.4 Special solution set for impermeable elliptical void	71
2.5 References of chapter 2	75

Chapter 3 : Multi-Region Trefftz Collocation Grains (MTCGs): A simple and efficient method for direct and inverse problems	76
3.1 Introduction	76
3.2 Multi-Region Trefftz Collocation Grain (MTCGs) Formulation for Direct Problems	77
3.3 Multi-Region Trefftz Collocation Grain (MTCGs) Formulation for Inverse Problems with Regularization	81
3.4 Numerical examples.....	82
3.4.1 Piezoelectric panel with impermeable void: Inverse problem	83
3.4.2 Convergence study for the inverse problem	86
3.4.3 Infinite piezoelectric domain with elliptical inclusion	87
3.4.4 Evaluation of material properties of piezoelectric composite.....	89
3.4.5 Damage detection in porous piezoelectric materials with arbitrary oriented elliptical voids	91
3.5 Summary and Conclusions of chapter 3	93
3.6 References of chapter 3	94
Chapter 4 : Trefftz-Lekhnitskii Computational Grains (TLCGs) for modeling porous and composite multifunctional materials.....	96
4.1 Introduction	96
4.2 Formulation of Trefftz-Lekhnitskii Computational Grain (TLCG) for piezoelectric/piezomagnetic materials with/without voids/inclusions	97
4.2.1 Using Collocation method.....	100
4.2.2 Using a least squares method.....	103
4.2.3 Using multi-field boundary variational principle	104
4.2.4 On the selection of the maximum order of Trefftz functions.....	106
4.2.5 Conditioning of system matrices	108
4.3 Numerical examples.....	109
4.3.1 Infinite Piezoelectric domain with impermeable arbitrarily-oriented elliptical void under mechanical or electrical loading	111
4.3.2 Evaluation of the effective material properties of porous piezoelectric materials.....	115
4.3.3 Damage detection in porous piezoelectric material.....	117
4.4 Summary and Conclusions	119
4.5 References of chapter 4	120

Chapter 5 : Hybrid Displacement Computational Grains (HDCGs): A general method for modeling multi-functional materials	122
5.1 Introduction	122
5.2 New Hybrid Variational Principles for Heterogeneous Piezoelectricity	123
5.3 Independent trial mechanical and electric fields, and the formulation of HDCG	127
5.4 Numerical examples.....	131
5.4.1 Infinite piezoelectric panel with an impermeable circular void	131
5.4.2 Piezoelectric panel with circular inclusion.....	133
5.4.3 Evaluation of the effective material properties of porous piezoelectric materials.....	134
5.4.4 Evaluation of the effective material properties of piezoelectric composite material.....	136
5.5 Summary and Conclusion.....	138
5.6 References of chapter 5	140
Chapter 6 : Radial-Basis-Functions Computational Grains (RBFCG) for modeling functionally-graded, magneto-electro-elastic (MEE) materials and the switching phenomena in ferroelectric materials	142
6.1 Introduction	142
6.2 Introduction to computational modeling of ferroelectric polycrystalline materials.....	144
6.3 Radial-Basis-Functions Computational Grains (RBFCGs) formulation for ferroelectric materials..	
.....	148
6.3.1 Interior and boundary primal variables	149
6.3.2 Finite element equation.....	158
6.3.3 Conditioning of the system matrices	161
6.4 Switching criterion and kinetics for ferroelectric materials.....	163
6.5 Solution method for simulating ferroelectric/ferroelastic switching	168
6.6 Numerical Examples.....	171
6.6.1 Patch test for Magneto-electro-elastic materials	171
6.6.2 Effective material properties determination for functionally graded materials	173
6.6.3 Simulating ferroelectric materials.....	177
6.7 Summary and Conclusions	190
6.8 References of chapter 6	192
Chapter 7 : Dissertation Summary and Conclusions.....	198

LIST OF FIGURES

Figure 1.1: Transformation from (a) cubic to (b) tetragonal unit cell of ABO_3 .	18
Figure 1.2: (left) 2D irregular polygon (grain) with an elliptical void/inclusion and its local coordinates as well as the global ($X_1 - X_3$), grain local ($\hat{x}_1 - \hat{x}_3$) Cartesian coordinate systems, matrix electric polling direction (x'_3), and matrix magnetic bias direction (x''_3).....	22
Figure 1.3: (left) 2D irregular polygon (grain) with an elliptical inclusion and its local coordinates as well as the global ($X_1 - X_3$), grain local ($\hat{x}_1 - \hat{x}_3$) Cartesian coordinate systems, inclusion electric polling direction (x'_{c3}), and inclusion magnetic bias direction (x''_{c3}).....	22
Figure 1.4: A schematic showing all governing equations in porous/composite piezoelectric-piezomagnetic material (MEE: Magneto-electro-elastic).....	29
Figure 1.5: Primary length scales for ferroelectric materials.....	33
Figure 1.6: (a) 180° switching induced by electric field; (b) 90° switching induced by electric field; (c) 90° switching induced by compressive stress; (d) 90° switching induced by tensile stress.....	34
Figure 1.7: Schematic sketches of (a) hysteresis loop of macroscopic polarization P versus applied electric field E and (b) butterfly loop of macroscopic strain ε versus electric field E . The dashed line represents the initial polarization process of the unpoled material.....	36
Figure 1.8: Schematic sketches for the polarization directions in the domains of the grains of a polycrystalline ferroelectric material through the polling process.	36
Figure 1.9: Ferroelectric and ferroelastic switching	38
Figure 1.10: Crystallographic axes in a ferroelectric crystal grain and the polarization directions of the 6 possible domain types or variants.....	42

Figure 1.11: 3D rotation of axes using Euler angles: (left) rotation by angle θ around x'_3 -axis, (middle) rotation by angle ϕ around x''_1 -axis, (right) rotation by angle ψ around x'''_3 -axis.....	43
Figure 1.12: Homogenization of heterogeneous materials: (left) heterogeneous material with microstructure, (right) homogenized continuum	48
Figure 1.13: Variety of configurations used in piezoelectric composites.....	52
Figure 1.14: Computational models to evaluate the effective properties of: (left) C_{11}^{eff} and C_{13}^{eff} , (middle) C_{33}^{eff} and C_{13}^{eff} , (right) e_{31}^{eff} , e_{33}^{eff} and h_{33}^{eff}	52
Figure 2.1: Elliptical void/inclusion with the local coordinate system as well as the polling direction (left), and magnetic bias direction (right)	59
Figure 3.1 (left) A Finite rectangular domain with arbitrarily oriented elliptical void, (right) collocation points considered in section 3.2	84
Figure 3.2: Variations of (left) σ_θ / σ_o , (right) D_θ / σ_o along the periphery of an elliptical void	85
Figure 3.3: Variations of (left) E_θ / σ_o , (right) E_r / σ_o along the periphery of an elliptical void	85
Figure 3.4: Effect of b/a on: (a) σ_θ / σ_o , (b) D_θ / σ_o , (c) E_θ / σ_o and (d) E_r / σ_o along the inclusion periphery.....	88
Figure 3.5: Predictions of the effective piezoelectric materials properties of PZT-7A/LaRC-SI as functions of particle volume fraction.....	90
Figure 3.6: Porous piezoelectric material under mechanical loading: Contour plot for (upper) Principal stress, (lower left) Strain energy density, (lower right) Dielectric energy density.....	92
Figure 3.7: COMSOL simulation: (left) mesh, (right) Strain energy density.....	93

Figure 3.8: Illustration of the methods used in the formulation of MTCGs to satisfy the governing equations and enforce the various boundary conditions in a polycrystalline sample with voids/inclusions	94
Figure 4.1: Variations of (a) σ_θ / σ_o , (b) D_θ / σ_o , (c) E_θ / σ_o , (d) E_r / σ_o along the periphery of an elliptic void with $\zeta = 0$ and $\zeta = \pi/4$ in an infinite piezoelectric medium under mechanical loading	113
Figure 4.2: distribution of the components of the stress and electric displacement around an elliptic void with $\zeta = \pi/4$ in an infinite piezoelectric medium under mechanical loading.....	113
Figure 4.3: Variations of (a) σ_θ / D_o , (b) D_θ / D_o , (c) E_θ / D_o , (d) E_r / D_o along the periphery of an elliptic void with $\zeta = 0$ and $\zeta = \pi/4$ in an infinite piezoelectric medium under electrical loading.....	114
Figure 4.4: distribution of the components of the stress and electric displacement around an elliptic void with $\zeta = \pi/4$ in an infinite piezoelectric medium under electrical loading.	114
Figure 4.5: Two representative volume elements (RVEs) used in the simulations	115
Figure 4.6: Predictions of the effective piezoelectric material properties of PZT-4 as functions of porosity volume fraction	116
Figure 4.7: Porous piezoelectric material under mechanical loading: Contour plot for (upper left) Principal stress, (upper right) Strain energy density, (lower) Dielectric energy density	118
Figure 4.8: Illustration of the methods used in the formulation of the different types of TLCGs to satisfy the governing equations and enforce the various boundary conditions in a polycrystalline sample with voids/inclusions (PVP refers to Primal Variational Principle, and BVP refers to Boundary Variational Principle).....	120

Figure 5.1: A 2D HDCG containing an inclusion or a void (independent trial displacement fields are used)	126
Figure 5.2: HDCG matrix and inclusion domains, boundaries and boundary nodes	127
Figure 5.3: A Finite rectangular domain with a circular void.....	132
Figure 5.4: Circumferential stress and electric displacement on the periphery of the void.....	132
Figure 5.5: Circumferential and radial components of electric field on the periphery of the void.	133
Figure 5.6: The effect of Γ on σ_θ / σ_o , D_θ / σ_o , E_θ / σ_o and E_r / σ_o along the inclusion periphery	134
Figure 5.7: Two Representative volume elements (RVEs) used in the simulations.....	135
Figure 5.8: Predictions of the effective piezoelectric materials properties of PZT-4 as functions of porosity volume fraction (m is the number of grains used).....	136
Figure 5.9: Predictions of the effective properties of SiC/PVDF piezoelectric composite as a function of particle volume fraction	138
Figure 5.10: Illustration of the methods used in the formulation of HDCGs to satisfy the governing equations and enforce the various boundary conditions in a polycrystalline sample with voids/inclusions (HVP refers to Hybrid Variational Principle, EM: Electro-mechanical).	140
Figure 6.1: 2D irregular polygon (Voronoi cell) with 5 nodes ($m = 5$)	150
Figure 6.2: Polyhedron (3D Voronoi cell) element with arbitrary number of polygonal faces..	151
Figure 6.3: Definition of triangles B_i and $A_i(\mathbf{x})$	152
Figure 6.4: (left) collocation points on one boundary surface of the 3D RBFCG. (right) triangulating each boundary surface and taking the Gaussian points in each triangle to be the RBF centers and collocation points	153

Figure 6.5: Patch test for 2D RBFCGs	172
Figure 6.6: (a) A schematic representation of the variation in a FGM microstructure: (b) and (d) typical microstructure at small volume fractions of the two materials; (c) typical microstructure at comparable volume fractions of the two materials	173
Figure 6.7: The three considered mesh configurations: the first with VF of $\text{Ni}_3\text{Al} \approx 0.6$, the second with VF of $\text{Ni}_3\text{Al} \approx 0.5$, the third with VF of $\text{Ni}_3\text{Al} \approx 0.4$ (The blue color denotes Ni_3Al and the red color denotes TiC).....	176
Figure 6.8: The results of the current model for the Effective Young's modulus (left) and effective Poisson's ratio (right) compared to the experimental and other models from the literature	177
Figure 6.9: 2D mesh used in the simulation with the x'_3 -crystallographic axis of each grain shown	178
Figure 6.10: 3D mesh used in the simulation (100 3D Voronoi cells)	179
Figure 6.11: surfaces of the ferroelectric specimen	180
Figure 6.12: Experimental observation of a ferroelectric polycrystal (PZT-51) under electromechanical loading conditions with a cyclic external electric field and constant external compressive stresses, taken from [44]: (a) macroscopic electric displacement and (b) macroscopic strain	181
Figure 6.13: Simulated response of ferroelectric polycrystalline under electromechanical loading conditions with a cyclic external electric field and constant external compressive stresses (2D mesh: 200 RBFCGs)	182

Figure 6.14: Simulated response of ferroelectric polycrystalline under electromechanical loading conditions with a cyclic external electric field and constant external compressive stresses (3D mesh: 100 RBFCGs)	183
Figure 6.15: Simulation results representing the local distribution of strain, stress (Pa), electric field (V/m) and electric displacement (C/m^2) at points “A”, “B”, and “C”	184
Figure 6.16: Simulation results representing the local distribution of strain, stress (Pa), electric potential (V), electric field (V/m) and electric displacement (C/m^2) at points “A”, “B”, and “C” (3D model: 100 RBFCGs)	187
Figure 6.17: Some grains are removed from the ferroelectric specimen to show the stress distribution (Pa) in the inner grains	187
Figure 6.18: (Left): Stress-strain hysteresis loop in ferroelastic switching, (right): X_1 - and X_3 - aligned volume fractions in ferroelastic switching (2D model).....	189
Figure 6.19: Stress-strain hysteresis loop in ferroelastic switching (3D model)	189
Figure 6.20: Illustration of the methods used in the formulation of RBFCGs to satisfy the governing equations and enforce the various boundary conditions in a polycrystalline sample (PVP refers to Primal Variational Principle)	191

LIST OF TABLES

Table 1.1: Material properties used in the numerical examples [C_{ij} in GPa, e_{ij} in C/m ² , h_{ii} in pC/(Vm)].....	54
Table 3.1: Discrete extreme mechanical and electrical errors as more collocation points are removed from the outer boundary (white noise with 40 dB SNR is added to the prescribed data on the outer boundary)	87
Table 4.1: different TLCGs and the corresponding methods used to satisfy the different conditions (BVP refers to “Boundary variational principle” and PVP refers to “Primitive variational principle”)	100
Table 4.2: Discrete extreme error for the considered grains in different cases	112
Table 7.1: The proposed numerical methods and their capabilities.....	199

ACKNOWLEDGMENTS

I would like to express the deepest appreciation to my committee chair and academic advisor, Professor Satya N. Atluri, for his outstanding professional advices, great care and encouragement, and financial support. Without his guidance and persistent help this dissertation would not have been possible.

I gratefully thank my colleague, Professor Leiting Dong, Hohai University, China, for the fruitful collaboration we made together and the excellent ideas he provided. I also thank Professor Jan Sladek, Slovak Academy of Science, Slovakia, for his help in part of my study.

I would like to thank my committee members, Professor Lorenzo Valdevit and Professor Timothy J. Rupert for their review of this study and for the time they spent with me in useful technical and professional discussions.

Finally, I thank my wife for her patience, care and understanding throughout my study, and our parents for their great love and encouragement.

CURRICULUM VITAE

Peter L. Bishay

Education

- **PhD program, Mechanical and Aerospace Engineering, the Henry Samueli School of Engineering, University of California Irvine, USA** Sept. 2011 – Feb. 2014
GPA: 4.0, Course Units: 16, Research Units: 68.
Dissertation: *Multi-Physics Computational Grains (MPCGs): Newly-Developed Accurate and Efficient Numerical Methods for Micromechanical Modeling of Multifunctional Materials and Composites.*
Advisor: Satya N. Atluri, Distinguished Professor, Mechanical and Aerospace Engineering, University of California, Irvine.
- **PhD program, Mechanical and Aerospace Engineering, Rutgers, the State University of New Jersey, USA** Sept. 2010 – Aug. 2011
GPA: 4.0, Course Credits: 24, Research Credits: 3.
- **MSc, Aerospace Engineering, Cairo University, Egypt** Sept. 2007 – July 2010
Equivalent GPA: 3.83 (94%), Course Credits: 24, Research Credits: 48.
Overall grade: Distinction.
Thesis: *Finite Element and Experimental Models of an Adaptive Magnetorheological Sandwich Beam Structure.*
- **BSc, Aerospace Engineering, Cairo University, Egypt** Sept. 2002 – July 2007
Equivalent GPA: 3.82 (91.69%), Course Credits: 150, Research Credits: 6.
Overall grade: Distinction with honorary degree, (Ranked “Second”).
Graduation project: *Sensitivity Analysis and Design Optimization of Micro-Satellite Structure.*

Fields of Interest

- Smart and Multifunctional Materials and Structures.
- Structural and Solid Mechanics.
- Computational Modeling.
- Experimental Modal Analysis.
- Aerospace Structures.

Employment

- **Postdoctoral Scholar (Assistant Specialist)**: University of California Irvine, Mechanical and Aerospace Engineering. Mar. 2014 - Aug. 2014

- **Research/Teaching Assistant, Instructor of Record (Teaching Associate):** University of California Irvine, Mechanical and Aerospace Engineering. Sept. 2011- Feb. 2014
- **Research/Teaching Assistant, Instructor of Record:** Rutgers, the state University of New Jersey, Mechanical and Aerospace Engineering. Sept. 2010- Aug. 2011
- **Research/Teaching Assistant:** Cairo University, Egypt, Aerospace Engineering. Sept. 2007- Aug. 2010

Honors and Awards

- “**Teaching Assistant Award of Excellence (2013)**”, Department of Mechanical and Aerospace Engineering, University of California, Irvine.
- “**Mechanical and Aerospace Engineering Teaching Assistant of the Year (2012-2013)**”, Engineering Student Council (ESC), University of California, Irvine.
- The Henry Samueli School of Engineering Fellowship Award – University of California, Irvine (Fall 2011, Spring 2012).
- School of Engineering Graduate Fellowship Award - Rutgers, the State University of New Jersey - Mechanical and Aerospace Engineering Department (Fall 2010- Spring 2011).
- Honorary degree for the overall Distinction grade - Cairo University - Aerospace Engineering Department (May 2007).

Research Experience

- **Research Assistant** Sept. 2011 – Feb. 2014
Mechanical and Aerospace Engineering, University of California Irvine.
- Center for Aerospace Research and Education (CARE).
- International Collaboratory for fundamental studies in the Engineering Sciences (ICES).

Research content and responsibilities: developing new accurate and efficient finite elements for modeling the macro- and the micro-mechanics of multifunctional materials (piezoelectric, ferroelectric material, piezoelectric/piezomagnetic composites, porous piezoelectric materials and functionally graded materials) named “Multi-Physics Computational Grains” (MPCGs) [Matlab was used in coding], contributing to the development of “Agile2D” code for fatigue and fracture mechanics using FEAM (Finite Element Alternating Method) as well as writing its user manual.

- **Research Assistant** Feb. 2011 – Aug. 2011
Mechanical and Aerospace engineering, Rutgers, the state university of New Jersey, USA.

Research content: developing an analytical model for the mechanics of a detaching retina with/without a tear [Maple symbolic solver was used in this research].

- **Research Assistant** Sept. 2008 – Aug. 2010
Aerospace Engineering, Cairo University.

Research content: experimental modal analysis of a magnetorheological sandwich beam structure using multichannel data acquisition system in the vibrations lab. Finite element modeling of the dynamics of a magnetorheological sandwich beam structure.

Publications

Journal Papers:

- 1- **Bishay, P. L.**; Alotaibi, A.; Atluri, S. N. (2014): Multi-Region Trefftz Collocation Grains (MTCGs) for Modeling Piezoelectric Composites and Porous Materials in Direct and Inverse Problems. Submitted for publication in *Journal of Mechanics of Materials & Structures*.
- 2- **Bishay, P. L.**; Dong, L.; Atluri, S. N. (2014): Multi-Physics Computational Grains (MPCGs) for Direct Numerical Simulation (DNS) of Piezoelectric Composite/Porous Materials and Structures. Submitted for publication in *Computational Mechanics*.
- 3- **Bishay, P. L.**; Atluri, S. N. (2014): Trefftz-Lekhnitskii Grains (TLGs) for Efficient Direct Numerical Simulation (DNS) of the Micro/Meso Mechanics of Porous Piezoelectric Materials. *Computational Materials Science*, vol. 83, pp. 235–249.
- 4- **Bishay, P. L.**; Atluri, S. N. (2013): 2D and 3D Multiphysics Voronoi Cells Based on Radial Basis Functions, for Direct Mesoscale Numerical Simulation (DMNS) of the Switching Phenomena in Ferroelectric Polycrystalline Materials. *CMC: Computers, Materials & Continua*, vol. 33, no. 1, pp. 19-62.
- 5- **Bishay, P. L.**; Sladek, J.; Sladek V.; Atluri, S. N. (2012): Analysis of Functionally Graded Magneto-Electro-Elastic Composites Using Hybrid/Mixed Finite Elements and Node-Wise Material Properties. *CMC: Computers, Materials & Continua*, vol. 29, no.3, pp. 213-262.
- 6- **Bishay, P. L.**; Atluri, S. N. (2012): High-Performance 3D Hybrid/Mixed, and Simple 3D Voronoi Cell Finite Elements, for Macro- & Micro-mechanical Modeling of Solids, Without Using Multi-field Variational Principles. *CMES: Computer Modeling in Engineering & Sciences*, vol.84, no.1, pp.41-97.
- 7- Bottega, W. J.; **Bishay, P. L.**; Prenner, J. L.; Fine, H. F. (2012): On the Mechanics of a Detaching Retina. *Mathematical Medicine and Biology*, doi: 10.1093/imammb/dqs024.

Under preparation:

- 1- **Bishay, P. L.**; Atluri, S. N. (2014): Micromechanical Modeling of Heterogeneous Piezoelectric/Piezomagnetic composites using Multi-Physics Trefftz Grains (MPTGs).

Conferences and Conference Papers:

- 1- **Bishay, P. L.**; Atluri, S. N. (2013): Simulating Ferroelectric Switching Phenomena Using 3D Multiphysics Voronoi Cells (MVC) Based on Radial Basis Functions and Washspress Coordinates. *ICCES'13*, Seattle, USA, May 24-28, 2013.

- 2- **Bishay, P. L.**; Atluri, S. N. (2013): Newly-Developed Finite Elements for Modeling Functionally Graded Materials (FGM) in Micro- and Macro-Scales. *ICCES'13*, Seattle, USA, May 24-28, 2013.
- 3- Fine, H. F.; Prenner, J. L.; **Bishay, P. L.**; Roth, D. B.; Bottega W. J. (2012): A Mechanics Based Model of A Detaching Retina. *ARVO 2012 Annual Meeting*, Fort Lauderdale, Florida, United States, May 6-10, 2012.
- 4- **Bishay, P. L.**; Tawfik, M.; Negm, H. M. (2010): Finite Element and Spectral Element Models for an Adaptive Magnetorheological Sandwich Beam. *Proceedings of the AMME-14 conference*, 25-27 May 2010, Military Technical College, Egypt.
- 5- **Bishay, P. L.**; Tawfik, M.; Negm, H. M. (2010): Analysis of an Adaptive Magnetorheological Sandwich Beam Structure Based on Experimental and Finite Element Models. *Proceedings of the ICSV-17 conference*, 18-22 July 2010, Cairo, Egypt.

User Manuals

- 1- “Agile2D” (Finite Element Alternating Method (FEAM) for crack analysis and propagation), Center for Aerospace Research and Education (CARE), University of California, Irvine, 2012.
- 2- “Vibration and Modal Analysis Using B&K Multichannel Analysis System Type 3550”, Dynamics and Vibration Laboratory, Aerospace Engineering, Cairo University, 2009.

Teaching Experience

- **Instructor of Record**, MAE80, CEE80, ENGR80: Dynamics (Spring 2013). Mechanical and Aerospace Engineering, University of California Irvine [150 students].
Responsibilities: conduct the entire instruction (three lectures a week), select textbook and design syllabus, create weekly quizzes (solved in lectures using i-clicker system), create midterm and final exams, direct the work of three teaching assistants, design and manage the course website using EEE online system, supervise the course forum and the online homework submission system (learn.uci.edu), conform with the ABET accreditation requirements and write ABET reports, publish weekly hints on homework problems, hold weekly office hours, reply to students’ e-mails, assign students’ final scores and letter grades, and proctor exams.
- **Instructor of Record**, MAE 650:291: Introduction to Mechanics of materials (Summer 2011). Rutgers, the state University of New Jersey, Mechanical and Aerospace Engineering [15 students].
Responsibilities: conduct the entire instruction (lectures and discussion sessions), select textbook and design syllabus, create and grade midterm and final exams, create and grade homework, design and manage the course website using “sakai” online system, hold weekly office hours, reply to students’ e-mails, assign students’ final scores and letter grades, and proctor exams.
- **Teaching Associate**, MAE295: Multifunctional materials and structures (Winter 2013). Mechanical and Aerospace Engineering, University of California Irvine [6 students].
Responsibilities: give lectures on the different types of smart materials and structures (ferroelectric, piezoelectric and pyroelectric materials, magnetorheological and

electrorheological fluids, active and passive vibration damping), hold weekly office hours, create and grade homework and final term project, arrange lab visits and reply to students' e-mails.

- **Teaching Assistant**, MAE150, ENGR150: Mechanics of structures (Fall 2012, Fall 2013). Mechanical and Aerospace Engineering, University of California Irvine [230 students].

Responsibilities: conduct 5 discussion sessions a week, hold weekly office hours, give few lectures in replacement of the instructor, grade two term projects, handle all issues related to "MasteringEngineering" online grading system, reply to students' e-mails, and proctor exams.

- **Teaching Assistant**, AER 403B: Aircraft Structural Design (Spring 2010).

AER 405B: Rocket Propulsion Systems (Spring 2010).

AER 403A: Structural Design of Flight Vehicles (Fall 2007, 2008, 2009).

AER 203A: Mechanics of Structures (Fall 2007).

Aerospace Engineering, Cairo University.

Responsibilities: conduct weekly discussion sessions, hold weekly office hours, lead lab sessions (PATRAN/Femap structural analysis software), grade students' homework, grade midterm and final exams, reply to students' e-mails, and proctor exams.

Courses Previously Taught

- **Dynamics** (MAE80, CEE80, ENGR80), Mechanical and Aerospace Engineering, University of California Irvine (Spring 2013).
- **Introduction to Mechanics of materials** (MAE 650:291), Rutgers, the state University of New Jersey, Mechanical and Aerospace Engineering (Summer 2011).
- **Multifunctional Materials and Structures** (MAE295), Mechanical and Aerospace Engineering, University of California Irvine (Winter 2013).
- **Mechanics of Structures** (MAE150, ENGR150), Mechanical and Aerospace Engineering, University of California Irvine (Fall 2012, Fall 2013).
- **Aircraft Structural Design** (AER 403B), Aerospace Engineering, Cairo University (Spring 2010).
- **Structural Design of Flight Vehicles** (AER 403A), Aerospace Engineering, Cairo University (Fall 2007, 2008, 2009).
- **Rocket Propulsion Systems** (AER 405B), Aerospace Engineering, Cairo University (Spring 2010).
- **Mechanics of Structures** (AER 203A), Aerospace Engineering, Cairo University (Fall 2007).

Teaching Certificates and Programs

- "2012 TA Professional Development Program" (Teaching, Learning and Technology Center, University of California, Irvine).
- "Creative Teaching Practices" workshop series 2010-2011 (Teaching Assistant Project, Graduate school, New Brunswick, Rutgers University).

- “Assessment in Higher Education” workshop series 2010-2011 (Teaching Assistant Project, Graduate School, New Brunswick, Rutgers University).
- “Quality Standards in Teaching” (Cairo University, June 2010).

Professional Service and Membership

- **Technical Reviewer:** Tech Science Press:
CMC: *Computers, Materials & Continua*, 2012 to present.
CMES: *Computer Modeling in Engineering and Sciences*, 2012 to present.
- Mentoring high-school student for 250 research hours in “St. Margaret’s Episcopal School Summer Internship Program” at The Henry Samueli School of Engineering, UCI, Summer 2013.
- Membership in American Society of Mechanical Engineers (ASME).
- Membership in the Mechanical and Aerospace Engineering Graduate Advisory Board, University of California, Irvine.

Skills

Computer Skills:

- Highly proficient in MATLAB and MAPLE.
- Highly proficient in structural analysis software (Patran, Nastran, Ansys, Femap, COMSOL).
- Highly proficient in CAD software (Pro-Engineer, SolidWorks, AutoCAD).
- Proficient in FORTRAN.
- Proficient in LMS CADA-PC and LMS Test.Lab Modal Analysis Software.
- Highly proficient in Microsoft office applications (Word, Excel, PowerPoint, Publisher and Outlook).

Additional Skills:

- Highly proficient in using Multichannel Analysis Systems and the related sensory and actuating devices in Dynamics and Vibrations labs.
- Microcontroller Architecture Programming and Interfacing skills.

Trainings:

- Maintenance Basics for Aeronautical Engineering Undergraduates, Egypt Air, Egypt (July 2005).

ABSTRACT OF THE DISSERTATION

Multi-Physics Computational Grains (MPCGs): Newly-Developed Accurate and Efficient
Numerical Methods for Micromechanical Modeling of Multifunctional Materials and
Composites

By

Peter L. Bishay

Doctor of Philosophy in Mechanical and Aerospace Engineering

University of California, Irvine, 2014

Professor Satya N. Atluri, Chair

This study presents a new family of highly accurate and efficient computational methods for modeling the multi-physics of multifunctional materials and composites in the micro-scale named “*Multi-Physics Computational Grains*” (MPCGs). Each “mathematical grain” has a random polygonal/polyhedral geometrical shape that resembles the natural shapes of the material grains in the micro-scale where each grain is surrounded by an arbitrary number of neighboring grains. The physics that are incorporated in this study include: Linear Elasticity, Electrostatics, Magnetostatics, Piezoelectricity, Piezomagnetism and Ferroelectricity. However, the methods proposed here can be extended to include more physics (thermo-elasticity, pyroelectricity, electric conduction, heat conduction, etc.) in their formulation, different analysis types (dynamics, fracture, fatigue, etc.), nonlinearities, different defect shapes, and some of the 2D methods can also be extended to 3D formulation.

We present “*Multi-Region Trefftz Collocation Grains*” (MTCGs) as a simple and efficient method for direct and inverse problems, “*Trefftz-Lekhnitskii Computational Gains*” (TLCGs) for modeling porous and composite smart materials, “*Hybrid Displacement*

Computational Grains” (HDCGs) as a general method for modeling multifunctional materials and composites, and finally “***Radial-Basis-Functions Computational Grains***” (RBFCGs) for modeling functionally-graded materials, magneto-electro-elastic (MEE) materials and the switching phenomena in ferroelectric materials.

The first three proposed methods are suitable for direct numerical simulation (DNS) of the micromechanics of smart composite/porous materials with non-symmetrical arrangement of voids/inclusions, and provide minimal effort in meshing and minimal time in computations, since each grain can represent the matrix of a composite and can include a pore or an inclusion. The last three methods provide stiffness matrix in their formulation and hence can be readily implemented in a finite element routine. Several numerical examples are provided to show the ability and accuracy of the proposed methods to determine the effective material properties of different types of piezo-composites, and detect the damage-prone sites in a microstructure under certain loading types.

The last method (RBFCGs) is also suitable for modeling the switching phenomena in ferro-materials (ferroelectric, ferromagnetic, etc.) after incorporating a certain nonlinear constitutive model and a switching criterion. Since the interaction between grains during loading cycles has a profound influence on the switching phenomena, it is important to simulate the grains with geometrical shapes that are similar to the real shapes of grains as seen in lab experiments. Hence the use of the 3D RBFCGs, which allow for the presence of all the six variants of the constitutive relations, together with the randomly generated crystallographic axes in each grain, as done in the present study, is considered to be the most realistic model that can be used for the direct mesoscale numerical simulation (DMNS) of polycrystalline ferro-materials.

INTRODUCTION

Nature offers numerous examples of materials that serve multiple functions. Biological materials routinely contain sensing, healing, actuation, and other functions built into the primary structures of an organism. The human skin, for instance, consists of many layers of cells, each of which contains oil and perspiration glands, sensory receptors, hair follicles, blood vessels, and other components with functions other than providing the basic structure and protection for the internal organs. These structures have evolved in nature over eons to the level of seamless integration and perfection with which they serve their functions. Scientists now seek to mimic these material systems in designing synthetic multifunctional materials using physics, chemistry, and mathematics to their advantage. The multifunctionality of these materials often occurs at scales that are nano through macro and on various temporal and compositional levels [1].

Multifunctional structural materials possess characteristics beyond the basic strength and stiffness that typically drive the science and engineering of the material for structural systems. Structural materials can be designed to have integrated electrical, magnetic, optical, locomotive, power generative, and possibly other functionalities that work together to provide advantages that reach new and unique capabilities beyond that of the individual capabilities. Traditional materials that provide high stiffness and strength, for instance, can be modified at the nanoscale to take on other properties such as energy absorption, self-healing, and even shape morphing. Materials of this kind have tremendous potential to impact future structural performance by reducing size, weight, cost, power consumption, and complexity while improving efficiency, safety, and versatility. The design of these new “smart” materials and systems has major implications for the defense, aerospace, energy, and semiconductor industries.

Bringing ferroelectricity and magnetism together in one material proved to be a difficult problem, as these phenomena turned out to be mutually exclusive [2]-[7]. Furthermore, it was found that the simultaneous presence of electric and magnetic dipoles does not guarantee strong coupling between the two, as microscopic mechanisms of ferroelectricity and magnetism are quite different and do not strongly interfere with each other [8]. However, designing composites made up of pure piezoelectric and pure piezomagnetic phases can lead to higher magnetoelectric (ME) coupling in the whole structure. Hence, the strong magnetoelectric effect is a *byproduct property* of the composite structure, which is absent in the individual phases [9]. Remarkably larger magnetoelectric effect is observed for composites than for either composite constituents in [10]-[12]. Strong megnetoelectric coupling can be utilized in energy conversion between the magnetic and electric fields, magnetic field probes, and smart sensors and transducers [13]. Due to the hysteretic nature of the ME effect, multiferroic composites may find applications in ME memory elements and memory devices. Further applications include magnetic field sensors and magnetically controlled opto-electronic devices. The transduction properties of the ME effect can also be employed in ME recording heads and electromagnetic pick-ups. Historical perspectives, status and future of multiferroic magnetoelectric composites are given in a review paper [14].

Piezoelectric materials are smart materials that are strained when subjected to electric fields (this is the so-called “direct effect”) and are electrically polarized when they are strained (which is the “converse effect”). Piezoelectric materials, together with corresponding sensing and actuating devices, which are featured with the coupled electromechanical behaviors, have experienced continuously growing applications within manufacturing, automotive and aerospace engineering, medical instruments, information & telecommunication, among many other civil and military industries. Transducers, actuators, frequency generators and smart material systems

for aerospace and medical industries, are among the several applications of these materials. During the last four decades, large amounts of experimental, analytical and computational research were conducted to study the linear and nonlinear behaviors of such materials in different applications under different loading conditions. In a market report by Acmite Market Intelligence [15] in 2010, the global demand on piezoelectric devices was valued at approximately *US\$14.8* billion in 2010, and has been healthily increasing even in the global economic downturns.

However, monolithic piezoelectric ceramics and piezoelectric polymers have their own limitations, such as high brittleness, low strength, high weight, undesired acoustic impedance, etc. Piezoelectric composites have therefore been studied and developed in the past two decades, by exploring the advantageous behaviors of both functional piezoelectric materials and load-bearing materials such as ceramics, polymers, metals, etc. Piezoelectric composites possess some enhanced properties over monolithic piezoelectric materials that enable them to be used in different industrial applications. Bigger range of coupled properties, better acoustic properties or figures of merit, and less brittleness are among these enhanced properties. Light-weight, easily-shaped, and relatively strong piezoelectric composites have found promising applications in various sensors, actuators, and other smart devices. Therefore, a thorough understanding of the global and local behaviors of piezoelectric materials and devices, from both top-down and bottom-up approaches has great practical values and has attracted much interest from many scholars.

Both “subtractive” and “additive” approaches were used to develop piezoelectric composites where, in the “subtractive” approach, controlled porosity was induced in piezoelectric materials to form porous piezoelectric materials with reduced density [16]. These porous piezoelectric materials found applications such as miniature accelerometers, vibration

sensors, contact microphones and hydrophones. Porous piezoelectric materials have several advantages such as lack of possibility of destructive chemical reactions between the piezoelectric ceramic and the second phase (the air) during production, ability to control pore size, shape and distribution (hence piezoelectric properties can be tailored), light weight compared to monolithic piezoelectric materials and other piezoelectric composites, reduced price of production compared to other piezoelectric composites, and low acoustic impedances compared to dense ceramics, hence they could be used to improve the mismatch of acoustic impedances at the interfaces of medical ultrasonic imaging devices or underwater sonar detectors [17].

On the other hand, in the “additive” approach, the effective properties of the composite are optimized by combining two or more constituents. The second phase is used to modulate the overall properties of piezoelectric composites and could be dielectric ceramic [18], metal [19], polymer [20], piezomagnetic [10] or another piezoelectric material. Piezoelectric ceramics are also used in smart composite materials where piezoelectric rods (fibers) or particles are embedded in an elastic matrix.

Piezoelectric-piezomagnetic composites can be developed in the form of secondary-phase piezoelectric (or piezomagnetic) inclusions embedded in a piezomagnetic (or piezoelectric) matrix. The secondary phase inclusions in the matrix of these composites could be long fibers, short fibers, disks, or dispersed particles. Piezoelectric-Piezomagnetic layered composites and functionally graded composites were also developed [9]-[14]. Obviously the introduction of inclusions into base media leads to the material being anisotropic, and complicated. Therefore, in order that the composite can offer a favorable behavior, it is important that the magnetoelectric effect be clearly analyzed from a micromechanics point of view so that the influence of each material parameter can be understood thoroughly.

Analytical models for porous and composite piezoelectric/piezomagnetic composites are only available for simple geometries such as an infinite piezoelectric plate with crack or circular /elliptical hole or inclusion as presented in [21]-[24] using either Lekhnitskii formalism [25] or the extended Stroh formalism [26], infinite domain with piezoelectric/piezomagnetic ellipsoidal inclusion using Eshelby type equivalent inclusion method [27]-[28]. However for more complicated geometries and practical problems, numerical methods such as finite elements, boundary elements, meshless or Trefftz methods should be used.

Modeling domains with defects (holes, inclusions or cracks) using the ordinary finite element method needs mesh refinement around defects in order to achieve acceptable results for the gradients of fields; hence it is very complex, time-consuming, and costly. Thus, special methods should be used to model defects. Special methods for Direct Numerical Simulation (DNS) of micro/meso structures were developed by Bishay and Atluri [29] for porous piezoelectric materials, by Bishay *et al.* [30] for piezoelectric composites, and by Dong and Atluri as 2D and 3D Trefftz [31]-[33] and SGBEM cells [34]-[35] for heterogeneous and functionally graded isotropic elastic materials, where each cell models an entire grain of the material, with elastic/rigid inclusions or voids, for direct numerical micromechanical analysis of composite and porous materials. Also 2D and 3D Radial-Basis-Function (RBF) grains were successfully used by Bishay and Atluri to model functionally-graded elastic materials in [36], and the switching phenomena in ferroelectric materials in [37]. Finite Elements with elliptical holes in elastic materials were also developed by Wang and Qin [38]. For piezoelectric materials, Wang *et al.* [39] developed a hybrid finite element with a hole based on Lekhnitskii formalism, while Cao *et al.* [40] developed a hybrid finite elements with defects based on the extended Stroh formalism. The boundary element method was also used by Xu and Rajapakse [41] to analyze

piezoelectric materials with elliptical holes. In addition, Trefftz methods were used to model microstructures with defects, using multi-source-point Trefftz method in [42] for plane elasticity, and Trefftz boundary collocation method based on Lekhnitskii formalism for plane piezoelectricity macromechanics developed by Sheng *et al.* [43], and for electromechanical direct and inverse problems in the micro-scale developed by Bishay *et al.* [44].

One of the most basic problems is to determine the electromechanical properties of composite materials, given geometry, distribution, volume fraction and electromechanical properties of each constitutive material. Besides, experimental methods and semi-analytical methods have been developed in the past two decades to predict the effective material coefficients, such as: piezoelectric Hanshin-Strikman type of bounds [45], and dilute, self-consistent, Mori-Tanaka methods ([46], [27]) based on an Eshelby type of solution in an infinite medium. Also, several studies have applied simple FEM to study the behavior of a unit-cell of piezoelectric composite, to predict the overall material coefficients, see [47]-[49].

It is also of great interest to understand the local behavior of piezoelectric composite materials and structures. On one hand, stress concentration in the local scale is one possible major factor that can cause damage of the material, especially for brittle piezoelectric constituents which are mostly used as fibers or particles buried into polymer matrices. On the other hand, the local stress and electric-displacement fields have also direct effects on the performance of various multi-functional smart devices. Among a few studies, Kim *et al.* [50] studied the multi-scale response of smart sandwich composites and the monitoring capabilities of piezoceramic wafers. Cook and Vel [51] developed a multi-scale model to study the macro-scale and micro-scale fields of laminate plates with piezoelectric composite actuators.

All the aforementioned methods are mostly oversimplified, and difficult to implement. For example, semi-analytical methods use Eshelby type of solution in an infinite domain, and cannot account for complex topology of microstructure. It is also very difficult for semi-analytical methods to study the local mechanical and electric fields. On the other hand, although simple FEM can model both global and local behaviors of composite materials and structures, it is very inefficient and requires significantly large times and resources for computing as well as human-labor in generating a complex mesh. For this reason, most simple FEM analyses in the literature use a simple unit-cell with only one inclusion, which oversimplifies the complicated material microstructure.

In this study, we present a new family of computational methods named “Multi-Physics Computational Grains” (MPCGs) for the direct numerical simulation (DNS) of the micromechanics of multifunctional materials with focus on piezoelectric, piezomagnetic, and ferroelectric materials and composites. However the formulation of these new methods can be directly extended to other types of material multifunctionality and the corresponding physics (such as thermoelectricity, pyroelectricity, ferromagnetism, etc.). This study just opens the gates for the development of these new accurate and efficient numerical tools. The MPCGs can not only accurately compute the overall stiffness and strength of materials, but can also easily compute the local stress/strain concentrations. The human labor of generating a compatible very fine FEM mesh is also saved, because each MPCG can represent a grain of the material in the most natural way.

The dissertation is organized as follows:

Chapter 1 gives the basic concepts that are essential for understanding the numerical methods in the remaining chapters. The chapter also presents brief descriptions of the behavior

of some types of smart materials such as piezoelectricity, piezomagnetism, and ferroelectricity. The governing equations and boundary conditions are also presented for the different types of the considered materials. Finally we provide a discussion on using the proposed numerical methods as a representative volume element (RVE) to determine the effective material properties and the special models used to predict these properties.

Chapter 2 is devoted for the generalized Lekhnitskii formulation for coupled/uncoupled electro-elastic/magneto-elastic materials. The chapter provides full expressions for all the mechanical, electrical and magnetic variables that can be used with coupled or uncoupled electro-elastic and magneto-elastic materials in interior and exterior domains. The chapter also presents the special solution set for the case of electromagnetically-impermeable elliptical voids.

Chapter 3 presents the first numerical method: “**Multi-Region Trefftz Collocation Grains**” (MTCGs). This method is very simple since it relies on collocation to enforce all boundary conditions. It can solve direct and inverse problems. Several numerical examples are given to show the capability and efficiency of this method to determine the effective material properties, detect damage locations and stress concentrations at some unreachable boundaries (cavities) in piezo-devices.

Chapter 4 uses Trefftz-Lekhnitskii formulation to formulate efficient and accurate polygonal finite elements that include voids/inclusions named “**Trefftz-Lekhnitskii Computational Grains**” (TLCGs) for the direct numerical simulation (DNS) of smart materials. Several numerical examples are given to illustrate the effectiveness of the proposed grains.

Chapter 5 presents “**Hybrid Displacement Computational Grains**” (HDCGs) that model piezo-composites accurately and efficiently without relying on Trefftz-Lekhnitskii formulation. Hence this method can be extended to model nonlinear problems. The HDCGs can

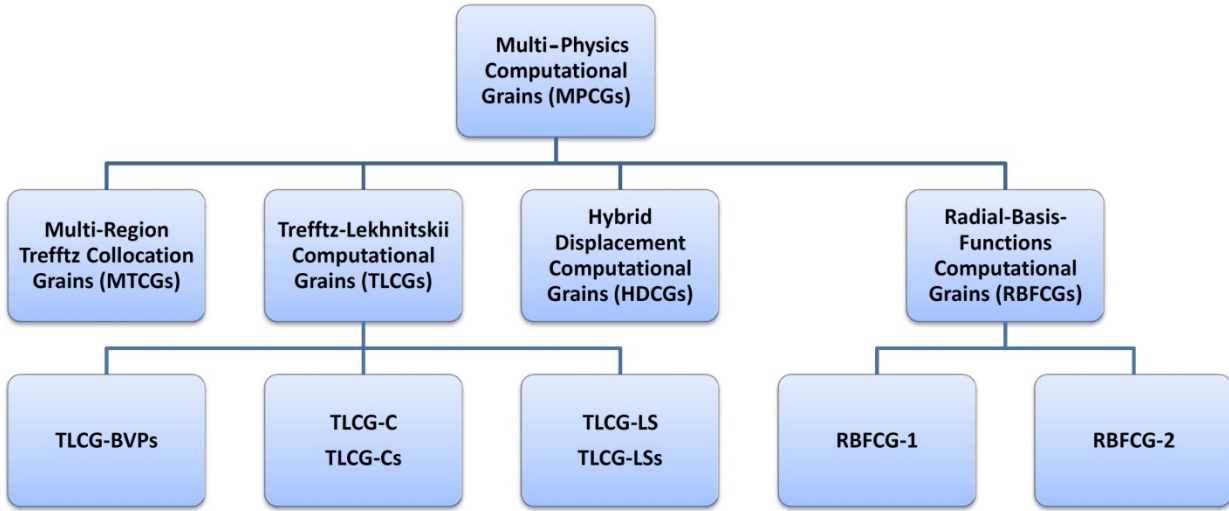
also be extended to the 3D case. The inclusion and the matrix in this new formulation are assembled exactly as any two finite elements are assembled because of the presence of nodes on the inclusion periphery. Numerical examples are given by the end of the chapter.

Chapter 6 presents 2D and 3D grains called “**Radial-Basis-Functions Computational Grains**” (RBFCGs) that can be used to model linear piezoelectric, piezomagnetic and functionally graded materials as well as the nonlinear ferroelectric materials when a switching criterion is incorporated. The results show the nonlinear hysteresis and butterfly loops that characterize ferroelectric materials when cyclic applied electric field causes domain switching. Stress concentrations in the microstructure can be accurately captured as well because the geometric shapes of the grains are similar to the natural shapes of grains in the micro-scale (random polyhedra in 3D). The method is based on Radial-Basis-Functions as interior fields and Washspress Barycentric Coordinates as the boundary fields in the 3D case.

By the end of each chapter, an illustrative drawing is given that summarizes the methods used to satisfy the governing equations and enforce the boundary conditions when the proposed numerical method is applied.

Finally chapter 7 gives final conclusions and summaries for the proposed methods and suggestions for the directions that can be taken to extend these methods to other important material types and practical engineering problems.

The figure below shows the “Mutli-Physics Computational Grains” (MPCGs) family presented in this dissertation. More details are given in the coming chapters.



References

- [1] Nemat-Nasser, S.; Nemat-Nasser, S.C.; Plaisted, T.; Starr, A.; Amirkhizi, A.V. (2005): *BIOMIMETICS: Biologically Inspired Technologies* (Ch. 12: Multifunctional Materials), CRC Press.
- [2] Schmid, H. (1994): Multi-ferroic magnetoelectrics. *Ferroelectrics*, vol. 162, pp. 317–338.
- [3] Hill, N. A. (2000): Why are there so few magnetic ferroelectrics? *J. Phys. Chem. B*, vol. 104, pp. 6694–6709.
- [4] Khomskii, D. I. (2001): Magnetism and ferroelectricity: why do they so seldom coexist? *Bull. Am. Phys. Soc.* C 21.002.
- [5] Lines, M. E.; Glass, A. M. (2001): *Principles and Applications of Ferroelectrics and Related Materials*, Oxford Univ. Press, Oxford.
- [6] Van Aken, B. B.; Palstra, T. T. M.; Filippetti, A.; Spaldin, N. A. (2004): The origin of ferroelectricity in magnetoelectric YMnO₃. *Nature Mater.*, vol. 3, pp. 164–170.

- [7] **Eerenstein, W.; Mathur, N.D.; Scott, J.F.** (2006): Multiferroic and magnetoelectric materials. *Nature*, vol. 442, pp. 759-765.
- [8] **Cheong, S.; Mostovoy, M** (2007): Multiferroics: a magnetic twist for ferroelectricity. *Nature Mater.*, vol. 6, pp. 13-20.
- [9] **Ryu, J.; Priya, S.; Uchino, K.; Kim, H.E.** (2002): Magnetoelectric effect in composites of magnetostrictive and piezoelectric materials. *J. Electroceramics*, vol. 8, pp. 107-119.
- [10] **Nan, C.W.** (1994): Magnetoelectric effect in composites of piezoelectric and piezomagnetic phases. *Phys. Rev. B*, vol. 50, pp. 6082-6088.
- [11] **Feng, W.J.; Su, R.K.L.** (2006): Dynamic internal crack problem of a functionally graded magneto-electro-elastic strip. *Int. J. Solids Structures*, vol. 43, pp. 5196-5216.
- [12] **Bishay, P. L.; Sladek, J.; Sladek V.; Atluri, S. N.** (2012): Analysis of functionally graded magneto-electro-elastic composites using hybrid/mixed finite elements and node-wise material properties. *CMC: Computers, Materials & Continua*, vol. 29, no.3, pp. 213-262.
- [13] **Wang, Y.; Yu, H.; Zheng, M.; Wan, J.G.; Zhang, M.F.; Liu, J.M.; Nan, C.W.** (2005): Numerical modeling of the magnetoelectric effect in magnetostrictive piezoelectric bilayer. *Applied Physics A*, vol. 81, pp. 1197-1202.
- [14] **Nan, C.W.; Bichurin, M.I.; Dong, S.X.; Viehland, D.** (2008): Multiferroic magnetoelectric composites: Historical perspective, status, and future directions. *Journal of Applied Physics*, 103,031101.
- [15] **Acmite Market Intelligence** (2010): *Market Report: World Piezoelectric Device Market*.

- [16] **Li, J.F.; Takagi, K.; Ono, M.; Pan, W.; Watanabe, R.; Almajid, A.** (2003): Fabrication and evaluation of porous piezoelectric ceramics and porosity-graded piezoelectric actuators. *J. Am. Ceram. Soc.*, vol. 86, pp. 1094-1098.
- [17] **Kumar, B.P.; Kumar H.H.; Kharat, D.K.** (2006): Effect of porosity on dielectric properties and microstructure of porous PZT ceramics, *Mater. Sci. Eng. B*, vol. 127, pp. 130–133.
- [18] **Jin, D.R.; Meng Z.Y.; Zhou, F.** (2003): Mechanism of resistivity gradient in monolithic PZT ceramics, *Mater. Sci. Eng. B*, vol. 99, pp. 83-87.
- [19] **Li, J.F.; Takagi, K.; Terakubo N.; Watanabe, R.** (2001): Electrical and mechanical properties of piezoelectric ceramic/metal composites in the Pb(Zr,Ti)O₃/Pt system, *Appl. Phys. Lett.*, vol. 79, pp. 2441-2443.
- [20] **Klicker, K.A.; Biggers J.V.; Newnham, R.E.** (1981): Composites of PZT and epoxy for hydrostatic transducer applications, *J. Am. Ceram. Soc.*, vol. 64, pp. 5-9.
- [21] **Sosa, H.** (1991): Plane problems in piezoelectric media with defects. *Int. J. Solids Struct.* vol. 28, no. 4, pp. 491–505.
- [22] **Xu X.L., Rajapakse R.K.N.D.** (1999): Analytical solution for an arbitrarily oriented void/crack and fracture of piezoceramics. *Acta Materialia*, vol. 47, pp.1735 –1747.
- [23] **Chung, M.Y.; Ting, T.C.T.** (1996): Piezoelectric solid with an elliptic inclusion or hole. *Int. J. Solids Struct.*, vol. 33, pp. 3343–3361.
- [24] **Lu, P; Williams, F.W.** (1998): Green functions of piezoelectric material with an elliptic hole or inclusion. *Int. J. Solids Struct.* vol. 35, pp. 651–664.
- [25] **Lekhnitskii, S.G.** (1968): *Anisotropic Plates*. Gordon and Breach, Science Publishers, New York.

- [26] **Stroh, A.N.** (1958): Dislocations and cracks in anisotropic elasticity. *Phil. Mag.* vol. 3, pp. 625–639.
- [27] **Dunn, M. L.; Taya, M.** (1993). Micromechanics predictions of the effective electroelastic moduli of piezoelectric composites. *International Journal of Solids and Structures*, vol. 30, no. 2, pp. 161-175.
- [28] **Huang, J. H.; Kuo, W** (1997): The analysis of piezoelectric/piezomagnetic composite materials containing ellipsoidal inclusions. *J. Appl. Phys.* vol. 81, no. 3, pp. 1378-1386.
- [29] **Bishay, P. L.; Atluri, S. N.** (2014): Trefftz-Lekhnitskii Grains (TLGs) for efficient direct numerical simulation (DNS) of the micro/meso mechanics of porous Piezoelectric materials, *Computational Materials Science*, vol. 83, pp. 235–249.
- [30] **Bishay, P. L.; Dong, L.; Atluri, S. N.** (2014): Multi-Physics Computational Grains (MPCGs) for direct numerical simulation (DNS) of piezoelectric composite/porous materials and structures. Submitted for publication in *Computational Mechanics*.
- [31] **Dong, L.; Atluri, S. N.** (2012a): T-Trefftz Voronoi cell finite elements with elastic/rigid inclusions or voids for micromechanical analysis of composite and porous materials. *CMES: Computer Modeling in Engineering & Sciences*, vol.83, no.2, pp.183-219.
- [32] **Dong, L.; Atluri, S. N.** (2012b): Development of 3D T-Trefftz Voronoi cell finite elements with/without spherical voids &/or elastic/rigid inclusions for micromechanical modeling of heterogeneous materials. *CMC: Computers, Materials & Continua*, vol. 29, no. 2, pp. 169–211.
- [33] **Dong, L.; Atluri, S. N.** (2012c): Development of 3D Trefftz Voronoi cells with ellipsoidal voids &/or elastic/rigid inclusions for micromechanical modeling of

heterogeneous materials. *CMC: Computers, Materials & Continua*, vol. 30, no. 1, pp. 39–82.

- [34] **Dong, L.; Atluri, S. N.** (2012d): SGBEM (using non-hyper-singular traction BIE), and super elements, for non-collinear fatigue-growth analyses of cracks in stiffened panels with composite-patch repairs. *CMES: Computer Modeling in Engineering & Sciences*, vol. 89, no. 5, pp. 417–458.
- [35] **Dong, L.; Atluri, S. N.** (2013a): SGBEM Voronoi Cells (SVCs), with embedded arbitrary-shaped inclusions, voids, and/or cracks, for micromechanical modeling of heterogeneous materials. *CMC: Computers, Materials & Continua*, vol. 33, no.2, pp.111-154.
- [36] **Bishay, P. L.; Atluri, S. N.** (2012): High-performance 3D hybrid/mixed, and simple 3D Voronoi cell finite elements, for macro- & micro-mechanical modeling of solids, without using multi-field variational principles, *CMES: Computer Modeling in Engineering & Sciences*, vol. 84, no. 1, pp. 41-98.
- [37] **Bishay, P. L.; Atluri, S. N.** (2013): 2D and 3D Multiphysics Voronoi cells, based on radial-basis-functions, for direct mesoscale numerical simulation (DMNS) of the switching phenomena in ferroelectric polycrystalline materials, *CMC: Computer Modeling in Engineering & Sciences*, vol. 33, no. 1, pp. 19-62.
- [38] **Wang, H.; Qin, Q.H.** (2012): A new special element for stress concentration analysis of a plate with elliptical holes. *Acta Mech.* vol. 223, pp. 1323–1340.
- [39] **Wang, X.W.; Zhou, Y.; Zhou, W.L.** (2004): A novel hybrid finite element with a hole for analysis of plane piezoelectric medium with defects. *International Journal of Solids and Structures*, vol. 41, pp. 7111–7128.

- [40] **Cao, C.; Yu, A.; Qin Q.H.** (2013): A new hybrid finite element approach for plane piezoelectricity with defects. *Acta Mech*, vol. 224, pp. 41–61.
- [41] **Xu X.L., Rajapakse R.K.N.D.** (1998): Boundary element analysis of piezoelectric solids with defects. *Composites B*, vol. 29, no. 5, pp. 655-669.
- [42] **Dong, L.; Atluri, S. N.** (2012e): A simple multi-source-point Trefftz method for solving direct/inverse SHM problems of plane elasticity in arbitrary multiply-connected domains. *CMES: Computer Modeling in Engineering & Sciences*, vol.85, no.1, pp.1–43.
- [43] **Sheng, N.; Sze, K.Y.; Cheung, Y.K.** (2006): Trefftz solutions for piezoelectricity by Lekhnitskii's formalism and boundary collocation method. *Int. J. Numer. Methods Eng.* vol. 65, pp. 2113–2138.
- [44] **Bishay, P. L.; Alotaibi, A.; Atluri, S. N.** (2014): Multi-region Trefftz Collocation Grains (MTCGs) for modeling piezoelectric composites and porous materials in direct and inverse problems. Submitted for publication in *Journal of Mechanics of Materials & Structures*.
- [45] **Bisegna, P.; Luciano, R.** (1996): Variational bounds for the overall properties of piezoelectric composites. *Journal of the Mechanics and Physics of Solids*, vol. 44, no. 4, pp. 583-602.
- [46] **Benveniste, Y.** (1993): Universal relations in piezoelectric composites with eigenstress and polarization fields. I: Binary media: local fields and effective behavior. *Journal of applied mechanics*, vol. 60, no. 2, pp. 265-269.
- [47] **Gaudenzi, P.** (1997): On the electromechanical response of active composite materials with piezoelectric inclusions. *Computers & Structures*, vol. 65, no. 2, pp. 157-168.

- [48] Berger, H.; Gabbert, U.; Koppe, H.; Rodriguez-Ramos, R.; Bravo-Castillero, J.; Guinovart-Diaz, R.; Otero, J. A.; Maugin G. A. (2003): Finite element and asymptotic homogenization methods applied to smart composite materials. *Computational Mechanics*, vol. 33, pp. 61–67.
- [49] Berger, H.; Kari, S.; Gabbert, U.; Rodriguez-Ramos, R.; Guinovart, R.; Otero, J. A.; Bravo-Castillero, J. (2005). An analytical and numerical approach for calculating effective material coefficients of piezoelectric fiber composites. *International journal of solids and structures*, vol. 42, no. 21, pp. 5692-5714.
- [50] Kim, J. S.; Aronche, L.; Farrugia; A., Muliana, A.; La Saponara, V. (2011): Multi-scale modeling of time-dependent response of smart sandwich constructions. *Composite Structures*, vol. 93, no. 9, pp. 2196-2207.
- [51] Cook, A. C.; Vel, S. S. (2012): Multiscale analysis of laminated plates with integrated piezoelectric fiber composite actuators. *Composite Structures*, vol. 94, no. 2, pp. 322-336.

Chapter 1 : Basic Concepts and Governing Equations

1.1 Introduction

In this chapter we present a brief description of piezoelectricity in section 1.2, and of piezomagnetism in section 1.3. This is followed by the governing equations for Magneto-Electro-Elastic (MEE) composites in section 1.4. Plane-stress and plane-strain assumptions commonly used in many engineering applications are discussed in section 1.5. Brief description of ferroelectricity is presented in section 1.6, and the additional governing equations for modeling ferroelectricity are addressed in section 1.7. The difference between Micromechanics and Macromechanics is covered in section 1.8. Discussion on using representative volume element (RVE) to predict the effective material properties of piezo-composites is mentioned in section 1.9, while section 1.10 presents special numerical models used to determine the effective material properties of piezo-composites. Finally the references mentioned in this chapter are listed in section 1.11.

1.2 Brief description of Piezoelectricity

The most widely used piezoelectric materials such as barium titanate (BaTiO_3) and lead zirconate titanate (PZT) crystallize in the perovskite structure [1]. The chemical compositions for perovskites can be expressed as ABO_3 , in which O denotes oxygen whereas A and B denote respectively a group 2 and a group 4 elements in the periodic table. In the case of barium titanate, A and B are respectively the divalent cation Ba^{2+} and the tetravalent cation Ti^{4+} . In the case of PZT ceramics, divalent (Pb^{2+}) and tetravalent ($\text{Zr}^{4+}, \text{Ti}^{4+}$) cations are substituted for A and B sites, respectively. The properties of the material can be modified by adding other metal oxides to form compounds such as $(\text{Pb},\text{La})(\text{Zr},\text{Sn},\text{Ti})\text{O}_3$ in which A can be $(\text{Pb}^{2+},\text{La}^{2+})$ and B can be $(\text{Zr}^{4+},\text{Sn}^{4+},\text{Ti}^{4+})$.

At high temperature, the large thermal agitation enables a large inter-atomic spacing and the unit cell for the ABO_3 perovskite is cubic with side length a_0 , see Figure 1.1(a). The A^{2+} ions are located at the corners of the unit cell, the B^{4+} ion is located at the body center of the unit cell, and the O^{2-} ions are located at the centers of the faces. Since the ions lie symmetrically in the unit cell, no polarization can be observed. The material is in a paraelectric phase and does not exhibit electromechanical coupling effect. As the temperature drops below a critical value which is known as the Curie point T_c , the unit cell shrinks and becomes non-cubic. The material is in a piezoelectric phase. A possible unit cell structure is the tetragonal one with the dimensions of $a \times a \times c$ as shown in Figure 1.1(b). In the tetragonal unit cell, the central B^{4+} ion is displaced relative to the surrounding O^{2-} ions. It leads to an ionic dipole moment which is a vector pointing from the center of the negative charges to that of the positive charges. Consequently, the tetragonal unit cell possesses a spontaneous polarization as a result of the dipole moment.

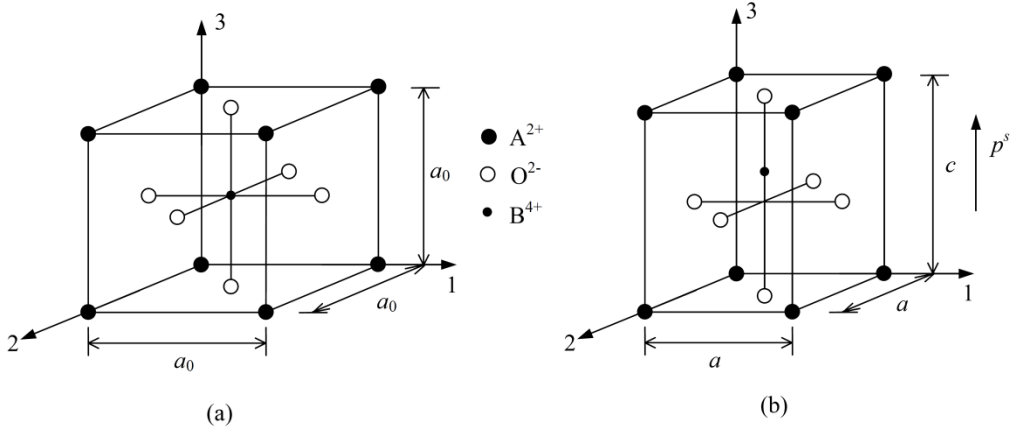


Figure 1.1: Transformation from (a) cubic to (b) tetragonal unit cell of ABO_3 .

There are six possible directions for each tetragonal unit cell to accommodate the central B^{4+} ion along the crystallographic axes (i.e. the axes 1, 2 and 3 of the original cube). In other words, there are six possible spontaneous polarization directions. Figure 1.1(b) shows one of the

spontaneous polarization directions along the positive crystallographic axis 3. In this case, the spontaneous polarization vector \mathbf{p}_i^S in the local coordinate system (1, 2, 3) can be expressed as:

$$\mathbf{p}_i^S = \begin{Bmatrix} 0 & 0 & p^S \end{Bmatrix}^T \quad (1.1)$$

where p^S is the magnitude of the spontaneous polarization vector. The transformation from paraelectric phase to piezoelectric phase also induces a spontaneous strain vector $\boldsymbol{\varepsilon}_i^S$ which can be seen from Figure 1.1 (b) to be:

$$\boldsymbol{\varepsilon}_i^S = \begin{Bmatrix} \varepsilon_{11}^S & \varepsilon_{22}^S & \varepsilon_{33}^S & 2\varepsilon_{12}^S & 2\varepsilon_{23}^S & 2\varepsilon_{31}^S \end{Bmatrix}^T = \begin{Bmatrix} \frac{a-a_0}{a_0} & \frac{a-a_0}{a_0} & \frac{a-a_0}{a_0} & 0 & 0 & 0 \end{Bmatrix}^T \quad (1.2)$$

It is the tetragonal unit cell structure that results in the well-known piezoelectricity, i.e. electromechanical coupling phenomenon of piezoelectric materials [1]. When a mechanical stress is applied to a piezoelectric material, the relative distance between the central B^{4+} ion and the surrounding O^{2-} ions in the unit cell will change in order to accommodate the geometric strain induced by the stress. This leads to a change in the spontaneous polarization. This phenomenon is called the direct piezoelectric effect. Conversely, when an electric load is applied, the central B^{4+} ion in the unit cell will be displaced relative to the surrounding O^{2-} ions and a geometric strain will be induced in the unit cell. This phenomenon is known as the inverse piezoelectric effect. The direct and inverse piezoelectric effects are approximately linear when the applied mechanical and electric loads are small [2]. The linear behavior of piezoelectrics can be described by the well-established classical linear theory of piezoelectricity [2]-[5].

1.3 Brief description of Piezomagnetism

Piezomagnetism is the linear magneto-mechanical effect analogous to the linear electromechanical effect of piezoelectricity. The piezomagnetic effect is made possible by an

absence of certain symmetry elements in a crystal structure [6]. The first experimental observation of piezomagnetism was made in 1960, in the fluorides of cobalt and manganese [7]. Piezomagnetism is a phenomenon observed in some antiferromagnetic crystals. It is characterized by a linear coupling between the system's magnetic polarization and mechanical strain. In a piezomagnetic, one may induce a spontaneous magnetic moment by applying physical stress, or a physical deformation by applying a magnetic field.

Piezomagnetism differs from the related property of magnetostriction; if an applied magnetic field is reversed in direction, the strain produced changes signs. Additionally, a non-zero piezomagnetic moment can be produced by mechanical strain alone, at zero field - this is not true of magnetostriction [8]. Magnetostriction and electrostriction are analogous second-order effects. These higher-order effects can be represented effectively as first-order when variations in the system parameters are small compared with the initial values of the parameters.

Since the sources of magnetic anisotropy are different from those of electrical and mechanical anisotropies, we allow the magnetic bias direction to be different from the polling direction or the axis normal to the plane of isotropy in transversely isotropic materials. Actually, in the proposed 2D analysis, any kind of anisotropy in material properties can be considered.

The sources of magnetic anisotropy are [9]: (1) *Magnetocrystalline anisotropy*: the atomic structure of a crystal introduces preferential directions for the magnetization, (2) *Shape anisotropy*: when a particle is not perfectly spherical, the demagnetizing field will not be equal for all directions, creating one or more easy axes, (3) *Magnetoelastic anisotropy*: tension may alter magnetic behavior, leading to magnetic anisotropy, (4) *Exchange anisotropy*: occurs when antiferromagnetic and ferromagnetic materials interact [10].

1.4 Governing equations for magneto-electro-elastic (MEE) composites

Consider a domain Ω filled with a general magnetoelectroelastic (MEE) material with piezoelectric, piezomagnetic and magnetoelectric couplings. On the boundary of the domain, denoted $\partial\Omega$, we can specify mechanical displacements on S_u or tractions on S_t (not both at any point. i.e, $S_u \cap S_t = \emptyset$). Similarly we can specify electric potential on S_φ or electric charge per unit area (electric displacement) on S_Q (where $S_\varphi \cap S_Q = \emptyset$). We can also specify magnetic potential on S_ψ or magnetic flux density (magnetic induction) on S_B (where again $S_\psi \cap S_B = \emptyset$). So $\partial\Omega = S_u \cup S_t = S_\varphi \cup S_Q = S_\psi \cup S_B$. The whole domain Ω can be divided into N regions $\Omega = \sum_{e=1}^N \Omega^e$ (where each region may represent a grain in the material). The intersection between the boundary of grain e , denoted $\partial\Omega^e$, and $S_u, S_t, S_\varphi, S_Q, S_\psi$ and S_B are $S_u^e, S_t^e, S_\varphi^e, S_Q^e, S_\psi^e$ and S_B^e , while the intersection with the neighboring region boundaries is denoted S_g^e . Hence $\partial\Omega^e = S_u^e \cup S_t^e \cup S_g^e = S_\varphi^e \cup S_Q^e \cup S_g^e = S_\psi^e \cup S_B^e \cup S_g^e$.

Each grain domain, Ω^e , may contain a void or an inclusion filling the domain Ω_c^e and has a boundary $\partial\Omega_c^e$ such that $\Omega_c^e \subset \Omega^e$ and $\partial\Omega_c^e \cap \partial\Omega^e = \emptyset$. In this case, the region outside the void/inclusion domain in grain e is called the matrix domain $\Omega_m^e = \Omega^e - \Omega_c^e$. Figure 1.2 shows one grain (irregular polygonal region in the 2D case) with an arbitrary void/inclusion. The figure also shows the matrix polling direction (left) and the matrix magnetic bias direction (right), while Figure 1.3 shows the inclusion polling direction (left) and the inclusion magnetic bias direction (right) in case the inclusion material is piezoelectric or piezomagnetic, respectively. As mentioned in the previous section, the magnetic bias direction and the polling direction are

allowed to be different in this study since the sources that affect the magnetic anisotropy may not affect the electrical and mechanical anisotropies. In [11] the direction of the applied magnetizing field on the ferrite particles was made different from the polling direction of the piezoelectric matrix. The inclusions and the matrix are assumed to be perfectly bonded, without any sliding, void nucleation, or growth on their interfaces.

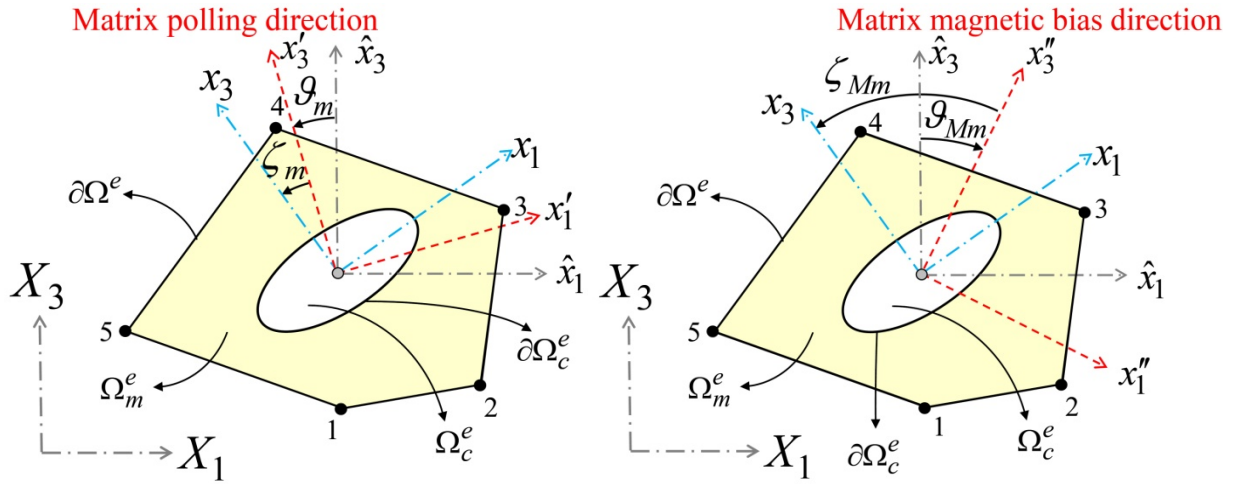


Figure 1.2: (left) 2D irregular polygon (grain) with an elliptical void/inclusion and its local coordinates as well as the global ($X_1 - X_3$), grain local ($\hat{x}_1 - \hat{x}_3$) Cartesian coordinate systems, matrix electric polling direction (x'_3), and matrix magnetic bias direction (x''_3).

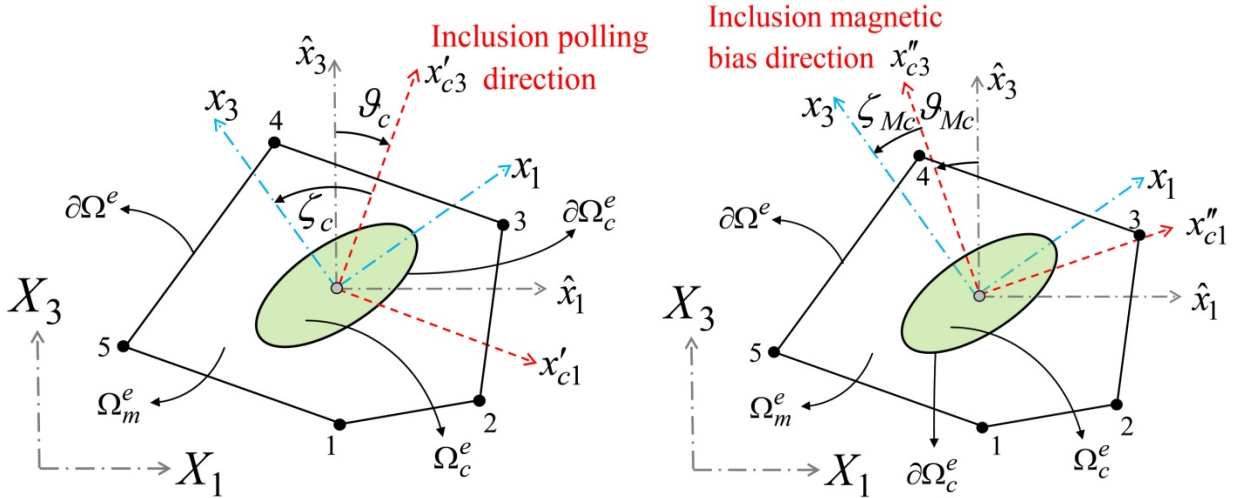


Figure 1.3: (left) 2D irregular polygon (grain) with an elliptical inclusion and its local coordinates as well as the global ($X_1 - X_3$), grain local ($\hat{x}_1 - \hat{x}_3$) Cartesian coordinate systems, inclusion electric polling direction (x'_{c3}), and inclusion magnetic bias direction (x''_{c3}).

Adopting matrix and vector notation and denoting \mathbf{u}^α (3 components), $\boldsymbol{\epsilon}^\alpha$ (6 components) and $\boldsymbol{\sigma}^\alpha$ (6 components) as the mechanical displacement vector, strain and stress tensors written in vector form respectively, φ^α (scalar), \mathbf{E}^α (3 components) and \mathbf{D}^α (3 components) as the electric potential, and electric field & electric displacement vectors respectively, and ψ^α (scalar), \mathbf{H}^α (3 components) and \mathbf{B}^α (3 components) as the magnetic potential, and magnetic field & magnetic induction (magnetic flux density) vectors respectively, where the superscript $\alpha = m$ or c (for matrix or inclusion), the following equations should be satisfied in the non-conducting matrix and inclusion domains (Ω_m^e and Ω_c^e):

1- Stress equilibrium and the electric and magnetic forms of Gauss's equations:

$$\partial_{\mathbf{u}}^T \boldsymbol{\sigma}^\alpha + \bar{\mathbf{b}}_f^\alpha = \mathbf{0}; \quad \boldsymbol{\sigma}^\alpha = (\boldsymbol{\sigma}^\alpha)^T, \quad \partial_{\mathbf{e}}^T \mathbf{D}^\alpha - \bar{\rho}_f^\alpha = 0, \quad \partial_{\mathbf{e}}^T \mathbf{B}^\alpha = 0 \quad (1.3)$$

where $\bar{\mathbf{b}}_f^\alpha$ is the body force vector, and $\bar{\rho}_f^\alpha$ is the electric free charge density (which is approximately zero for dielectric and piezoelectric materials). Note that the right hand-side of the third equation in eqs. (1.3) is zero because magnetic free charges do not exist in nature.

2- Strain-displacement (for infinitesimal deformations), Electric field-electric potential, Magnetic field-magnetic potential relations:

$$\boldsymbol{\epsilon}^\alpha = \partial_{\mathbf{u}} \mathbf{u}^\alpha, \quad \mathbf{E}^\alpha = -\partial_{\mathbf{e}} \varphi^\alpha \quad \mathbf{H}^\alpha = -\partial_{\mathbf{e}} \psi^\alpha \quad (1.4)$$

$$\text{where } \partial_{\mathbf{u}} = \begin{bmatrix} \frac{\partial}{\partial x_1} & 0 & 0 & \frac{\partial}{\partial x_2} & 0 & \frac{\partial}{\partial x_3} \\ 0 & \frac{\partial}{\partial x_2} & 0 & \frac{\partial}{\partial x_1} & \frac{\partial}{\partial x_3} & 0 \\ 0 & 0 & \frac{\partial}{\partial x_3} & 0 & \frac{\partial}{\partial x_2} & \frac{\partial}{\partial x_1} \end{bmatrix}^T \quad \partial_{\mathbf{e}} = \begin{bmatrix} \frac{\partial}{\partial x_1} & \frac{\partial}{\partial x_2} & \frac{\partial}{\partial x_3} \end{bmatrix}^T$$

This representation of electric and magnetic fields (eqs. (1.4)), as gradients of electric and magnetic potentials includes the assumption that Faraday's equation ($\nabla \times \mathbf{E}^\alpha = -\frac{\partial \mathbf{B}^\alpha}{\partial t} = \mathbf{0}$) and Ampere's law with Maxwell's correction ($\nabla \times \mathbf{H}^\alpha = \mathbf{J}^\alpha + \frac{\partial \mathbf{D}^\alpha}{\partial t} = \mathbf{0}$, where \mathbf{J}^α is the electric current density) are satisfied for electrostatics and magnetostatics. We assume that the materials are electrically non-conducting. Piezoelectrics are good dielectrics so they are normally non-conductors, while piezomagnetic (or magnetostrictive) materials may be insulators (like NiFe_2O_4 [11] and $\text{Mn}_{1-x}\text{Zn}_x\text{Fe}_2\text{O}_4$ [12]) and may be conductors (like CoFeV and Terfenol D [13]). So when dealing with piezoelectric-piezomagnetic fiber or particle composites subjected to electric loadings, we only consider electrically insulating (or non-conducting) piezomagnetic materials. Hence we assume, $\mathbf{J}^\alpha = \mathbf{J}_{\text{piezo}}^\alpha = \mathbf{J}_{\text{magneto}}^\alpha = \mathbf{0}$. Actually without this assumption, the analogy between piezoelectric and piezomagnetic materials breaks because in this case they are physically different and cannot be modeled with the same set of differential equations [14].

3- Constitutive laws:

$$\begin{Bmatrix} \mathbf{\sigma}^\alpha \\ \mathbf{D}^\alpha \\ \mathbf{B}^\alpha \end{Bmatrix} = \begin{Bmatrix} \mathbf{C}^\alpha & \mathbf{e}^{\alpha T} & \mathbf{d}^{\alpha T} \\ \mathbf{e}^\alpha & -\mathbf{h}^\alpha & -\mathbf{n}^{\alpha T} \\ \mathbf{d}^\alpha & -\mathbf{n}^\alpha & -\mathbf{m}^\alpha \end{Bmatrix} \begin{Bmatrix} \mathbf{\varepsilon}^\alpha \\ -\mathbf{E}^\alpha \\ -\mathbf{H}^\alpha \end{Bmatrix} \quad \text{Or,} \quad \begin{Bmatrix} \mathbf{\varepsilon}^\alpha \\ -\mathbf{E}^\alpha \\ -\mathbf{H}^\alpha \end{Bmatrix} = \begin{Bmatrix} \mathbf{S}^\alpha & \mathbf{g}^{\alpha T} & \mathbf{b}^{\alpha T} \\ \mathbf{g}^\alpha & -\boldsymbol{\beta}^\alpha & -\boldsymbol{\kappa}^{\alpha T} \\ \mathbf{b}^\alpha & -\boldsymbol{\kappa}^\alpha & -\mathbf{v}^\alpha \end{Bmatrix} \begin{Bmatrix} \mathbf{\sigma}^\alpha \\ \mathbf{D}^\alpha \\ \mathbf{B}^\alpha \end{Bmatrix} \quad (1.5)$$

where \mathbf{C}^α , \mathbf{h}^α , \mathbf{m}^α , \mathbf{S}^α , $\boldsymbol{\beta}^\alpha$ and \mathbf{v}^α are, respectively, the elastic stiffness tensor measured under constant electric and magnetic fields, dielectric permittivity tensor measured under constant strain and magnetic field, magnetic permeability tensor measured under constant strain and electric field, elastic compliance tensor measured under constant electric displacement and magnetic induction, inverse of the permittivity tensor measured under constant stress and

magnetic induction, and reluctivity tensor measured under constant stress and electric displacement. \mathbf{e}^α and \mathbf{g}^α are piezoelectric tensors, \mathbf{d}^α and \mathbf{b}^α are piezomagnetic tensors, and \mathbf{n}^α and $\mathbf{\kappa}^\alpha$ are electromagnetic tensors. The diagonal matrices in eq. (1.5) are positive definite.

The SI units of the mentioned fields are as follows: stress σ^α (Pa or N/m²), strain ϵ^α (m/m), electric displacement \mathbf{D}^α (C/m²), electric field \mathbf{E}^α (V/m or N/C), magnetic induction or magnetic flux density \mathbf{B}^α (N/Am or Vs/m²), magnetic field \mathbf{H}^α (A/m or C/ms), and the SI units of the material matrices are: \mathbf{C}^α (Pa or N/m²), \mathbf{S}^α (m²/N), \mathbf{h}^α (C/Vm), $\mathbf{\beta}^\alpha$ (Vm/C), \mathbf{m}^α (N/A²), \mathbf{v}^α (A²/N), \mathbf{e}^α (C/m²), \mathbf{g}^α (m²/C), \mathbf{d}^α (N/Am), \mathbf{b}^α (Am/N), \mathbf{n}^α (N/AV), and $\mathbf{\kappa}^\alpha$ (AV/N).

Note that $\mathbf{S}^\alpha \neq (\mathbf{C}^\alpha)^{-1}$, $\mathbf{\beta}^\alpha \neq (\mathbf{h}^\alpha)^{-1}$ and $\mathbf{m}^\alpha \neq (\mathbf{v}^\alpha)^{-1}$. The material constants in eqs. (1.5) are related through:

$$\begin{bmatrix} \mathbf{S}^\alpha & \mathbf{g}^{\alpha T} & \mathbf{b}^{\alpha T} \\ \mathbf{g}^\alpha & -\mathbf{\beta}^\alpha & -\mathbf{\kappa}^{\alpha T} \\ \mathbf{b}^\alpha & -\mathbf{\kappa}^\alpha & -\mathbf{v}^\alpha \end{bmatrix} = \begin{bmatrix} \mathbf{C}^\alpha & \mathbf{e}^{\alpha T} & \mathbf{d}^{\alpha T} \\ \mathbf{e}^\alpha & -\mathbf{h}^\alpha & -\mathbf{n}^{\alpha T} \\ \mathbf{d}^\alpha & -\mathbf{n}^\alpha & -\mathbf{m}^\alpha \end{bmatrix}^{-1} \quad (1.6)$$

If the material of the matrix or the inclusion is not piezoelectric, then the coupling piezoelectric matrices $\mathbf{e}^\alpha = \mathbf{g}^\alpha = \mathbf{0}$ in eq. (1.5) and if the material is not piezomagnetic, then $\mathbf{d}^\alpha = \mathbf{b}^\alpha = \mathbf{0}$. Commercially available monolithic piezoelectric and piezomagnetic materials have very small or no electromagnetic coupling, hence $\mathbf{n}^\alpha = \mathbf{\kappa}^\alpha = \mathbf{0}$.

1.4.1 Matrix boundary conditions

1- Mechanical natural (traction) and essential (displacement) boundary conditions:

$$\mathbf{n}_\sigma \boldsymbol{\sigma}^m = \bar{\mathbf{t}} \quad \text{at } S_t \text{ or } S_t^e, \quad \mathbf{u}^m = \bar{\mathbf{u}} \quad \text{at } S_u \text{ or } S_u^e, \quad (1.7)$$

2- Electric natural and essential boundary conditions:

$$\mathbf{n}_e \mathbf{D}^m = \bar{Q} \quad \text{at } S_Q \text{ or } S_Q^e, \quad \varphi^m = \bar{\varphi} \quad \text{at } S_\varphi \text{ or } S_\varphi^e, \quad (1.8)$$

3- Magnetic natural and essential boundary conditions:

$$\mathbf{n}_e \mathbf{B}^m = \bar{Q}_M \quad \text{at } S_B \text{ or } S_B^e, \quad \psi^m = \bar{\psi} \quad \text{at } S_\psi \text{ or } S_\psi^e, \quad (1.9)$$

$$\text{Where } \mathbf{n}_\sigma = \begin{bmatrix} n_1 & 0 & 0 & n_2 & 0 & n_3 \\ 0 & n_2 & 0 & n_1 & n_3 & 0 \\ 0 & 0 & n_3 & 0 & n_2 & n_1 \end{bmatrix}, \quad \text{and} \quad \mathbf{n}_e = [n_1 \ n_2 \ n_3], \quad (1.10)$$

$\bar{\mathbf{t}}$ is the specified boundary traction vector, \bar{Q} is the specified surface charge density (or electric displacement) and \bar{Q}_M is the specified surface magnetic flux density (or magnetic induction). n_1 , n_2 and n_3 , the three components present in \mathbf{n}_σ and \mathbf{n}_e are the components of the unit outward normal to the boundaries S_t (or S_t^e), S_Q (or S_Q^e), or S_B (or S_B^e) respectively. $\bar{\mathbf{u}}$ is the specified mechanical displacement vector at the boundary S_u (or S_u^e), $\bar{\varphi}$ is the specified electric potential at the boundary S_φ (or S_φ^e), and $\bar{\psi}$ is the specified magnetic potential at the boundary S_ψ (or S_ψ^e).

The following conditions should also be satisfied at each inter-grain boundary S_g^e :

1- Mechanical displacement, electric and magnetic potential compatibility conditions:

$$\mathbf{u}^{m+} = \mathbf{u}^{m-}, \quad \varphi^{m+} = \varphi^{m-}, \quad \psi^{m+} = \psi^{m-} \quad (1.11)$$

2- Mechanical traction, electric and magnetic reciprocity conditions:

$$(\mathbf{n}_\sigma \boldsymbol{\sigma}^m)^+ + (\mathbf{n}_\sigma \boldsymbol{\sigma}^m)^- = 0, \quad (\mathbf{n}_e \mathbf{D}^m)^+ + (\mathbf{n}_e \mathbf{D}^m)^- = 0, \quad (\mathbf{n}_e \mathbf{B}^m)^+ + (\mathbf{n}_e \mathbf{B}^m)^- = 0 \quad (1.12)$$

where superscript “+” indicates variables calculated from grain e and directed toward the outward normal direction from its boundaries, while superscript “−” indicates variables calculated from the neighboring grains and directed toward the grain in question (grain e).

1.4.2 Impermeable void boundary conditions

The impermeable assumption treats the void as being fully insulated to the electromagnetic field (as a result, the electromagnetic field inside the void is always zero), while the permeable assumption treats the void as being fully conductive to the electromagnetic field (therefore, the jumps of the electric and magnetic potentials across the void surface in the direction of the applied field are always zero).

The electric permittivity of piezoelectric materials is three orders of magnitude higher than that of air or vacuum inside the void, while the magnetic permeability of piezomagnetic materials (for example CoFe_2O_4) is about two orders of magnitude higher than that of air or vacuum. Hence, the electromagnetic impermeable assumption can be adopted. We then have *traction-free and vanishing surface charge density and magnetic flux density (normal electric displacement and magnetic induction)* conditions along the void boundary, $\partial\Omega_c^e$:

$$\mathbf{t}^m = \mathbf{n}_\sigma \boldsymbol{\sigma}^m = \mathbf{0}, \quad Q^m = \mathbf{n}_e \mathbf{D}^m = 0, \quad Q_M^m = \mathbf{n}_e \mathbf{B}^m = 0 \quad (1.13)$$

If the magnetic permeability of a porous piezomagnetic material is close to that of air, vacuum or the fluid inside the void, then the void domain should be treated magnetically as an inclusion. This will not be covered in this study.

1.4.3 Inclusion boundary conditions

We have the following conditions along the inclusion boundary, $\partial\Omega_c^e$:

- 1- Mechanical displacements, electric and magnetic potential continuity conditions:

$$\mathbf{u}^m = \mathbf{u}^c, \quad \varphi^m = \varphi^c, \quad \psi^m = \psi^c \quad (1.14)$$

2- Traction reciprocity and continuities of normal electric displacement and magnetic induction:

$$-\mathbf{n}_\sigma \boldsymbol{\sigma}^m + \mathbf{n}_\sigma \boldsymbol{\sigma}^c = 0, \quad \mathbf{n}_e \mathbf{D}^m = \mathbf{n}_e \mathbf{D}^c, \quad \mathbf{n}_e \mathbf{B}^m = \mathbf{n}_e \mathbf{B}^c \quad (1.15)$$

These inclusion boundary conditions can be used for piezoelectric/piezomagnetic particles or fibers in an elastic matrix (i.e. polymer), in a piezomagnetic/piezoelectric matrix, or in a piezoelectric/piezomagnetic matrix made up of different material. They can also be used to model elastic particles or fibers in a piezoelectric or piezomagnetic matrix.

Figure 1.4 shows a schematic for a porous/composite piezoelectric-piezomagnetic material with all governing equations and boundary conditions discussed in this section. This schematic is used in the last section of chapters 3-6 to summarize how each proposed numerical method (member of the multiphysics computational grains methods) enforce the aforementioned governing equations and boundary conditions.

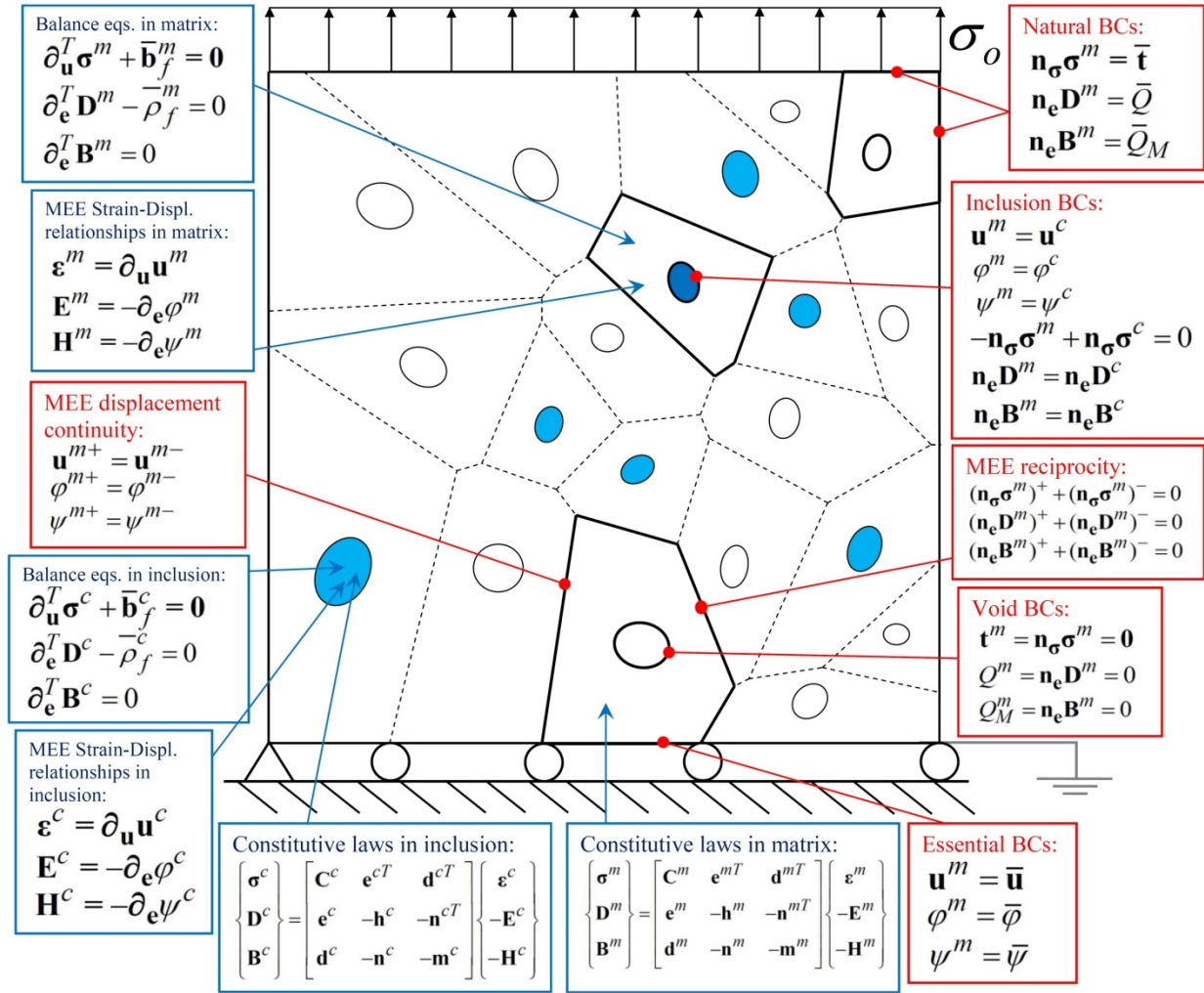


Figure 1.4: A schematic showing all governing equations in porous/composite piezoelectric-piezomagnetic material (MEE: Magneto-electro-elastic).

1.5 Plane-stress and plane-strain assumptions

In this subsection, the superscripts α in eq. (1.5) that indicates whether we are talking about the matrix (m) or the inclusion (c) are ignored for simplicity. Eq. (1.5) for transversely isotropic magneto-electro-elastic (MEE) material electrically poled and magnetically biased in the x'_3 -direction can be expanded with respect to the crystallographic axes $x'_1 - x'_2 - x'_3$ as:

$$\left\{ \begin{array}{c} \varepsilon'_1 \\ \varepsilon'_2 \\ \varepsilon'_3 \\ \varepsilon'_4 \\ \varepsilon'_5 \\ \varepsilon'_6 \\ -E'_1 \\ -E'_2 \\ -E'_3 \\ -H'_1 \\ -H'_2 \\ -H'_3 \end{array} \right\} = \left[\begin{array}{cccccc|ccc|ccc} S'_{11} & S'_{12} & S'_{13} & 0 & 0 & 0 & 0 & 0 & g'_{31} & 0 & 0 & b'_{31} \\ S'_{12} & S'_{11} & S'_{13} & 0 & 0 & 0 & 0 & 0 & g'_{31} & 0 & 0 & b'_{31} \\ S'_{13} & S'_{13} & S'_{33} & 0 & 0 & 0 & 0 & 0 & g'_{33} & 0 & 0 & b'_{33} \\ 0 & 0 & 0 & S'_{55} & 0 & 0 & 0 & g'_{15} & 0 & 0 & b'_{15} & 0 \\ 0 & 0 & 0 & 0 & S'_{55} & 0 & g'_{15} & 0 & 0 & b'_{15} & 0 & 0 \\ 0 & 0 & 0 & 0 & 0 & S'_{66} & 0 & 0 & 0 & 0 & 0 & 0 \\ \hline 0 & 0 & 0 & 0 & g'_{15} & 0 & -\beta'_{11} & 0 & 0 & -\kappa'_{11} & 0 & 0 \\ 0 & 0 & 0 & g'_{15} & 0 & 0 & 0 & -\beta'_{11} & 0 & 0 & -\kappa'_{11} & 0 \\ g'_{31} & g'_{31} & g'_{33} & 0 & 0 & 0 & 0 & 0 & -\beta'_{33} & 0 & 0 & -\kappa'_{33} \\ \hline 0 & 0 & 0 & 0 & b'_{15} & 0 & -\kappa'_{11} & 0 & 0 & -v'_{11} & 0 & 0 \\ 0 & 0 & 0 & b'_{15} & 0 & 0 & 0 & -\kappa'_{11} & 0 & 0 & -v'_{11} & 0 \\ b'_{31} & b'_{31} & b'_{33} & 0 & 0 & 0 & 0 & 0 & -\kappa'_{33} & 0 & 0 & -v'_{33} \end{array} \right] \left\{ \begin{array}{c} \sigma'_1 \\ \sigma'_2 \\ \sigma'_3 \\ \sigma'_4 \\ \sigma'_5 \\ \sigma'_6 \\ D'_1 \\ D'_2 \\ D'_3 \\ B'_1 \\ B'_2 \\ B'_3 \end{array} \right\} \quad (1.16)$$

Or

$$\left\{ \begin{array}{c} \sigma'_1 \\ \sigma'_2 \\ \sigma'_3 \\ \sigma'_4 \\ \sigma'_5 \\ \sigma'_6 \\ D'_1 \\ D'_2 \\ D'_3 \\ B'_1 \\ B'_2 \\ B'_3 \end{array} \right\} = \left[\begin{array}{cccccc|ccc|ccc} C'_{11} & C'_{12} & C'_{13} & 0 & 0 & 0 & 0 & 0 & e'_{31} & 0 & 0 & d'_{31} \\ C'_{12} & C'_{11} & C'_{13} & 0 & 0 & 0 & 0 & 0 & e'_{31} & 0 & 0 & d'_{31} \\ C'_{13} & C'_{13} & C'_{33} & 0 & 0 & 0 & 0 & 0 & e'_{33} & 0 & 0 & d'_{33} \\ 0 & 0 & 0 & C'_{55} & 0 & 0 & 0 & e'_{15} & 0 & 0 & d'_{15} & 0 \\ 0 & 0 & 0 & 0 & C'_{55} & 0 & e'_{15} & 0 & 0 & d'_{15} & 0 & 0 \\ 0 & 0 & 0 & 0 & 0 & C'_{66} & 0 & 0 & 0 & 0 & 0 & 0 \\ \hline 0 & 0 & 0 & 0 & e'_{15} & 0 & -h'_{11} & 0 & 0 & -n'_{11} & 0 & 0 \\ 0 & 0 & 0 & e'_{15} & 0 & 0 & 0 & -h'_{11} & 0 & 0 & -n'_{11} & 0 \\ e'_{31} & e'_{31} & e'_{33} & 0 & 0 & 0 & 0 & 0 & -h'_{33} & 0 & 0 & -n'_{33} \\ \hline 0 & 0 & 0 & 0 & d'_{15} & 0 & -n'_{11} & 0 & 0 & -m'_{11} & 0 & 0 \\ 0 & 0 & 0 & d'_{15} & 0 & 0 & 0 & -n'_{11} & 0 & 0 & -m'_{11} & 0 \\ d'_{31} & d'_{31} & d'_{33} & 0 & 0 & 0 & 0 & 0 & -n'_{33} & 0 & 0 & -m'_{33} \end{array} \right] \left\{ \begin{array}{c} \varepsilon'_1 \\ \varepsilon'_2 \\ \varepsilon'_3 \\ \varepsilon'_4 \\ \varepsilon'_5 \\ \varepsilon'_6 \\ -E'_1 \\ -E'_2 \\ -E'_3 \\ -H'_1 \\ -H'_2 \\ -H'_3 \end{array} \right\} \quad (1.17)$$

with $C'_{66} = \frac{C'_{11} - C'_{12}}{2}$.

If the considered body is very thin in the x'_2 -direction (plane stress case), we can use the following assumptions:

$$\sigma'_2 = \sigma'_4 = \sigma'_6 = 0, \quad D'_2 = B'_2 = 0 \quad (1.18)$$

Substituting this into eq. (1.16) we get the constitutive equation for plane stress problems:

$$\begin{Bmatrix} \varepsilon'_1 \\ \varepsilon'_3 \\ \varepsilon'_5 \\ -E'_1 \\ -E'_3 \\ -H'_1 \\ -H'_3 \end{Bmatrix} = \begin{bmatrix} S'_{11} & S'_{13} & 0 & 0 & g'_{31} & 0 & b'_{31} \\ S'_{13} & S'_{33} & 0 & 0 & g'_{33} & 0 & b'_{33} \\ 0 & 0 & S'_{55} & g'_{15} & 0 & b'_{15} & 0 \\ 0 & 0 & g'_{15} & -\beta'_{11} & 0 & -\kappa'_{11} & 0 \\ g'_{31} & g'_{33} & 0 & 0 & -\beta'_{33} & 0 & -\kappa'_{33} \\ 0 & 0 & b'_{15} & -\kappa'_{11} & 0 & -\nu'_{11} & 0 \\ b'_{31} & b'_{33} & 0 & 0 & -\kappa'_{33} & 0 & -\nu'_{33} \end{bmatrix} \begin{Bmatrix} \sigma'_1 \\ \sigma'_3 \\ \sigma'_5 \\ D'_1 \\ D'_3 \\ B'_1 \\ B'_3 \end{Bmatrix} \quad (1.19)$$

Using $\sigma'_2 = 0$ assumption, we can express ε'_2 as:

$$\varepsilon'_2 = \frac{-C'_{12}\varepsilon'_1 - C'_{13}\varepsilon'_3 + e'_{31}E'_3 + b'_{31}H'_3}{C'_{11}} \quad (1.20)$$

and substituting this into eq. (1.17), we get:

$$\begin{Bmatrix} \sigma'_1 \\ \sigma'_3 \\ \sigma'_5 \\ D'_1 \\ D'_3 \\ B'_1 \\ B'_3 \end{Bmatrix} = \begin{bmatrix} \bar{C}'_{11} & \bar{C}'_{13} & 0 & 0 & \bar{e}'_{31} & 0 & \bar{d}'_{31} \\ \bar{C}'_{13} & \bar{C}'_{33} & 0 & 0 & \bar{e}'_{33} & 0 & \bar{d}'_{33} \\ 0 & 0 & \bar{C}'_{55} & \bar{e}'_{15} & 0 & \bar{d}'_{15} & 0 \\ 0 & 0 & \bar{e}'_{15} & -\bar{h}'_{11} & 0 & -\bar{n}'_{11} & 0 \\ \bar{e}'_{31} & \bar{e}'_{33} & 0 & 0 & -\bar{h}'_{33} & 0 & -\bar{n}'_{33} \\ 0 & 0 & \bar{d}'_{15} & -\bar{n}'_{11} & 0 & -\bar{m}'_{11} & 0 \\ \bar{d}'_{31} & \bar{d}'_{33} & 0 & 0 & -\bar{n}'_{33} & 0 & -\bar{m}'_{33} \end{bmatrix} \begin{Bmatrix} \varepsilon'_1 \\ \varepsilon'_3 \\ \varepsilon'_5 \\ -E'_1 \\ -E'_3 \\ -H'_1 \\ -H'_3 \end{Bmatrix} \quad (1.21)$$

where

$$\bar{C}'_{11} = \frac{C'^2_{11} - C'^2_{12}}{C'_{11}}, \quad \bar{C}'_{13} = \frac{C'_{13}(C'_{11} - C'_{12})}{C'_{11}}, \quad \bar{C}'_{33} = \frac{C'_{11}C'_{33} - C'^2_{13}}{C'_{11}}, \quad \bar{C}'_{55} = C'_{55}$$

$$\bar{e}'_{31} = \frac{e'_{31}(C'_{11} - C'_{12})}{C'_{11}}, \quad \bar{e}'_{33} = \frac{C'_{11}e'_{33} - C'_{13}e'_{31}}{C'_{11}}, \quad \bar{e}'_{15} = e'_{15},$$

$$\bar{d}'_{31} = \frac{d'_{31}(C'_{11} - C'_{12})}{C'_{11}}, \quad \bar{d}'_{33} = \frac{C'_{11}d'_{33} - C'_{13}d'_{31}}{C'_{11}}, \quad \bar{d}'_{15} = d'_{15}, \quad \bar{h}'_{11} = h'_{11}, \quad \bar{h}'_{33} = \frac{C'_{11}h'_{33} + e'^2_{31}}{C'_{11}},$$

$$\bar{m}'_{11} = m'_{11}, \quad \bar{m}'_{33} = \frac{C'_{11}m'_{33} + d'^2_{31}}{C'_{11}}, \quad \bar{n}'_{11} = n'_{11}, \quad \bar{n}'_{33} = \frac{C'_{11}n'_{33} + e'_{31}d'_{31}}{C'_{11}}$$

If the body is very long (infinite) in the x'_2 -direction (plane strain case), then we have the assumptions:

$$\varepsilon'_2 = \varepsilon'_4 = \varepsilon'_6 = 0, \quad E'_2 = H'_2 = 0 \quad (1.22)$$

Substituting this directly into eq. (1.17) we get the constitutive equation for plane strain problems:

$$\begin{Bmatrix} \sigma'_1 \\ \sigma'_3 \\ \sigma'_5 \\ D'_1 \\ D'_3 \\ B'_1 \\ B'_3 \end{Bmatrix} = \begin{Bmatrix} C'_{11} & C'_{13} & 0 & 0 & e'_{31} & 0 & d'_{31} \\ C'_{13} & C'_{33} & 0 & 0 & e'_{33} & 0 & d'_{33} \\ 0 & 0 & C'_{44} & e'_{15} & 0 & d'_{15} & 0 \\ 0 & 0 & e'_{15} & -h'_{11} & 0 & -n'_{11} & 0 \\ e'_{31} & e'_{33} & 0 & 0 & -h'_{33} & 0 & -n'_{33} \\ 0 & 0 & d'_{15} & -n'_{11} & 0 & -m'_{11} & 0 \\ d'_{31} & d'_{33} & 0 & 0 & -n'_{33} & 0 & -m'_{33} \end{Bmatrix} \begin{Bmatrix} \varepsilon'_1 \\ \varepsilon'_3 \\ \varepsilon'_5 \\ E'_1 \\ E'_3 \\ H'_1 \\ H'_3 \end{Bmatrix} \quad (1.23)$$

Using $\varepsilon'_2 = 0$ assumption, we can express σ'_2 as:

$$\sigma'_2 = \frac{-S'_{12}\sigma'_1 - S'_{13}\sigma'_3 - g'_{31}D'_3 - b'_{31}B'_3}{S'_{11}} \quad (1.24)$$

and substituting this into eq. (1.16), we get:

$$\begin{Bmatrix} \varepsilon'_1 \\ \varepsilon'_3 \\ \varepsilon'_5 \\ -E'_1 \\ -E'_3 \\ -H'_1 \\ -H'_3 \end{Bmatrix} = \begin{Bmatrix} \bar{S}'_{11} & \bar{S}'_{13} & 0 & 0 & \bar{g}'_{31} & 0 & \bar{b}'_{31} \\ \bar{S}'_{13} & \bar{S}'_{33} & 0 & 0 & \bar{g}'_{33} & 0 & \bar{b}'_{33} \\ 0 & 0 & \bar{S}'_{55} & \bar{g}'_{15} & 0 & \bar{b}'_{15} & 0 \\ 0 & 0 & \bar{g}'_{15} & -\bar{\beta}'_{11} & 0 & -\bar{\kappa}'_{11} & 0 \\ \bar{g}'_{31} & \bar{g}'_{33} & 0 & 0 & -\bar{\beta}'_{33} & 0 & -\bar{\kappa}'_{33} \\ 0 & 0 & \bar{b}'_{15} & -\bar{\kappa}'_{11} & 0 & -\bar{\nu}'_{11} & 0 \\ \bar{b}'_{31} & \bar{b}'_{33} & 0 & 0 & -\bar{\kappa}'_{33} & 0 & -\bar{\nu}'_{33} \end{Bmatrix} \begin{Bmatrix} \sigma'_1 \\ \sigma'_3 \\ \sigma'_5 \\ D'_1 \\ D'_3 \\ B'_1 \\ B'_3 \end{Bmatrix} \quad (1.25)$$

where

$$\bar{S}'_{11} = \frac{S'^2_{11} - S'^2_{12}}{S'_{11}}, \quad \bar{S}'_{13} = \frac{S'_{13}(S'_{11} - S'_{12})}{S'_{11}}, \quad \bar{S}'_{33} = \frac{S'_{11}S'_{33} - S'^2_{13}}{S'_{11}}, \quad \bar{S}'_{55} = S'_{55}$$

$$\bar{g}'_{31} = \frac{g'_{31}(S'_{11} - S'_{12})}{S'_{11}}, \quad \bar{g}'_{33} = \frac{S'_{11}g'_{33} - S'_{13}g'_{31}}{S'_{11}}, \quad \bar{g}'_{15} = g'_{15},$$

$$\bar{b}'_{31} = \frac{b'_{31}(S'_{11} - S'_{12})}{S'_{11}}, \quad \bar{b}'_{33} = \frac{S'_{11}b'_{33} - S'_{13}b'_{31}}{S'_{11}}, \quad \bar{b}'_{15} = b'_{15}, \quad \bar{\beta}'_{11} = \beta'_{11}, \quad \bar{\beta}'_{33} = \frac{S'_{11}\beta'_{33} + g'_{31}^2}{S'_{11}}$$

$$\vec{v}'_{11} = v'_{11}, \quad \vec{v}'_{33} = \frac{S'_{11}v'_{33} + b'_{31}^2}{S'_{11}}, \quad \vec{\kappa}'_{11} = \kappa'_{11}, \quad \vec{\kappa}'_{33} = \frac{S'_{11}\kappa'_{33} + g'_{31}b'_{31}}{S'_{11}}.$$

1.6 Brief description of ferroelectricity

Ferroelectric materials have a linear behavior, similar to piezoelectric materials, at very low values of applied mechanical and electrical loads. Piezoelectric materials have spontaneous polarization; ferroelectric materials have the ability to reorient their spontaneous polarization with the application of an external field. This macroscopic behavior is actually based on mechanisms that happen in smaller scales. A polycrystalline ferroelectric ceramic is composed of an aggregate of grains separated by grain-boundaries, in the meso/micro-scale. Within a grain, all unit cells have the same crystallographic axes. Each grain has a random shape and is subdivided into several domains. A domain is a region in the grain where all the unit cells composing it have the same orientation of their asymmetry or the same spontaneous polarization direction. Domains of a grain are separated by domain walls. The reorientation of spontaneous polarization in ferroelectric materials is principally controlled by motion of domain walls [15].

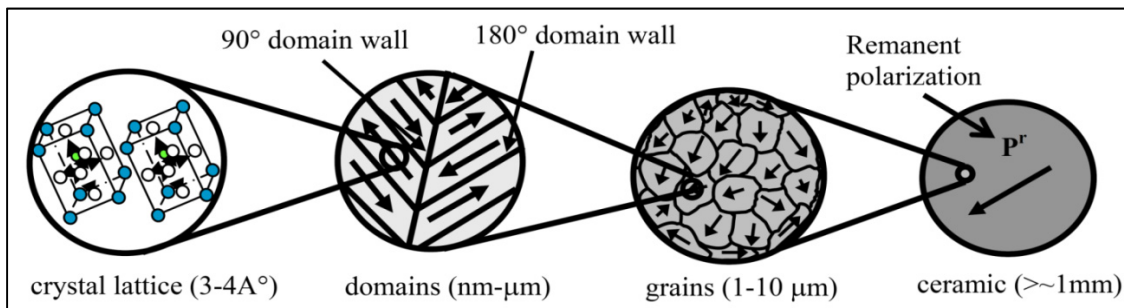


Figure 1.5: Primary length scales for ferroelectric materials

When a sufficiently large electric field or mechanical stress is applied, the direction of spontaneous polarization of a tetragonal unit cell can be switched by either 180° or 90° as shown in Figure 1.6. Noticeably, the 180° switching is accommodated with unchanged tetragonality of the unit cell, whereas the 90° switching is accompanied by a reorientation of the tetragonality. The spontaneous polarization switching of unit cells yield the phenomenon of ferroelectricity, i.e. piezoelectric materials have the ability to switch their polarization direction under a sufficiently large electric or mechanical field. Such piezoelectric materials are referred to as ferroelectrics.

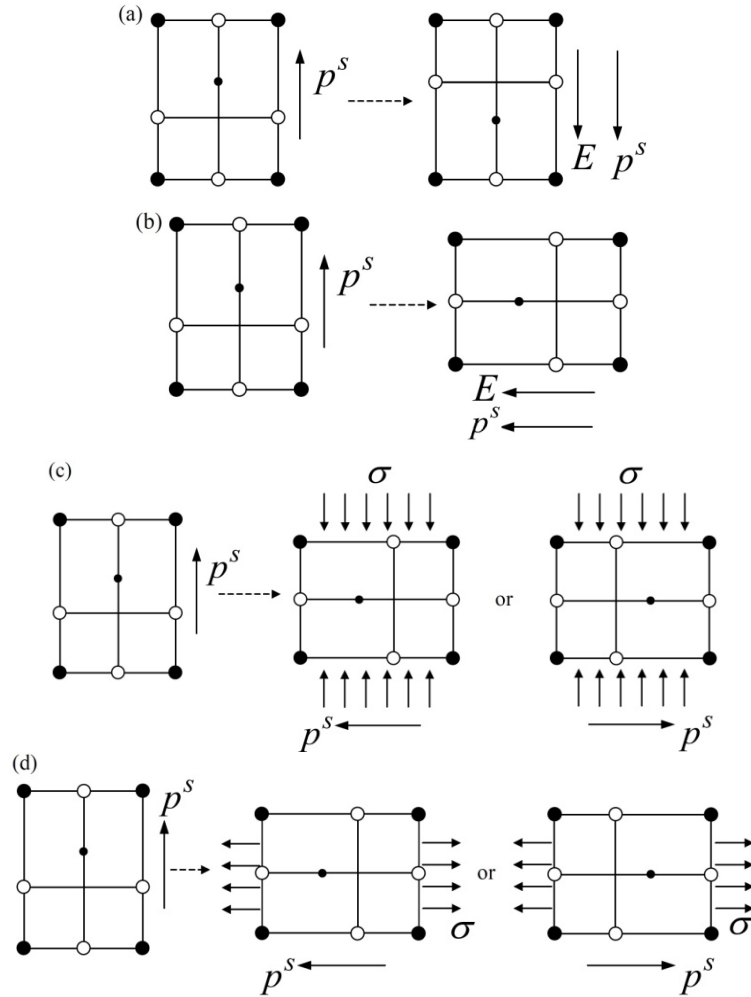


Figure 1.6: (a) 180° switching induced by electric field; (b) 90° switching induced by electric field; (c) 90° switching induced by compressive stress; (d) 90° switching induced by tensile stress.

As mentioned before, there are six possible spontaneous polarization directions in a tetragonal unit cell. They are parallel to the crystallographic axes along the 1, 2 and 3 directions as shown in Figure 1.1. Hence, a crystal grain in a ferroelectric material can possess up to six different types of domains, and each domain is made up of unit cells with the same spontaneous polarization direction. In an unpoled ferroelectric crystal grain, the mass fractions of different types of domains in a crystal grain are approximately the same. Therefore, the average polarization and strain of each crystal grain is low. For an unpoled ferroelectric material which is prepared through the conventional steps of sintering and then cooling, the macroscopic polarization and the macroscopic strain obtained by averaging the polarization and strain over all crystal grains are essentially zero due to the randomness of the crystallographic orientation.

Point 1 in Figure 1.7 represents an unpoled multi-crystalline ferroelectric. As a sufficiently large electric field is applied, the polarization direction of a domain is changed due to the 180° or 90° switching of the spontaneous polarization of the unit cells. This effect is commonly called *domain switching* or *domain wall motion*. The domain switching occurs until finally the polarization directions of all domains are switched to the admissible ones closest to the applied electric field. Consequently, a maximum (saturation) polarization P_{sat} and a maximum (saturation) strain ε_{sat} are attained as indicated by point 2 in Figure 1.7 (a) and (b), respectively. As the applied electric field is reduced to zero, some of the domains maintain their state and thus a remanent polarization P_r and a remanent strain ε_r are observed as indicated by point 3 in Figure 1.7 (a) and (b), respectively.

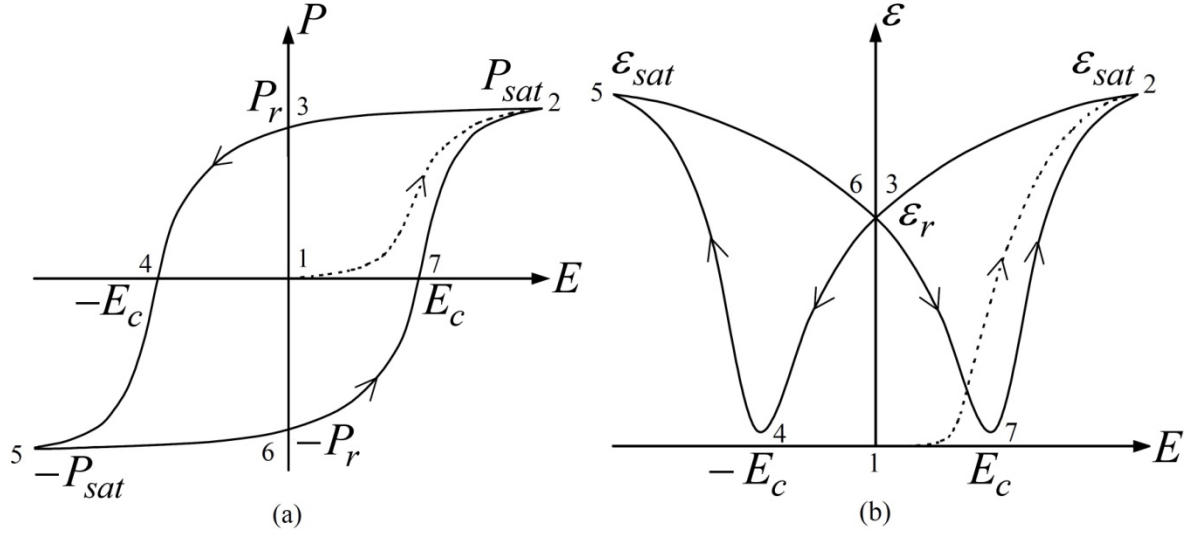


Figure 1.7: Schematic sketches of (a) hysteresis loop of macroscopic polarization P versus applied electric field E and (b) butterfly loop of macroscopic strain ε versus electric field E . The dashed line represents the initial polarization process of the unpoled material.

Figure 1.8 shows schematic sketches for a polycrystalline ferroelectric material as it goes from point 1 to point 3 (or through the polling process). The figure illustrates the domain switching phenomena in the grains composing the polycrystalline ferroelectric sample.

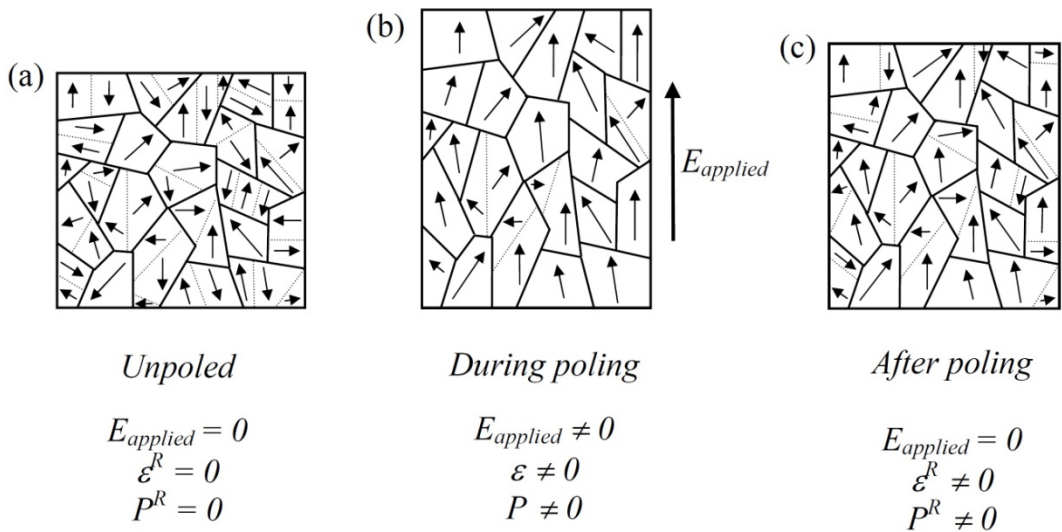


Figure 1.8: Schematic sketches for the polarization directions in the domains of the grains of a polycrystalline ferroelectric material through the polling process.

By applying an electric field in the opposite direction, the domains switch again to align their polarization directions with that of the electric field. The polarization and the strain keep decreasing until the negative coercive field of the material, $-E_c$, is reached at point 4, where zero polarization and minimum strain are observed. Further increase in the magnitude of the applied electric field reverses the polarization direction and increases the strain. Negative maximum polarization $-P_{sat}$ and positive maximum strain ε_{sat} are attained at point 5 in Figure 1.7 (a) and (b). Decreasing the electric field again till zero causes the polarization to reach the negative remnant polarization, $-P_r$, and the strain to reach the remnant strain, ε_r , at point 6. Increasing the electric field again till the coercive field E_c at point 7 is reached, brings the strain to its minimum value and causes the polarization to switch its direction. The loop then continues to point 2 and keeps repeating as the applied electric field oscillates. The material responds in the same manner as before. It can be seen from Figure 1.7 (a) that the reversal of polarization follows the change of electric field with some delay and the *hysteresis loop* results. In addition, the *butterfly loop* is symmetric with respect to the strain axis in Figure 1.7 (b).

As a matter of fact, the non-linear hysteresis loop of macroscopic polarization versus applied electric field and the butterfly loop of macroscopic strain versus applied electric field are commonly accepted criteria to judge whether a material is ferroelectric or not [1].

Polarization reorientation within one phase can be induced by either electric field (ferroelectric switching) or applied stress (ferroelastic switching). See Figure 1.9.

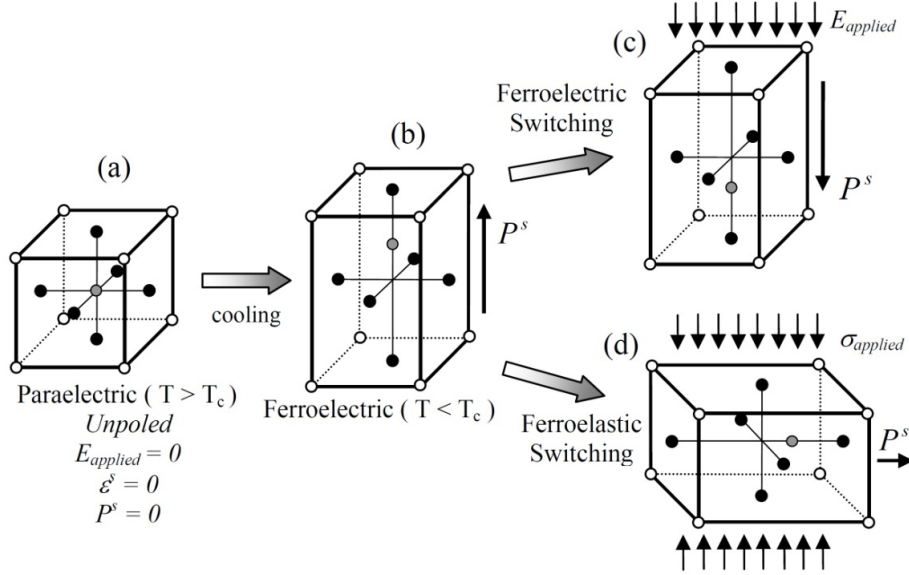


Figure 1.9: Ferroelectric and ferroelastic switching

1.7 Constitutive equations for ferroelectric materials

Constitutive relations for type-*i*-domain in a ferroelectric material can be written as:

$$\begin{aligned}\boldsymbol{\varepsilon}_i &= \mathbf{S}_i \boldsymbol{\sigma}_i + \mathbf{g}_i^T \mathbf{E}_i + \boldsymbol{\varepsilon}_i^s \\ \mathbf{D}_i &= \mathbf{g}_i \boldsymbol{\sigma}_i + \boldsymbol{\beta}_i \mathbf{E}_i + \mathbf{P}_i^s\end{aligned}\tag{1.26}$$

where $\boldsymbol{\varepsilon}_i$ and $\boldsymbol{\sigma}_i$ are, respectively, the strain and stress tensors, \mathbf{E}_i and \mathbf{D}_i are the electric field intensity and electric displacement vectors of type-*i*-domain, $\boldsymbol{\varepsilon}_i^s$ and \mathbf{P}_i^s are the spontaneous strain tensor and spontaneous polarization vector of type-*i*-domain, respectively. \mathbf{S}_i , \mathbf{g}_i , $\boldsymbol{\beta}_i$ are, respectively, the elastic compliance tensor measured under constant electric field, piezoelectric tensor, and dielectric tensor measured under constant stress of type-*i*-domain. The stress, strain, and spontaneous strain tensors can be cast in a vector form, while the elastic compliance and piezoelectric tensors can be cast in a matrix form.

For three-dimensional analysis, there are six possible spontaneous polarization directions in a tetragonal unit cell. These directions are parallel/normal to the crystal axes which are

denoted as the 1-, 2- and 3- directions. But for two-dimensional analysis, there are only four possible spontaneous polarization directions. The crystallographic axes are the reference directions for expressing all constitutive relations. As a result, each crystal grain in a polycrystalline ferroelectric material has six different types of domains in a 3D analysis, and four types in a 2D analysis.

To determine the average physical properties of a ferroelectric crystal grain, a simple averaging method is used. The method is based on the assumptions that all domains in a crystal grain are subjected to uniform stress and electric field intensity, and that the strain and electric displacement of the crystal grain are the summation of those of all domains in the crystal grain weighted by their volume fractions c_i s, i.e.

$$\boldsymbol{\sigma}_i = \boldsymbol{\sigma}, \quad \mathbf{E}_i = \mathbf{E}, \quad \boldsymbol{\varepsilon} = \sum_{i=1}^{N_d} c_i \boldsymbol{\varepsilon}_i, \quad \mathbf{D} = \sum_{i=1}^{N_d} c_i \mathbf{D}_i \quad (1.27)$$

where N_d is the number of domain types in the crystal grain (4 for 2D analysis and 6 for 3D analysis, considering only ferroelectric materials entirely composed of tetragonal unit cells). The volume fractions, c_i s, should always satisfy the consistency conditions:

$$c_i \geq 0, \quad \sum_{i=1}^{N_d} c_i = 1, \quad \sum_{i=1}^{N_d} \dot{c}_i = 0 \quad (1.28)$$

Substituting equation (1.27) into equation (1.26), we get the constitutive equation for a ferroelectric crystal grain as:

$$\begin{Bmatrix} \boldsymbol{\varepsilon} \\ \mathbf{D} \end{Bmatrix} = \begin{bmatrix} \mathbf{S} & \mathbf{g}^T \\ \mathbf{g} & \boldsymbol{\beta} \end{bmatrix} \begin{Bmatrix} \boldsymbol{\sigma} \\ \mathbf{E} \end{Bmatrix} + \begin{Bmatrix} \boldsymbol{\varepsilon}^R \\ \mathbf{P}^R \end{Bmatrix} = \begin{Bmatrix} \boldsymbol{\varepsilon}^L \\ \mathbf{D}^L \end{Bmatrix} + \begin{Bmatrix} \boldsymbol{\varepsilon}^R \\ \mathbf{P}^R \end{Bmatrix} \quad (1.29)$$

where

$$\boldsymbol{\varepsilon}^R = \sum_{i=1}^{N_d} c_i \boldsymbol{\varepsilon}_i^S, \quad \mathbf{P}^R = \sum_{i=1}^{N_d} c_i \mathbf{P}_i^S, \quad \mathbf{S} = \sum_{i=1}^{N_d} c_i \mathbf{S}_i, \quad \mathbf{g} = \sum_{i=1}^{N_d} c_i \mathbf{g}_i, \quad \boldsymbol{\beta} = \sum_{i=1}^{N_d} c_i \boldsymbol{\beta}_i \quad (1.30)$$

Here $\boldsymbol{\varepsilon}$, $\boldsymbol{\sigma}$, \mathbf{E} and \mathbf{D} are the average vectors of strain, stress, electric field intensity and electric displacement in the crystal grain respectively; $\boldsymbol{\varepsilon}^L$ and \mathbf{D}^L are the average linear (reversible) strain and electric displacement vectors respectively; $\boldsymbol{\varepsilon}^R$ and \mathbf{P}^R are the average remnant (irreversible) strain and polarization vectors respectively; \mathbf{S} , \mathbf{g} , $\boldsymbol{\beta}$ are the average material matrices for the grain in question.

Equation (1.26) can also be written as:

$$\begin{aligned} \boldsymbol{\sigma}_i &= \mathbf{C}_i \left(\boldsymbol{\varepsilon}_i - \boldsymbol{\varepsilon}_i^S \right) - \mathbf{e}_i^T \mathbf{E}_i \\ \mathbf{D}_i &= \mathbf{e}_i \left(\boldsymbol{\varepsilon}_i - \boldsymbol{\varepsilon}_i^S \right) + \mathbf{h}_i \mathbf{E}_i + \mathbf{P}_i^S \end{aligned} \quad (1.31)$$

where $\mathbf{C}_i = \mathbf{S}_i^{-1}$, $\mathbf{e}_i = \mathbf{g}_i \mathbf{C}_i$ and $\mathbf{h}_i = \boldsymbol{\beta}_i - \mathbf{g}_i \mathbf{e}_i^T$ are the elastic tensor measured under constant electric field, piezoelectric tensor, and dielectric tensor measured under constant strain of type- i -domain. Again the elastic and piezoelectric tensors can be cast in a matrix form.

Similarly the constitutive equation for a ferroelectric crystal grain, equation (1.29), can be written as:

$$\begin{Bmatrix} \boldsymbol{\sigma} \\ \mathbf{D} \end{Bmatrix} = \begin{bmatrix} \mathbf{C} & \mathbf{e}^T \\ \mathbf{e} & -\mathbf{h} \end{bmatrix} \begin{Bmatrix} \boldsymbol{\varepsilon} - \boldsymbol{\varepsilon}^R \\ -\mathbf{E} \end{Bmatrix} + \begin{Bmatrix} \mathbf{0} \\ \mathbf{P}^R \end{Bmatrix} \quad (1.32)$$

with $\mathbf{C} = \mathbf{S}^{-1}$, $\mathbf{e} = \mathbf{g}\mathbf{C}$ and $\mathbf{h} = \boldsymbol{\beta} - \mathbf{g}\mathbf{e}^T$.

Usually \mathbf{C}_i , \mathbf{e}_i and \mathbf{h}_i are the given material properties. From them we can get $\mathbf{S}_i = \mathbf{C}_i^{-1}$, $\mathbf{g}_i = \mathbf{e}_i \mathbf{C}_i^{-1}$, and $\boldsymbol{\beta}_i = \mathbf{h}_i + \mathbf{g}_i \mathbf{e}_i^T = \mathbf{h}_i + \mathbf{e}_i \mathbf{C}_i^{-1} \mathbf{e}_i^T$. Then we can get the average material matrices \mathbf{S} , \mathbf{g} and $\boldsymbol{\beta}$ using eq. (1.30) and \mathbf{C} , \mathbf{e} and \mathbf{h} using eq. (1.32).

If the spontaneous (irreversible) strain and polarization are assumed to vanish, we then get the linear constitutive equations in the piezoelectric response region:

$$\begin{Bmatrix} \boldsymbol{\epsilon}^R \\ \mathbf{P}^R \end{Bmatrix} = \begin{Bmatrix} \mathbf{0} \\ \mathbf{0} \end{Bmatrix}, \quad \begin{Bmatrix} \boldsymbol{\epsilon} \\ \mathbf{D} \end{Bmatrix} = \begin{Bmatrix} \boldsymbol{\epsilon}^L \\ \mathbf{D}^L \end{Bmatrix} = \begin{bmatrix} \mathbf{S} & \mathbf{g}^T \\ \mathbf{g} & \boldsymbol{\beta} \end{bmatrix} \begin{Bmatrix} \boldsymbol{\sigma} \\ \mathbf{E} \end{Bmatrix}, \quad \text{or} \quad \begin{Bmatrix} \boldsymbol{\sigma} \\ \mathbf{D}^L \end{Bmatrix} = \begin{bmatrix} \mathbf{C} & \mathbf{e}^T \\ \mathbf{e} & -\mathbf{h} \end{bmatrix} \begin{Bmatrix} \boldsymbol{\epsilon}^L \\ -\mathbf{E} \end{Bmatrix} \quad (1.33)$$

When dealing with ferroelectric materials, we should also include the first and second laws of thermodynamics for deformable electric materials in our formulation:

$$\rho \dot{U} = \boldsymbol{\sigma} : \dot{\boldsymbol{\epsilon}} + \mathbf{E} \cdot \dot{\mathbf{D}} - \nabla \cdot \mathbf{r}, \quad (1.34)$$

$$\rho \dot{\eta} - \nabla \cdot \left(\frac{\mathbf{r}}{T} \right) \geq 0, \quad (1.35)$$

Where $\rho, U, \mathbf{r}, \eta$ and T denote density, internal energy per unit mass, heat flux, entropy per unit mass and absolute temperature. Over-dot denotes material time derivative.

The SI unit of the new variables in eq. (1.34) and (1.35) are as follows: Density ρ (Kg/m^3), internal energy per unit mass U (J/Kg), heat flux \mathbf{r} (J/m^2), entropy per unit mass, η (J/(Kg.K)), and absolute temperature, T (K).

1.7.1 Material properties for the different domain types

Figure 1.10 shows the global coordinate system and the crystallographic axes of a ferroelectric crystal grain with the polarization directions of the 6 possible domain types aligned with the crystallographic axes.

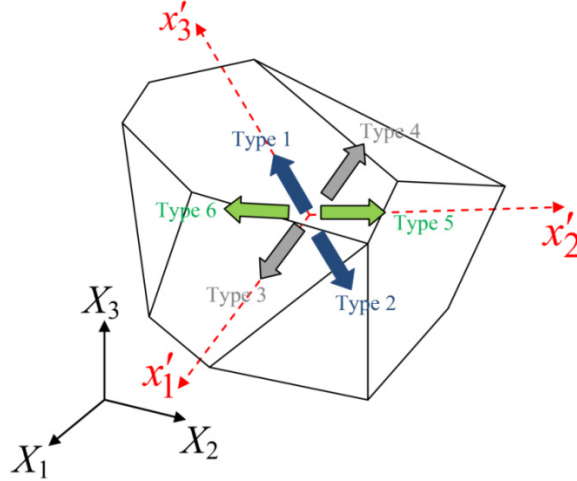


Figure 1.10: Crystallographic axes in a ferroelectric crystal grain and the polarization directions of the 6 possible domain types or variants

For the 3D case, domains of types 1 and 2 with spontaneous polarization direction along the \pm crystal axis 3, the material properties with respect to the crystallographic axes $x'_1 - x'_2 - x'_3$ can be written as:

$$\mathbf{C}'_i = \begin{bmatrix} C'_{11} & C'_{12} & C'_{13} & 0 & 0 & 0 \\ C'_{12} & C'_{11} & C'_{13} & 0 & 0 & 0 \\ C'_{13} & C'_{13} & C'_{33} & 0 & 0 & 0 \\ 0 & 0 & 0 & C'_{55} & 0 & 0 \\ 0 & 0 & 0 & 0 & C'_{55} & 0 \\ 0 & 0 & 0 & 0 & 0 & C'_{66} \end{bmatrix}, \quad \boldsymbol{\epsilon}_i^{S'} = \begin{Bmatrix} \epsilon_{11}^{S'} \\ \epsilon_{11}^{S'} \\ \epsilon_{33}^{S'} \\ 0 \\ 0 \\ 0 \end{Bmatrix}, \quad (1.36)$$

$$\mathbf{e}'_i = \pm \begin{bmatrix} 0 & 0 & 0 & 0 & e'_{15} & 0 \\ 0 & 0 & 0 & e'_{15} & 0 & 0 \\ e'_{31} & e'_{31} & e'_{33} & 0 & 0 & 0 \end{bmatrix}, \quad \mathbf{h}'_i = \begin{bmatrix} h'_{11} & 0 & 0 \\ 0 & h'_{11} & 0 \\ 0 & 0 & h'_{33} \end{bmatrix}, \quad \mathbf{P}_i^{S'} = \begin{Bmatrix} 0 \\ 0 \\ \pm p^{S'} \end{Bmatrix}$$

Denoting the unit vectors of the local crystal orthogonal coordinate system ($x'_1 - x'_2 - x'_3$) as $\mathbf{g}'_1, \mathbf{g}'_2$, and \mathbf{g}'_3 , all material tensors can be rotated to any other orthogonal coordinate system ($x_1 - x_2 - x_3$) whose unit vectors are $\mathbf{g}_1, \mathbf{g}_2$, and \mathbf{g}_3 using the rotation matrix \mathbf{R} :

$$\mathbf{x} = \mathbf{R} \mathbf{x}', \quad \mathbf{g}_k = \mathbf{R} \mathbf{g}'_k \quad (1.37)$$

Where $R_{kl} = \mathbf{g}_k \cdot \mathbf{g}'_l$ and $\mathbf{R} = R_{kl} \mathbf{g}_k \mathbf{g}'_l$.

For 2D rotation around x'_2 -axis by angle θ , \mathbf{R} has the form:

$$\mathbf{R} = \begin{bmatrix} \cos(\theta) & 0 & \sin(\theta) \\ 0 & 1 & 0 \\ -\sin(\theta) & 0 & \cos(\theta) \end{bmatrix} \quad (1.38)$$

For 3D rotation characterized by the three Euler angles (θ, ϕ, ψ) , the rotations are done according to the following sequence: rotation by angle θ around x'_3 -axis to get $x''_1 - x''_2 - x''_3$ coordinate axes, then rotation by angle ϕ around the new x''_1 -axis to get $x'''_1 - x'''_2 - x'''_3$ coordinate axes, followed by rotation by angle ψ around the new x'''_3 -axis to get $x_1 - x_2 - x_3$ coordinate axes. This is shown in Figure 1.10. \mathbf{R} in this case can be written as:

$$\mathbf{R} = \begin{bmatrix} c(\psi) & s(\psi) & 0 \\ -s(\psi) & c(\psi) & 0 \\ 0 & 0 & 1 \end{bmatrix} \begin{bmatrix} 1 & 0 & 0 \\ 0 & c(\phi) & s(\phi) \\ 0 & -s(\phi) & c(\phi) \end{bmatrix} \begin{bmatrix} c(\theta) & s(\theta) & 0 \\ -s(\theta) & c(\theta) & 0 \\ 0 & 0 & 1 \end{bmatrix} \quad (1.39)$$

where $c()$ means $\cos()$ and $s()$ means $\sin()$.

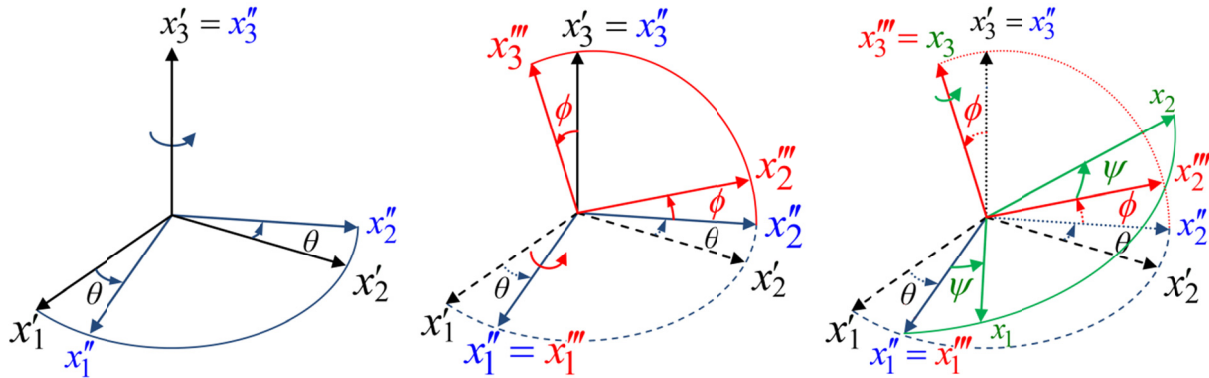


Figure 1.11: 3D rotation of axes using Euler angles: (left) rotation by angle θ around x'_3 -axis, (middle) rotation by angle ϕ around x''_1 -axis, (right) rotation by angle ψ around x'''_3 -axis.

For any material tensor, such as the elastic stiffness tensor (which is a fourth order tensor), the components of the tensor in the new coordinate axes can be expressed in terms of the components in the old coordinate system as follows:

$$\begin{aligned}\mathbf{C} &= C'_{pqrs} \mathbf{g}'_p \mathbf{g}'_q \mathbf{g}'_r \mathbf{g}'_s = C_{ijkl} \mathbf{g}_i \mathbf{g}_j \mathbf{g}_k \mathbf{g}_l \\ C_{ijkl} &= C'_{pqrs} (\mathbf{g}'_p \cdot \mathbf{g}_i)(\mathbf{g}'_q \cdot \mathbf{g}_j)(\mathbf{g}'_r \cdot \mathbf{g}_k)(\mathbf{g}'_s \cdot \mathbf{g}_l)\end{aligned}\quad (1.40)$$

So for domains of types 3 and 4 with spontaneous polarization direction along the \pm crystal axis 1, the material properties with respect to the crystallographic axes $x'_1 - x'_2 - x'_3$ can be obtained by a rotation of $\pm 90^\circ$ around x'_2 -axis (using the rotation matrix in eq. (1.38)). For domains of types 5 and 6 with spontaneous polarization direction along the \pm crystal axis 2, the material properties with respect to the crystallographic axes $x'_1 - x'_2 - x'_3$ can be obtained by a rotation of $\pm 90^\circ$ around x'_1 -axis (using the rotation matrix in eq. (1.39) with $\theta = \psi = 0$).

For the 2D case, if the body is very long (infinite) in the 2-direction (plane strain case), then we have the assumptions:

$$\varepsilon'_2 = \varepsilon'_4 = \varepsilon'_6 = 0, \quad E'_2 = 0, \quad \text{and} \quad \varepsilon_2^{S'} = 0, \quad P_2^{S'} = 0 \quad (1.41)$$

This reduces the problem into 2D case in the $X_1 - X_3$ plane with only 4 types of domains (types 1, 2, 3 and 4). In this case, the material matrices in eq. (1.36) of domain types 1 and 2, with spontaneous polarization direction along the \pm crystal axis 3, reduce to:

$$\begin{aligned}\mathbf{C}_i &= \begin{bmatrix} C'_{11} & C'_{13} & 0 \\ C'_{13} & C'_{33} & 0 \\ 0 & 0 & C'_{55} \end{bmatrix}, \quad \boldsymbol{\varepsilon}_i^{S'} = \begin{Bmatrix} \varepsilon_{11}^{S'} \\ \varepsilon_{33}^{S'} \\ 0 \end{Bmatrix}, \\ \mathbf{e}'_i &= \pm \begin{bmatrix} 0 & 0 & e'_{15} \\ e'_{31} & e'_{33} & 0 \end{bmatrix}, \quad \mathbf{h}'_i = \begin{bmatrix} h'_{11} & 0 \\ 0 & h'_{33} \end{bmatrix}, \quad \mathbf{P}_i^{S'} = \begin{Bmatrix} 0 \\ \pm p^{S'} \end{Bmatrix}\end{aligned}\quad (1.42)$$

The material matrices of domains of types 3 and 4, with spontaneous polarization direction along the \pm crystal axis 1, reduce similarly from the matrices of the 3D case.

When dealing with polycrystalline ferroelectric ceramic with many grains of arbitrary shapes, the crystallographic coordinate system is randomly oriented in each grain. Hence, with respect to the global coordinate axes ($X_1 - X_2 - X_3$) of the aggregate, the material matrices of each domain inside a grain can also be obtained using the rotation matrix \mathbf{R} , where the angle θ in eq. (1.38) for the 2D case, or the angles θ, ϕ and ψ in eq. (1.39) for the 3D case, are the angles between the global coordinate system and the local crystallographic coordinate system of the grain.

1.8 Heterogeneous materials and Micromechanics

The homogeneity of materials depends on the scale of measurement. All materials are inhomogeneous in the microscale. Manufactured composites, natural soils and rocks as well as biological tissues are typical examples. The magnitude of the micro-scale used differs for specific materials. In general, the approximate range of the micro-scale is 10^{-7} m to 10^{-4} m. The continuum is a model of materials in the macroscopic scale. In classical continuum mechanics, materials are viewed as ideal continuous homogeneous media. The aim of continuum mechanics is to describe the response of homogeneous materials to external forces using approximate constitutive relations without microstructural considerations [16].

Heterogeneous materials exist in both synthetic products and nature. Some examples of natural heterogeneous materials are polycrystals, soils, sandstone, granular media, earth's crust, sea ice, wood, bone, lungs, blood, animal and plant tissue, cell aggregates, and tumors [17]. Synthetic examples include aligned and chopped fiber composites, particulate composites, interpenetrating multiphase composites, cellular solids, gels, foams, and concrete. Composites,

which are manufactured mixtures of two or more constituents usually bonded together, have inhomogeneous properties for different domains or different directions due to the inhomogeneity of their microstructures. This is an important feature and merit of heterogeneous materials [18]. These heterogeneous materials have a legible microstructure.

The microstructures of composite materials can be designed to meet various desired properties and functions. The materials may possess very high properties in one or two directions and very weak properties in other directions, depending on the design for structural performance. Because of their excellent designable characteristics, composite materials are increasingly applied to industrial fields, for example, aeronautics and astronautics, electronics, chemical engineering, biomedical fields and so on.

Heterogeneous materials often exhibit very complex properties, presenting new challenges and opportunities to scientists and engineers. In recent years several new composite materials have been developed which display not only good mechanical properties but also some new functions such as thermal, electric, magnetic, photic, and chemical effects. At the same time, composite materials can create new functions and performance which are absent in their constituents. Such multiple physical properties are usually coupled with each other. Consequently, the coupling properties and deformation behavior of heterogeneous materials are topics of great interest for qualitative and quantitative investigation.

A number of heterogeneous materials can fulfill the transfer between mechanical and non-mechanical energy (thermal, electrical, chemical energy, etc). Such materials are usually called *intelligent materials*. These materials can be used in adaptive structures, sensors, and actuators. Intelligent materials are sensitive to variables of the external environment, adjusting their shape or size to adapt to changes in that environment. This multi-field coupling behavior is

a unique characteristic of intelligent materials. For instance, piezoelectric ceramics, piezoelectric polymers, and some biological tissues (e.g. bone, skin, etc) exhibit thermo-electro-elastic coupling properties [19]. Electric current and heat flow will be excited when the material is subject to a mechanical loading, and vice versa.

As an example, a composite material consisting of a piezoelectric phase and a piezomagnetic phase exhibits considerable multifield coupling properties, i.e. both electro-mechanical and magneto-mechanical coupling. In addition, it displays a remarkably large coupling coefficient between static electric and magnetic fields, which is absent in either constituent. The magnetoelectric coupling in the composite is created through the interaction between the piezoelectric phase and the piezomagnetic phase, which is called a *product property*. The product property of composites offers great engineering opportunities to develop new materials.

Research into heterogeneous media has a long history. Two approaches have been adopted: macro-mechanical and micro-mechanical approaches. Macromechanics deals with material as a homogeneous continuum based on the approximate constitutive model, ignoring heterogeneity of the microstructure. The macroscopic or averaged properties of heterogeneous materials are studied. However, the macroscopic properties of materials depend on micro-structural information, such as the geometric and physical properties of the constituents and the behavior of their interface. Micromechanics has been developed to investigate the relations between the effective properties and microstructures of heterogeneous materials and the interactions among the constituents [20]-[21]. As the characteristic length of microstructure is far less than the characteristic length of the whole body, a homogenization is carried out to capture the macroscopic behavior of the materials, as shown in Figure 1.12. Denoting y as the

microscopic scale and x as the structural scale, since $y \ll x$, the composite is replaced by the homogenized continuum.

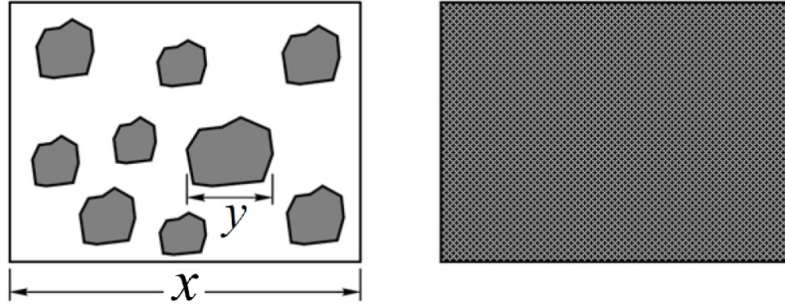


Figure 1.12: Homogenization of heterogeneous materials: (left) heterogeneous material with microstructure, (right) homogenized continuum.

In the frame of micromechanics, the emphasis is placed on the bridging between effective properties and microstructure parameters of materials. An understanding of the relations between effective properties and microstructure of materials is very vital in the design of new composite materials.

Heterogeneous materials such as composites, solids with micro-defects, rocks, and natural biomaterials consist of combinations of different media that form regions large enough to be regarded as continua, which are usually firmly bonded together at the interface. Their microstructure can be observed by means of electric scanning microscopes. Generally, for a heterogeneous composite, continuous constituent or phase can be referred to as a *matrix*, and a discrete phase as an *inclusion* which is embedded in the matrix. The inclusion may be a particle, a fiber, a micro-void, or a micro-crack. The overall (effective or macroscopic) properties of composite materials depend on the geometric and physical properties of the phases.

The microstructure of heterogeneous materials may be very disordered and complex in that the distribution, size and shape of inclusions are random. Moreover, there are local fluctuations of the phase volume fraction in a composite. Therefore, mathematical description of the

microstructure of a composite is a difficult issue. From a practical point of view, a composite material can be considered as an assembly of periodic unit cells. A unit cell is also called a *representative volume element* (RVE). A homogeneous material which has the effective properties of composite material is referred to as an *effective medium*. Periodic homogeneous boundary conditions should be applied to the RVE in order to ensure that the mechanical behavior of the RVE is equivalent to the mechanical behavior of the effective medium.

1.9 On using Representative Volume Element (RVE) to predict the effective material properties of piezo-composites

In order to determine the overall properties of piezoelectric/piezomagnetic composites from known properties of their constituents (matrix and particles or fibers), two approaches were used in the literature: macro-mechanical and micro-mechanical. In the macro-mechanical approach, the heterogeneous structure of the composite is replaced by a homogeneous medium with anisotropic properties, while in the micro-mechanical approach, a periodic representative volume element (RVE) or a unit cell model is used to obtain the global properties of the composite [22]. A unit cell is the smallest part that contains sufficient information on the geometrical and material parameters at the microscopic level to allow for prediction of the effective properties of the composite. The numerical methods, such as the finite elements, are well-suited to model the RVE and to describe the behavior of these composite materials because there are no restrictions on the geometry, the material properties, the number of phases and the size of the composite constituents. When employing unit cell models, the local fields in the constituent phases can be accurately determined by the numerical method, and various mechanisms such as damage initiation and propagation can be studied through the analysis.

Numerical homogenization method is based on finding a globally homogeneous medium equivalent to the original composite, where the strain energy stored in both systems is approximately the same. In order to do so, first, a representative volume element which captures the overall behavior of a composite structure is created. Then the effective material properties are calculated by applying periodic boundary conditions and appropriate load cases, which are connected to specific deformation patterns, to the unit cell [23].

It is known that the advantages of the analytical approaches over the FE analyses are their ability to model statistical distributions of fibers/particles in the composite and their low computational time, while the FE analysis, in contrast, is appropriate for estimating the effective properties of composites with a given periodic fiber/particle distribution and more complicated geometries (different shapes of fibers' cross-section, more than two phases, etc.), and in the same time, the local fields can be obtained accurately. Berger *et al.* [22] found that in order to get sufficiently accurate results from the FE model, the mesh density should be chosen in such a way that the average element width is at least 5% of the unit cell width. This means that at least 400 two-dimensional regular elements are required to accurately model a two-dimensional unit cell that includes only one fiber or particle. Finite element results are sensitive to mesh density; hence it could be a difficult task to find appropriate meshes for the RVE [24]. The disadvantages of the numerical models can be avoided if we resort to the newly developed techniques such as those presented in this study and in [25]-[30] because these advanced methods can model a grain with its void or inclusion using only one element or region whose geometric shape is arbitrary. Hence any statistical random distribution of fibers or particles can be accounted for with relatively very small computational cost and with high resolution in local fields' calculation.

In the coming chapters, we show the ability of the different types of the proposed computational grains to predict the effective material properties of piezo-composites using only one grain or using many grains with random distributions of the second phase, and to obtain high resolution of the local fields that enables studying damage initiation mechanisms in the micro level.

1.10 Special models to determine the effective material properties of piezoelectric composites

There are varieties of configurations used in designing piezoelectric particle- and fiber-composites. Figure 1.13 shows an illustrative representative volume element (RVE) with only one particle or one fiber in four different configurations. In this figure, piezoelectric materials are in gray color while non-piezoelectric materials are in green color. The red arrows indicate the polling direction in piezoelectric materials. Piezoelectric polymers (like PVDF) can be reinforced by embedding ceramic particles or fibers in the piezoelectric matrix (see the first 2 figures in Figure 1.13). Examples are SiC particles in PVDF matrix and graphite fibers in PVDF matrix. PVDF is an orthotropic, semi-crystalline polymer which exhibits piezoelectric effect when subjected to an electric field in x_3 -direction. The reinforcing fibers can be aligned in x_1 -direction in order to maintain high level of material compliance (hence maximizing the piezoelectric effect) in the transverse direction, while providing reinforcement in the direction in which little piezoelectric effect and maximum mechanical reinforcement are required. On the other hand, piezoelectric particles or fibers can be embedded in polyimide matrix (see the last 2 figures in Figure 1.13). Examples are PZT-7A ceramic particles or fibers in LaRC-SI matrix. LaRC-SI (Langley Research Center - Soluble Imide) is a thermoplastic polyimide that was developed for aerospace applications. In case of piezoelectric fibers, usually the fibers are aligned and poled in x_3 -direction.

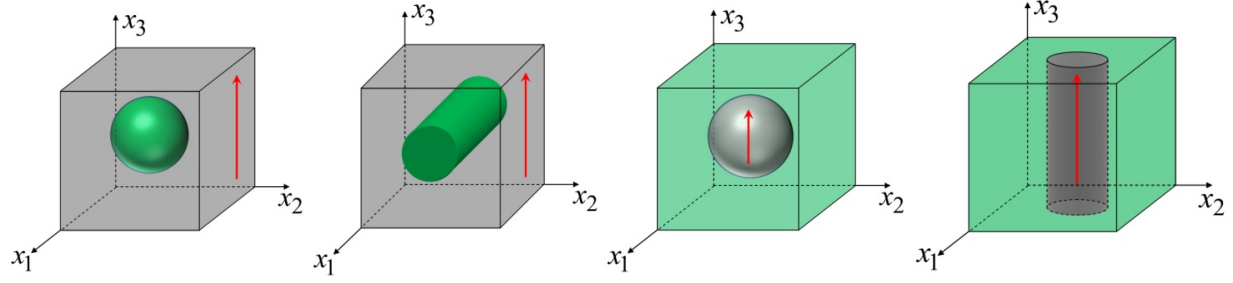


Figure 1.13: Variety of configurations used in piezoelectric composites

Our 2D models can be used to estimate all effective material properties of composites with particles or voids, while for composites with fibers, only effective properties in the plane perpendicular to the fiber axis can be obtained. So in Figure 1.13, all properties in the first and third figures can be obtained; in the second figure, only $x_2 - x_3$ plane can be considered, while in the last figure, only $x_1 - x_2$ plane can be considered.

Considering $x_1 - x_3$ plane as an example, computational models that ensure the presence of ϵ_{11} , ϵ_{33} , E_1 or E_3 alone in each model should be used. This is done by prescribing constant mechanical displacement or electric potential on the right or upper sides of the sample while enforcing zero electromechanical displacements on the other three sides.

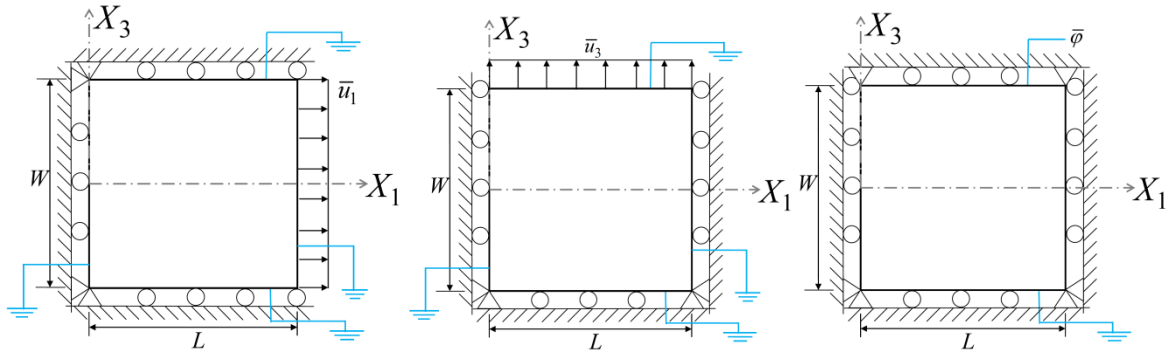


Figure 1.14: Computational models to evaluate the effective properties of: (left) C_{11}^{eff} and C_{13}^{eff} , (middle) C_{33}^{eff} and C_{13}^{eff} , (right) e_{31}^{eff} , e_{33}^{eff} and h_{33}^{eff}

Three computational models, shown in Figure 1.14, are used to calculate the effective properties of piezoelectric composite materials: C_{11}^{eff} , C_{33}^{eff} , C_{13}^{eff} , e_{31}^{eff} , e_{33}^{eff} and h_{33}^{eff} .

The first model ensures that $\varepsilon_{33} = 0$ and $E_3 = 0$ and is used to calculate C_{11}^{eff} and C_{13}^{eff} as:

$$C_{11}^{eff} = \frac{\sigma_{11}}{\varepsilon_{11}} = \frac{\int_{x_1=L} t_1.ds / W}{\bar{u}_1 / L}, \quad C_{13}^{eff} = \frac{\sigma_{33}}{\varepsilon_{11}} = \frac{\int_{x_3=W} t_3.ds / L}{\bar{u}_1 / L} \quad (1.43)$$

The second model ensures that $\varepsilon_{11} = 0$ and $E_3 = 0$ and is used to calculate C_{33}^{eff} , C_{13}^{eff} as:

$$C_{33}^{eff} = \frac{\sigma_{33}}{\varepsilon_{33}} = \frac{\int_{x_3=W} t_3.ds / L}{\bar{u}_3 / W}, \quad C_{13}^{eff} = \frac{\sigma_{11}}{\varepsilon_{33}} = \frac{\int_{x_1=L} t_1.ds / W}{\bar{u}_3 / W} \quad (1.44)$$

Finally, the third model ensures that $\varepsilon_{11} = \varepsilon_{33} = 0$ and is used to calculate e_{33}^{eff} , e_{13}^{eff} and h_{33}^{eff} as:

$$e_{33}^{eff} = -\frac{\sigma_{33}}{E_3} = \frac{\int_{x_3=W} t_3.ds / L}{\bar{\varphi} / W}, \quad e_{13}^{eff} = -\frac{\sigma_{11}}{E_3} = \frac{\int_{x_1=L} t_1.ds / W}{\bar{\varphi} / W}, \quad h_{33}^{eff} = \frac{D_3}{E_3} = \frac{\int_{x_3=W} Q.ds / L}{\bar{\varphi} / W} \quad (1.45)$$

The three Young's moduli Y_1 , Y_2 and Y_3 can be obtained from the stiffness matrix constants C_{ij} .

The numerical methods proposed in the coming chapters allow the used representative volume element (RVE) to be composed of any number of arbitrarily shaped grains with arbitrarily-distributed, arbitrarily-sized and arbitrarily-oriented elliptical voids or inclusions.

Finally, the material properties used in the numerical examples in the coming chapters are presented in Table 1.1. The properties of PZT-4 are taken from two references: Xu and Rajapakse [31], and denoted here by PZT-4(1), and Wang *et al.* [32] and denoted as PZT-4(2). The material properties of PZT-7A, PVDF, LaRC-SI and SiC are taken from [33].

Table 1.1: Material properties used in the numerical examples [C_{ij} in GPa, e_{ij} in C/m², h_{ii} in nC/(Vm)]

Property	C'_{11}	C'_{12}	C'_{13}	C'_{22}	C'_{23}	C'_{33}	C'_{44}	C'_{55}
PZT-4(1)	139	77.8	74.3	139	74.3	113	25.3	25.3
PZT-4(2)	126	77.8	74.3	126	74.3	115	25.6	25.6
PZT-7A	148	76.2	74.2	148	74.2	131	25.4	25.4
PVDF	3.8	1.9	1.0	3.2	0.9	1.2	0.7	0.9
LaRC-SI	8.1	5.4	5.4	8.1	5.4	8.1	1.4	1.4
SiC	483.7	99.1	99.1	483.7	99.1	483.7	192.3	192.3
Property	C'_{66}	e'_{31}	e'_{32}	e'_{33}	$e'_{15} = e'_{24}$	h'_{11}	h'_{22}	h'_{33}
PZT-4(1)	30.6	-6.98	-6.98	13.84	13.44	6	6	5.47
PZT-4(2)	30.6	-5.2	-5.2	15.1	12.7	6.464	6.464	5.622
PZT-7A	35.9	460	460	235	9.2	-2.1	-2.1	9.5
PVDF	0.9	0.024	0.001	-0.027	0	7.4	9.3	7.6
LaRC-SI	1.4	0	0	0	0	2.8	2.8	2.8
SiC	192.3	0	0	0	0	10.0	10.0	10.0

1.11 References of chapter 1

- [1] **Jaffe, B.; Cook, W.R.; Jaffe, H.** (1971): *Piezoelectric Ceramics*. Academic Press, New York.
- [2] **Cady, W.G.** (1964): *Piezoelectricity*. Vols. 1 & 2, Dover, New York.
- [3] **Lines, M.E.; Glass, A.M.** (1977): *Principles and Applications of Ferroelectrics and Related Materials*. Clarendon Press, Oxford.
- [4] **Parton, V.Z.; Kudryavtsev, B.A.** (1988): *Electromagnetoelasticity, Piezoelectrics and Electrically Conductive Solids*. Gordon and Breach, New York.
- [5] **Ikeda, T.** (1990): *Fundamentals of Piezoelectricity*. Oxford Science Publications, New York.
- [6] **Dzialoshinskii, I. E.** (1958): The problem of piezomagnetism. *Soviet Phys. JETP*, vol. 6, 621.
- [7] **Borovik-Romanov, A.S.** (1960): Piezomagnetism in the antiferromagnetic fluorides of cobalt and manganese. *Soviet Phys. JETP*, vol. 11, 786.

- [8] **Cullity, B. D.** (1971): Fundamentals of magnetostriction. *Journal of Metals*, vol. 1, 323.
- [9] **McCaig, M.** (1977): *Permanent magnets in theory and practice*. Pentech press. ISBN 0-7273-1604-4.
- [10] **Meiklejohn, W.H.; Bean, C.P.** (1957): New Magnetic Anisotropy. *Physical Review* vol.105 no. 3, pp. 904–913.
- [11] **Zhai, J.; Cai, N.; Shi, Z.; Lin, Y.; Nan, C.-W.** (2004): Magnetic-dielectric properties of NiFe₂O₄/PZT particulate composites. *J. Phys. D*, vol. 37, pp.823-827.
- [12] **Kamentsev, K. E.; Fetisov, Y. K.; Srinivasan, G.** (2006): Low-frequency nonlinear magnetoelectric effects in a ferrite-piezoelectric multilayer. *Appl. Phys. Lett.*, vol. 89, no.14, pp. 142510 - 142510-3.
- [13] **Laletsin, U.; Padubnaya, N.; Srinivasan, G.; Devreugd, C. P.** (2004): Frequency dependence of magnetoelectric interactions in layered structures of ferromagnetic alloys and piezoelectric oxides. *Appl. Phys. A: Mater. Sci. Process.*, vol. 78, pp. 33-36.
- [14] **Blackburn, J. F.; Vopsaroiu, M.; Cain, M. G.** (2008): Verified finite element simulation of multiferroic structures Solutions for conducting and insulating systems. *Journal of applied physics*, vol. 104, no. 7, p. 074104.
- [15] **Webber K.G.** (2008): *Effect of Domain Wall Motion and Phase Transformations on Nonlinear Hysteretic Constitutive Behavior in Ferroelectric Materials*, PhD dissertation, Georgia institute of technology.
- [16] **Qin Q.; Yang, Q.** (2009): *Macro-Micro theory on multifield coupling behavior of heterogeneous materials*. Springer, Berlin Heidelberg.
- [17] **Torquato, S.** (2002): *Random heterogeneous materials, microstructure and macroscopic properties*. Springer-Verlag, New York.

- [18] **Muhammad, S.** (2003): *Heterogeneous materials*. Springer, New York,.
- [19] **Qin Q.** (2001): *Fracture mechanics of piezoelectric materials*. Southampton, WIT Press.
- [20] **Nemat-Nasser S.; Hori, M.** (1993): *Micromechanics: overall properties of heterogeneous materials*. Elsevier, Amsterdam.
- [21] **Mura T.** (1987): *Micromechanics of defects in solids*. Dordrecht, Martinus Nijhoff.
- [22] **Berger H.; Kari, S.; Gabbert, U.; Rodriguez-Ramos, R.; Bravo-Castillero, J.; Guinovart-Diaz, R.; Sabina, F. J.; Maugin, G. A.** (2006): Unit cell models of piezoelectric fiber composites for numerical and analytical calculation of effective properties. *Smart Materials and Structures*, vol. 15, pp. 451-458.
- [23] **Kari, S.; Berger, H.; Gabbert, U.** (2008): Numerical evaluation of effective material properties of piezoelectric fibre composites. In *Micro-Macro-interaction*. A. Bertram and J. Tomas, Springer, Berlin Heidelberg, pp. 109-120.
- [24] **Berger H.; Kari, S.; Gabbert, U.; Rodriguez-Ramos, R.; Guinovart, R.; Otero, J. A.; Bravo-Castillero, J.** (2005): An analytical and numerical approach for calculating effective material coefficients of piezoelectric fiber composites. *International Journal of Solids and Structures*, vol. 42, pp. 5692-5714.
- [25] **Bishay, P. L.; Atluri, S. N.** (2014): Trefftz-Lekhnitskii Grains (TLGs) for efficient direct numerical simulation (DNS) of the micro/meso mechanics of porous piezoelectric materials, *Computational Materials Science*, vol. 83, pp. 235–249.
- [26] **Bishay, P. L.; Dong, L.; Atluri, S. N.** (2014): Multi-Physics Computational Grains (MPCGs) for direct numerical simulation (DNS) of piezoelectric composite/porous materials and structures. Submitted for publication in *Computational Mechanics*.

- [27] **Dong, L.; Atluri, S. N.** (2012a): T-Trefftz Voronoi cell finite elements with elastic/rigid inclusions or voids for micromechanical analysis of composite and porous materials. *CMES: Computer Modeling in Engineering & Sciences*, vol.83, no.2, pp.183-219.
- [28] **Dong, L.; Atluri, S. N.** (2012b): Development of 3D T-Trefftz Voronoi cell finite elements with/without spherical voids &/or elastic/rigid inclusions for micromechanical modeling of heterogeneous materials. *CMC: Computers, Materials & Continua*, vol. 29, no. 2, pp. 169–211.
- [29] **Dong, L.; Atluri, S. N.** (2012c): Development of 3D Trefftz Voronoi cells with ellipsoidal voids &/or elastic/rigid inclusions for micromechanical modeling of heterogeneous materials. *CMC: Computers, Materials & Continua*, vol. 30, no. 1, pp. 39–82.
- [30] **Dong, L.; Atluri, S. N.** (2012d): A simple multi-source-point Trefftz method for solving direct/inverse SHM problems of plane elasticity in arbitrary multiply-connected domains. *CMES: Computer Modeling in Engineering & Sciences*, vol.85, no.1, pp. 1–43.
- [31] **Xu X.L., Rajapakse R.K.N.D.** (1999): Analytical solution for an arbitrarily oriented void/crack and fracture of piezoceramics. *Acta Materialia*, vol. 47, pp. 1735 –1747.
- [32] **Wang, H.; Tan, G.; Cen S.; Yao, Z.** (2005): Numerical determination of effective properties of voided piezoelectric materials using BNM, *Engineering Analysis with Boundary Elements*, vol. 29, pp. 636–646.
- [33] **Odegard, G.M.** (2004): Constitutive modeling of piezoelectric polymer composites. *Acta Materialia*, vol.52, pp. 5315–5330.

Chapter 2 : Lekhnitskii formalism for coupled/uncoupled electro-elastic and magneto-elastic materials

2.1 Introduction

The basic idea of the various Trefftz methods is to use the so-called Trefftz functions which satisfy the homogenous governing equations of the relevant physical phenomenon as the trial and/or weight functions. A complete set of Trefftz functions that satisfy only the homogenous governing equations is termed as a *basic solution set*. A complete set of Trefftz functions that satisfy both the homogenous governing equations and the homogenous boundary conditions is termed as a *special solution set* such as the special solution set presented in this chapter for electromagnetic impermeable voids that considers the void to be fully insulated to electromagnetic fields, and hence satisfies the *traction-free* and *vanishing surface charge density and magnetic flux density (normal electric displacement and magnetic induction)* conditions along the void periphery. To formulate any Trefftz method, Trefftz functions must be available.

This chapter is devoted for presenting Lekhnitskii formulation for coupled/uncoupled electro-elastic and magneto-elastic materials because the computational grains proposed in chapters 3 and 4 depend on Trefftz functions that are based on this formulation in this study. The basic formulation is presented in section 2.2, while the basic solution set and the special solution set for impermeable elliptical voids are presented in sections 2.3 and 2.4. The chapter is summarized in section 2.5. Finally, references are listed in section 2.6.

2.2 Basic formulation

The following formulation is suitable for three types of materials: piezoelectric (with electromechanical coupling), piezomagnetic (with magnetomechanical coupling) and elastic (with no couplings). The formulation also can be used for external domains (matrix), or internal

domains (inclusions: fibers or particles). As mentioned in sections 1.3 and 1.4, the magnetic bias direction in the matrix or in the inclusion is allowed to be different from the poling direction or the axis normal to the plane of isotropy in transversely isotropic materials.

Let $(x'_{\alpha 1}, x'_{\alpha 3})$ be the principal material (crystallographic) coordinates in the matrix ($\alpha = m$) or in the inclusion ($\alpha = c$), $x'_{\alpha 3}$ be the poling direction (for piezoelectric or dielectric materials) in the matrix or in the inclusion, and $x''_{\alpha 3}$ be the magnetic bias direction in the matrix or in the inclusion (see Figure 2.1). The (x_1, x_3) coordinates are obtained by rotating $(x'_{\alpha 1}, x'_{\alpha 3})$ through an anti-clockwise rotation ζ_α , or by rotating $(x''_{\alpha 1}, x''_{\alpha 3})$ through an anti-clockwise rotation $\zeta_{M\alpha}$, as shown in Figure 2.1. In the rest of this chapter, the subscript, α , that indicates whether we are talking about the matrix ($\alpha = m$) or the inclusion ($\alpha = c$) is omitted for simplicity.

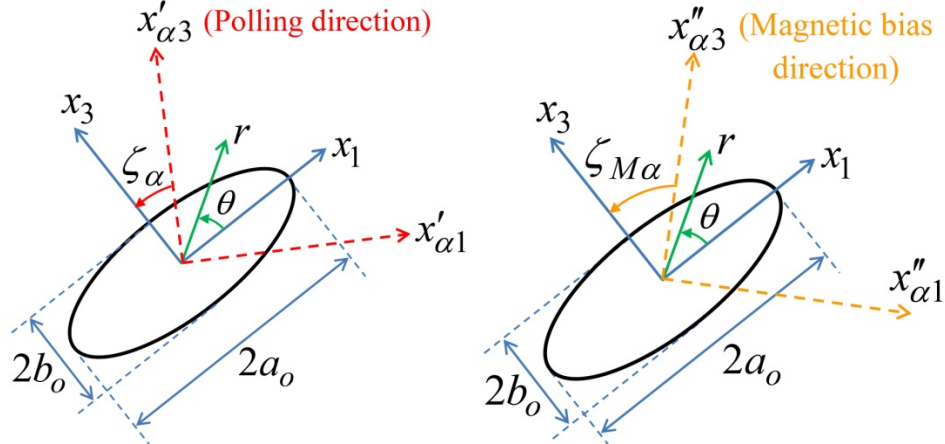


Figure 2.1: Elliptical void/inclusion with the local coordinate system as well as the polling direction (left), and magnetic bias direction (right)

Using Lekhnitskii formalism [1]-[2], Xu and Rajapakse [3] derived the general solution of plane piezoelectricity with respect to (x_1, x_3) coordinate system. Because Lekhnitskii's solution for piezoelectric materials breaks down if there is no coupling between the mechanical and the electrical variables, this study presents this solution in a general form that can be used for coupled as well as uncoupled materials. The formulation is also extended here by including the

magnetic variables. Hence, the matrix and the inclusion materials can be piezoelectric, piezomagnetic or elastic (with no electromechanical or magnetomechanical couplings) to allow modeling the different types of piezoelectric-piezomagnetic composites.

The constitutive equation with respect to (x_1, x_3) coordinate system for plane stress and plane strain problems, with the stress, electric displacement and magnetic induction as the objectives of the equations, can be written in compact form as:

$$\left\{ \begin{array}{c} \varepsilon_1 \\ \varepsilon_3 \\ \varepsilon_5 \\ E_1 \\ E_3 \\ H_1 \\ H_3 \end{array} \right\} = \left[\begin{array}{ccc|cc|cc} S_{11} & S_{13} & S_{15} & g_{11} & g_{31} & b_{11} & b_{31} \\ S_{13} & S_{33} & S_{35} & g_{13} & g_{33} & b_{13} & b_{33} \\ S_{15} & S_{35} & S_{55} & g_{15} & g_{35} & b_{15} & b_{35} \\ \hline -g_{11} & -g_{13} & -g_{15} & \beta_{11} & \beta_{13} & \kappa_{11} & \kappa_{13} \\ -g_{31} & -g_{33} & -g_{35} & \beta_{13} & \beta_{33} & \kappa_{13} & \kappa_{33} \\ \hline -b_{11} & -b_{13} & -b_{15} & \kappa_{11} & \kappa_{13} & v_{11} & v_{13} \\ -b_{31} & -b_{33} & -b_{35} & \kappa_{13} & \kappa_{33} & v_{13} & v_{33} \end{array} \right] \left\{ \begin{array}{c} \sigma_1 \\ \sigma_3 \\ \sigma_5 \\ D_1 \\ D_3 \\ B_1 \\ B_3 \end{array} \right\} \quad (2.1)$$

or $\left\{ \begin{array}{c} \boldsymbol{\varepsilon} \\ \mathbf{E} \\ \mathbf{H} \end{array} \right\} = \left[\begin{array}{ccc} \mathbf{S} & \mathbf{g}^T & \mathbf{b} \\ -\mathbf{g} & \boldsymbol{\beta} & \boldsymbol{\kappa} \\ -\mathbf{b} & -\boldsymbol{\kappa} & \mathbf{v} \end{array} \right] \left\{ \begin{array}{c} \boldsymbol{\sigma} \\ \mathbf{D} \\ \mathbf{B} \end{array} \right\}$

where superscripts of the material matrices in eq. (1.5) are omitted for simplicity. Tensor transformation rules can be used to express the material properties in (x_1, x_3) coordinate system in terms of those in the crystallographic coordinate system, (x'_1, x'_3) , such as $\mathbf{S}', \mathbf{g}', \boldsymbol{\beta}'$ and $\boldsymbol{\kappa}'$, or in terms of those in the (x''_1, x''_3) coordinate system, such as $\mathbf{v}'', \mathbf{b}''$:

$$\begin{aligned} \mathbf{S} &= \mathbf{T}_2^T \mathbf{S}' \mathbf{T}_2, & \mathbf{g} &= \mathbf{T}_1^T \mathbf{g}' \mathbf{T}_2, & \boldsymbol{\beta} &= \mathbf{T}_1^T \boldsymbol{\beta}' \mathbf{T}_1, & \boldsymbol{\kappa} &= \mathbf{T}_1^T \boldsymbol{\kappa}' \mathbf{T}_1 \\ \mathbf{b} &= \mathbf{T}_{\mathbf{M}2}^T \mathbf{b}'' \mathbf{T}_{\mathbf{M}2}, & \mathbf{v} &= \mathbf{T}_{\mathbf{M}1}^T \mathbf{v}'' \mathbf{T}_{\mathbf{M}1} \end{aligned} \quad (2.2)$$

In the above equations,

$$\mathbf{T}_1 = \begin{bmatrix} \cos \zeta & -\sin \zeta \\ \sin \zeta & \cos \zeta \end{bmatrix} \quad \text{and} \quad \mathbf{T}_2 = \begin{bmatrix} \cos^2 \zeta & \sin^2 \zeta & -2 \sin \zeta \cos \zeta \\ \sin^2 \zeta & \cos^2 \zeta & 2 \sin \zeta \cos \zeta \\ \sin \zeta \cos \zeta & -\sin \zeta \cos \zeta & \cos^2 \zeta - \sin^2 \zeta \end{bmatrix} \quad (2.3)$$

\mathbf{T}_{M1} and \mathbf{T}_{M2} have the same form of \mathbf{T}_1 and \mathbf{T}_2 respectively in eq. (2.3) after replacing ζ by ζ_M . It can be seen that the coefficients $\mathbf{S}, \mathbf{g}, \mathbf{\beta}, \mathbf{v}, \mathbf{b}$ and $\mathbf{\kappa}$ are functions of the angles ζ and ζ_M . Piezoelectric materials have no magneto-mechanical and electromagnetic couplings, so $\mathbf{b} = \mathbf{\kappa} = \mathbf{0}$; piezomagnetic materials have no electromechanical and electromagnetic couplings, hence $\mathbf{g} = \mathbf{\kappa} = \mathbf{0}$; while elastic dielectric materials have no couplings at all, and $\mathbf{g} = \mathbf{b} = \mathbf{\kappa} = \mathbf{0}$.

Lekhnitskii's formalism is extended here for the case of magneto-electro-elastic materials. Three complex potential functions: Airy stress function, $\phi(x_1, x_3)$, electric scalar potential function, $\vartheta(x_1, x_3)$, and magnetic scalar potential function, $\rho(x_1, x_3)$, are introduced as:

$$\begin{aligned} \sigma_1 &= \frac{\partial^2 \phi(x_1, x_3)}{\partial x_3^2}, & \sigma_3 &= \frac{\partial^2 \phi(x_1, x_3)}{\partial x_1^2}, & \sigma_5 &= -\frac{\partial^2 \phi(x_1, x_3)}{\partial x_1 \partial x_3}, \\ D_1 &= \frac{\partial \vartheta(x_1, x_3)}{\partial x_3}, & D_3 &= -\frac{\partial \vartheta(x_1, x_3)}{\partial x_1}, & B_1 &= \frac{\partial \rho(x_1, x_3)}{\partial x_3}, & B_3 &= -\frac{\partial \rho(x_1, x_3)}{\partial x_1} \end{aligned} \quad (2.4)$$

The balance rules for plane magneto-electro-elasticity (eqs. (1.3)) in the absence of body force and free-charge density ($\bar{\mathbf{b}}_f = \mathbf{0}$, $\bar{\rho}_f = 0$) are satisfied using eq. (2.4). By substituting eq. (2.4) into eq. (2.1) and invoking the following strain compatibility, Faraday's and Ampere's equations for electrostatics and magnetostatics:

$$\frac{\partial^2 \epsilon_1}{\partial x_3^2} + \frac{\partial^2 \epsilon_3}{\partial x_1^2} - \frac{\partial^2 \epsilon_5}{\partial x_1 \partial x_3} = 0, \quad \frac{\partial E_1}{\partial x_3} - \frac{\partial E_3}{\partial x_1} = 0, \quad \frac{\partial H_1}{\partial x_3} - \frac{\partial H_3}{\partial x_1} = 0 \quad (2.5)$$

Three differential equations coupled in $\phi(x_1, x_3)$, $\vartheta(x_1, x_3)$ and $\rho(x_1, x_3)$ can be obtained as:

$$\begin{aligned}
L_6\phi(x_1, x_3) - L_5\vartheta(x_1, x_3) - L_4\rho(x_1, x_3) &= 0, \\
L_5\phi(x_1, x_3) + L_3\vartheta(x_1, x_3) + L_2\rho(x_1, x_3) &= 0, \\
L_4\phi(x_1, x_3) + L_2\vartheta(x_1, x_3) + L_1\rho(x_1, x_3) &= 0
\end{aligned} \tag{2.6}$$

where

$$\begin{aligned}
L_1 &= \nu_{11} \frac{\partial^2}{\partial x_3^2} - 2\nu_{13} \frac{\partial^2}{\partial x_1 \partial x_3} + \nu_{33} \frac{\partial^2}{\partial x_1^2}, & L_2 &= \kappa_{11} \frac{\partial^2}{\partial x_3^2} - 2\kappa_{13} \frac{\partial^2}{\partial x_1 \partial x_3} + \kappa_{33} \frac{\partial^2}{\partial x_1^2}, \\
L_3 &= \beta_{11} \frac{\partial^2}{\partial x_3^2} - 2\beta_{13} \frac{\partial^2}{\partial x_1 \partial x_3} + \beta_{33} \frac{\partial^2}{\partial x_1^2}, \\
L_4 &= -b_{11} \frac{\partial^3}{\partial x_3^3} + (b_{15} + b_{31}) \frac{\partial^3}{\partial x_3^2 \partial x_1} - (b_{13} + b_{35}) \frac{\partial^3}{\partial x_3 \partial x_1^2} + b_{33} \frac{\partial^3}{\partial x_1^3}, \\
L_5 &= -g_{11} \frac{\partial^3}{\partial x_3^3} + (g_{15} + g_{31}) \frac{\partial^3}{\partial x_3^2 \partial x_1} - (g_{13} + g_{35}) \frac{\partial^3}{\partial x_3 \partial x_1^2} + g_{33} \frac{\partial^3}{\partial x_1^3}, \\
L_6 &= S_{11} \frac{\partial^4}{\partial x_3^4} - 2S_{15} \frac{\partial^4}{\partial x_3^3 \partial x_1} + (2S_{13} + S_{55}) \frac{\partial^4}{\partial x_3^2 \partial x_1^2} - 2S_{35} \frac{\partial^4}{\partial x_3 \partial x_1^3} + S_{33} \frac{\partial^4}{\partial x_1^4}.
\end{aligned}$$

Eliminating $\vartheta(x_1, x_3)$ and $\rho(x_1, x_3)$ from eqs. (2.6), the governing equations of plane magneto-electro-elasticity are reduced to the following eighth-order differential equation:

$$(L_1 L_5^2 - 2L_2 L_4 L_5 + L_1 L_3 L_6 + L_3 L_4^2 - L_2^2 L_6) \phi(x_1, x_3) = 0 \tag{2.7}$$

If the material is piezoelectric ($\mathbf{b} = \boldsymbol{\kappa} = 0$), then $L_2 = L_4 = 0$, and eqs. (2.6) and (2.7) reduce to:

$$(L_5^2 + L_3 L_6) \phi(x_1, x_3) = 0, \quad L_1 \rho(x_1, x_3) = 0, \tag{2.8}$$

if it is piezomagnetic ($\mathbf{g} = \boldsymbol{\kappa} = \mathbf{0}$), then $L_2 = L_5 = 0$, and eqs. (2.6) and (2.7) take the form:

$$(L_4^2 + L_1 L_6) \phi(x_1, x_3) = 0, \quad L_3 \vartheta(x_1, x_3) = 0, \tag{2.9}$$

while if it is only elastic dielectric ($\mathbf{g} = \mathbf{b} = \boldsymbol{\kappa} = \mathbf{0}$), then $L_2 = L_4 = L_5 = 0$, and eqs. (2.6) and (2.7)

are reduced to:

$$L_6 \phi(x_1, x_3) = 0, \quad L_3 \vartheta(x_1, x_3) = 0, \quad L_1 \rho(x_1, x_3) = 0 \tag{2.10}$$

Eqs. (2.8) for piezoelectric materials can be written symbolically as sixth and second degree differential equations for piezoelectricity [4] and magnetostatics, respectively:

$$F_1 F_2 F_3 F_5 F_6 F_7 \phi(x_1, x_3) = 0, \quad F_4 F_8 \rho(x_1, x_3) = 0 \quad (2.11)$$

where $F_k = (\partial / \partial x_3) - \mu_k (\partial / \partial x_1)$ and μ_k ($k = 1, \dots, 8$) are the roots of the characteristic eqs. (2.12) and (2.13). $\mu_1, \mu_2, \mu_3, \mu_5, \mu_6$ and μ_7 are obtained from the piezoelectricity equation (2.12) while μ_4 and μ_8 are obtained from the magnetostatics equation (2.13):

$$c_6 \mu^6 + c_5 \mu^5 + c_4 \mu^4 + c_3 \mu^3 + c_2 \mu^2 + c_1 \mu + c_0 = 0. \quad (2.12)$$

$$v_{11} \mu^2 - 2v_{13} \mu + v_{33} = 0 \quad (2.13)$$

where

$$\begin{aligned} c_0 &= S_{33} \beta_{33} + g_{33}^2, & c_1 &= -2S_{35} \beta_{33} - 2S_{33} \beta_{13} - 2g_{33}(g_{13} + g_{35}), \\ c_2 &= S_{33} \beta_{11} + 4S_{35} \beta_{13} + \beta_{33}(2S_{13} + S_{55}) + 2g_{33}(g_{31} + g_{15}) + (g_{13} + g_{35})^2, \\ c_3 &= -2g_{11}g_{33} - 2S_{15} \beta_{33} - 2S_{35} \beta_{11} - 2\beta_{13}(2S_{13} + S_{55}) - 2(g_{31} + g_{15})(g_{13} + g_{35}), \\ c_4 &= S_{11} \beta_{33} + 4S_{15} \beta_{13} + \beta_{11}(2S_{13} + S_{55}) + 2g_{11}(g_{13} + g_{35}) + (g_{31} + g_{15})^2, \\ c_5 &= -2S_{11} \beta_{13} - 2S_{15} \beta_{11} - 2g_{11}(g_{31} + g_{15}), & c_6 &= S_{11} \beta_{11} + g_{11}^2. \end{aligned}$$

Similarly, eqs. (2.9) for piezomagnetic materials can be written symbolically as sixth and second degree differential equations for piezomagnetism and electrostatics, respectively:

$$F_1 F_2 F_4 F_5 F_6 F_8 \phi(x_1, x_3) = 0, \quad F_3 F_7 \vartheta(x_1, x_3) = 0 \quad (2.14)$$

where μ_k are the roots of the characteristic eqs. (2.15) and (2.16). $\mu_1, \mu_2, \mu_4, \mu_5, \mu_6$ and μ_8 are obtained from the piezomagnetism equation (2.15) while μ_3 and μ_7 are obtained from the electrostatics equation (2.16):

$$d_6 \mu^6 + d_5 \mu^5 + d_4 \mu^4 + d_3 \mu^3 + d_2 \mu^2 + d_1 \mu + d_0 = 0. \quad (2.15)$$

$$\beta_{11} \mu^2 - 2\beta_{13} \mu + \beta_{33} = 0 \quad (2.16)$$

where

$$\begin{aligned} d_0 &= S_{33}\nu_{33} + b_{33}^2, & d_1 &= -2S_{35}\nu_{33} - 2S_{33}\nu_{13} - 2b_{33}(b_{13} + b_{35}), \\ d_2 &= S_{33}\nu_{11} + 4S_{35}\nu_{13} + \nu_{33}(2S_{13} + S_{55}) + 2b_{33}(b_{31} + b_{15}) + (b_{13} + b_{35})^2, \\ d_3 &= -2b_{11}b_{33} - 2S_{15}\nu_{33} - 2S_{35}\nu_{11} - 2\nu_{13}(2S_{13} + S_{55}) - 2(b_{31} + b_{15})(b_{13} + b_{35}), \\ d_4 &= S_{11}\nu_{33} + 4S_{15}\nu_{13} + \nu_{11}(2S_{13} + S_{55}) + 2b_{11}(b_{13} + b_{35}) + (b_{31} + b_{15})^2, \\ d_5 &= -2S_{11}\nu_{13} - 2S_{15}\nu_{11} - 2b_{11}(b_{31} + b_{15}), & d_6 &= S_{11}\nu_{11} + b_{11}^2. \end{aligned}$$

Eqs. (2.10) for elastic dielectric materials can be written symbolically as forth degree differential equation for elasticity and two second degree differential equations for electrostatics and magnetostatics:

$$F_1 F_2 F_5 F_6 \phi(x_1, x_3) = 0, \quad F_3 F_7 \vartheta(x_1, x_3) = 0, \quad F_4 F_8 \rho(x_1, x_3) = 0 \quad (2.17)$$

where μ_k are the roots of the characteristic eqs. (2.18), (2.16) and (2.13). μ_1, μ_2, μ_5 and μ_6 are obtained from the elasticity equation (2.18), μ_3 and μ_7 are obtained from the electrostatics equation (2.16), while μ_4 and μ_8 are obtained from the magnetostatics equation (2.13):

$$S_{11}\mu^4 - 2S_{15}\mu^3 + (2S_{13} + S_{55})\mu^2 - 2S_{35}\mu^3 + S_{33} = 0 \quad (2.18)$$

Note that if there are no piezoelectric and piezomagnetic couplings, eqs. (2.12) and (2.15) break down, and eqs. (2.18), (2.16) and (2.13) should be used to obtain the roots μ_k .

In general, the roots of eqs. (2.12) and (2.13) for piezoelectric materials, (2.15) and (2.16) for piezomagnetic materials, or those of eqs. (2.18), (2.16) and (2.13) for elastic dielectric materials are complex with three conjugate pairs:

$$\begin{aligned} \mu_1 &= A_{\mu 1} + iB_{\mu 1}, & \mu_2 &= A_{\mu 2} + iB_{\mu 2}, & \mu_3 &= A_{\mu 3} + iB_{\mu 3}, & \mu_4 &= A_{\mu 4} + iB_{\mu 4}, \\ \mu_5 &= \bar{\mu}_1, & \mu_6 &= \bar{\mu}_2, & \mu_7 &= \bar{\mu}_3, & \mu_8 &= \bar{\mu}_4 \end{aligned} \quad (2.19)$$

in which $i = \sqrt{-1}$, $A_{\mu k}$ and $B_{\mu k}$ ($k = 1, 2, 3, 4$) are all distinct. Over-bar denotes complex conjugate.

Integration of eqs. (2.11) leads to the general solution for the complex potential functions $\phi(x_1, x_3)$ and $\rho(x_1, x_3)$ for piezoelectric materials as:

$$\phi(x_1, x_3) = 2 \operatorname{Re} \sum_{k=1}^3 \phi_k(z_k), \quad \rho(x_1, x_3) = 2 \operatorname{Re}(\omega_4(z_4)) \quad (2.20)$$

where $\phi_k(z_k)$ is an arbitrary function of the complex variable $z_k = x_1 + \mu_k x_3$, and $\omega_4(z_4)$ is an arbitrary function of the complex variable $z_4 = x_1 + \mu_4 x_3$. By virtue of eqs. (2.6) and (2.20), the general solution for the complex potential function $\vartheta(x_1, x_3)$ can be expressed as:

$$\vartheta(x_1, x_3) = 2 \operatorname{Re} \sum_{k=1}^3 \eta_k \frac{\partial \phi_k(z_k)}{\partial z_k} \quad (2.21)$$

where

$$\begin{aligned} \eta_k &= -\frac{I_2(\mu_k)}{I_1(\mu_k)}, & I_1(\mu_k) &= \beta_{11}\mu_k^2 - 2\beta_{13}\mu_k + \beta_{33}, \\ I_2(\mu_k) &= -g_{11}\mu_k^3 + (g_{15} + g_{31})\mu_k^2 - (g_{13} + g_{35})\mu_k + g_{33}. \end{aligned}$$

Similarly, integration of eqs. (2.14) leads to the general solution for the complex potential functions $\phi(x_1, x_3)$ and $\vartheta(x_1, x_3)$ for piezomagnetic materials as:

$$\phi(x_1, x_3) = 2 \operatorname{Re} \sum_{k=1,2,4} \phi_k(z_k), \quad \vartheta(x_1, x_3) = 2 \operatorname{Re}(\omega_3(z_3)) \quad (2.22)$$

By virtue of eqs. (2.6) and (2.22), the general solution for the complex potential function $\rho(x_1, x_3)$ can be expressed as:

$$\rho(x_1, x_3) = 2 \operatorname{Re} \sum_{k=1,2,4} \tau_k \frac{\partial \phi_k(z_k)}{\partial z_k} \quad (2.23)$$

where

$$\begin{aligned}\tau_k &= -\frac{I_4(\mu_k)}{I_3(\mu_k)}, & I_3(\mu_k) &= v_{11}\mu_k^2 - 2v_{13}\mu_k + v_{33}, \\ I_4(\mu_k) &= -b_{11}\mu_k^3 + (b_{15} + b_{31})\mu_k^2 - (b_{13} + b_{35})\mu_k + b_{33}.\end{aligned}$$

Integration of eqs. (2.17) leads to the general solution for the complex potential functions $\phi(x_1, x_3)$, $\vartheta(x_1, x_3)$ and $\rho(x_1, x_3)$ for elastic dielectric materials as:

$$\phi(x_1, x_3) = 2 \operatorname{Re} \sum_{k=1}^2 \phi_k(z_k), \quad \vartheta(x_1, x_3) = 2 \operatorname{Re}(\omega_3(z_3)), \quad \rho(x_1, x_3) = 2 \operatorname{Re}(\omega_4(z_4)) \quad (2.24)$$

Introducing new complex potential functions:

$$\omega_k(z_k) = \frac{\partial \phi_k(z_k)}{\partial z_k} \quad (2.25)$$

where $k=1,2,3$ for the piezoelectric case ($\omega_4(z_4)$ is already defined in eq. (2.20) for this case), $k=1,2,4$ for the piezomagnetic case ($\omega_3(z_3)$ is already defined in eq. (2.22) for this case), and $k=1,2$ for the mechanical part of the uncoupled material ($\omega_3(z_3)$ and $\omega_4(z_4)$ is already defined in eq. (2.24) for this case).

The expressions of $\phi(x_1, x_3)$, $\vartheta(x_1, x_3)$ and $\rho(x_1, x_3)$ in eqs. (2.20)-(2.24) can be generalized to account for all cases as:

$$\begin{aligned}\phi(x_1, x_3) &= 2 \operatorname{Re} \sum_{k=1}^4 \gamma_k \phi_k(z_k), & \vartheta(x_1, x_3) &= 2 \operatorname{Re} \sum_{k=1}^4 \lambda_k \omega_k(z_k), \\ \rho(x_1, x_3) &= 2 \operatorname{Re} \sum_{k=1}^4 \Delta_k \omega_k(z_k)\end{aligned} \quad (2.26)$$

where for uncoupled (elastic dielectric) materials: $\gamma_k = \delta_{k1} + \delta_{k2}$, $\lambda_k = \delta_{k3}$, $\Delta_k = \delta_{k4}$, for piezoelectric: $\gamma_k = 1 - \delta_{k4}$, $\Delta_k = \delta_{k4}$,

$$\lambda_k = \gamma_k \eta_k = (1 - \delta_{k4}) \frac{g_{11}\mu_k^3 - (g_{15} + g_{31})\mu_k^2 + (g_{13} + g_{35})\mu_k - g_{33}}{\beta_{11}\mu_k^2 - 2\beta_{13}\mu_k + \beta_{33}}$$

and for piezomagnetic: $\gamma_k = 1 - \delta_{k3}$, $\lambda_k = \delta_{k3}$,

$$\Delta_k = \gamma_k \tau_k = (1 - \delta_{k3}) \frac{b_{11}\mu_k^3 - (b_{15} + b_{31})\mu_k^2 + (b_{13} + b_{35})\mu_k - b_{33}}{\nu_{11}\mu_k^2 - 2\nu_{13}\mu_k + \nu_{33}}$$

δ_{ij} is the Kronecker delta. Substituting eq. (2.26) into eq. (2.4), general expressions for stress, electric displacement, magnetic induction, strain, electric field and magnetic field components for any type of material can be obtained in terms of the complex potential functions $\omega_k(z_k)$ as:

$$\begin{aligned} \begin{Bmatrix} \sigma_1 \\ \sigma_3 \\ \sigma_5 \end{Bmatrix} &= 2 \operatorname{Re} \sum_{k=1}^4 \begin{Bmatrix} \gamma_k \mu_k^2 \\ \gamma_k \\ -\gamma_k \mu_k \end{Bmatrix} \omega'_k(z_k), & \begin{Bmatrix} \varepsilon_1 \\ \varepsilon_3 \\ \varepsilon_5 \end{Bmatrix} &= 2 \operatorname{Re} \sum_{k=1}^4 \begin{Bmatrix} \gamma_k p_k \\ \gamma_k q_k \\ \gamma_k r_k \end{Bmatrix} \omega'_k(z_k), \\ \begin{Bmatrix} D_1 \\ D_3 \end{Bmatrix} &= 2 \operatorname{Re} \sum_{k=1}^4 \begin{Bmatrix} \lambda_k \mu_k \\ -\lambda_k \end{Bmatrix} \omega'_k(z_k), & \begin{Bmatrix} E_1 \\ E_3 \end{Bmatrix} &= -2 \operatorname{Re} \sum_{k=1}^4 \begin{Bmatrix} \lambda_k s_k \\ \lambda_k t_k \end{Bmatrix} \omega'_k(z_k), \\ \begin{Bmatrix} B_1 \\ B_3 \end{Bmatrix} &= 2 \operatorname{Re} \sum_{k=1}^4 \begin{Bmatrix} \Delta_k \mu_k \\ -\Delta_k \end{Bmatrix} \omega'_k(z_k), & \begin{Bmatrix} H_1 \\ H_3 \end{Bmatrix} &= -2 \operatorname{Re} \sum_{k=1}^4 \begin{Bmatrix} \Delta_k h_k \\ \Delta_k l_k \end{Bmatrix} \omega'_k(z_k) \end{aligned} \quad (2.27)$$

where the prime (') denotes derivative with respect to z_k and,

$$\begin{aligned} p_k &= S_{11}\mu_k^2 + S_{13} - S_{15}\mu_k + \lambda_k(g_{11}\mu_k - g_{31}), & q_k &= S_{13}\mu_k^2 + S_{33} - S_{35}\mu_k + \lambda_k(g_{13}\mu_k - g_{33}), \\ r_k &= S_{15}\mu_k^2 + S_{35} - S_{55}\mu_k + \lambda_k(g_{15}\mu_k - g_{35}), & s_k &= g_{11}\mu_k^2 + g_{13} - g_{15}\mu_k - \lambda_k(\beta_{11}\mu_k - \beta_{13}), \\ t_k &= g_{31}\mu_k^2 + g_{33} - g_{35}\mu_k - \lambda_k(\beta_{13}\mu_k - \beta_{33}), & h_k &= b_{11}\mu_k^2 + b_{13} - b_{15}\mu_k - \lambda_k(\nu_{11}\mu_k - \nu_{13}), \\ l_k &= b_{31}\mu_k^2 + b_{33} - b_{35}\mu_k - \lambda_k(\nu_{13}\mu_k - \nu_{33}). \end{aligned}$$

Invoking the gradient relations in eqs. (1.4), the general solution for mechanical displacements, electric and magnetic potentials can be obtained as:

$$\begin{Bmatrix} u_1 \\ u_3 \\ \varphi \\ \psi \end{Bmatrix} = 2 \operatorname{Re} \sum_{k=1}^4 \begin{Bmatrix} \gamma_k p_k \\ \gamma_k q_k / \mu_k \\ \lambda_k s_k \\ \Delta_k h_k \end{Bmatrix} \omega_k(z_k) \quad (2.28)$$

2.3 Basic Solution Set

For elliptical void as shown in Figure 2.1, the following conformal mapping can be used to transform the ellipse in z_k -plane into a unit circle in ξ_k -plane [2]:

$$z_k = \frac{a_o - i\mu_k b_o}{2} \xi_k + \frac{a_o + i\mu_k b_o}{2} \xi_k^{-1}, \quad k=1,2,3,4 \quad (2.29)$$

where a_o and b_o are the half lengths of the void axes as shown in Figure 2.1. The inverse mapping has the form:

$$\xi_k = \frac{z_k \pm \sqrt{z_k^2 - (a_o^2 + \mu_k^2 b_o^2)}}{a_o - i\mu_k b_o}, \quad k=1,2,3,4 \quad (2.30)$$

where the sign of the square root (\pm) is chosen in such a way that $|\xi_k| \geq 1$.

Using the general solution, the plane magneto-electro-mechanical problem has been reduced to the one of solving the complex potential functions ω_k . For interior domain problems without flux singularities, ω_k can be represented by Taylor series [5], i.e.

$$\omega_k(z_k) = \sum_{n=0}^{\infty} (a_k^{(n)} + i b_k^{(n)}) z_k^n \quad \text{for } k=1,2,3,4 \quad (2.31)$$

In the case of a domain exterior to an elliptical void, ω_k can be represented by Laurent series in terms of ξ_k instead of z_k [5].

$$\omega_k(\xi_k) = \sum_{n=0}^{\infty} (a_k^{(n)} + i b_k^{(n)}) \xi_k^n + \sum_{n=1}^{\infty} (a_k^{(-n)} + i b_k^{(-n)}) \xi_k^{-n} \quad \text{for } k=1,2,3,4 \quad (2.32)$$

where $a_k^{(\pm n)}$ and $b_k^{(\pm n)}$ ($k = 1,2,3,4$ and $n = 1,2,3,\dots$) are real coefficients. Along the void boundary which is a unit circle in the ξ_k -plane, we have: $|\xi_k| = 1$ or $\xi_1 = \xi_2 = \xi_3 = \xi_4 = e^{i\Theta}$ where $\Theta \in [-\pi, \pi]$. Note that $\bar{\xi}_k^n = \xi_k^{-n}$ on the unit circle.

For exterior domains, $\omega_k(z_k)$ and $\omega'_k(z_k)$ are replaced by $\omega_k(\xi_k)$ and $\frac{\omega'_k(\xi_k)}{z'_k(\xi_k)}$ in eqs.

(2.27) and (2.28), where $z'_k = A - B\xi_k^{-2}$, $A = \frac{a_o - i\mu_k b_o}{2}$; $B = \frac{a_o + i\mu_k b_o}{2}$ and the prime (')

now denotes derivative with respect to ξ_k . Hence, in the coming equations, the following will be used:

$$Z_k = \begin{cases} z_k & \text{for interior domains} \\ \xi_k & \text{for exterior domains} \end{cases} \quad Y_k^{n-1} = \begin{cases} z_k^{n-1} & \text{for interior domains} \\ \frac{\xi_k^{n-1}}{A - B\xi_k^{-2}} & \text{for exterior domains} \end{cases}$$

By substituting the ω_k in eq. (2.31), or eq. (2.32) into eq. (2.28), the *basic set* of Trefftz functions for magneto-electro-mechanical displacements $\underline{\mathbf{u}} = \{u_1, u_3, \varphi, \psi\}^T$, magneto-electro-mechanical stresses and strains $\underline{\boldsymbol{\sigma}} = \{\sigma_1, \sigma_3, \sigma_5, D_1, D_3, B_1, B_3\}^T$,

$\underline{\boldsymbol{\varepsilon}} = \{\varepsilon_1, \varepsilon_3, \varepsilon_5, E_1, E_3, H_1, H_3\}^T$, for interior or exterior domain problems respectively,

can be obtained as:

$$\begin{aligned} \underline{\mathbf{u}} = 2 \sum_{n=M_s}^M \sum_{k=1}^4 & \left[\left(\operatorname{Re}(\mathcal{D}_k) \operatorname{Re}(Z_k^n) - \operatorname{Im}(\mathcal{D}_k) \operatorname{Im}(Z_k^n) \right) a_k^{(n)} \right. \\ & \left. - \left(\operatorname{Re}(\mathcal{D}_k) \operatorname{Im}(Z_k^n) + \operatorname{Im}(\mathcal{D}_k) \operatorname{Re}(Z_k^n) \right) b_k^{(n)} \right] \end{aligned} \quad (2.33)$$

$$\begin{aligned} \underline{\boldsymbol{\sigma}} = 2 \sum_{n=M_s}^M \sum_{k=1}^4 & \left[\left(\operatorname{Re}(\mathcal{G}_k) \operatorname{Re}(nY_k^{n-1}) - \operatorname{Im}(\mathcal{G}_k) \operatorname{Im}(nY_k^{n-1}) \right) a_k^{(n)} \right. \\ & \left. - \left(\operatorname{Re}(\mathcal{G}_k) \operatorname{Im}(nY_k^{n-1}) + \operatorname{Im}(\mathcal{G}_k) \operatorname{Re}(nY_k^{n-1}) \right) b_k^{(n)} \right] \end{aligned} \quad (2.34)$$

$$\underline{\boldsymbol{\varepsilon}} = 2 \sum_{n=M_s}^M \sum_{k=1}^4 \left[\left(\operatorname{Re}(\mathcal{H}_k) \operatorname{Re}(nY_k^{n-1}) - \operatorname{Im}(\mathcal{H}_k) \operatorname{Im}(nY_k^{n-1}) \right) a_k^{(n)} - \left(\operatorname{Re}(\mathcal{H}_k) \operatorname{Im}(nY_k^{n-1}) + \operatorname{Im}(\mathcal{H}_k) \operatorname{Re}(nY_k^{n-1}) \right) b_k^{(n)} \right] \quad (2.35)$$

In the above: $\mathcal{D}_k = \{\gamma_k p_k, \gamma_k q_k / \mu_k, \lambda_k s_k, \Delta_k h_k\}^T$,

$$\mathcal{G}_k = \{\gamma_k \mu_k^2, \gamma_k, -\gamma_k \mu_k, \lambda_k \mu_k, -\lambda_k, \Delta_k \mu_k, -\Delta_k\}^T,$$

$$\mathcal{H}_k = \{\gamma_k p_k, \gamma_k q_k, \gamma_k r_k, -\lambda_k s_k, -\lambda_k t_k, -\Delta_k h_k, -\Delta_k l_k\}^T$$

and the upper limit of n (the maximum order of Z_k used in Trefftz functions) is taken to be M for numerical implementation, while the lower limit M_s is taken as:

$$M_s = \begin{cases} 0 & \text{for interior domains} \\ -M & \text{for exterior domains} \end{cases}$$

For interior/exterior solutions, when n is increased by one, eight/sixteen Trefftz functions with their corresponding undetermined real coefficients $\{a_1^{(\pm n)}, b_1^{(\pm n)}, a_2^{(\pm n)}, b_2^{(\pm n)}, a_3^{(\pm n)}, b_3^{(\pm n)}, a_4^{(\pm n)}, b_4^{(\pm n)}\}$ are added to the solution. So the number of Trefftz functions m_T (which is also equivalent to the number of the undetermined real coefficients) is:

$$m_T = \begin{cases} 8(M+1) & \text{for interior domain solution} \\ 8(2M+1) & \text{for exterior domain solution} \end{cases} \quad (2.36)$$

Note that when $n = 0$, the associated eight Trefftz functions correspond to rigid-body and constant potentials modes, and vanishing stress, strain, electric displacement, electric field,

magnetic induction & magnetic field: $\underline{\boldsymbol{\sigma}} = \mathbf{0}$, $\underline{\boldsymbol{\varepsilon}} = \mathbf{0}$, $\underline{\mathbf{u}} = 2 \sum_{k=1}^4 [\operatorname{Re}(\mathcal{D}_k) a_k^{(0)} - \operatorname{Im}(\mathcal{D}_k) b_k^{(0)}]$.

Generally speaking, it is impossible to find a closed form solution for $\omega_k(Z_k)$ for arbitrary boundary conditions. For the case of impermeable elliptic void, a special solution set can be found as presented in the next subsection.

2.4 Special solution set for impermeable elliptical void

The Trefftz special solution set accounts for the homogeneous boundary conditions of voids, cracks etc. Wang *et al.* [6] constructed a special solution set of Trefftz functions for electrically impermeable elliptical voids with axes parallel/perpendicular to polling direction. Sheng *et al.* [7] extended this to the case of an arbitrarily oriented electrically impermeable elliptical voids. Here we extend this special solution set to the case of electromagnetically impermeable elliptical voids. Note that generally along any boundary surface, we can write:

$$\begin{aligned} g &= 2 \operatorname{Re} \sum_{k=1}^4 \lambda_k \omega_k(z_k) = - \int_0^s (D_1 n_1 + D_3 n_3) ds = - \int_0^s Q ds \\ \rho &= 2 \operatorname{Re} \sum_{k=1}^4 \Delta_k \omega_k(z_k) = - \int_0^s (B_1 n_1 + B_3 n_3) ds = - \int_0^s Q_M ds = 0 \\ \frac{\partial \phi(x_1, x_3)}{\partial x_3} &= 2 \operatorname{Re} \sum_{k=1}^4 \gamma_k \mu_k \omega_k(z_k) = \int_0^s (n_1 \sigma_1 + n_3 \sigma_5) ds = \int_0^s t_1 ds \\ \frac{\partial \phi(x_1, x_3)}{\partial x_1} &= 2 \operatorname{Re} \sum_{k=1}^4 \gamma_k \omega_k(z_k) = - \int_0^s (n_1 \sigma_5 + n_3 \sigma_3) ds = - \int_0^s t_3 ds \end{aligned} \quad (2.37)$$

where t_1 and t_2 are the components of the traction vector. The equality to zero in the second line in eqs. (2.37) comes from the integral form of Gauss's law for magnetism. So for *traction-free* and *vanishing normal electric displacement and magnetic induction (surface charge density and magnetic flux density)* boundary conditions along the void surface, the following conditions should be satisfied:

$$\begin{aligned} \operatorname{Re} \sum_{k=1}^4 \gamma_k \omega_k(\xi_k) &= 0, & \operatorname{Re} \sum_{k=1}^4 \gamma_k \mu_k \omega_k(\xi_k) &= 0, \\ \operatorname{Re} \sum_{k=1}^4 \lambda_k \omega_k(\xi_k) &= 0, & \operatorname{Re} \sum_{k=1}^4 \Delta_k \omega_k(\xi_k) &= 0 \quad \text{for } |\xi_k| = 1 \end{aligned} \quad (2.38)$$

which can be written in matrix form as,

$$\begin{Bmatrix} \bar{\omega}_1 \\ \bar{\omega}_2 \\ \bar{\omega}_3 \\ \bar{\omega}_4 \end{Bmatrix} = \begin{Bmatrix} E_{11} & E_{12} & E_{13} & E_{14} \\ E_{21} & E_{22} & E_{23} & E_{24} \\ E_{31} & E_{32} & E_{33} & E_{34} \\ E_{41} & E_{42} & E_{43} & E_{44} \end{Bmatrix} \begin{Bmatrix} \omega_1 \\ \omega_2 \\ \omega_3 \\ \omega_4 \end{Bmatrix} \quad \text{for } |\xi_k| = 1 \quad (2.39)$$

Where

$$\begin{Bmatrix} E_{11} & E_{12} & E_{13} & E_{14} \\ E_{21} & E_{22} & E_{23} & E_{24} \\ E_{31} & E_{32} & E_{33} & E_{34} \\ E_{41} & E_{42} & E_{43} & E_{44} \end{Bmatrix} = - \begin{Bmatrix} \gamma_1 & \gamma_2 & \gamma_3 & \gamma_4 \\ \gamma_1 \bar{\mu}_1 & \gamma_2 \bar{\mu}_2 & \gamma_3 \bar{\mu}_3 & \gamma_4 \bar{\mu}_4 \\ \bar{\lambda}_1 & \bar{\lambda}_2 & \bar{\lambda}_3 & \bar{\lambda}_4 \\ \bar{\Delta}_1 & \bar{\Delta}_2 & \bar{\Delta}_3 & \bar{\Delta}_4 \end{Bmatrix}^{-1} \begin{Bmatrix} \gamma_1 & \gamma_2 & \gamma_3 & \gamma_4 \\ \gamma_1 \mu_1 & \gamma_2 \mu_2 & \gamma_3 \mu_3 & \gamma_4 \mu_4 \\ \lambda_1 & \lambda_2 & \lambda_3 & \lambda_4 \\ \Delta_1 & \Delta_2 & \Delta_3 & \Delta_4 \end{Bmatrix}$$

Assuming $\omega_k(\xi_k)$ in a form similar to that of eq. (2.32) and substituting it into eq. (2.39)

yields eight constraint equations on the sixteen real coefficients $a_k^{(n)}, b_k^{(n)}, a_k^{(-n)}$ and $b_k^{(-n)}$ ($k = 1, 2, 3, 4$). By expressing $a_k^{(-n)}$ and $b_k^{(-n)}$ in terms of $a_k^{(n)}$ and $b_k^{(n)}$, we get:

$$a_k^{(-n)} = \sum_{j=1}^4 \left[\operatorname{Re}(E_{kj}) a_j^{(n)} - \operatorname{Im}(E_{kj}) b_j^{(n)} \right], \quad b_k^{(-n)} = - \sum_{j=1}^4 \left[\operatorname{Im}(E_{kj}) a_j^{(n)} + \operatorname{Re}(E_{kj}) b_j^{(n)} \right] \quad (2.40)$$

So the number of Trefftz functions m_T (which is also equivalent to the number of the undetermined real coefficients) is reduced to $m_T = 8(M+1)$.

Substituting eq. (2.40) into eqs. (2.33)-(2.35) yields the following *special set* of Trefftz functions:

$$\begin{aligned}\underline{\mathbf{u}}_{void} &= \sum_{n=0}^{\infty} \sum_{k=1}^4 \left[\Phi_{a_k}^{(n)} a_k^{(n)} + \Phi_{b_k}^{(n)} b_k^{(n)} \right], \quad \underline{\mathbf{\sigma}}_{void} = \sum_{n=0}^{\infty} \sum_{k=1}^4 \left[\Psi_{a_k}^{(n)} a_k^{(n)} + \Psi_{b_k}^{(n)} b_k^{(n)} \right] \\ \underline{\mathbf{\epsilon}}_{void} &= \sum_{n=0}^{\infty} \sum_{k=1}^4 \left[\Gamma_{a_k}^{(n)} a_k^{(n)} + \Gamma_{b_k}^{(n)} b_k^{(n)} \right]\end{aligned}\tag{2.41}$$

where:

$$\begin{aligned}\Phi_{a_k}^{(n)} &= \chi_{a_k}^{(n)} + \sum_{j=1}^4 \left[\operatorname{Re}(E_{jk}) \chi_{a_j}^{(-n)} - \operatorname{Im}(E_{jk}) \chi_{b_j}^{(-n)} \right], \quad \Phi_{b_k}^{(n)} = \chi_{b_k}^{(n)} - \sum_{j=1}^4 \left[\operatorname{Im}(E_{jk}) \chi_{a_j}^{(-n)} + \operatorname{Re}(E_{jk}) \chi_{b_j}^{(-n)} \right] \\ \Psi_{a_k}^{(n)} &= \Sigma_{a_k}^{(n)} + \sum_{j=1}^4 \left[\operatorname{Re}(E_{jk}) \Sigma_{a_j}^{(-n)} - \operatorname{Im}(E_{jk}) \Sigma_{b_j}^{(-n)} \right], \quad \Psi_{b_k}^{(n)} = \Sigma_{b_k}^{(n)} - \sum_{j=1}^4 \left[\operatorname{Im}(E_{jk}) \Sigma_{a_j}^{(-n)} + \operatorname{Re}(E_{jk}) \Sigma_{b_j}^{(-n)} \right] \\ \Gamma_{a_k}^{(n)} &= \Upsilon_{a_k}^{(n)} + \sum_{j=1}^4 \left[\operatorname{Re}(E_{jk}) \Upsilon_{a_j}^{(-n)} - \operatorname{Im}(E_{jk}) \Upsilon_{b_j}^{(-n)} \right], \quad \Gamma_{b_k}^{(n)} = \Upsilon_{b_k}^{(n)} - \sum_{j=1}^4 \left[\operatorname{Im}(E_{jk}) \Upsilon_{a_j}^{(-n)} + \operatorname{Re}(E_{jk}) \Upsilon_{b_j}^{(-n)} \right]\end{aligned}\tag{2.42}$$

and in (2.42):

$$\begin{aligned}\chi_{a_k}^{(\pm n)} &= 2 \operatorname{Re}(\mathcal{D}_k) \operatorname{Re}(\xi_k^{\pm n}) - 2 \operatorname{Im}(\mathcal{D}_k) \operatorname{Im}(\xi_k^{\pm n}), \\ \chi_{b_k}^{(\pm n)} &= -2 \operatorname{Re}(\mathcal{D}_k) \operatorname{Im}(\xi_k^{\pm n}) - 2 \operatorname{Im}(\mathcal{D}_k) \operatorname{Re}(\xi_k^{\pm n}) \\ \Sigma_{a_k}^{(\pm n)} &= \pm 2n \left[\operatorname{Re}(\mathcal{G}_k) \operatorname{Re} \left(\frac{\xi_k^{\pm n-1}}{z'_k} \right) - \operatorname{Im}(\mathcal{G}_k) \operatorname{Im} \left(\frac{\xi_k^{\pm n-1}}{z'_k} \right) \right] \\ \Sigma_{b_k}^{(\pm n)} &= \mp 2n \left[\operatorname{Re}(\mathcal{G}_k) \operatorname{Im} \left(\frac{\xi_k^{\pm n-1}}{z'_k} \right) + \operatorname{Im}(\mathcal{G}_k) \operatorname{Re} \left(\frac{\xi_k^{\pm n-1}}{z'_k} \right) \right] \\ \Upsilon_{a_k}^{(\pm n)} &= \pm 2n \left[\operatorname{Re}(\mathcal{H}_k) \operatorname{Re} \left(\frac{\xi_k^{\pm n-1}}{z'_k} \right) - \operatorname{Im}(\mathcal{H}_k) \operatorname{Im} \left(\frac{\xi_k^{\pm n-1}}{z'_k} \right) \right] \\ \Upsilon_{b_k}^{(\pm n)} &= \mp 2n \left[\operatorname{Re}(\mathcal{H}_k) \operatorname{Im} \left(\frac{\xi_k^{\pm n-1}}{z'_k} \right) + \operatorname{Im}(\mathcal{H}_k) \operatorname{Re} \left(\frac{\xi_k^{\pm n-1}}{z'_k} \right) \right]\end{aligned}$$

Note that for the case of elliptical boundary, using the following ellipse parametric equation:

$$x_1(t) = a_o \cos t; \quad x_3(t) = b_o \sin t;\tag{2.43}$$

ds can be written in terms of the parameter t :

$$ds = \sqrt{dx_1^2 + dx_3^2} = Jdt = \left(\sqrt{a_o^2 \sin^2 t + b_o^2 \cos^2 t} \right) dt\tag{2.44}$$

where J is the Jacobian of the transformation. Then any boundary integration can be written as a function of t as follows:

$$\oint_{\partial\Omega_c^e} f(\xi_k) ds = \int_{t=0}^{t=2\pi} f(\xi_k(t)) J dt \quad (2.45)$$

$$\text{where } \xi_k(t) = \frac{z_k(t) \pm \sqrt{(z_k(t))^2 - (a_o^2 + \mu_k^2 b_o^2)}}{a_o - i\mu_k b_o}, \quad z_k(t) = x_1(t) + \mu_k x_3(t).$$

In the following two chapters, we present two numerical methods for modeling piezoelectric/piezomagnetic composites in direct and inverse problems. In chapter 3, Multi-Region Trefftz Collocation Grains (MTCGs) method is presented, and in chapter 4, Trefftz-Lekhnitskii Computational Grains (TLCGs) method is proposed. In formulating these numerical methods, all variables should be expressed in the grain's Cartesian local coordinate system ($\hat{x}_1 - \hat{x}_3$ is Figure 1.2 and Figure 1.3), hence tensor transformation rule can be used again to do this rotation by an angle $-(\zeta_\alpha + \vartheta_\alpha)$.

2.5 Summary for chapter 2

Lekhnitskii formalism is extended in this chapter to the general case of coupled/uncoupled electro-elastic and magneto-elastic materials. Hence this formulation can be used to represent interior and exterior domains in piezoelectric, piezomagnetic and uncoupled elastic materials. The special solution set for electromagnetically impermeable arbitrarily oriented elliptical voids was also presented. Modeling piezoelectric-piezomagnetic composites using MTCGs and TLCGs in the following two chapters depends on the formulation presented in this chapter.

2.6 References of chapter 2

- [1] **Lekhnitskii, S.G.** (1968): *Anisotropic plates*. Gordon and Breach, Science Publishers, New York.
- [2] **Lekhnitskii, S. G.** (1981): *Theory of elasticity of an anisotropic body*. Mir Publishers, Moscow.
- [3] **Xu X.L., Rajapakse R.K.N.D.** (1999): Analytical solution for an arbitrarily oriented void/crack and fracture of piezoceramics. *Acta Materialia* vol. 47, pp. 1735 –1747.
- [4] **Sosa, H.** (1991): Plane problems in piezoelectric media with defects. *Int. J. Solids Struct.* vol. 28, no.4, pp. 491–505.
- [5] **Domingues, J.S.; Portela, A.; Castro, P.M.S.T.** (1999): Trefftz boundary element method applied to fracture mechanics. *Engineering Fracture Mechanics*, vol. 64, pp. 67-86.
- [6] **Wang, X.W.; Zhou, Y.; Zhou, W.L.** (2004): A novel hybrid finite element with a hole for analysis of plane piezoelectric medium with defects. *International Journal of Solids and Structures* vol. 41, pp. 7111–7128.
- [7] **Sheng, N.; Sze, K.Y.; Cheung, Y.K.** (2006): Trefftz solutions for piezoelectricity by Lekhnitskii's formalism and boundary collocation method. *Int. J. Numer. Methods Eng.* vol. 65, pp. 2113–2138.

Chapter 3 : Multi-Region Trefftz Collocation Grains (MTCGs): A simple and efficient method for direct and inverse problems

3.1 Introduction

In this chapter, Multi-Region Trefftz Collocation Grains (MTCGs) are developed for modeling porous piezoelectric materials as well as piezoelectric composites where the materials of the matrix and the inclusions could be piezoelectric or elastic dielectric (anisotropic in general). The formulation is very simple and efficient since there are no simple polynomial-based elements in the finite element sense. The formulation can be directly extended to the case of piezoelectric-piezomagnetic composites. As mentioned in section 1.4, each grain has an arbitrarily polygonal shape to mimic the physical shape of grains in the micro-scale. Each grain may contain a circular or an arbitrarily oriented elliptical void or inclusion and has its own crystallographic orientation (polling direction). Each grain may be surrounded by an arbitrary number of neighboring grains; hence MTCGs are expected to show field distributions that cannot be obtained using regular triangular and four-sided polynomial-based finite elements. Dirichlet tessellation is used to construct the mesh or the geometric shapes of the grains. The formulation is also very effective in inverse problems where the boundary conditions over some portions of the problem boundary are completely unknown while on other portions extra conditions are known or measured.

Lekhnitskii formalism, presented in chapter 2, is employed here due to the relatively explicit nature of the derived Trefftz functions. However in this chapter the magnetic variables are dropped from the formulation presented in chapter 2 because the main focus here is on piezoelectric composites. For the case of impermeable voids, the *special solution set* that satisfies the *traction-free, charge-free* conditions can be used. Hence there is no need to enforce

the void boundary conditions by collocation or any other method. Using the special solution set is more efficient. However, for the case of grains with inclusions, the special solution set does not exist and collocation/least squares method should be used instead to enforce the inclusion boundary conditions.

The chapter is organized as follows: the Multi-Region Trefftz Collocation Grains (MTCGs) formulation for piezoelectric composites with/without voids/inclusions is introduced in section 3.2 for direct problems and in section 3.3 for inverse problems. Numerical examples are provided in section 3.4, conclusions are summarized in section 3.5, while references are listed in section 3.6.

3.2 Multi-Region Trefftz Collocation Grain (MTCGs) Formulation for Direct Problems

Consider a 2D irregular m -sided polygonal grain with/without void/inclusion as shown in Figure 1.2 (left). The basic solution set in eqs. (2.33) and (2.34) can be used, after dropping the magnetic variables, as the interior/exterior fields, which satisfy the constitutive law, the strain-displacement relationship, the electric field-electric potential relationship and equilibrium and Gauss's equations. For the case of impermeable elliptical voids, the special solution set in eqs. (2.41) which additionally satisfies the void stress-free charge-free boundary conditions can be used. In matrix and vector notation, these interior/exterior fields in Ω^e when $\alpha = m$, and in Ω_c^e when $\alpha = c$, can be written in the form:

$$\begin{aligned} \begin{Bmatrix} \mathbf{u}^\alpha \\ \varphi^\alpha \end{Bmatrix} &= \begin{Bmatrix} \mathbf{N}_{\mathbf{u}}^\alpha \\ \mathbf{N}_\varphi^\alpha \end{Bmatrix} \mathbf{c}^\alpha, & \begin{Bmatrix} \boldsymbol{\sigma}^\alpha \\ \mathbf{D}^\alpha \end{Bmatrix} &= \begin{Bmatrix} \mathbf{M}_{\boldsymbol{\sigma}}^\alpha \\ \mathbf{M}_{\mathbf{D}}^\alpha \end{Bmatrix} \mathbf{c}^\alpha, \\ \text{or } \underline{\mathbf{u}}^\alpha &= \mathbf{N}^\alpha \mathbf{c}^\alpha, & \underline{\boldsymbol{\sigma}}^\alpha &= \mathbf{M}^\alpha \mathbf{c}^\alpha \end{aligned} \tag{3.1}$$

where \mathbf{N}^α are the Trefftz functions in the order of $M_s, \dots, 0, 1, \dots, M$ and \mathbf{c}^α denotes the unknown real coefficients ($a_k^{(\pm n)}, b_k^{(\pm n)}$, $k = 1, 2, 3$ and $n = M_s, \dots, M$) associated with Trefftz functions. If there is no void/inclusion, only the non-negative exponents are used in the basic solution set.

The tractions and density of free charge on the boundaries $\partial\Omega^e$ when $\alpha = m$, and $\partial\Omega_c^e$ when $\alpha = c$, can be written as:

$$\begin{aligned} \mathbf{t}^\alpha &= \mathbf{n}_\sigma \boldsymbol{\sigma}^\alpha = \mathbf{n}_\sigma \mathbf{M}_\sigma^\alpha \mathbf{c}^\alpha, & Q &= \mathbf{n}_e \mathbf{D}^\alpha = \mathbf{n}_e \mathbf{M}_D^\alpha \mathbf{c}^\alpha, \\ \text{or } \underline{\mathbf{t}}^\alpha &= \begin{Bmatrix} \mathbf{t}^\alpha \\ Q^\alpha \end{Bmatrix} = \begin{bmatrix} \mathbf{n}_\sigma & \mathbf{0} \\ \mathbf{0} & \mathbf{n}_e \end{bmatrix} \begin{Bmatrix} \boldsymbol{\sigma}^\alpha \\ \mathbf{D}^\alpha \end{Bmatrix} = \underline{\mathbf{n}} \underline{\boldsymbol{\sigma}}^\alpha = \underline{\mathbf{n}} \mathbf{M}^\alpha \mathbf{c}^\alpha \end{aligned} \quad (3.2)$$

Now the following conditions should be enforced:

- 1- Continuities of primal fields (electromechanical displacements), in eqs. (1.11), as well as reciprocity conditions, in eqs. (1.12), at all boundaries, S_g^e , between a grain and its neighboring grains, if any.
- 2- Essential boundary conditions (in eqs. (1.7) and (1.8)) if prescribed on boundaries S_u^e and S_φ^e ,
- 3- Natural boundary conditions (eqs. (1.7) and (1.8)) if prescribed on boundaries S_t^e and S_Q^e .
- 4- Void/inclusion interface conditions as mentioned in subsections 1.4.2 and 1.4.3 (When an inclusion is present in the grain or when a void is present in the grain and the basic solution set is to be used).

In this work, we use the simple collocation/least squares method to enforce all these conditions. Galerkin method can also be used and may yield a slightly better accuracy, but it is more susceptible to round-off errors [1] as compared to the straightforward collocation method. When the void/inclusion boundary $\partial\Omega_c^e$ shrinks to zero, the grain is reduced to the case of a grain with no void/inclusion.

For the case of an impermeable elliptical void, using the special solution set, which already satisfies the void traction-free charge-free boundary conditions, is clearly more efficient than using the basic set because there is no need to enforce any conditions on the void boundary, however if the void is pressurized, filled with conducting fluid or replaced by any type of inclusions, the basic set should be used as mentioned earlier (there is no special solution set in this case).

The aforementioned conditions are enforced in a strong sense at several pre-selected collocation points along the grain boundary $\partial\Omega^e$. R points, ($\mathbf{x}^{(r)}$, $r = 1, 2, \dots R$), are selected along each side of the grain's outer boundary. Also when using the basic solution set, (eqs. (2.33)-(2.35)), void/inclusion boundary conditions are enforced by dividing the void/inclusion periphery into a number of curved segments, n_s , along the void/inclusion boundary

$\partial\Omega_c^e = \sum_{j=1}^{n_s} \partial\Omega_{cj}^e$, and enforcing the boundary conditions on each segment. So,

- 1- Continuity of electromechanical displacements and reciprocity of electromechanical tractions along S_g^{ab} , the boundary side that separates any two neighboring grains a and b :

$$\begin{aligned} \underline{\mathbf{u}}^{m(\Omega^a)}\left(\mathbf{x}^{(r)}, \mathbf{c}_a^m\right) - \underline{\mathbf{u}}^{m(\Omega^b)}\left(\mathbf{x}^{(r)}, \mathbf{c}_b^m\right) &= \mathbf{0}, & \mathbf{x}^{(r)} \in S_g^{ab} \\ \underline{\mathbf{t}}^{m(\Omega^a)}\left(\mathbf{x}^{(r)}, \mathbf{c}_a^m\right) + \underline{\mathbf{t}}^{m(\Omega^b)}\left(\mathbf{x}^{(r)}, \mathbf{c}_b^m\right) &= \mathbf{0} & \mathbf{x}^{(r)} \in S_g^{ab} \end{aligned} \quad (3.3)$$

2- Essential boundary conditions along the boundaries S_u^e and S_φ^e in grain e :

$$\begin{aligned} \mathbf{u}^m(\mathbf{x}^{(r)}, \mathbf{c}_e^m) &= \bar{\mathbf{u}} & \mathbf{x}^{(r)} \in S_u^e, \\ \varphi^m(\mathbf{x}^{(r)}, \mathbf{c}_e^m) &= \bar{\varphi} & \mathbf{x}^{(r)} \in S_\varphi^e, \end{aligned} \quad (3.4)$$

3- Natural boundary conditions along the boundaries S_t^e and S_Q^e in grain e :

$$\begin{aligned} \mathbf{t}^m(\mathbf{x}^{(r)}, \mathbf{c}_e^m) &= \bar{\mathbf{t}} & \mathbf{x}^{(r)} \in S_t^e, \\ Q^m(\mathbf{x}^{(r)}, \mathbf{c}_e^m) &= \bar{Q} & \mathbf{x}^{(r)} \in S_Q^e, \end{aligned} \quad (3.5)$$

4- Void/inclusion interface conditions along $\partial\Omega_c^e$ (when using the basic solution set):

a- Impermeable void: traction-free and charge-free conditions along $\partial\Omega_c^e$:

$$\int_{\partial\Omega_{cj}^e} \underline{\mathbf{t}}^m(\mathbf{x}, \mathbf{c}_e^m) ds = 0, \quad j = 1, 2, \dots n_s \quad (3.6)$$

b- Inclusion: primal fields' continuity, traction reciprocity and charge continuity conditions along $\partial\Omega_c^e$:

$$\begin{aligned} \underline{\mathbf{u}}^m(\mathbf{x}^{(j)}, \mathbf{c}_e^m) - \underline{\mathbf{u}}^c(\mathbf{x}^{(j)}, \mathbf{c}_e^c) &= \mathbf{0}, & j = 1, 2, \dots n_s \\ \underline{\mathbf{t}}^m(\mathbf{x}^{(j)}, \mathbf{c}_e^m) + \underline{\mathbf{t}}^c(\mathbf{x}^{(j)}, \mathbf{c}_e^c) &= \mathbf{0}, & j = 1, 2, \dots n_s \end{aligned} \quad (3.7)$$

In this study, three collocation points on each side of the outer boundary of each grain are used and 48 points or segments are used on the void/inclusion boundary in each grain. Combining all these conditions in a matrix/vector form leads to:

$$\mathbf{Ac} = \mathbf{b} \quad \text{or} \quad \mathbf{c} = \mathbf{A}^{-1}\mathbf{b} \quad (3.8)$$

where \mathbf{c} is a column matrix containing the unknown coefficients of the matrix and inclusions of all grains. We ensure that the number of equations is larger than the number of unknowns; hence

the system is over-constrained and is solved using singular value decomposition (SVD). The SVD method can solve even the singular system of equations and produces the least squares solutions to the over-constrained systems.

3.3 Multi-Region Trefftz Collocation Grain (MTCGs) Formulation for Inverse Problems with Regularization

If both electromechanical displacements and tractions (or strains) are specified or known only on a part of the boundary, the inverse problem is to determine the electromechanical displacements, tractions and strains in the domain as well as the other part of the boundary where everything is unknown. One example is in health monitoring of piezoelectric composites and devices when data are known or measured on the outer boundaries, but not available at the inaccessible cavities in the domain.

Now let S_c^e be a part of the boundary of grain e (part of the outer boundaries for a grain containing an inclusion, or part of both inner and outer boundaries for a grain with a void) where electromechanical displacements and tractions (or strains) are known. We use the available data and select enough collocation points ($\mathbf{x}^{(p)} \in S_c^e, p = 1, 2, \dots, P$) along S_c^e to get:

$$\mathbf{u}^m(\mathbf{x}^{(p)}, \mathbf{c}_e^m) = \bar{\mathbf{u}} \quad \varphi^m(\mathbf{x}^{(p)}, \mathbf{c}_e^m) = \bar{\varphi} \quad (3.9)$$

and

$$\mathbf{t}^m(\mathbf{x}^{(p)}, \mathbf{c}_e^m) = \bar{\mathbf{t}} \quad Q^m(\mathbf{x}^{(p)}, \mathbf{c}_e^m) = \bar{Q} \quad (3.10)$$

or

$$\boldsymbol{\epsilon}^m(\mathbf{x}^{(p)}, \mathbf{c}_e^m) = \bar{\boldsymbol{\epsilon}} \quad \mathbf{E}^m(\mathbf{x}^{(p)}, \mathbf{c}_e^m) = \bar{\mathbf{E}} \quad (3.11)$$

In addition to the continuity of electromechanical displacements and reciprocity of electromechanical tractions along S_g^e in eq. (3.3), and the inclusion boundary conditions in eq. (3.7) for grains with inclusions. Combining all these equations that represent the measured or known data in all grains, and writing them in a matrix form, we get:

$$\mathbf{A_I} \mathbf{c_I} = \mathbf{b_I} \quad (3.12)$$

This equation cannot be solved directly using the least squares method because the system of equations in inverse problems is known to be ill-posed and generally very-sensitive to perturbation in the measurement data on the boundary S_c^e . Hence, regularization techniques should be used to mitigate this ill-posedness. There are several regularization methods that were used in the literature, among which are the Truncated Singular Value Decomposition (TSVD), Selective Singular Value Decomposition (SSVD), and the Tikhonov regularization [2]-[3]. In this work, TSCV method was used and the regularization parameter is obtained using the Generalized Cross-Validation (GCV) method. For details about the aforementioned methods, the reader is referred to [2].

This formulation is generally suitable for any selection of S_c^e . For a plate with a hole modeled with only one region ($N = e = 1$), for instance, S_c could be all or part of the outer boundary where all measurements can be taken.

3.4 Numerical examples

The formulation described above is programmed using MATLAB in a 64-bit WINDOWS operating system, and executed on a PC computer equipped with Intel Q8300 2.5GHz CPU, and 8GB RAM. The material properties of the materials used in the examples in this section are listed in Table 1.1.

Simple problems that use grains with no voids or inclusions, such as patch test and bending of a piezoelectric panel, can be easily and accurately modeled using any number of grains (with no voids or inclusions) to mesh the problem domain, and the error in the whole structure is less than 1%. Patch test with any number of grains containing inclusions having the same material properties as that of the matrix can also be passed with error less than 1%.

In the following, we show some numerical examples using the proposed MTCGs. In the first subsection we present inverse problem where electromechanical displacements and tractions are all measured with white noise on the outer boundary of a piezoelectric domain with an impermeable elliptical void under mechanical loading, and the variables on the unreachable void surface are predicted. Then we study the convergence of this inverse problem as the accessible part on the outer boundary of the domain shrinks. The problem of a piezoelectric inclusion in an infinite piezoelectric matrix is then studied. This is followed by evaluation of material properties of a piezoelectric particle composite material as functions of particle volume fraction. Finally we present contour plots that detect damage-prone sites in porous piezoelectric material samples with arbitrary elliptical voids. Comparisons with other analytical and computational results are presented whenever possible.

3.4.1 Piezoelectric panel with impermeable void: Inverse problem

Consider a piezoelectric panel with an arbitrarily oriented elliptical void whose semi-axes are a and b and the inclination angle between the elliptical void minor axis and the polling direction is ζ as shown in Figure 3.1 (left). The local coordinate system of the ellipse is denoted $x_1 - x_3$, while the global coordinate system is denoted $X_1 - X_3$. The polling direction is aligned with the global vertical X_3 axis (shown in blue in the figure). The material is PZT-4(1) whose properties are presented in Table 1.1 (taken from Xu and Rajapakse [4]) and plane strain

assumption is used in this problem. Now consider that the electromechanical displacements and tractions are all measured at the outer boundary and that there is some white noise in the measurements. The inverse problem is to use these available measurements to predict the electromechanical tractions and displacements at the inner cavity. In this example, we use the analytical solution presented in [4] for an elliptical void in an infinite piezoelectric panel as the prescribed (or measured) data on the outer boundary after adding certain level of white noise. Mechanical load $\sigma_o = 1 \text{ Pa}$ is applied on the panel's upper and lower edges. In this example we take $L = W = 6a$, $b/a = 0.6$, $\zeta = 0$, $M = 4$ (equivalent to 54 unknown coefficients) and we use 3 collocation points per side (giving 72 collocation equations). Hence, in this case S_c , mentioned in section 3.3, is all the outer boundary of the plate where all data are measured.

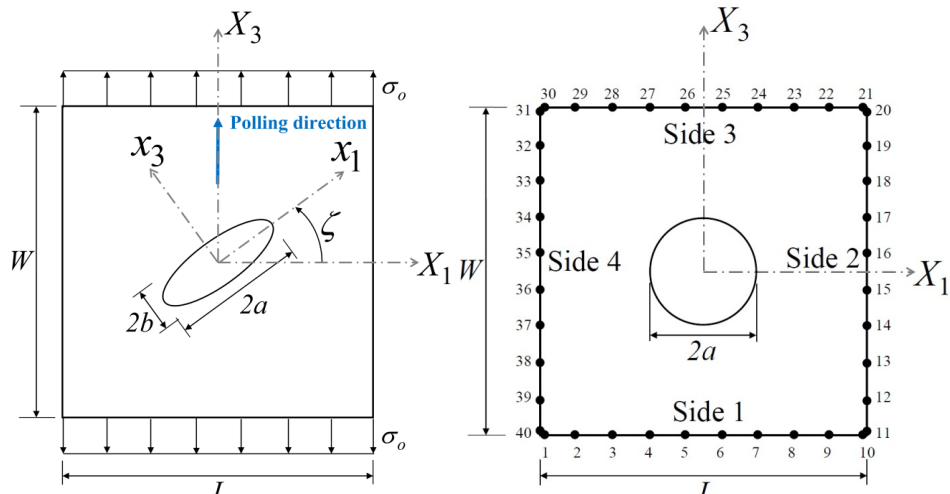


Figure 3.1 (left) A Finite rectangular domain with arbitrarily oriented elliptical void, (right) collocation points considered in section 3.2

Figure 3.2 and Figure 3.3 show the computed circumferential distributions of σ_θ , D_θ , E_θ and E_r divided by σ_o obtained by the solution of the inverse problem with different levels of white noise added to the measured electromechanical displacements and tractions. The figures show that when there is no noise present, this approach can always exactly reproduce the

electromechanical tractions in the domain. When white noise of 40 dB and 30 dB signal-to-noise ratio (SNR), which is equivalent to 1% and 3.3% amplitude of noise in the measurements, is added, only limited error is obtained in the predicted stress, electric displacement and electric field on the void periphery.

The effects of varying ζ , a/b and W/a ratios on the stress, electric displacement and electric field are presented in [5].

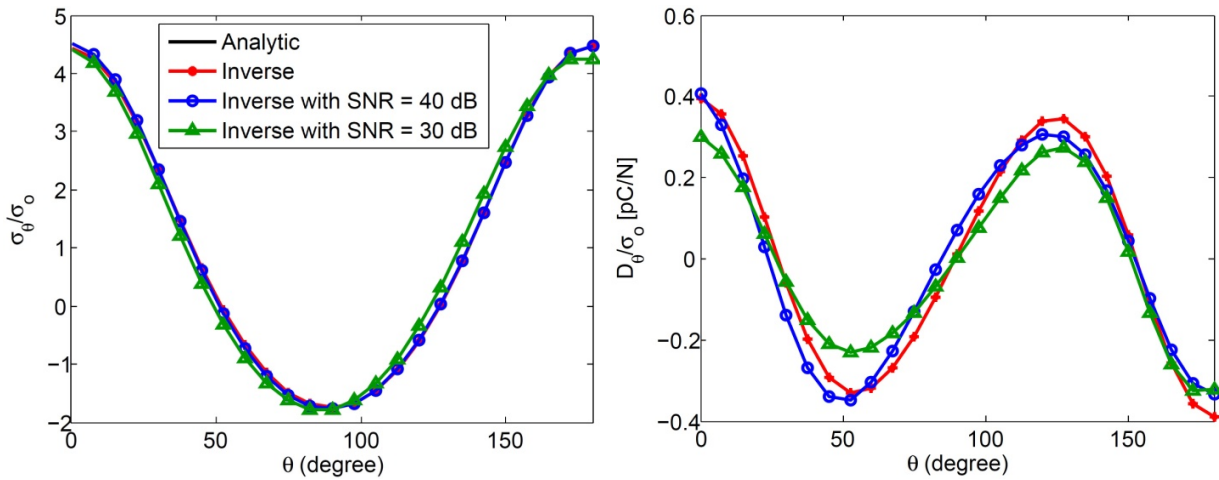


Figure 3.2: Variations of (left) σ_θ / σ_0 , (right) D_θ / σ_0 along the periphery of an elliptical void

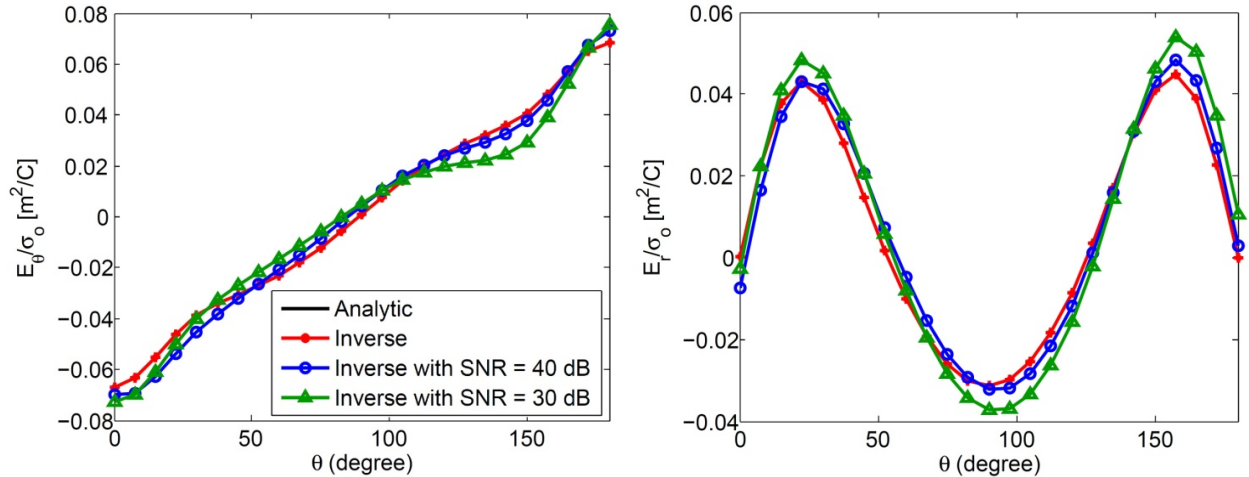


Figure 3.3: Variations of (left) E_θ / σ_0 , (right) E_r / σ_0 along the periphery of an elliptical void

3.4.2 Convergence study for the inverse problem

In this study, the same problem presented in subsection 3.4.1 is considered again but with circular void ($a = b$), and not the entire outer boundary is accessible. Hence we rely on measurements taken from only limited part of the outer boundary. Ten collocation points are used along each side of the outer boundary as shown in Figure 3.1 (right) and we keep removing collocation equations corresponding to these points from side 2 first (starting from point 11 in the figure) followed by side 3, then side 4. Every time we remove two points, we solve the problem and calculate the discrete extreme mechanical and electrical errors, expressed as:

$$E_{mech} = \max_{\mathbf{x}_r \in \partial\Omega_c} \left(\frac{|\sigma_\theta(\mathbf{x}_r) - \tilde{\sigma}_\theta(\mathbf{x}_r)|}{\tilde{\sigma}_{\max}} \right), \quad E_{elect} = \max_{\mathbf{x}_r \in \partial\Omega_c} \left(\frac{|D_\theta(\mathbf{x}_r) - \tilde{D}_\theta(\mathbf{x}_r)|}{\tilde{D}_{\max}} \right) \quad (3.13)$$

where $\tilde{\sigma}_\theta(\mathbf{x}_r)$ and $\tilde{D}_\theta(\mathbf{x}_r)$ are the exact solutions at boundary points \mathbf{x}_r along the periphery of the void; $\tilde{\sigma}_{\max}$ and \tilde{D}_{\max} are respectively the maximum magnitudes of $\tilde{\sigma}_\theta(\mathbf{x}_r)$ and $\tilde{D}_\theta(\mathbf{x}_r)$.

It was found that when there is no noise in the prescribed (measured) data, only 9 points (equivalent to 54 collocation equations, which is equal to the number of unknown coefficients when $M = 4$ is used) are required to get accurate results with E_{mech} and E_{elect} less than 0.001. These 9 points could be prescribed on only a small part (quarter) of side 1 only, side 3 only, or on both sides 2 and 4 such that at least one point is on one of these two sides and the remaining points are on the other side. However when there is a white noise in the prescribed (measured) data, the errors increase as we remove more points (or take our measurements from only limited part of the outer boundary). The mechanical and electrical discrete extreme errors are presented in Table 3.1, when white noise of 40 dB signal-to-noise ratio (SNR) is added to the prescribed data, as more points are removed from the collocation points in Figure 3.1. It is clear from the table that the errors increase as more collocation points are removed from the outer boundary.

When all collocation points on side 2 are not used, we get $E_{mech} \approx 3\%$, and $E_{elect} \approx 12\%$. When all collocation points on both side 2 and side 3 are not used, we get $E_{mech} \approx 17.5\%$, and $E_{elect} \approx 51\%$. Removing additional points from side 4, results in highly increasing E_{elect} .

Table 3.1: Discrete extreme mechanical and electrical errors as more collocation points are removed from the outer boundary (white noise with 40 dB SNR is added to the prescribed data on the outer boundary)

Points removed	None	11-12	11-14	11-16	11-18	11-20	11-22
E_{mech}	0.0045	0.0106	0.0177	0.0225	0.0260	0.0297	0.0392
E_{elect}	0.0117	0.0525	0.0642	0.1030	0.1133	0.1207	0.1570
Points removed	11-24	11-26	11-28	11-30	11-32	11-34	11-36
E_{mech}	0.0423	0.0875	0.1004	0.1753	0.2807	0.4458	1.9738
E_{elect}	0.2393	0.2825	0.3373	0.5123	2.1058	5.4703	8.0255

It should be noted that the numbers in Table 3.1 change slightly every time we change the added random white noise. In addition, the errors increase as the noise level increases.

3.4.3 Infinite piezoelectric domain with elliptical inclusion

Consider an infinite piezoelectric plane with an elliptical inclusion subjected to vertical mechanical loading in the far field. For numerical implementations, the infinite domain is truncated into a rectangle with length L and width W , as shown in Figure 3.1 (left) with $\zeta = 0$, $L = W = 6a$, and $\sigma_o = 1Pa$. The matrix material is PZT-4(1) whose properties are presented in Table 1.1 and plane strain assumption is used. The properties of the inclusion are given as:

$$\begin{bmatrix} \mathbf{C}^c & -\mathbf{e}^{cT} \\ \mathbf{e}^c & \mathbf{h}^c \end{bmatrix} = \Gamma \begin{bmatrix} \mathbf{C}^m & -\mathbf{e}^{mT} \\ \mathbf{e}^m & \mathbf{h}^m \end{bmatrix}$$

where Γ is a factor that can be varied. $\Gamma > 1$ is equivalent to an inclusion material with stronger properties than those of the matrix material (larger stiffness, dielectric and piezoelectric material constants), while $\Gamma < 1$ is equivalent to an inclusion with weaker properties.

Figure 3.4 shows the effect of b/a on σ_θ / σ_o , D_θ / σ_o , E_θ / σ_o and E_r / σ_o along the inclusion periphery with $\Gamma = 0.5$.

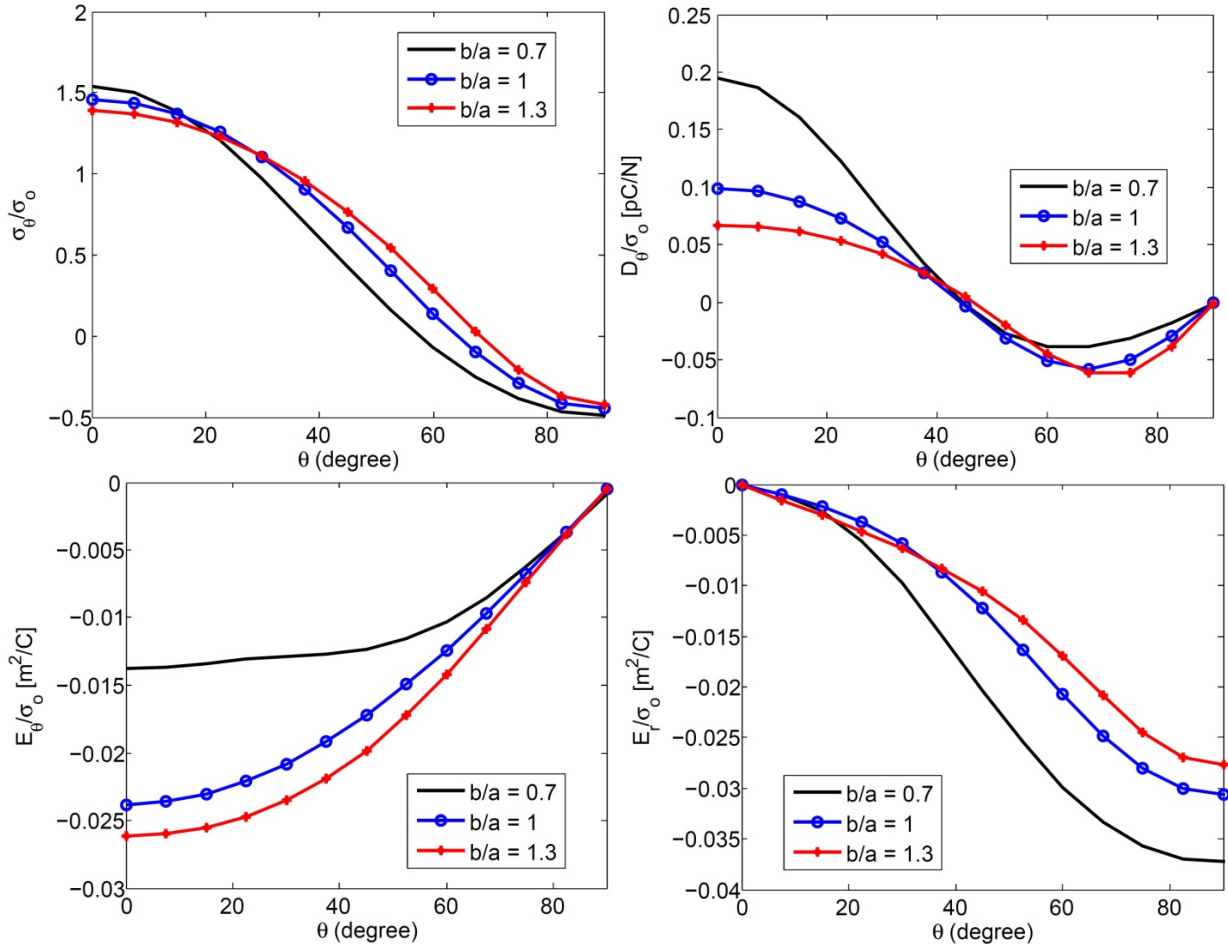


Figure 3.4: Effect of b/a on: (a) σ_θ / σ_o , (b) D_θ / σ_o , (c) E_θ / σ_o and (d) E_r / σ_o along the inclusion periphery

It can be seen from the figure that controlling the shape of the inclusion can result in varying the distribution and the maximum absolute values of the circumferential stress and electric displacement, as well as the circumferential and radial electric fields, along the inclusion

periphery. The effect of varying Γ on the aforementioned variables along the inclusion periphery is presented in subsection 5.4.2 or in [6].

3.4.4 Evaluation of material properties of a piezoelectric composite

In this subsection, we determine the material properties of PZT-7A/LaRC-SI piezoelectric composites (PZT-7A piezoelectric particles embedded in LaRC-SI polyimide matrix) as functions of particle volume fraction. PZT-7A is a ceramic that exhibits a piezoelectric effect with electric fields applied along all three principle axes. LaRC-SI (Langley Research Center - Soluble Imide) is a thermoplastic polyimide that was developed for aerospace applications. The material properties of all constituents are listed in Table 1.1.

In order to calculate the effective material properties, the computational models presented in section 1.10 are used. The representative volume element (RVE) used is composed of just one region (grain) that includes an inclusion. Plane strain assumption is used in this study and the direction of polarization is vertically upward.

Figure 3.5 shows the predictions of the different effective material constants as functions of particle volume fraction, compared with Mori-Tanaka (MT), Self-Consistent (SC), Finite Element models using ANSYS (with large number of elements) and Odegard's proposed models, all presented in [7].

It can be seen that the proposed model gives very accurate predictions using only one MTCG. The proposed method is much more computationally efficient as well as numerically more accurate, than the simple finite element models using ANSYS, and can be used to model piezo-composites even if the arrangement of particles is not symmetrical which is the main assumption used with all the analytical models previously mentioned.

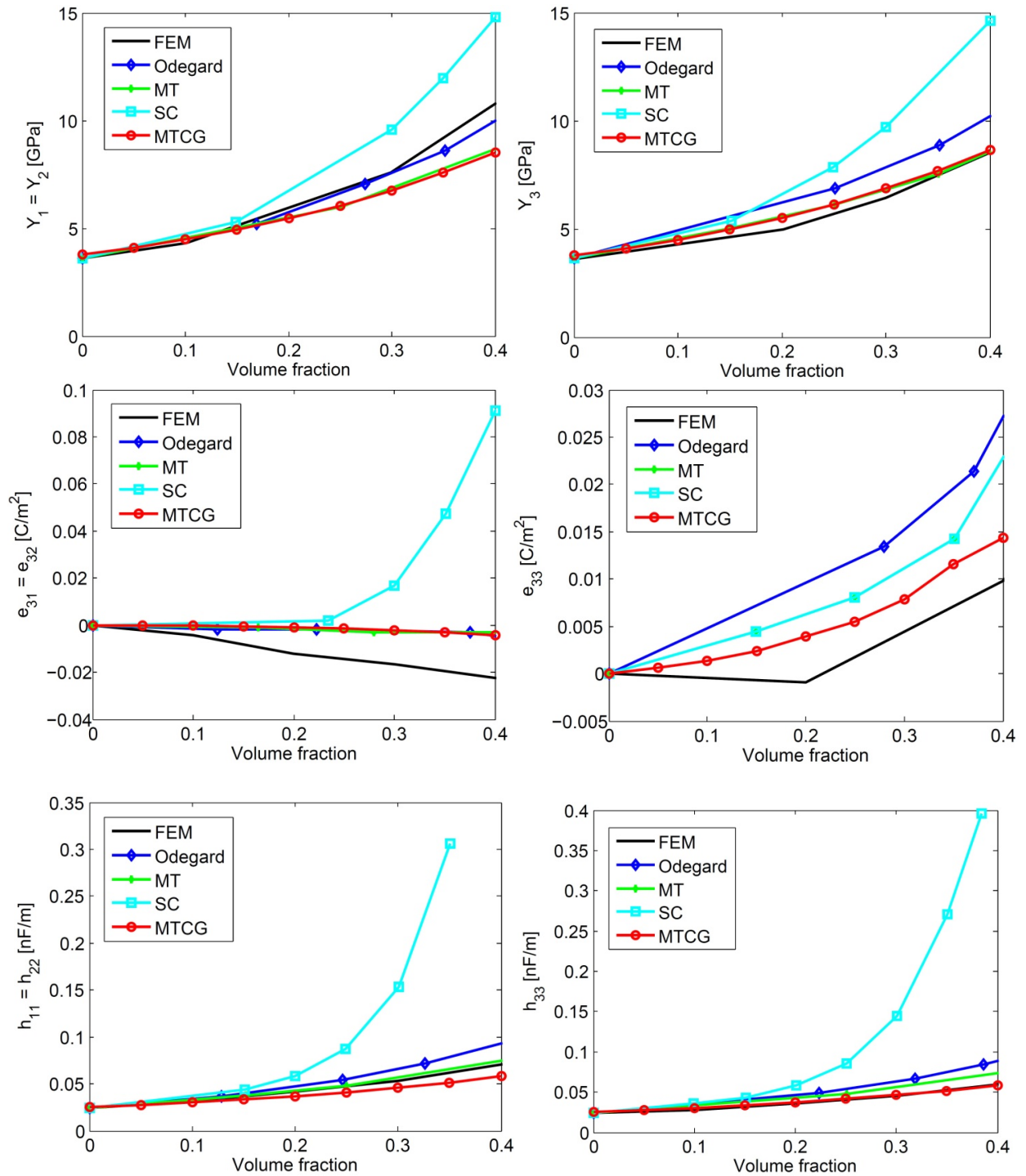


Figure 3.5: Predictions of the effective piezoelectric materials properties of PZT-7A/LaRC-SI as functions of particle volume fraction

3.4.5 Damage detection in porous piezoelectric materials with arbitrary-sized elliptical voids

We consider a porous piezoelectric representative volume element (RVE) made of 20 PZT-4 piezoelectric grains with arbitrary sized elliptical voids whose b/a ratios are in the range of 0.7 – 1.3. The dimensions of the RVE are $L = W = 1\text{mm}$ and the porosity volume fraction is 0.05. The direction of polarization is vertically upward in all grains. The lower edge is prevented from motion in the vertical direction while the lower left corner node is electrically grounded and constrained in the horizontal direction. A mechanical loading $\sigma_o = 1\text{GPa}$ is applied on the upper edge. The contour plots of maximum principal stress, strain energy density (SED) as well as dielectric energy density are shown in Figure 3.6.

As can be seen from the figures, high principal stress and strain energy density concentrations are observed near the cavities, in the direction perpendicular to the loading direction. On the other hand, at the locations near the voids, in the direction parallel to the loading direction, very low stress values and strain energy density are observed. Higher stress and strain energy density concentrations can be observed around voids that have lower values of b/a (because these voids are sharper and are approaching the shapes of cracks). This gives us an idea about where damage is more likely to initiate and develop in porous piezoelectric materials. It is also interesting to note that the dielectric energy concentrates around voids at angles $\pm 45^\circ$ from the mechanical loading direction, and decreases around the voids in the direction perpendicular to the loading direction.

Increasing the maximum order of Trefftz functions, and the number of collocation points per side in each grain generally has the effect of increasing the accuracy of the solution.

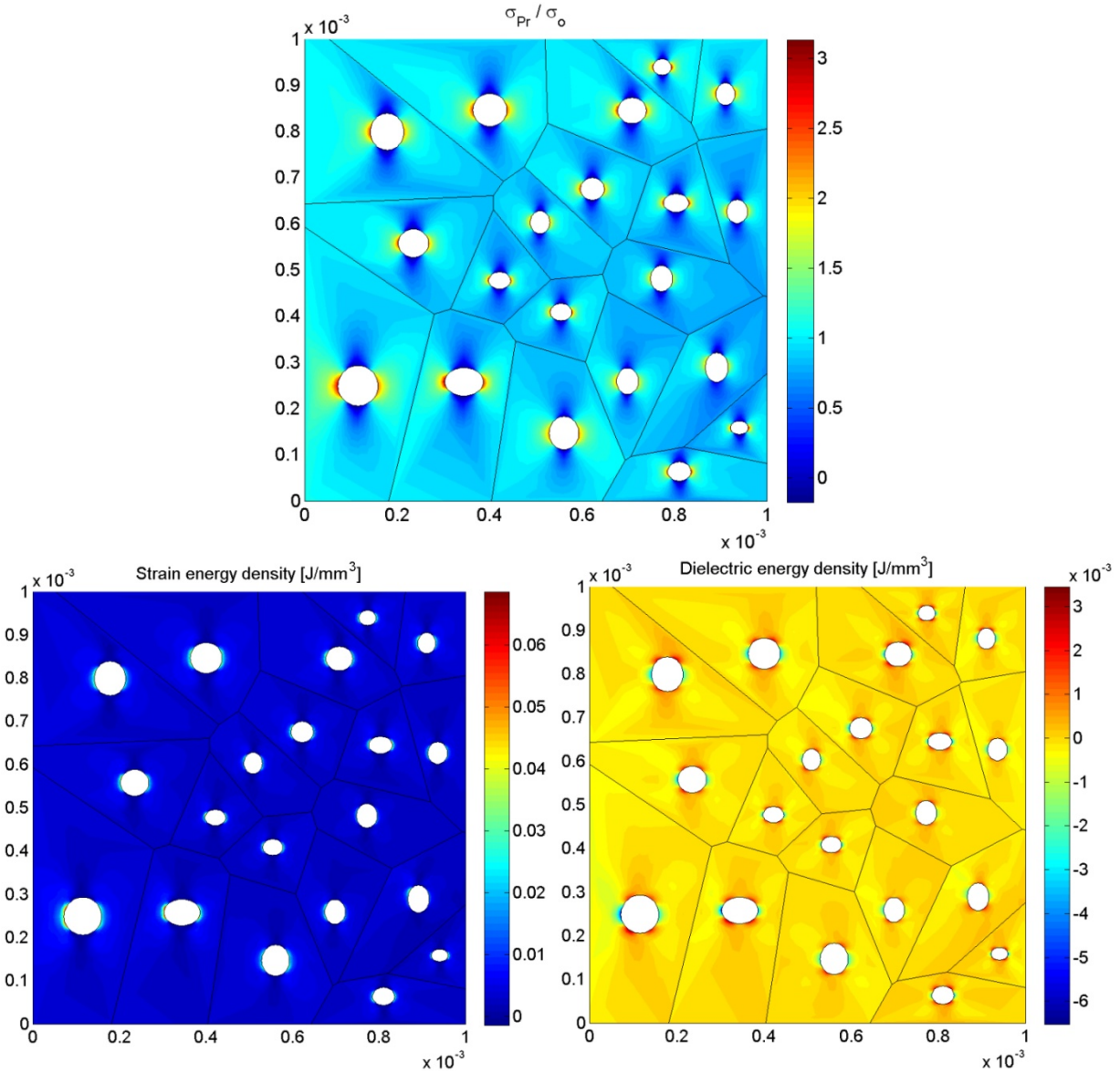


Figure 3.6: Porous piezoelectric material under mechanical loading: Contour plot for (upper) Principal stress, (lower left) Strain energy density, (lower right) Dielectric energy density

In order to solve the same problem using COMSOL Multiphysics commercially available software, 10,163 triangular elements are required as shown in Figure 3.7 (left). This mesh is created using the “Normal” element size. COMSOL has several options for element size: Extremely Coarse, Extra Coarse, Coarser, Coarse, Normal, Fine, Finer, Extra Fine and Extremely Fine. The figure also shows the Strain energy density distribution.

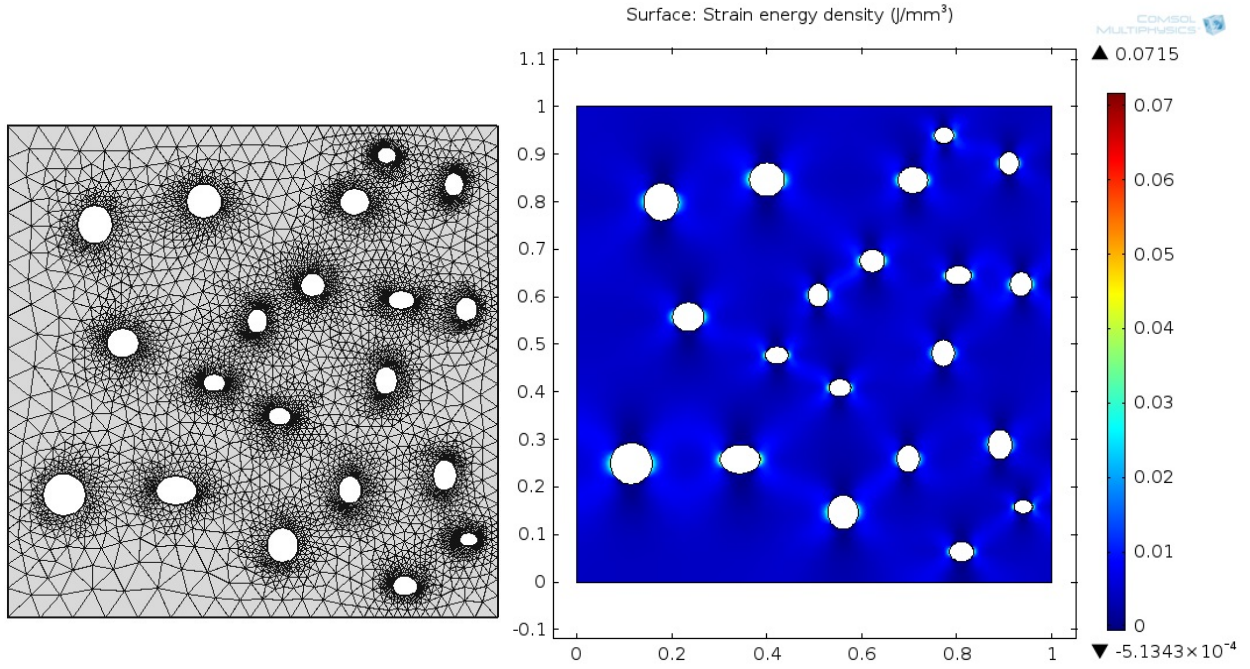


Figure 3.7: COMSOL simulation: (left) mesh, (right) Strain energy density

3.5 Summary and Conclusions of chapter 3

Multi-region Trefftz Computational Grains (MTCGs) method is proposed based on Lekhnitskii formalism to model different porous and composite materials in the micro and meso scales where each computational grain has an irregular polygonal shape that resembles the shape of a material grain with arbitrary number of sides and neighboring grains. Each grain also may contain a circular or an arbitrary oriented elliptical void or inclusion, and may have its own direction of polarization. Collocation method is used to enforce the electromechanical natural and essential boundary conditions, continuity and reciprocity conditions along grain boundaries, and void/inclusion interface conditions. Figure 3.8 illustrates the methods used in the formulation of MTCGs to satisfy the governing equations and enforce the various boundary conditions in a polycrystalline sample with voids/inclusions. Applications of the proposed method include: (1) solving inverse problems by predicting the electromechanical stress at some unreachable locations in structures (like voids) using all the available or measured data even with noise

(Regularization methods should be used), (2) determination of effective material properties of different piezoelectric composites, (3) obtaining the distribution of all secondary fields and the strain and dielectric energy densities in the microstructure to predict locations of damage.

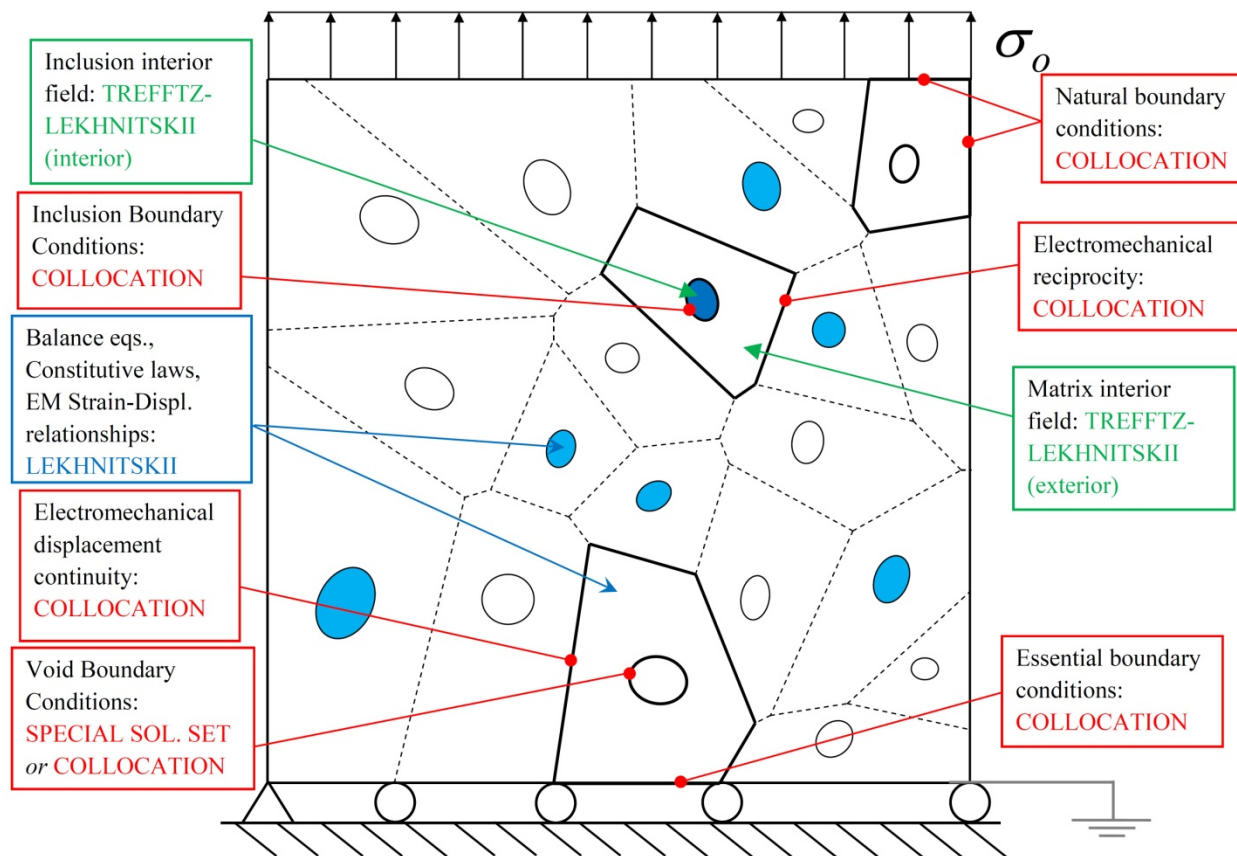


Figure 3.8: Illustration of the methods used in the formulation of MTCGs to satisfy the governing equations and enforce the various boundary conditions in a polycrystalline sample with voids/inclusions

3.6 References of chapter 3

- [1] **Sheng, N.; Sze, K.Y.; Cheung, Y.K.** (2006): Trefftz solutions for piezoelectricity by Lekhnitskii's formalism and boundary collocation method. *Int. J. Numer. Methods Eng.* vol. 65, pp. 2113–2138.

- [2] **Hansen, C.** (1994): REGULARIZATION TOOLS: A Matlab package for analysis and solution of discrete ill-posed problems. *Numerical Algorithms*, vol. 6, no. 1, pp. 1-35.
- [3] **Tikhonov, A.N.; Arsenin, V.Y.** (1977): *Solutions of ill-posed problems*. John Wiley & Sons, New York.
- [4] **Xu X.L., Rajapakse R.K.N.D.** (1999): Analytical solution for an arbitrarily oriented void/crack and fracture of piezoceramics. *Acta Materialia*, vol. 47, pp. 1735 –1747.
- [5] **Xu X.L., Rajapakse R.K.N.D.** (1998): Boundary element analysis of piezoelectric solids with defects. *Composites B*, vol. 29, no. 5, pp. 655-669.
- [6] **Bishay, P. L.; Dong, L.; Atluri, S. N.** (2014): Multi-Physics Computational Grains (MPCGs) for direct numerical simulation (DNS) of piezoelectric composite/porous materials and structures. Submitted for publication in *Computational Mechanics*.
- [7] **Odegard, G.M.** (2004): Constitutive modeling of piezoelectric polymer composites. *Acta Materialia*, vol. 52, pp. 5315–5330.

Chapter 4 : Trefftz-Lekhnitskii Computational Grains (TLCGs) for modeling porous and composite multifunctional materials

4.1 Introduction

Porous ceramics are classified by the International Union of Pure and Applied Chemistry (IUPAC) according to their pore size (or diameter d) as follows: macro-porous ($d > 50$ nm), meso-porous (2 nm $< d < 50$ nm), and micro-porous ($d < 2$ nm). Also, they are classified according to the pore geometry [1] as: foam, interconnected, pore spaces between particles, plates and fibers, large or small pore networks.

In this chapter, Trefftz-Lekhnitskii Computational Grains (TLCGs) are developed for porous and composite piezoelectric/piezomagnetic materials where each computational grain has an arbitrarily polygonal shape, and may or may not include a circular or an arbitrarily oriented elliptical void or inclusion, for Direct Numerical Simulation (DNS) of the micromechanics of piezoelectric-piezomagnetic composites and porous materials. The advantage of using TLCGs is that each TLCG may represent a single grain in the material that has its own polling and magnetic bias directions. The Dirichlet tessellation used to construct the mesh and the geometric shapes of TLCGs resemble the physical configurations of grains in the meso-mechanics, wherein each grain may be surrounded by an arbitrary number of neighboring grains; hence TLCGs are expected to show field distributions that cannot be obtained using the regular triangular and four-sided elements. Lekhnitskii's formalism, presented in chapter 2, is employed here due to the relatively explicit nature of the derived Trefftz functions.

The matrix boundary primal fields' continuity can be enforced using three methods: boundary variational principle (BVP), collocation (C), or the least squares (LS), while the void/inclusion boundary conditions can be enforced using the collocation/least squares method.

For TLCGs that include voids, the *special solution set* for electromagnetically impermeable elliptical voids, presented in section 2.4, can be used alternatively. Accordingly, five types of computational grains are presented here and denoted as TLCG-C, TLCG-LS, TLCG-BVPs, TLCG-Cs and TLCG-LSSs (where the last “s” in the latter three denotes “special solution set”). There is no need to enforce the void boundary conditions in the latter three grains, because the special solution set already satisfies the electromagnetically impermeable conditions. This makes these grains more efficient for modeling grains with electromagnetically impermeable voids. However, for other cases, such as grains with inclusions, the special solution set does not exist.

The chapter is organized as follows: Trefftz-Lekhnitskii Computational Grains (TLCGs) formulation for piezoelectric/piezomagnetic materials with/without voids/inclusions is presented in section 4.2. Numerical examples are provided in section 4.3 and conclusions are summarized in section 4.4. References are listed in section 4.5.

4.2 Formulation of Trefftz-Lekhnitskii Computational Grains (TLCGs) for piezoelectric/piezomagnetic materials with/without voids/inclusions

Consider a 2D irregular m -sided polygonal grain with/without a void or an inclusion as shown in Figure 1.2 (left). We can define linear displacements, electric and magnetic potential fields along each grain boundary in terms of the nodal values of the mechanical displacements $\mathbf{q}_{\mathbf{u}_i}$, electric potential \mathbf{q}_ϕ , and magnetic potential \mathbf{q}_ψ , as:

$$\begin{aligned} \tilde{\mathbf{u}} &= \tilde{\mathbf{N}}_{\mathbf{u}} \mathbf{q}_{\mathbf{u}}, \quad \tilde{\phi} = \tilde{\mathbf{N}}_\phi \mathbf{q}_\phi, \quad \tilde{\psi} = \tilde{\mathbf{N}}_\psi \mathbf{q}_\psi \\ \text{or } \tilde{\underline{\mathbf{u}}} &= \begin{Bmatrix} \tilde{\mathbf{u}} \\ \tilde{\phi} \\ \tilde{\psi} \end{Bmatrix} = \begin{Bmatrix} \tilde{\mathbf{N}}_{\mathbf{u}} & \mathbf{0} & \mathbf{0} \\ \mathbf{0} & \tilde{\mathbf{N}}_\phi & \mathbf{0} \\ \mathbf{0} & \mathbf{0} & \tilde{\mathbf{N}}_\psi \end{Bmatrix} \begin{Bmatrix} \mathbf{q}_{\mathbf{u}} \\ \mathbf{q}_\phi \\ \mathbf{q}_\psi \end{Bmatrix} = \tilde{\mathbf{N}} \mathbf{q} \quad \text{at } \partial\Omega^e \end{aligned} \quad (4.1)$$

where $\tilde{\mathbf{N}}_{\mathbf{u}}$, $\tilde{\mathbf{N}}_{\phi}$ and $\tilde{\mathbf{N}}_{\psi}$ are linear shape functions, $\tilde{\mathbf{u}} = [\tilde{u}_1 \quad \tilde{u}_3 \quad \tilde{\phi} \quad \tilde{\psi}]^T$ and $\mathbf{q}^T = \{\mathbf{q}_{\mathbf{u}}^T \quad \mathbf{q}_{\phi}^T \quad \mathbf{q}_{\psi}^T\}.$

The basic solution set in eqs. (2.33) and (2.34) can be used as the interior/exterior fields, which satisfy the constitutive law, the strain-displacement, the electric field-electric potential, and magnetic field-magnetic potential relationships, and the equilibrium and Maxwell's equations. For the case of impermeable elliptical voids, the special solution set in eqs. (2.41) which satisfies the void *stress-free* and *vanishing surface charge and magnetic flux densities* boundary conditions can be used instead. In matrix and vector notation, these interior/exterior fields can be written in the form:

$$\begin{aligned} \begin{Bmatrix} \mathbf{u} \\ \phi \\ \psi \end{Bmatrix} &= \begin{Bmatrix} \mathbf{N}_{\mathbf{u}} \\ \mathbf{N}_{\phi} \\ \mathbf{N}_{\psi} \end{Bmatrix} \mathbf{a}, & \begin{Bmatrix} \boldsymbol{\sigma} \\ \mathbf{D} \\ \mathbf{B} \end{Bmatrix} &= \begin{Bmatrix} \mathbf{M}_{\sigma} \\ \mathbf{M}_{\mathbf{D}} \\ \mathbf{M}_{\mathbf{B}} \end{Bmatrix} \mathbf{a}, & \text{in } \Omega^e \\ \text{or } \underline{\mathbf{u}} &= \mathbf{Na}, & \underline{\boldsymbol{\sigma}} &= \mathbf{Ma}, & \text{in } \Omega^e \end{aligned} \quad (4.2)$$

Where \mathbf{N} are the Trefftz functions in the order of $M_s, \dots, 0, 1, \dots, M$ and \mathbf{a} denotes the unknown real coefficients ($a_k^{(\pm n)}, b_k^{(\pm n)}$, $k = 1, 2, 3, 4$ and $n = M_s, \dots, M$) associated with Trefftz functions. If there is no void, only the non-negative exponents are used.

The tractions, surface electric charge density and surface magnetic flux density (normal electric displacement and normal magnetic induction) on the boundaries can be written as:

$$\begin{aligned} \mathbf{t} &= \mathbf{n}_{\sigma} \boldsymbol{\sigma} = \mathbf{n}_{\sigma} \mathbf{M}_{\sigma} \mathbf{a}, & Q &= \mathbf{n}_{\mathbf{e}} \mathbf{D} = \mathbf{n}_{\mathbf{e}} \mathbf{M}_{\mathbf{D}} \mathbf{a}, & Q_M &= \mathbf{n}_{\mathbf{e}} \mathbf{B} = \mathbf{n}_{\mathbf{e}} \mathbf{M}_{\mathbf{B}} \mathbf{a} \quad \text{at } \partial\Omega^e, \\ \text{or } \underline{\mathbf{t}} &= \begin{Bmatrix} \mathbf{t} \\ Q \\ Q_M \end{Bmatrix} = \begin{bmatrix} \mathbf{n}_{\sigma} & \mathbf{0} & \mathbf{0} \\ \mathbf{0} & \mathbf{n}_{\mathbf{e}} & \mathbf{0} \\ \mathbf{0} & \mathbf{0} & \mathbf{n}_{\mathbf{e}} \end{bmatrix} \begin{Bmatrix} \boldsymbol{\sigma} \\ \mathbf{D} \\ \mathbf{B} \end{Bmatrix} = \underline{\mathbf{n}\boldsymbol{\sigma}} = \underline{\mathbf{n}\mathbf{M}\mathbf{a}} \quad \text{at } \partial\Omega^e, \end{aligned} \quad (4.3)$$

Since the matrix interior fields already satisfy the equilibrium and Maxwell's equations (1.3), the constitutive equations (1.5), as well as the strain-mechanical displacement, electric field-electric potential and magnetic field-magnetic potential relations (eqs. (1.4)), three steps should be done:

- 1- Step one: the matrix interior primal fields should be related to the matrix boundary primal fields. Once the mechanical displacements, and the electric and magnetic potentials are expressed in terms of their nodal values in each grain, their continuities (eqs. (1.11)) are automatically satisfied, and the essential boundary conditions (in eqs. (1.7) and(1.8)) can be easily enforced after generating the global system of equations.
- 2- Step two: the reciprocity conditions (eqs. (1.12)) as well as the natural boundary conditions (in eqs. (1.7) and (1.8)) should be enforced.
- 3- Step three: (if a void or an inclusion exists in the grain) the conditions on the void/inclusion boundary should also be satisfied as mentioned in section 2.

There are at least three ways to accomplish step one: using multi-field boundary variational principle (BVP), using collocation method and using the least squares method. If a void or an inclusion exists in the grain, then the collocation/least squares method can be used to satisfy step three. For the case of a void, the special solution set, presented in section 2.4, can alternatively be used to satisfy step 3. In the following, we present different Trefftz-Lekhnitskii Computational Grains (TLCGs) with/without voids/inclusions. Table 4.1 presents the considered computational grains and the methods used to satisfy the previously mentioned conditions. When the void/inclusion boundary $\partial\Omega_c^e$ shrinks to zero, the grain is reduced to the case of a grain with no void.

It should be noted that the three grain types that are based on the special solution set (TLCG-BVPs, TLCG-Cs, TLCG-LSs) are expected to be more efficient than the other grain types, because the special solution set already satisfies the void boundary conditions and there is no need to collocate along the void boundary. However, the special solution set is only valid for the case of electromagnetically impermeable voids and it is not available in the literature for other cases. Actually, these grains are not valid if the void is pressurized, filled with conducting fluid or if the void is replaced by any type of inclusions.

Table 4.1: different TLCGs and the corresponding methods used to satisfy the different conditions (BVP refers to “Boundary variational principle” and PVP refers to “Primitive variational principle”)

Grain	Matrix interior and boundary primal fields continuity	Void/inclusion boundary conditions	Reciprocity and natural BCs
TLCG-C	Collocation	Collocation/ least squares	PVP
TLCG-LS	Least squares	Collocation/ least squares	PVP
TLCG-Cs	Collocation	Special solution set (void only)	PVP
TLCG-LSs	Least squares	Special solution set (void only)	PVP
TLCG-BVPs	BVP	Special solution set (void only)	BVP

4.2.1 Using collocation method

In this method, the continuity between the matrix interior and boundary primal fields (mechanical displacements, electric and magnetic potentials) are enforced in a strong sense at several pre-selected collocation points $\mathbf{x}^{(r)}$, $r = 1, 2, \dots R$ along the grain boundary $\partial\Omega^e$ (this is in contrast to the boundary variational principle where this compatibility is enforced in a variational sense through the use of Lagrangian multipliers which renders the formulation plagued by LBB conditions as will be discussed in subsection 4.2.3), and also when using the basic solution set (eqs. (2.33)-(2.35)), the void/inclusion boundary conditions are enforced by dividing the void/inclusion periphery into number of curved segments, n_s , along the

void/inclusion boundary $\partial\Omega_c^e = \sum_{j=1}^{n_s} \partial\Omega_{cj}^e$, and enforcing the boundary conditions on each segment. So we have:

1- Compatibility between matrix interior and boundary primal fields along $\partial\Omega^e$:

$$\underline{\mathbf{u}}(\mathbf{x}^{(r)}, \boldsymbol{\alpha}) = \tilde{\underline{\mathbf{u}}}(\mathbf{x}^{(r)}, \mathbf{q}), \quad \mathbf{x}^{(r)} \in \partial\Omega^e \quad r = 1, 2, \dots, R \quad (4.4)$$

2- *Traction-free and vanishing surface charge and magnetic flux densities* conditions along $\partial\Omega_c^e$:

$$\int_{\partial\Omega_{cj}^e} \underline{\mathbf{t}}(\mathbf{x}, \boldsymbol{\alpha}) ds = 0, \quad j = 1, 2, \dots, n_s \quad (4.5)$$

By selecting enough number of void/inclusion boundary segments, and solving (4.4) and (4.5) in a least-square sense, $\boldsymbol{\alpha}$ is related to \mathbf{q} as follows:

$$\mathbf{A}\boldsymbol{\alpha} = \mathbf{B}\mathbf{q} \quad \text{or} \quad \boldsymbol{\alpha} = \mathbf{A}^{-1}\mathbf{B}\mathbf{q} = \mathbf{Z}\mathbf{q} \quad (4.6)$$

Now, the interior fields are related to the nodal primal variables (step one), and the void/inclusion boundary conditions are enforced (step three), we just need to enforce the natural boundary conditions as well as the reciprocity conditions on the outer boundary (step two) using the following simple primitive field variational principle:

$$\Pi_1(u_i, \varphi, \psi) = \sum_{e=1}^N \left\{ \int_{\partial\Omega^e} \frac{1}{2} (t_i u_i + Q\varphi + Q_M \psi) dS - \int_{S_l^e} \bar{t}_l u_i dS - \int_{S_Q^e} \bar{Q} \varphi dS - \int_{S_B^e} \bar{Q}_M \psi dS \right\} \quad (4.7)$$

where $i = 1, 3$ in eq. (4.7) and the equations to follow. Euler-Lagrange equations of this functional are:

$$t_i = n_{\sigma j} \sigma_{ij} = \bar{t}_i \quad \text{at } S_t^e, \quad Q = n_{ei} D_i = \bar{Q} \quad \text{at } S_Q^e, \quad Q_M = n_{ei} B_i = \bar{Q}_M \quad \text{at } S_B^e, \quad (4.8)$$

$$(n_{\sigma j} \sigma_{ij})^+ + (n_{\sigma j} \sigma_{ij})^- = 0, \quad (n_{ei} D_i)^+ + (n_{ei} D_i)^- = 0, \quad (n_{ei} B_i)^+ + (n_{ei} B_i)^- = 0 \quad \text{at } S_g^e$$

In matrix and vector notation Π_1 can be written as:

$$\Pi_1(\underline{\mathbf{u}}) = \sum_{e=1}^N \left\{ \int_{\partial\Omega^e} \frac{1}{2} \underline{\mathbf{t}} \cdot \underline{\mathbf{u}} dS - \int_{S_t^e} \bar{\mathbf{t}} \cdot \underline{\mathbf{u}} dS - \int_{S_Q^e} \bar{Q} \varphi dS - \int_{S_B^e} \bar{Q}_M \psi dS \right\} \quad (4.9)$$

$$\begin{aligned} \Pi_1(\mathbf{q}) &= \sum_{e=1}^N \left\{ \frac{1}{2} \mathbf{q}^T \mathbf{Z}^T \left(\int_{\partial\Omega^e} \mathbf{M}^T \underline{\mathbf{n}}^T \mathbf{N} dS \right) \mathbf{Z} \mathbf{q} - \left[\int_{S_t^e} \bar{\mathbf{t}}^T \tilde{\mathbf{N}}_{\mathbf{u}} dS \quad \int_{S_Q^e} \bar{Q} \tilde{\mathbf{N}}_{\varphi} dS \quad \int_{S_B^e} \bar{Q}_M \tilde{\mathbf{N}}_{\psi} dS \right] \mathbf{q} \right\} \\ &= \sum_{e=1}^N \left\{ \frac{1}{2} \mathbf{q}^T \mathbf{Z}^T \mathbf{H}_{\mathbf{mm}} \mathbf{Z} \mathbf{q} - \mathbf{q}^T \mathbf{Q} \right\} \end{aligned} \quad (4.10)$$

where

$$\mathbf{H}_{\mathbf{mm}} = \int_{\partial\Omega^e} \mathbf{M}^T \underline{\mathbf{n}}^T \mathbf{N} dS, \quad \mathbf{Q}^T = \left[\int_{S_t^e} \bar{\mathbf{t}}^T \tilde{\mathbf{N}}_{\mathbf{u}} dS \quad \int_{S_Q^e} \bar{Q} \tilde{\mathbf{N}}_{\varphi} dS \quad \int_{S_B^e} \bar{Q}_M \tilde{\mathbf{N}}_{\psi} dS \right] \quad (4.11)$$

The variation of Π_1 is:

$$\delta\Pi_1(\delta\mathbf{q}) = \sum_{e=1}^N \left\{ \delta\mathbf{q}^T (\mathbf{Z}^T \mathbf{H}_{\mathbf{mm}} \mathbf{Z}) \mathbf{q} - \delta\mathbf{q}^T \mathbf{Q} \right\} = \sum_{e=1}^N \left\{ \delta\mathbf{q}^T \mathbf{K}_c \mathbf{q} - \delta\mathbf{q}^T \mathbf{Q} \right\} \quad (4.12)$$

where $\mathbf{K}_c = \mathbf{Z}^T \mathbf{H}_{\mathbf{mm}} \mathbf{Z}$ is the stiffness matrix of “TLCG-C” grain. This grain does not suffer from LBB conditions, because there is no Lagrangian multipliers involved. In order to obtain the stiffness matrix of this grain, only one matrix, $\mathbf{H}_{\mathbf{mm}}$, requires integration over the outer boundary, as well as the evaluation of \mathbf{Z} .

For an impermeable elliptical void, the special solution set (eq. (2.41)) can be used as an alternative to the collocation method to enforce the void boundary conditions. In this case, eq. (4.5) is not used in obtaining α in eq.(4.6). This grain is then denoted as “TLCG-Cs”.

4.2.2 Using a least squares method

When the number of collocation points is increased to a limit of infinity, it is equivalent to enforcing the compatibility between boundary and interior primal fields using the least squares method; that is minimizing the functional $L_1(\underline{\mathbf{u}}, \tilde{\underline{\mathbf{u}}})$:

$$\begin{aligned} L_1(\underline{\mathbf{u}}, \tilde{\underline{\mathbf{u}}}) &= \int_{\partial\Omega^e} (\underline{\mathbf{u}} - \tilde{\underline{\mathbf{u}}})^T (\underline{\mathbf{u}} - \tilde{\underline{\mathbf{u}}}) dS \\ L_1(\alpha, \mathbf{q}) &= \int_{\partial\Omega^e} (\alpha^T \mathbf{N}^T \mathbf{N} \alpha - 2\alpha^T \mathbf{N}^T \tilde{\mathbf{N}} \mathbf{q} + \mathbf{q}^T \tilde{\mathbf{N}}^T \tilde{\mathbf{N}} \mathbf{q}) dS = \alpha^T \mathbf{A}_1 \alpha - 2\alpha^T \mathbf{B}_1 \mathbf{q} + \mathbf{q}^T \mathbf{D}_1 \mathbf{q} \end{aligned} \quad (4.13)$$

where $\mathbf{A}_1 = \int_{\partial\Omega^e} \mathbf{N}^T \mathbf{N} dS$, $\mathbf{B}_1 = \int_{\partial\Omega^e} \mathbf{N}^T \tilde{\mathbf{N}} dS$ and $\mathbf{D}_1 = \int_{\partial\Omega^e} \tilde{\mathbf{N}}^T \tilde{\mathbf{N}} dS$.

To minimize $L_1(\alpha, \mathbf{q})$ for a fixed \mathbf{q} , we have:

$$\delta L_1(\delta\alpha, \mathbf{q}) = 2\delta\alpha^T \mathbf{A}_1 \alpha - 2\delta\alpha^T \mathbf{B}_1 \mathbf{q} = 0 \quad (4.14)$$

This should be true for any $\delta\alpha$, hence together with eq. (4.5) that enforces the void/inclusion BCs, we obtain α :

$$\begin{bmatrix} \mathbf{A}_1 \\ \mathbf{A}_2 \end{bmatrix} \alpha = \begin{bmatrix} \mathbf{B}_1 \\ \mathbf{0} \end{bmatrix} \mathbf{q} \quad \text{or} \quad \alpha = \mathbf{Z}_1 \mathbf{q} \quad (4.15)$$

Eq. (4.15) is to be used instead of eq.(4.6), and hence all the steps used in constructing TLCG-C grain are exactly the same by replacing \mathbf{Z} by \mathbf{Z}_1 in all equations following eq. (4.6) in the previous subsection where the functional $\Pi_1(\mathbf{q})$ was used to derive the grain equation. This grain is labeled as “TLCG-LS”. Note that this method requires additional integration in

evaluating \mathbf{A}_1 and \mathbf{B}_1 as well as matrix inversion. Again, when using the special solution set (eq. (2.41)) to enforce the impermeable void boundary conditions instead of collocating at the void boundary, the resulting grain is denoted as “TLCG-LSS”.

4.2.3 Using multi-field boundary variational principle

Using the special solution set that satisfies the void boundary conditions if the grain contains a void, or the basic solution set for interior domains if the grain contains no void, then a multi-field boundary variational principle whose Euler-Lagrange equations (stationarity conditions) are the natural BCs, the reciprocity conditions, as well as the compatibility between interior and boundary fields can be used to derive the grain equation.

$$\Pi_2(u_i, \tilde{u}_i, \varphi, \tilde{\varphi}, \psi, \tilde{\psi}) = \sum_{e=1}^N \left\{ \begin{array}{l} - \int_{\partial\Omega^e} \frac{1}{2} (t_i u_i + Q\varphi + Q_M \psi) dS + \int_{\partial\Omega^e} (t_i \tilde{u}_i + Q\tilde{\varphi} + Q_M \tilde{\psi}) dS \\ - \int_{S_t^e} \bar{t}_i \tilde{u}_i dS - \int_{S_Q^e} \bar{Q} \tilde{\varphi} dS - \int_{S_B^e} \bar{Q}_M \tilde{\psi} dS \end{array} \right\} \quad (4.16)$$

Euler-Lagrange equations derived from the functional Π_2 are:

$$\begin{aligned} t_i &= n_{\sigma j} \sigma_{ij} = \bar{t}_i \quad \text{at } S_t^e, \quad Q = n_{ei} D_i = \bar{Q} \quad \text{at } S_Q^e, \quad Q_M = n_{ei} B_i = \bar{Q}_M \quad \text{at } S_B^e, \\ (n_{\sigma j} \sigma_{ij})^+ + (n_{\sigma j} \sigma_{ij})^- &= 0, \quad (n_{ei} D_i)^+ + (n_{ei} D_i)^- = 0, \quad (n_{ei} B_i)^+ + (n_{ei} B_i)^- = 0 \quad \text{at } S_g^e \quad (4.17) \\ u_i^+ &= u_i^- = \tilde{u}_i, \quad \varphi^+ = \varphi^- = \tilde{\varphi}, \quad \psi^+ = \psi^- = \tilde{\psi} \quad \text{at } S_g^e \end{aligned}$$

thus achieving the three steps simultaneously. In matrix and vector notation, Π_2 can be written as:

$$\Pi_2(\underline{\mathbf{u}}, \tilde{\underline{\mathbf{u}}}) = \sum_{e=1}^N \left\{ - \int_{\partial\Omega^e} \frac{1}{2} \underline{\mathbf{t}} \cdot \underline{\mathbf{u}} dS + \int_{\partial\Omega^e} \underline{\mathbf{t}} \cdot \tilde{\underline{\mathbf{u}}} dS - \int_{S_t^e} \bar{\mathbf{t}} \cdot \tilde{\underline{\mathbf{u}}} dS - \int_{S_Q^e} \bar{\mathbf{Q}} \tilde{\underline{\mathbf{u}}} dS - \int_{S_B^e} \bar{\mathbf{Q}}_M \tilde{\underline{\mathbf{u}}} dS \right\} \quad (4.18)$$

$$\Pi_2(\alpha, \mathbf{q}) = \sum_{e=1}^N \left\{ -\alpha^T \left(\frac{1}{2} \int_{\partial\Omega^e} \mathbf{M}^T \underline{\mathbf{n}}^T \mathbf{N} dS \right) \alpha + \alpha^T \left(\int_{\partial\Omega^e} \mathbf{M}^T \underline{\mathbf{n}}^T \tilde{\mathbf{N}} dS \right) \mathbf{q} \right. \\ \left. - \left(\int_{S_t^e} \bar{\mathbf{t}}^T \tilde{\mathbf{N}}_{\mathbf{u}} dS \right) \mathbf{q}_{\mathbf{u}} - \left(\int_{S_Q^e} \bar{Q} \tilde{\mathbf{N}}_{\varphi} dS \right) \mathbf{q}_{\varphi} - \left(\int_{S_B^e} \bar{Q}_M \tilde{\mathbf{N}}_{\psi} dS \right) \mathbf{q}_{\psi} \right\} \quad (4.19)$$

The variation of Π_2 is:

$$\delta\Pi_2(\delta\alpha, \delta\mathbf{q}) = \delta \sum_{e=1}^N \left\{ -\frac{1}{2} \alpha^T \mathbf{H}_{\mathbf{mm}} \alpha + \alpha^T \mathbf{G}_{\mathbf{mq}} \mathbf{q} - \mathbf{q}^T \mathbf{Q} \right\} \\ = \sum_{e=1}^N \left\{ -\delta\alpha^T \mathbf{H}_{\mathbf{mm}} \alpha + \delta\alpha^T \mathbf{G}_{\mathbf{mq}} \mathbf{q} + \delta\mathbf{q}^T \mathbf{G}_{\mathbf{mq}}^T \alpha - \delta\mathbf{q}^T \mathbf{Q} \right\} \\ = \sum_{e=1}^N \left\{ \delta\mathbf{q}^T (\mathbf{G}_{\mathbf{mq}}^T \alpha - \mathbf{Q}) + \delta\alpha^T (\mathbf{G}_{\mathbf{mq}} \mathbf{q} - \mathbf{H}_{\mathbf{mm}} \alpha) \right\} \quad (4.20)$$

$$\text{where } \mathbf{G}_{\mathbf{mq}} = \int_{\partial\Omega^e} \mathbf{M}^T \underline{\mathbf{n}}^T \tilde{\mathbf{N}} dS,$$

and the matrix interior fields to be used are those presented in eqs. (2.41) for the case of a grain with a void, or eqs. (2.33) and (2.34) for interior domains for a grain with no void. We do not use this computational grain to model grains with inclusions.

Using $\delta\Pi_2 = 0$ and for arbitrary $\delta\mathbf{q}$ and $\delta\alpha$ we get for each grain:

$$\mathbf{G}_{\mathbf{mq}}^T \alpha - \mathbf{Q} = \mathbf{0}, \quad \mathbf{G}_{\mathbf{mq}} \mathbf{q} - \mathbf{H}_{\mathbf{mm}} \alpha = \mathbf{0}$$

Using the second equation α can be written in terms of \mathbf{q} as:

$$\alpha = \mathbf{H}_{\mathbf{mm}}^{-1} \mathbf{G}_{\mathbf{mq}} \mathbf{q} \quad (4.21)$$

Substituting this into the other equations to get the grain equation in terms of \mathbf{q} as:

$$\mathbf{K}_{\mathbf{bvp}} \mathbf{q} = \mathbf{Q}, \quad \mathbf{K}_{\mathbf{bvp}} = \mathbf{G}_{\mathbf{mq}}^T \mathbf{H}_{\mathbf{mm}}^{-1} \mathbf{G}_{\mathbf{mq}} \quad (4.22)$$

We denote this grain as “TLCG-BVPs” (boundary variational principle with special solution set) for grains with voids and as “TLCG-BVP” for grains with no voids. This formulation clearly involves Lagrangian multipliers and hence suffers from LBB conditions (see [2],[3]), which are impossible to be satisfied a priori. This means that the eigen values of the stiffness matrix of an arbitrarily distorted grain, without a void for instance, may include more than five zeros (for the three rigid-body and the two constant electric and magnetic potential modes) which indicates that the numerical formulation of the grain is not always stable. The stiffness matrix of TLCG-BVPs (or TLCG-BVP) grain requires integration along the grain boundary to evaluate $\mathbf{G}_{\mathbf{mq}}$ and $\mathbf{H}_{\mathbf{mm}}$, as well as matrix inversion ($\mathbf{H}_{\mathbf{mm}}$).

Note that the first eight Trefftz functions (corresponding to $n = 0$) should be eliminated from \mathbf{N} and \mathbf{M} when using this method because they correspond to rigid-body and constant potentials modes which do not contribute to the energy stored in the grain.

4.2.4 On the selection of the maximum order of Trefftz functions

There are two conditions that should be considered in determining the maximum order of Trefftz functions, M , to be used in developing TLCG grains. These two conditions are:

- 1- The number of Trefftz functions (or undetermined coefficients) m_T should be larger than the number of grain’s degrees of freedom (DOF) in order to ensure that the number of independent Trefftz modes are larger than or equal to the number of the grain’s DOFs.

Note that Lekhnitskii formulation (eqs. (2.33) and (2.34) or eqs. (2.41)) generates some repeated modes. For example, and as mentioned earlier, the first eight Trefftz functions (corresponding to $n = 0$) corresponds to the five rigid-body and constant potential modes (two translational, one rotational, one constant electric potential and one constant magnetic potential modes). The number of degrees of freedom in any grain equals to the

number of nodes \times the number of degrees of freedom per node i.e. $4m$. Hence for rank sufficiency of the grain, the number of non-rigid-body Trefftz modes, $8M$ (or $16M$ when using the basic solution set for exterior domains), should be larger than the number of non-rigid-body degrees of freedom which is $4m - 5$. This ensures that all grain types except TLCG-BVP (or TLCG-BVPs) are stable or rank sufficient. (It is impossible to ensure this for TLCG-BVP grain because the grain formulation involves Lagrangian multipliers as mentioned earlier).

- 2- The number of equations used to solve for the undetermined coefficients should be larger than or equal to the number of these undetermined coefficients (m_T). In developing TLCG-C (for grains with no voids) and TLCG-Cs, we should select the number of collocation points used with any m -sided grain. Each collocation point provides four equations since we are collocating the four primal variables (two mechanical displacements, electric and magnetic potentials). If we use only two collocation points per edge then the total number of collocation equations in any m -sided polygonal grain is $m \times 2 \times 4 = 8m$. For TLCG-C grains with voids where the basic solution set is to be used, $m_T = 8(2M + 1)$ because the negative exponents are also considered, thus increasing the number of unknowns; however $4n_s$ additional equations are added to enforce the void/inclusion boundary conditions on the void/inclusion periphery. Here, we take $n_s = 48$ (where again n_s is the number of void/inclusion boundary segments).

When using the basic solution set (interior domains) or the special solution set, these two conditions can be expressed as:

$$8M > 4m - 5 \quad \text{and} \quad m_T = 8(M + 1) \leq 2 \times 4m$$

When using the basic solution set (exterior domains), the two conditions are:

$$16M > 4m - 5 \quad \text{and} \quad m_T = 8(2M + 1) \leq 2 \times 4m + 4n_s$$

So the conditions on the maximum order of Trefftz functions can be written as:

$$\begin{aligned} \frac{4m-5}{8} < M \leq m-1 & \quad \text{when using basic solution set (interior domains)} \\ & \quad \text{or special solution set} \\ \frac{4m-5}{16} < M \leq \frac{2m+n_s-2}{4} & \quad \text{when using basic solution set (exterior domains)} \end{aligned} \tag{4.23}$$

When using the basic solution set (interior domains) or the special solution set, we can

use $M = \left\lceil \frac{4m-5}{8} \right\rceil$, where $\lceil \rceil$ is a function that rounds a number up to an integer. This satisfies

the two conditions. In this work we also use $M = \left\lceil \frac{4m+3}{8} \right\rceil$ which is larger by one order. This is

suitable for grains with no voids or inclusions, or for grains with voids and based on the special solution set. When using the basic solution set (exterior domains), larger values of M are to be used to increase the accuracy of the solution without violating the second condition.

Equation (4.6) for TLCG-C and TLCG-Cs grains is over-constrained whenever the number of collocation points exceeds the number of undetermined coefficients, m_T . In addition, the system matrices in both TLCG-C and TLCG-LS (eqs. (4.6) and (4.15)) are singular because of the repeated Trefftz functions. Hence in order to solve such systems, singular value decomposition (SVD) technique should be used. The SVD method can solve even the singular system of equations and produces the least squares solutions to the over-constrained systems.

4.2.5 Conditioning of the system matrices

The system of equations to be solved using any of the previous methods is ill-conditioned because of the exponential growth of the term Z_k^n as n is increased; hence we introduce a characteristic length to scale the Trefftz solution set.

For an arbitrary polygonal grain as shown in Figure 1.2 (left), where the coordinate of the nodes are (x_1^j, x_3^j) , $j=1,2,\dots,N$, the center point of the polygon has coordinates (x_1^c, x_3^c) .

Relative to the local coordinates at the center point, we have $\hat{z}_k = \hat{x}_1 + \mu_k \hat{x}_3$

$$= (x_1 - x_1^c) + \mu_k (x_3 - x_3^c), \quad k = 1, 2, 3, 4 \quad \text{and correspondingly,} \quad \hat{\xi}_k = \frac{\hat{z}_k \pm \sqrt{\hat{z}_k^2 - (a_o^2 + \mu_k^2 b_o^2)}}{a_o - i\mu_k b_o}.$$

Now, Z_k (\hat{z}_k for interior domains or $\hat{\xi}_k$ for exterior domains) will be replaced by \hat{Z}_k / R_c

where:

$$R_c = \max(R_{ck}), \quad R_{ck} = \max_j \sqrt{\left[\operatorname{Re}(\hat{Z}_k^j) \right]^2 + \left[\operatorname{Im}(\hat{Z}_k^j) \right]^2}, \quad j = 1, 2, \dots, N \quad (4.24)$$

This is done only for terms with positive exponents. In this way, the exponential growth of Z_k^n is prevented as n increases because $0 < |\hat{Z}_k^n| < 1$ for any point within the grain or along the grain boundaries.

Note also that using \hat{Z}_k / R_c instead of Z_k in eqs. (2.28) or (2.33), generates $\hat{u}_i = \frac{u_i}{R_c}$, $\hat{\varphi} = \frac{\varphi}{R_c}$

and $\hat{\psi} = \frac{\psi}{R_c}$ (not u_i , φ and ψ), so that eqs. (1.4) are consistent. Hence,

$\{u_1 \ u_3 \ \varphi \ \psi\}^T = R_c \{\hat{u}_1 \ \hat{u}_3 \ \hat{\varphi} \ \hat{\psi}\}^T$ should be used in eq. (4.1) for terms with positive exponents.

4.3 Numerical examples

All grain types described above are programmed using MATLAB in a 64-bit WINDOWS operating system, and executed on a PC computer equipped with Intel Q8300 2.5GHz CPU, and

8GB RAM. In this section we illustrate the method by giving three examples focused on porous piezoelectric materials. A commercially available piezoelectric materials (PZT-4) whose properties are listed in Table 1.1 from two references: Xu and Rajapakse [4] and Wang *et al.* [5] and denoted PZT-4(1) and PZT-4(2) respectively, is used in this section.

Eigen value analysis of a single grain proved that all the presented grain types are invariant to global coordinate system rotation (whatever the rotation, we get exactly the same eigenvalues). Regarding stability, it is guaranteed that TLCG-C, TLCG-Cs, TLCG-LS and TLCG-LSS are stable (or rank sufficient) for any grain shape, because these types of grains avoid LBB conditions completely. However, it is not guaranteed that TLCG-BVP grain is stable (has only four zero eigenvalues equivalent to the four rigid-body modes) for any other arbitrarily shaped grain, because this type of grain is plagued by LBB conditions of stability. Simple problems that use grains with no voids, such as patch test and bending of a meso-scale piezoelectric or piezomagnetic panel, can be easily and accurately modeled using any grain type and any number of grains (with no voids) to mesh the problem domain, and the error in the whole structure is less than 1%.

In the following, we show some numerical examples focused on porous piezoelectric materials using the proposed TLCG grains. First we present a piezoelectric domain with an impermeable horizontal or inclined elliptical void under mechanical or electrical loadings, followed by evaluation of the material properties of porous piezoelectric material as functions of porosity volume fraction. Finally we present contour plots that detect the damage-prone sites in a porous piezoelectric material.

4.3.1 Infinite Piezoelectric domain with impermeable arbitrarily-oriented elliptical void under mechanical or electrical loading

Consider an infinite piezoelectric plane with an arbitrarily oriented elliptic void subjected to vertical mechanical or electrical loading in the far field. For numerical implementations, the infinite domain is truncated into a rectangle with length L and width W , as shown in Figure 3.1 (left). The semi-axes of the elliptical void are a and b and the inclination angle between the elliptical void minor axis and the polling direction is ζ . The local coordinate system of the ellipse is denoted $x_1 - x_3$, while the global coordinate system is denoted $X_1 - X_3$. The polling direction is aligned with the global vertical X_3 axis (shown in blue in the figure). The material is PZT-4(1) whose properties are presented in Table 1.1 and plane strain assumption is used in this problem. Here we take $L = W = 50a$, $\sigma_o = 1 Pa$ for the mechanical loading problem and $D_o = 1 C/m^2$ for the electrical loading problem.

Table 4.2 shows the discrete extreme error defined in eq. (4.25) for the five considered grain types where we used $M = 2$ for TLCG-BVPs, TLCG-Cs and TLCG-LSSs and $M = 5$ for the other two types. The table presents the results for both mechanical and electrical loadings and for the cases of circular hole and elliptical hole with $b/a = 2$ and $\zeta = 0, \pi/4$. The last row in the table also shows the average computational time in calculating the stiffness matrices of the proposed grains.

$$E^e = \max_{\mathbf{x}_i \in \partial\Omega_c} \left(\frac{|\sigma_\theta(\mathbf{x}_i) - \tilde{\sigma}_\theta(\mathbf{x}_i)|}{\tilde{\sigma}_{\max}}, \frac{|D_\theta(\mathbf{x}_i) - \tilde{D}_\theta(\mathbf{x}_i)|}{\tilde{D}_{\max}} \right) \quad (4.25)$$

where $\tilde{\sigma}_\theta(\mathbf{x}_i)$ and $\tilde{D}_\theta(\mathbf{x}_i)$ are the exact solutions at boundary points \mathbf{x}_i along the periphery of the void; $\tilde{\sigma}_{\max}$ and \tilde{D}_{\max} are respectively the maximum magnitudes of $\tilde{\sigma}_\theta(\mathbf{x}_i)$ and $\tilde{D}_\theta(\mathbf{x}_i)$.

Table 4.2: Discrete extreme error for the considered grains in different cases

Loading	Void shape	TLCG-BVPs	TLCG-Cs	TLCG-LSS	TLCG-C	TLCG-LS
Mechanical load	Circular	1.11 (10^{-3})	1.60 (10^{-3})	1.88 (10^{-3})	3.08 (10^{-3})	3.26 (10^{-3})
	Elliptic ($\zeta = 0$)	8.90 (10^{-4})	1.02 (10^{-3})	1.04 (10^{-3})	9.17 (10^{-3})	9.34 (10^{-3})
	Elliptic ($\zeta = \pi/4$)	9.12 (10^{-4})	1.09 (10^{-3})	1.34 (10^{-3})	7.14 (10^{-3})	7.48 (10^{-3})
Electrical load	Circular	1.53 (10^{-2})	3.19 (10^{-2})	3.00 (10^{-2})	6.26 (10^{-2})	8.15 (10^{-2})
	Elliptic ($\zeta = 0$)	5.50 (10^{-3})	2.95 (10^{-2})	2.85 (10^{-2})	5.37 (10^{-2})	6.22 (10^{-2})
	Elliptic ($\zeta = \pi/4$)	6.31 (10^{-3})	2.04 (10^{-2})	1.75 (10^{-2})	2.12 (10^{-2})	2.91 (10^{-2})
Average time (sec.)		0.0584	0.0695	0.0602	0.172	0.165

It can be seen from the table that TLCG-C and TLCG-LS are more expensive than the other three grain types when $M = 5$ is used with the basic solution set. However, and as mentioned before, the formulation of only these two grain types can be extended to other void/inclusion boundary condition cases.

Figure 4.1 and Figure 4.3 show the computed circumferential distributions of σ_θ , D_θ , E_θ and E_r divided by σ_o (for mechanical loading) or D_o (for electrical loading) with $\zeta = 0$ and $\zeta = \pi/4$ using one TLCG grain of any type (all types give very similar results). The analytical solution [4] is also included for comparison.

Perfect agreement with the analytical solution can be seen from the table and the figures. The effects of varying ζ , a/b and W/a ratios on the stress, electric displacement and electric field are presented in [6].

Figure 4.2 and Figure 4.4 show contour plots of the components of the stress and the electric displacement around the elliptic void with $\zeta = \pi/4$ and $a/b = 2$ subjected to mechanical and electrical loadings respectively and modeled using a single TLCG grain. These figures only show the region around the void.

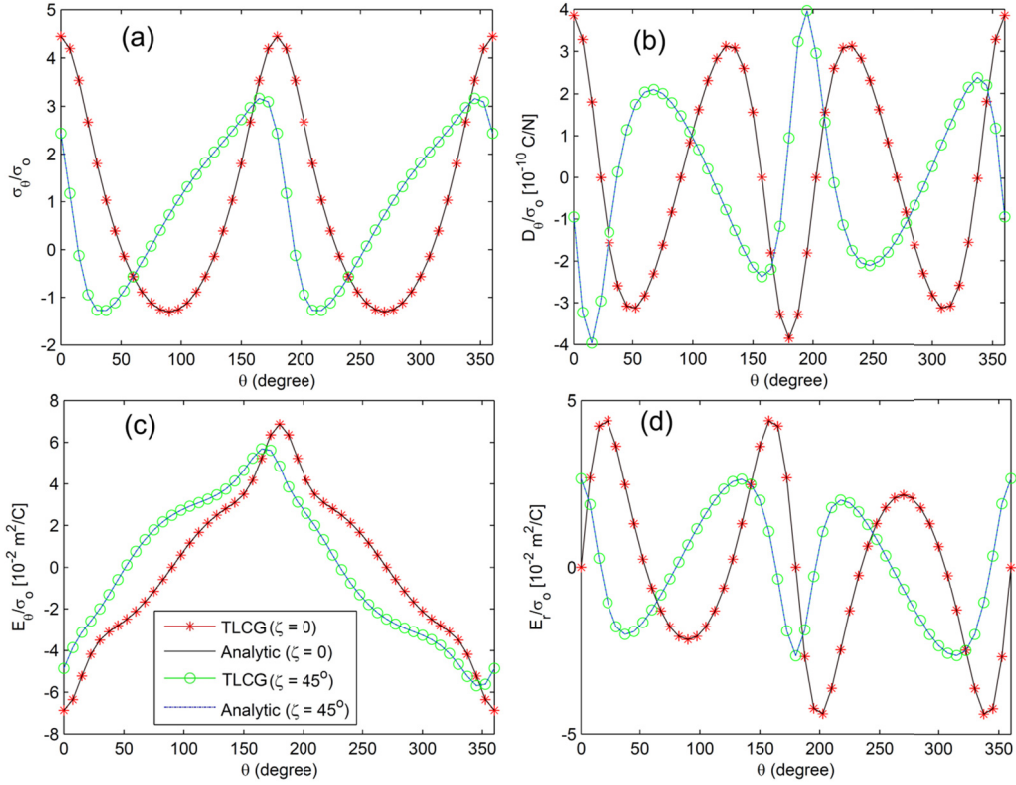


Figure 4.1: variations of (a) σ_θ / σ_0 , (b) D_θ / σ_0 , (c) E_θ / σ_0 , (d) E_r / σ_0 along the periphery of an elliptic void with $\zeta = 0$ and $\zeta = \pi/4$ in an infinite piezoelectric medium under mechanical loading.

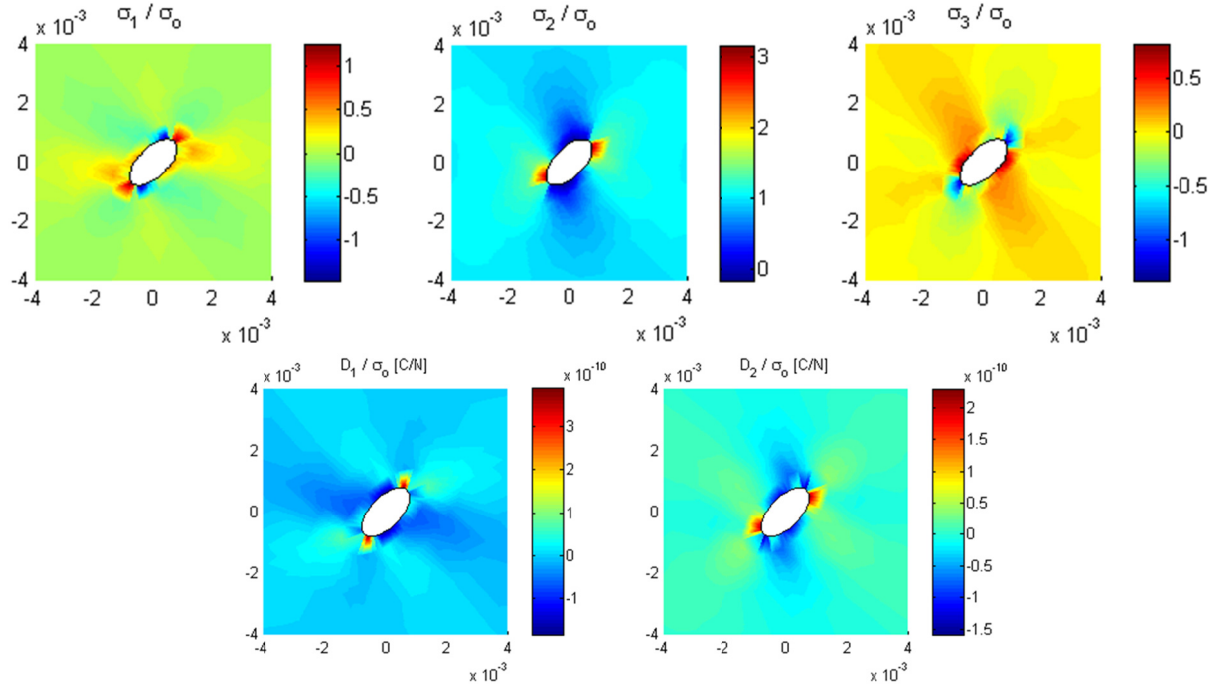


Figure 4.2: distribution of the components of stress and electric displacement around an elliptic void with $\zeta = \pi/4$ in an infinite piezoelectric medium under mechanical loading.

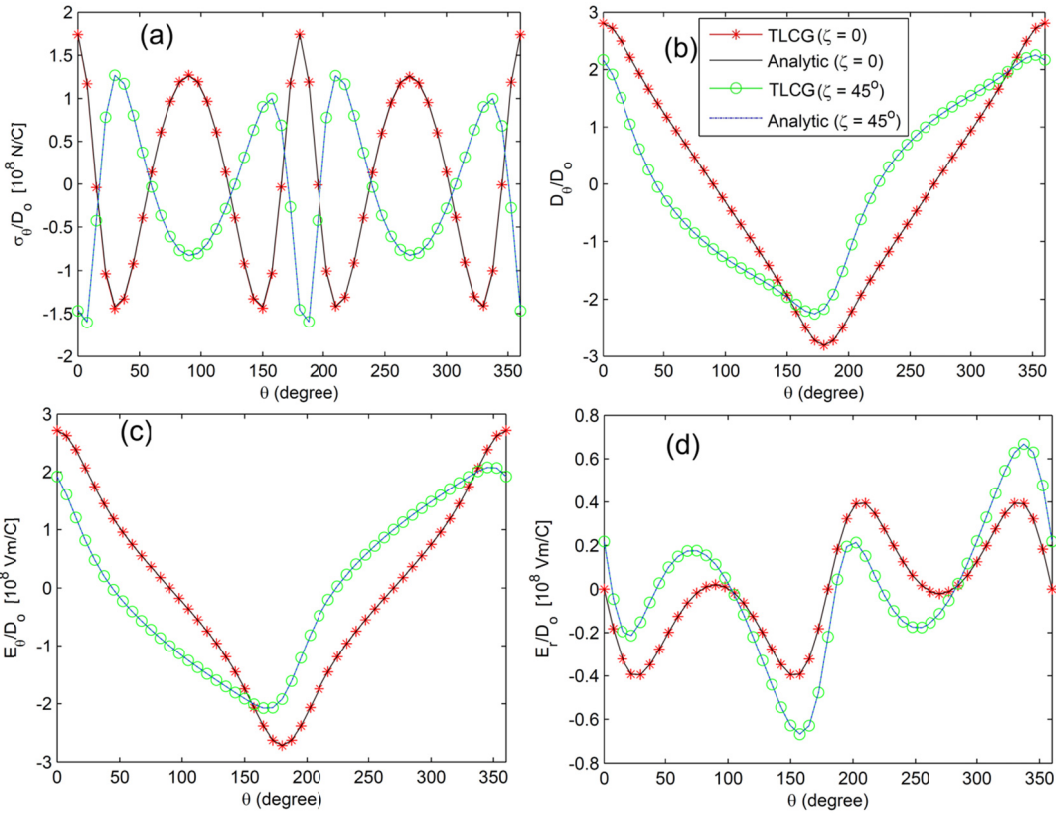


Figure 4.3: variations of (a) σ_θ / D_0 , (b) D_θ / D_0 , (c) E_θ / D_0 , (d) E_r / D_0 along the periphery of an elliptic void with $\zeta = 0$ and $\zeta = \pi/4$ in an infinite piezoelectric medium under electrical loading.

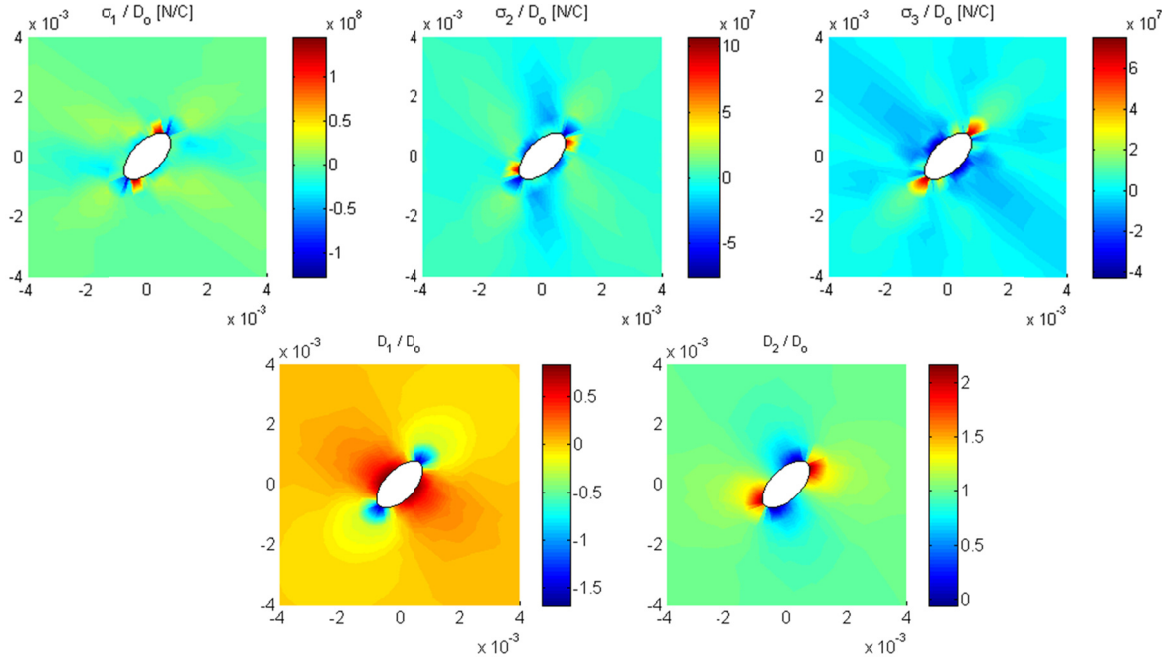


Figure 4.4: distribution of the components of stress and electric displacement around an elliptic void with $\zeta = \pi/4$ in an infinite piezoelectric medium under electrical loading.

4.3.2 Evaluation of the effective material properties of porous piezoelectric materials

In this subsection, we determine the material properties of a porous PZT-4 ceramic sample as functions of porosity volume fraction using different TLCG samples. The material properties of non-porous PZT-4 are listed in Table 1.1 (denoted PZT-4(2)).

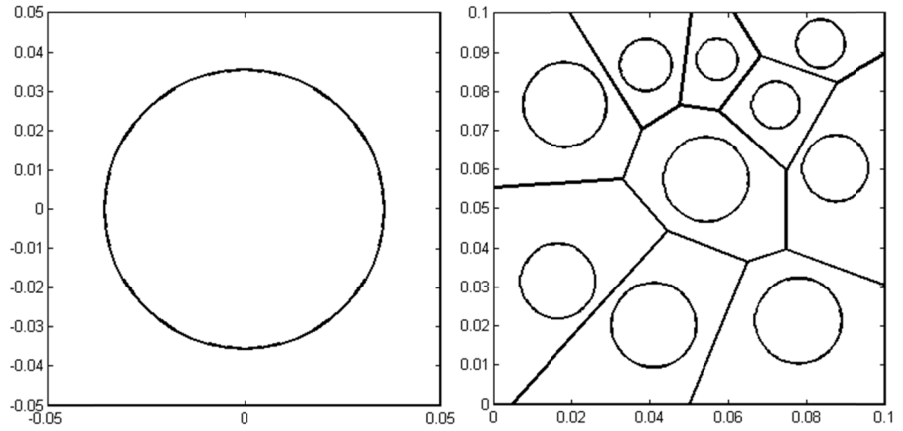


Figure 4.5: Two representative volume elements (RVEs) used in the simulations

In order to calculate the effective material properties, the computational models presented in section 1.10 are used. Two types of representative volume element (RVE) are used here as shown in Figure 4.5: (1) a unit cell grain with a circular void (the figure shows the case of VF=40%), (2) 10 TLCG grains with random circular voids (the figure shows the case of VF=25%). Plane strain assumption is used in this study and the direction of polarization is vertically upward in all grains. Since all grain types give very similar results, the simulations are showing only the results of TLCG-Cs grain type. The results are compared with the predictions of Mori-Tanaka's model ([7], [8]) presented in [5] for PZT-4.

Figure 4.6 shows the predictions of the effective properties of PZT-4 as functions of porosity volume fraction. The results of the RVE with 10 TLCG grains extends only to VF=25%. A constraint was used in this mesh in order to prevent the radius of the void in any grain from exceeding 80% of the distance between the center of the void and the closest point to it on the

grain's outer boundary. The figure shows very good agreement with the predictions of Mori-Tanaka's analytical model.

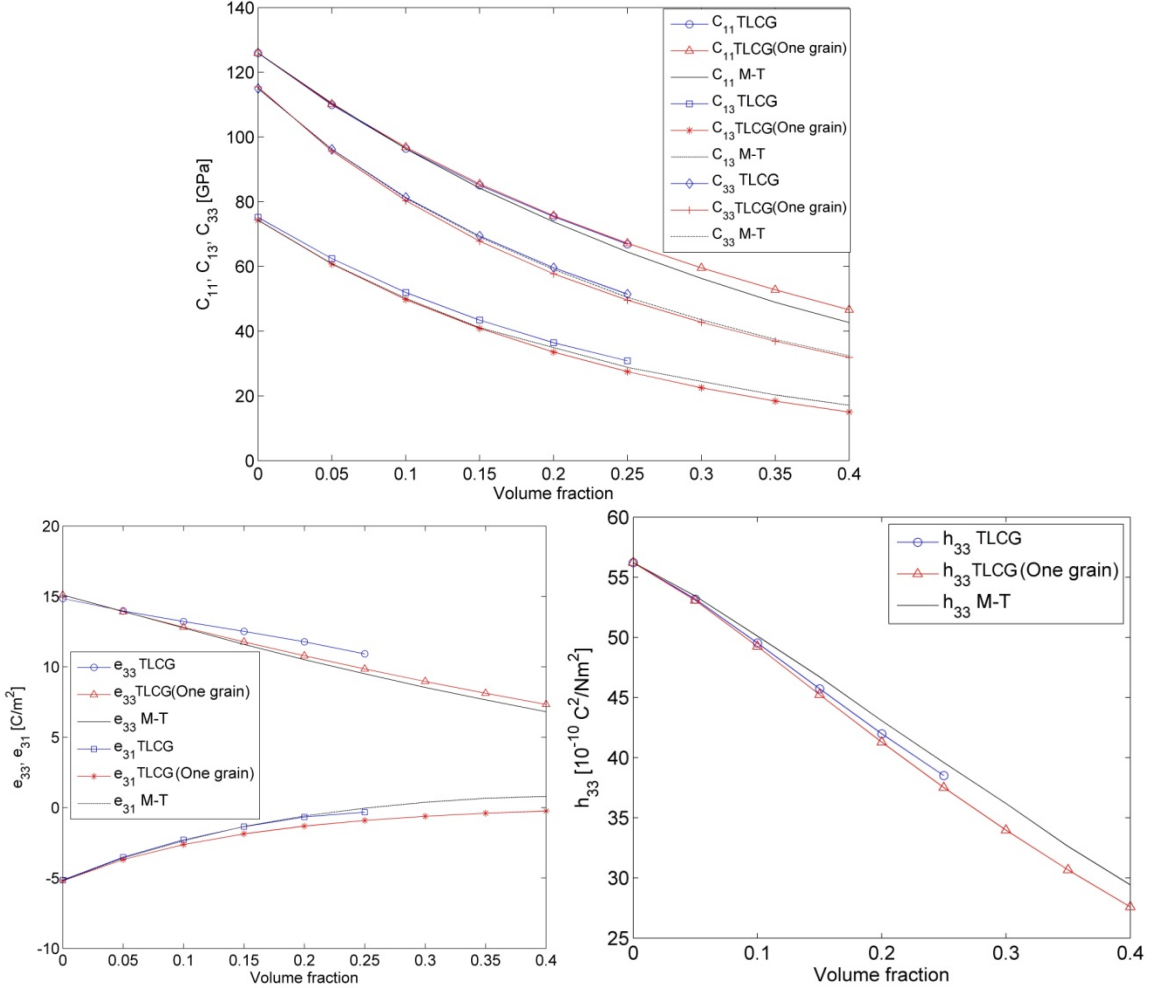


Figure 4.6: Predictions of the effective piezoelectric material properties of PZT-4 as functions of porosity volume fraction

It should be noted that, with the same number of grains, the results slightly change as the irregular mesh changes because stiffness matrices depend on grain shapes. Changing the mesh changes the integrands of the stiffness matrices, and the number and locations of the collocation points in TLCG-C and TLCG-Cs. Increasing the number of grains, the maximum order of Trefftz functions used (without violating the conditions in subsection 4.2.4), and the number of nodes

per side in each grain (i.e., using more than two nodes per side) generally has the effect of decreasing the error. Also increasing the number of collocation points in TLCG-C and TLCG-Cs, increases the accuracy of the solution.

4.3.3 Damage detection in porous piezoelectric material

We consider a porous piezoelectric representative volume element (RVE) composed of 20 porous piezoelectric grains made of PZT-4(1) and polled in the vertical direction. The dimensions of the RVE are $L = W = 1\text{mm}$ and the porosity volume fraction is 0.1. The direction of polarization is vertically upward in all grains. Voids in grains are randomly sized circles. A constraint was used in this mesh in order to prevent the value of the radius of the void in any grain from exceeding 80% of the distance between the center of the void and the closest point to it on the grain's outer boundary. The lower edge is prevented from motion in the vertical direction while the lower left corner node is electrically grounded and constrained in the horizontal direction. A mechanical loading $\sigma_o = 100\text{MPa}$ is applied on the upper edge. The contour plots of the maximum principal stress, the strain energy density (SED) as well as the dielectric energy density are shown in Figure 4.7. The results shown here are computed using TLCG-C grain type.

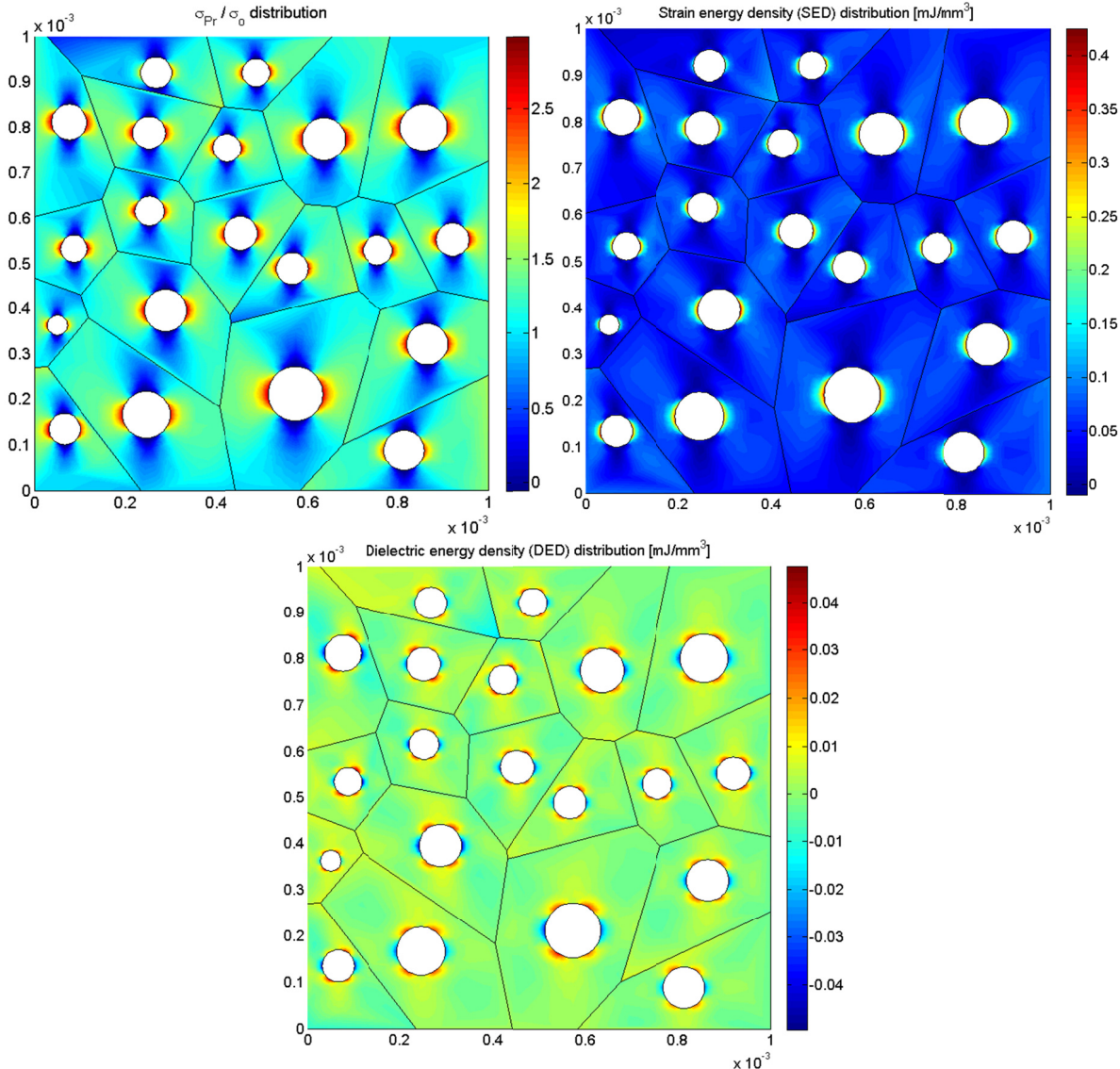


Figure 4.7: Porous piezoelectric material under mechanical loading: Contour plot for (upper left) Principal stress, (upper right) Strain energy density, (lower) Dielectric energy density

As can be seen from the figures, high principal stress and strain energy density concentrations are observed near the cavities, in the direction perpendicular to the loading direction. On the other hand, at the locations near the cavities, in the direction parallel to the loading direction, very low stress values and strain energy density are observed. This gives us an idea about where damage is more likely to initiate and develop in porous piezoelectric materials.

It is also interesting to note that the dielectric energy concentrates around the voids at angles $\pm 45^\circ$ from the mechanical loading directions, and decreases around the voids in the direction perpendicular to the loading direction. As the void gets sharper (b/a ratio is decreased), variations in the values of the principal stress, as well as the strain and dielectric energy densities on the periphery of the void get larger since the void is approaching the shape of a crack. As discussed in subsection 3.4.5, commercial FEM software like COMSOL uses more than 10,000 regular triangular elements of “Normal” element size in order to mesh this geometry, while only 20 TLCGs are required to model the same problem.

4.4 Summary and Conclusions

The proposed TLCG grains are capable of modeling porous/composite piezoelectric or piezomagnetic materials at the micro and meso scales: (a) effective material properties, (b) distribution of all secondary fields, and (c) distribution of strain and dielectric energy densities in the microstructure that allows predicting the locations of damage. Each computational grain has an irregular polygonal shape that resembles the shape of a material grain with arbitrary number of sides and neighboring grains. Each grain also may contain a circular or an arbitrary oriented elliptical void or inclusion, and may have its own direction of polarization. The grains that used the special solution sets (TLCG-BVPs, TLCG-Cs and TLCG-LSs) are the best in modeling grains with impermeable elliptical voids because of their simplicity and efficiency. However these grain formulations cannot model grains with inclusions. On the other hand, TLCG-C and TLCG-LS are more expensive but could be used to enforce any void/inclusion boundary conditions on the void/inclusion periphery. All grain types except TLCG-BVP have the advantage of guaranteed stability since Lagrangian multipliers are not involved in their formulations. Figure 4.8 illustrates the methods used in the formulation of the different types of

TLCGs to satisfy the governing equations and enforce the various boundary conditions in a polycrystalline sample with voids/inclusions (TLCG: Trefftz- Lekhnitskii Computational Grains, BVP: Boundary Variational Principle, C: Collocation, LS: Least Squares, s: Special solution set).

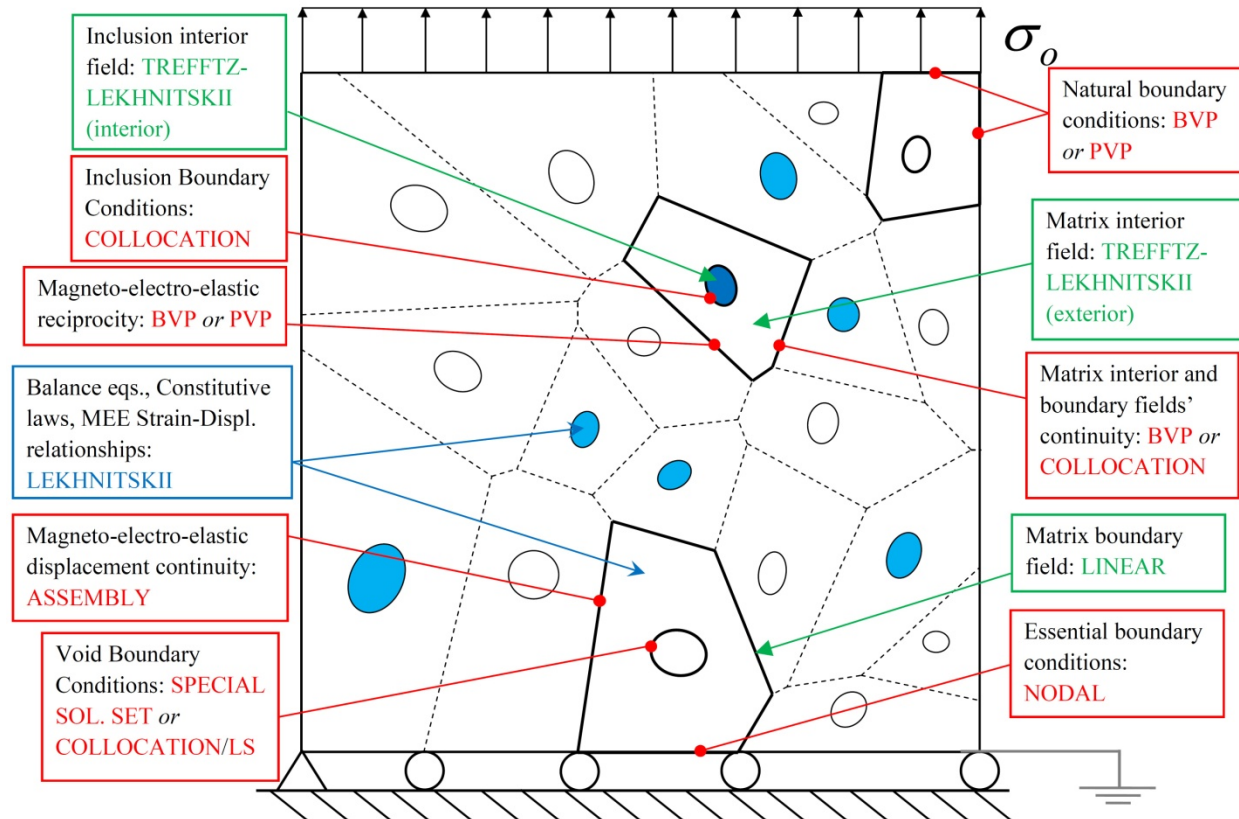


Figure 4.8: Illustration of the methods used in the formulation of the different types of TLCGs to satisfy the governing equations and enforce the various boundary conditions in a polycrystalline sample with voids/inclusions (PVP refers to Primal Variational Principle, and BVP refers to Boundary Variational Principle)

4.5 References of chapter 4

- [1] Araki, K.; Halloran, J.W. (2005): Porous ceramic with interconnected pore channels by a novel freeze casting technique. *J. Am. Ceram. Soc.*, vol. 88, no. 5, pp. 1108-1114.
- [2] Babuska, I. (1973): The finite element method with Lagrangian multipliers. *Numerische Mathematik*, vol. 20, no. 3, pp. 179–192.

- [3] **Brezzi, F.** (1974): On the existence, uniqueness and approximation of saddle-point problems arising from Lagrangian multipliers. *Revue Française D'automatique, Informatique, Recherche Opérationnelle, Analyse Numérique*, vol. 8, no. 2, pp. 129–151.
- [4] **Xu X.L., Rajapakse R.K.N.D.** (1999): Analytical solution for an arbitrarily oriented void/crack and fracture of piezoceramics. *Acta Materialia*, vol. 47, pp. 1735 –1747.
- [5] **Wang, H.; Tan, G.; Cen S.; Yao, Z.** (2005): Numerical determination of effective properties of voided piezoelectric materials using BNM, *Engineering Analysis with Boundary Elements*, vol. 29, pp. 636–646.
- [6] **Xu X.L., Rajapakse R.K.N.D.** (1998): Boundary element analysis of piezoelectric solids with defects. *Composites B*, vol. 29, no. 5, pp. 655-669.
- [7] **Dunn M, Taya M.** (1993): Electromechanical properties of porous piezoelectric ceramics. *J Am Ceram Soc*, vol. 76, no.7, pp. 1697–706.
- [8] **Mikata Y.** (2000): Determination of piezoelectric Eshelby tensor in transversely isotropic piezoelectric solids. *Int J Eng Sci*, vol. 38, pp. 605–41.

Chapter 5 : Hybrid Displacement Computational Grains (HDCGs): A general method for modeling multi-functional materials

5.1 Introduction

Trefftz-Lekhnitskii Computational Grains, presented in chapter 4, are featured with a complete Trefftz trial displacement field in each grain (which satisfies the governing differential equations a-priori), and a polynomial trial function on the grain boundaries. Because of the complete Trefftz trial functions, TLCGs can not only accurately compute the overall stiffness and strength of material, but can also easily compute the local magneto-electro-mechanical stress/strain concentrations. The human labor of generating a compatible very fine FEM mesh is also saved, because each TLCG can represent a grain of the material in the most natural way.

For general anisotropic magneto-electro-mechanical problems, finding a complete Trefftz trial function, under the condition of possible body forces and charges, initial strains, electric fields, and magnetic fields as well as inertia, will be very difficult, if not impossible. In this chapter, Hybrid Displacement Computational Grains (HDCGs) are proposed to model the micromechanics of multifunctional materials. However we illustrate the method by focusing only on piezoelectric composites. Similar to TLCGs developed in chapters 3 and 4, an HDCG represents a grain of the composite as in Figure 5.1 (left), which can include a matrix material, an inclusion material or a pore. Independent displacements and electric-potentials are also assumed in each grain. Quite differently from TLCGs, the trial solutions in each HDCG do not need to satisfy the governing differential equations. However, the trial solutions in each HDCG are still complete, and can efficiently model concentration of electric and mechanical fields. HDCGs are conceptually simpler than TLCGs, and can be used to model any generally anisotropic as well as

nonlinear problems. The essential idea can also be easily applied to accurately solve other multi-physical problems, such as complex thermal-electro-magneto-mechanical materials.

The chapter is organized as follows: the proposed theoretical and algorithmic formulation of the HDCG is presented in sections 5.2 and 5.3, numerical results are given in section 5.4 and a summary is given in section 5.5. Section 5.6 lists the references.

5.2 New Hybrid Variational Principles for Heterogeneous Piezoelectricity

Consider a solid piezoelectric body Ω undergoing infinitesimal deformation. Using indicial notation, the Cartesian coordinates x_i identify material particles in the solid. $\sigma_{ij}, \varepsilon_{ij}, u_i$ are components of the stress tensor, strain tensor and displacement vector respectively. D_i, E_i, φ represent the electric displacement, electric field and the electric potential respectively. \bar{b}_i and $\bar{\rho}$ represent the body force and electric charge density in Ω . We use $(\)_i$ to denote partial differentiation with respect to x_i . We consider linearized electromechanical constitutive equations:

$$\begin{cases} \sigma_{ij} = \frac{\partial H}{\partial \varepsilon_{ij}} \\ D_i = \frac{\partial H}{\partial (-E_i)} \end{cases} \quad (5.1)$$

with the enthalpy defined as:

$$H(\varepsilon_{ij}, -E_i) = \frac{1}{2} C_{ijkl} \varepsilon_{ij} \varepsilon_{kl} - \frac{1}{2} h_{ij} E_i E_j - e_{kij} E_k \varepsilon_{ij} \quad (5.2)$$

Thus the governing differential equations can be expressed in terms of the primitive variables u_i and φ :

$$\left[\frac{\partial H}{\partial u_{(i,j)}} \right]_i + \bar{b}_j = 0 \quad \text{in } \Omega \quad (5.3)$$

$$\left[\frac{\partial H}{\partial \varphi_i} \right]_i + \bar{\rho} = 0 \quad \text{in } \Omega \quad (5.4)$$

In matrix and vector notation, the electromechanical constitutive equation can be written as:

$$\begin{Bmatrix} \underline{\sigma} \\ \underline{\mathbf{D}} \end{Bmatrix} = \begin{Bmatrix} \mathbf{C} & -\mathbf{e}^T \\ \mathbf{e} & \mathbf{h} \end{Bmatrix} \begin{Bmatrix} \underline{\boldsymbol{\varepsilon}} \\ \underline{\mathbf{E}} \end{Bmatrix} \quad \text{or} \quad \underline{\sigma} = \underline{\mathbf{C}} \underline{\boldsymbol{\varepsilon}} \quad (5.5)$$

where \mathbf{C} , \mathbf{e} and \mathbf{h} are, respectively, the material stiffness and piezoelectric tensors written in matrix form, and the dielectric matrix. The underline denotes electromechanical (combined mechanical and electrical) fields or matrices.

We further use \bar{u}_i, \bar{t}_i to denote the prescribed displacement at S_u and the prescribed traction at S_t , respectively. We use $\bar{\varphi}, \bar{Q}$ to denote the prescribed electric potential at S_φ and the prescribed surface charge density at S_Q . Moreover, we consider that the domain Ω is discretized into subdomains (or grains), Ω^e , so that $\Omega = \sum_e \Omega^e$. The division of $\partial\Omega_e$ according to the boundary conditions leads to $\partial\Omega^e = S_u^e + S_t^e + S_g^e = S_\varphi^e + S_Q^e + S_g^e$, where S_g^e represents the intersection of grain e with the neighboring grains.

Primitive field variational principle, corresponding to the stationary condition of the following functional, is generally used to develop primal FEMs:

$$\begin{aligned} \pi_p(u_i, \varphi) &= \sum_e \pi_p^e, \\ \pi_p^e &= \int_{\Omega^e} [H(u_{(i,j)}, \varphi_i) - \bar{f}_i u_i + \bar{q} \varphi] d\Omega - \int_{S_t^e} \bar{t}_i u_i dS + \int_{S_Q^e} \bar{Q} \varphi dS \end{aligned} \quad (5.6)$$

However, simple FEMs (including those in off-the-shelf commercial programs) involve extremely large time and resource for computation as well as mesh-generation. We propose to model composite piezoelectric materials using a new efficient tool named HDCGs.

In order to develop HDCGs, we consider independently assumed complete functions u_i and φ in each subdomain (or grain), Ω^e , and introduce additional inter-element compatible fields \tilde{u}_i and $\tilde{\varphi}$ which satisfy displacement continuity and essential boundary conditions a-priori. Then we can derive the following hybrid variational principle, which is an extension of the pure mechanical model of [1]:

$$\begin{aligned} \pi(u_i, \varphi, \tilde{u}_i, \tilde{\varphi}) &= \sum_e \pi^e, \\ \pi^e &= \int_{\Omega^e} [H(u_{(i,j)}, \varphi_{,i}) - \bar{f}_i u_i + \bar{q} \varphi] d\Omega - \int_{S_t^e} \bar{t}_i \tilde{u}_i dS + \int_{S_Q^e} \bar{Q} \tilde{\varphi} dS \\ &\quad - \int_{\partial\Omega^e} t_i (u_i - \tilde{u}_i) dS + \int_{\partial\Omega^e} Q (\varphi - \tilde{\varphi}) dS \\ \text{where } t_j &= n_i \frac{\partial H}{\partial u_{(i,j)}}, \quad \omega = -n_i \frac{\partial H}{\partial \varphi_{,i}} \end{aligned} \tag{5.7}$$

Now we consider that an inclusion or a void Ω_c^e is present inside each Ω^e , which satisfies $\Omega_c^e \subset \Omega^e$, $\partial\Omega_c^e \cap \partial\Omega^e = \emptyset$. We denote the matrix material as Ω_m^e , such that $\Omega_m^e = \Omega^e - \Omega_c^e$, $\partial\Omega_m^e = \partial\Omega^e + \partial\Omega_c^e$. Detailed illustration of the geometry can be seen in Figure 5.1.

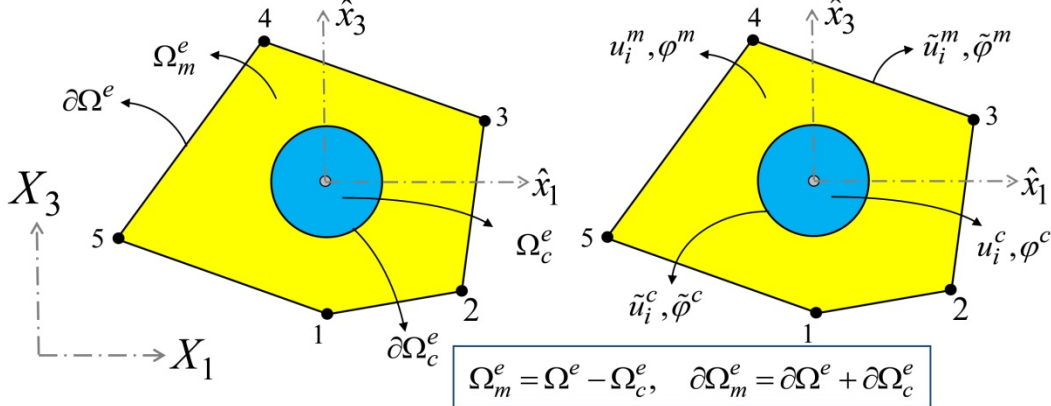


Figure 5.1: A 2D HDCG containing an inclusion or a void (independent trial displacement fields are used)

We use u_i^m, φ^m and u_i^c, φ^c to denote fields in Ω_m^e and Ω_c^e respectively. Linear inter-element compatible fields $\tilde{u}_i^m, \tilde{\varphi}^m$ are assumed at the outer boundary $\partial\Omega^e$. Parabolic inter-element compatible fields $\tilde{u}_i^c, \tilde{\varphi}^c$ are assumed at the matrix-inclusion interface $\partial\Omega_c^e$ (See Figure 5.1 (right)). If the grain contains a void instead of an inclusion, u_i^c, φ^c do not exist.

We deal with this configuration by constructing finite element equations for the inclusion material alone as a homogeneous (simply-connected) domain with nodes along the inclusion boundary as shown in Figure 5.2, and finite element equations for the matrix material alone as a doubly-connected domain with nodes on both outer and inner boundaries. Special trial functions are needed in dealing with the doubly-connected domain and are presented in the next section. Figure 5.2 shows an inclusion with eight boundary nodes which are also among the nodes of the matrix material together with the outer element (grain) nodes.

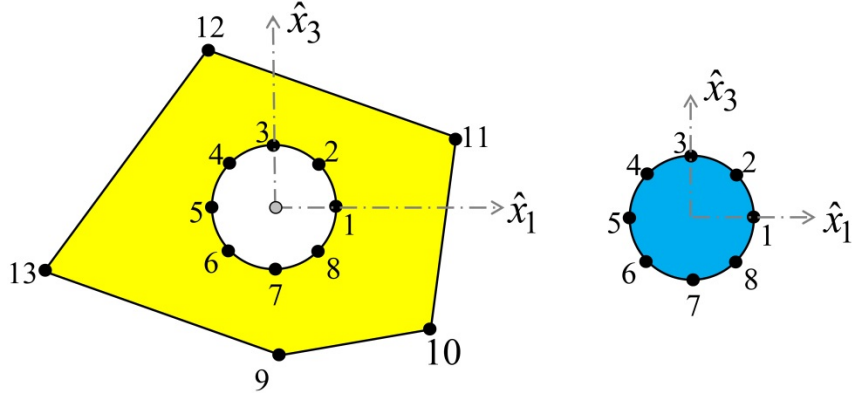


Figure 5.2: HDCG matrix and inclusion domains, boundaries and boundary nodes

Assembling the matrix element and the inclusion element in the same way we assemble any two finite elements will assure the stress and electric displacement reciprocity as well as the continuity of the primal fields along the inclusion boundaries, and results in an element that describe the composite. If a grain contains a void instead of an inclusion, there is no need for this assembly.

5.3 Independent trial mechanical and electric fields, and the formulation of HDCG

It is clear that the boundary fields, $\tilde{u}_i^c, \tilde{\varphi}^c, \tilde{u}_i^m, \tilde{\varphi}^m$, should all be interpolated using node-based polynomial shape functions. On the other hand, the trial mechanical and electrical fields inside the matrix material and the inclusion material, i.e. $u_i^m, \varphi^m, u_i^c, \varphi^c$ should be carefully selected. In the following discussion, we only focus on displacements because the electric-potential trial functions are selected similarly.

We take a 2D HDCG with an inclusion for example (see Figure 5.1). Because the inclusion is a simply-connected domain, it is clear that the trial displacement field u_i^c can be represented as:

$$\begin{aligned} u_i^c &= f^c(R)g^c(\theta) \\ f^c(R) &= \alpha_0 + \alpha_1 R + \alpha_2 R^2 \dots \\ g^c(\theta) &= \beta_0 + \beta_1 \cos \theta + \beta_2 \sin \theta + \beta_3 \cos 2\theta + \beta_4 \sin 2\theta \dots \end{aligned} \tag{5.8}$$

where (R, θ) are the polar coordinates. On the other hand, because the matrix material is a doubly connected domain, singular fields are included in the assumption of u_i^m :

$$\begin{aligned} u_i^m &= f^m(R)g^m(\theta) \\ f^m(R) &= \gamma_0 + \gamma_1 R + \gamma_2 R^2 \dots + \gamma_{-1} R^{-1} + \gamma_{-2} R^{-2} \dots \\ g^m(\theta) &= \lambda_0 + \lambda_1 \cos \theta + \lambda_2 \sin \theta + \lambda_3 \cos 2\theta + \lambda_4 \sin 2\theta \dots \end{aligned} \tag{5.9}$$

It is obvious that for 3D problems, the displacement field should be assumed in the form of $u_i = f(R)g(\theta)h(\phi)$, where (R, θ, ϕ) are the spherical coordinates. The trial electric potential can be assumed in a similar fashion.

Using matrix and vector formulation, we express the electromechanical displacements as:

$$\begin{aligned} \tilde{\mathbf{u}}^m &= \begin{Bmatrix} \tilde{\mathbf{u}}^m \\ \tilde{\varphi}^m \end{Bmatrix} = \tilde{\mathbf{N}}_m \begin{Bmatrix} \mathbf{q} \\ \mathbf{q}_c \end{Bmatrix} = \tilde{\mathbf{N}}_m \mathbf{q}_m \quad \text{at } \partial\Omega^e + \partial\Omega_c^e \\ \underline{\mathbf{u}}^m &= \begin{Bmatrix} \mathbf{u}^m \\ \varphi^m \end{Bmatrix} = \mathbf{N}_m \mathbf{a}_m \quad \text{in } \Omega_m^e \quad \quad \quad \tilde{\mathbf{u}}^c = \begin{Bmatrix} \tilde{\mathbf{u}}^c \\ \tilde{\varphi}^c \end{Bmatrix} = \tilde{\mathbf{N}}_c \mathbf{q}_c \quad \text{at } \partial\Omega_c^e \end{aligned} \tag{5.10}$$

and in case there is an inclusion, we also have:

$$\underline{\mathbf{u}}^c = \begin{Bmatrix} \mathbf{u}^c \\ \varphi^c \end{Bmatrix} = \mathbf{N}_c \mathbf{a}_c \quad \text{in } \Omega_c^e \tag{5.11}$$

where \mathbf{q} and \mathbf{q}_c are nodal electromechanical displacements on the outer and inner boundaries respectively, while \mathbf{a}_m and \mathbf{a}_c are undetermined coefficients. $\tilde{\mathbf{N}}_m$ and $\tilde{\mathbf{N}}_c$ are

shape functions (linear along the outer boundary and parabolic along the circular void/inclusion boundary), while \mathbf{N}_m and \mathbf{N}_c are functions extracted from eqs. (5.9) and (5.8) respectively.

The secondary fields are derived from the primary fields and expressed as:

$$\begin{aligned}\underline{\boldsymbol{\varepsilon}}^m &= \begin{Bmatrix} \boldsymbol{\varepsilon}^m \\ \mathbf{E}^m \end{Bmatrix} = \mathbf{B}_m \mathbf{a}_m \quad \text{in } \Omega_m^e & \underline{\mathbf{t}}^m &= \begin{Bmatrix} \mathbf{t}^m \\ \mathcal{Q}^m \end{Bmatrix} = \mathbf{n} \underline{\boldsymbol{\sigma}}^m = \mathbf{n} \underline{\mathbf{C}}_m \underline{\boldsymbol{\varepsilon}}^m = \mathbf{T}_m \mathbf{a}_m \quad \text{at } \partial\Omega_m^e \\ \underline{\boldsymbol{\varepsilon}}^c &= \begin{Bmatrix} \boldsymbol{\varepsilon}^c \\ \mathbf{E}^c \end{Bmatrix} = \mathbf{B}_c \mathbf{a}_c \quad \text{in } \Omega_c^e & \underline{\mathbf{t}}^c &= \begin{Bmatrix} \mathbf{t}^c \\ \mathcal{Q}^c \end{Bmatrix} = \mathbf{n} \underline{\boldsymbol{\sigma}}^c = \mathbf{n} \underline{\mathbf{C}}_c \underline{\boldsymbol{\varepsilon}}^c = \mathbf{T}_c \mathbf{a}_c \quad \text{at } \partial\Omega_c^e\end{aligned}\tag{5.12}$$

where $\underline{\mathbf{C}}_m$ and $\underline{\mathbf{C}}_c$ are the electromechanical material properties matrices of the matrix and the inclusion respectively, and

$$\mathbf{n} = \begin{bmatrix} n_x & 0 & n_y & 0 & 0 \\ 0 & n_y & n_x & 0 & 0 \\ 0 & 0 & 0 & n_x & n_y \end{bmatrix}$$

Where n_x and n_y are the components of the unit outward normal to the grain boundary.

Substituting the trial solutions (5.10)-(5.12) into the hybrid variational principle of (5.7) and ignoring the body force and the electric charge density for now, an FEM-type of equation can be developed for the inclusion as:

$$\pi_c^e(\mathbf{a}_c, \mathbf{q}_c) = \mathbf{a}_c^T \frac{1}{2} \mathbf{H}_c \mathbf{a}_c - \mathbf{a}_c^T \mathbf{P}_c \mathbf{a}_c + \mathbf{a}_c^T \mathbf{G}_c \mathbf{q}_c - \mathbf{q}_c^T \mathbf{f}_c\tag{5.13}$$

where

$$\mathbf{H}_c = \int_{\Omega_c^e} \mathbf{B}_c^T \underline{\mathbf{C}}_c \mathbf{B}_c d\Omega, \quad \mathbf{G}_c = \int_{\partial\Omega_c^e} \mathbf{T}_c^T \tilde{\mathbf{N}}_c dS, \quad \mathbf{P}_c = \int_{\partial\Omega_c^e} \mathbf{T}_c^T \mathbf{N}_c dS, \quad \mathbf{f}_c = \int_{(S_t^e)_c, (S_Q^e)_c} \bar{\mathbf{t}} \tilde{\mathbf{N}}_c dS$$

Setting the variation of π_c^e to zero, we get the FEM equation as:

$$\delta\pi_c^e(\delta\mathbf{a}_c, \delta\mathbf{q}_c) = \delta\mathbf{a}_c^T \left[(\mathbf{H}_c - \mathbf{P}_c - \mathbf{P}_c^T) \mathbf{a}_c + \mathbf{G}_c \mathbf{q}_c \right] + \delta\mathbf{q}_c^T (\mathbf{G}_c^T \mathbf{a}_c - \mathbf{f}_c) = 0\tag{5.14}$$

and for arbitrary $\delta\mathbf{a}_c^T$ and $\delta\mathbf{q}_c^T$, we get:

$$\mathbf{a}_c = (\mathbf{P}_c + \mathbf{P}_c^T - \mathbf{H}_c)^{-1} \mathbf{G}_c \mathbf{q}_c = \mathbf{V}_c \mathbf{q}_c, \quad \mathbf{G}_c^T \mathbf{a}_c = \mathbf{G}_c^T \mathbf{V}_c \mathbf{q}_c = \mathbf{K}_c \mathbf{q}_c = \mathbf{f}_c \quad (5.15)$$

Similarly for the matrix domain,

$$\mathbf{a}_m = (\mathbf{P}_m + \mathbf{P}_m^T - \mathbf{H}_m)^{-1} \mathbf{G}_m \mathbf{q}_m = \mathbf{V}_m \mathbf{q}_m, \quad \mathbf{G}_m^T \mathbf{a}_m = \mathbf{G}_m^T \mathbf{V}_m \mathbf{q}_m = \mathbf{K}_m \mathbf{q}_m = \mathbf{f}_m \quad (5.16)$$

where

$$\mathbf{H}_m = \int_{\Omega_m^e} \mathbf{B}_m^T \mathbf{C}_m \mathbf{B}_m d\Omega, \quad \mathbf{G}_m = \int_{\partial\Omega_m^e} \mathbf{T}_m^T \tilde{\mathbf{N}}_m dS, \quad \mathbf{P}_m = \int_{\partial\Omega_m^e} \mathbf{T}_m^T \mathbf{N}_m dS, \quad \mathbf{f}_m = \int_{(S_t^e)_m, (S_Q^e)_m} \bar{\mathbf{t}} \tilde{\mathbf{N}}_m dS$$

Assembling the matrix and the inclusion matrices, we get:

$$\begin{bmatrix} \mathbf{K}_{m1} & \mathbf{K}_{m2} \\ \mathbf{K}_{m2}^T & \mathbf{K}_{m3} + \mathbf{K}_c \end{bmatrix} \begin{Bmatrix} \mathbf{q} \\ \mathbf{q}_c \end{Bmatrix} = \begin{Bmatrix} \mathbf{f}_{m1} \\ \mathbf{f}_{m2} + \mathbf{f}_c \end{Bmatrix} \quad (5.17)$$

Recognizing that $\mathbf{f}_{m2} + \mathbf{f}_c = \mathbf{0}$, \mathbf{q}_c can be expressed in terms of \mathbf{q} as:

$$\mathbf{q}_c = -(\mathbf{K}_{m3} + \mathbf{K}_c)^{-1} \mathbf{K}_{m2}^T \mathbf{q} = \mathbf{V} \mathbf{q} \quad (5.18)$$

Then we can write the final FEM equation in terms of the outer boundary nodal electromechanical displacements as:

$$(\mathbf{K}_{m1} + \mathbf{K}_{m2} \mathbf{V}) \mathbf{q} = \mathbf{K} \mathbf{q} = \mathbf{f} \quad (5.19)$$

where $\mathbf{f} = \mathbf{f}_{m1}$ is the load vector on the grain's outer boundary. From the development of HDCGs, we can clearly see that the discretization of the domain requires minimal efforts, since each HDCG can represent a physical grain of material, with an inclusion or void. For a typical RVE with a few hundred physical material grains, the meshing using HDCGs can take only few seconds. On the other hand, meshing using FEM takes enormous time, which makes the study of composite multifunctional materials with simple FEM very difficult or impossible.

5.4 Numerical examples

The formulation described above is programmed using MATLAB in a 64-bit WINDOWS operating system, and executed on a PC computer equipped with Intel Q8300 2.5GHz CPU, and 8GB RAM. The properties of the materials used in this section are listed in Table 1.1: PZT-4(1), PZT-4(2), PVDF and SiC.

Simple problems that use grains with no voids or inclusions, such as patch test and bending of a meso-scale piezoelectric panel, can be easily and accurately modeled using any number of grains (with no voids or inclusions) to mesh the problem domain, and the error in the whole structure is less than 1%. Patch test with any number of grains containing inclusions having the same material properties as that of the matrix can also be passed with error less than 1%.

In the following, we show some numerical examples using the proposed HDCGs. In the first two subsections we present a piezoelectric domain with an impermeable circular void or inclusion under mechanical loading, followed by evaluation of the material properties of porous piezoelectric material as functions of porosity volume fraction. Material properties of piezoelectric particle-composites (SiC particles in PVDF matrix) are also determined as functions of particle volume fraction in the last subsection. Comparisons with other analytical and computational results are presented whenever possible.

5.4.1 Infinite piezoelectric panel with an impermeable circular void

Consider an infinite piezoelectric plane with a circular void subjected to vertical mechanical loading in the far field. For numerical implementations, the infinite domain is truncated into a rectangle with length L and width W , as shown in Figure 5.3. The global coordinate system is denoted $X_1 - X_3$ and the polling direction is aligned with the global vertical

X_3 axis (shown in blue in the figure). The material is PZT-4(1) whose properties are presented in Table 1.1 and plane strain assumption is used in this problem. Here we take $L = W = 20a$, $\sigma_o = 1 Pa$.

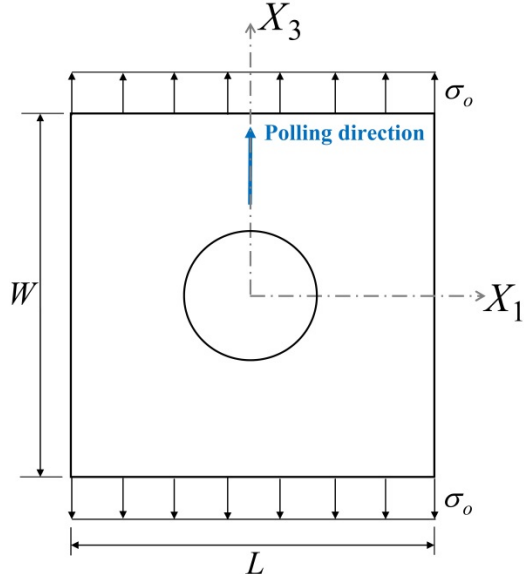


Figure 5.3: A Finite rectangular domain with a circular void

The discrete extreme error defined in eq. (4.25) is 0.0740. Figure 5.4 and Figure 5.5 show the computed circumferential distributions of σ_θ , D_θ , E_θ and E_r divided by σ_o using one HDCG. Because of symmetry, the figures show the variables as θ goes from 0 to 90 degrees. The analytical solution [2] is also included for comparison. Very good agreement can be seen.

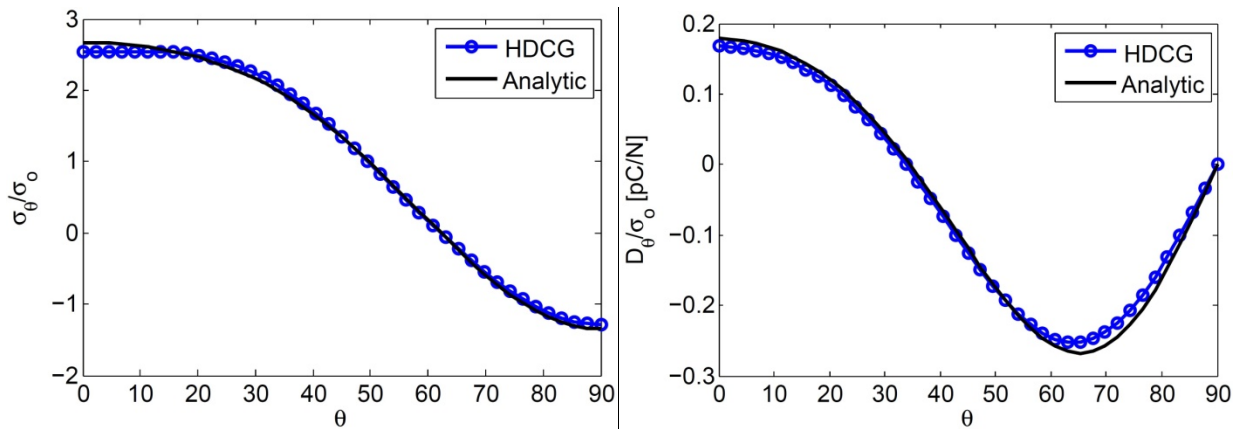


Figure 5.4: Circumferential stress and electric displacement on the periphery of the void

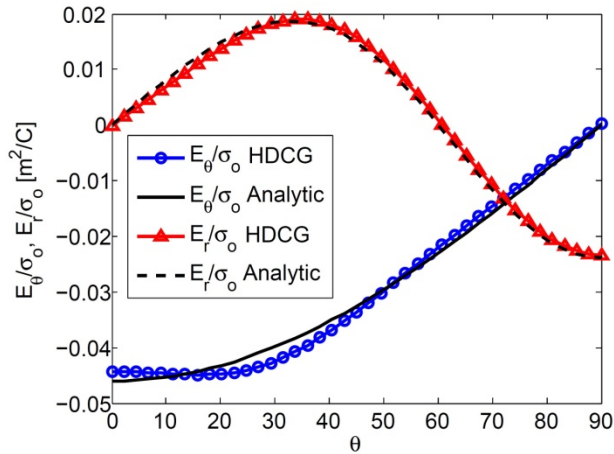


Figure 5.5: Circumferential and radial components of electric field on the periphery of the void.

5.4.2 Piezoelectric panel with circular inclusion

Now consider replacing the void in the previous example with an inclusion whose properties are given as: $\mathbf{C}_c = \Gamma \mathbf{C}_m$ where Γ is a factor that can be varied. $\Gamma > 1$ is equivalent to an inclusion material with stronger properties than those of the matrix material (larger stiffness, dielectric and piezoelectric material constants), while $\Gamma < 1$ is equivalent to an inclusion with weaker properties. Figure 5.6 shows the effect of Γ on σ_θ / σ_o , D_θ / σ_o , E_θ / σ_o and E_r / σ_o along the inclusion periphery.

It can be seen from the figure that both location and magnitude of the maximum circumferential stress and electric displacement along the inclusion periphery are affected by the value of Γ . The maximum radial electric field also behaves similarly. As Γ increases (stronger inclusion properties), the peak value of the circumferential stress is significantly decreased. Hence, we conclude that controlling the material properties of inclusions can result in preventing high stress concentrations around inclusions. This variable can be used in optimal design of piezoelectric microstructure where stress concentrations around fibers and inclusions are taken into account. This was not considered in the optimal design of piezoelectric

microstructures presented in many published research papers such as [3] for instance where topology optimization was used.

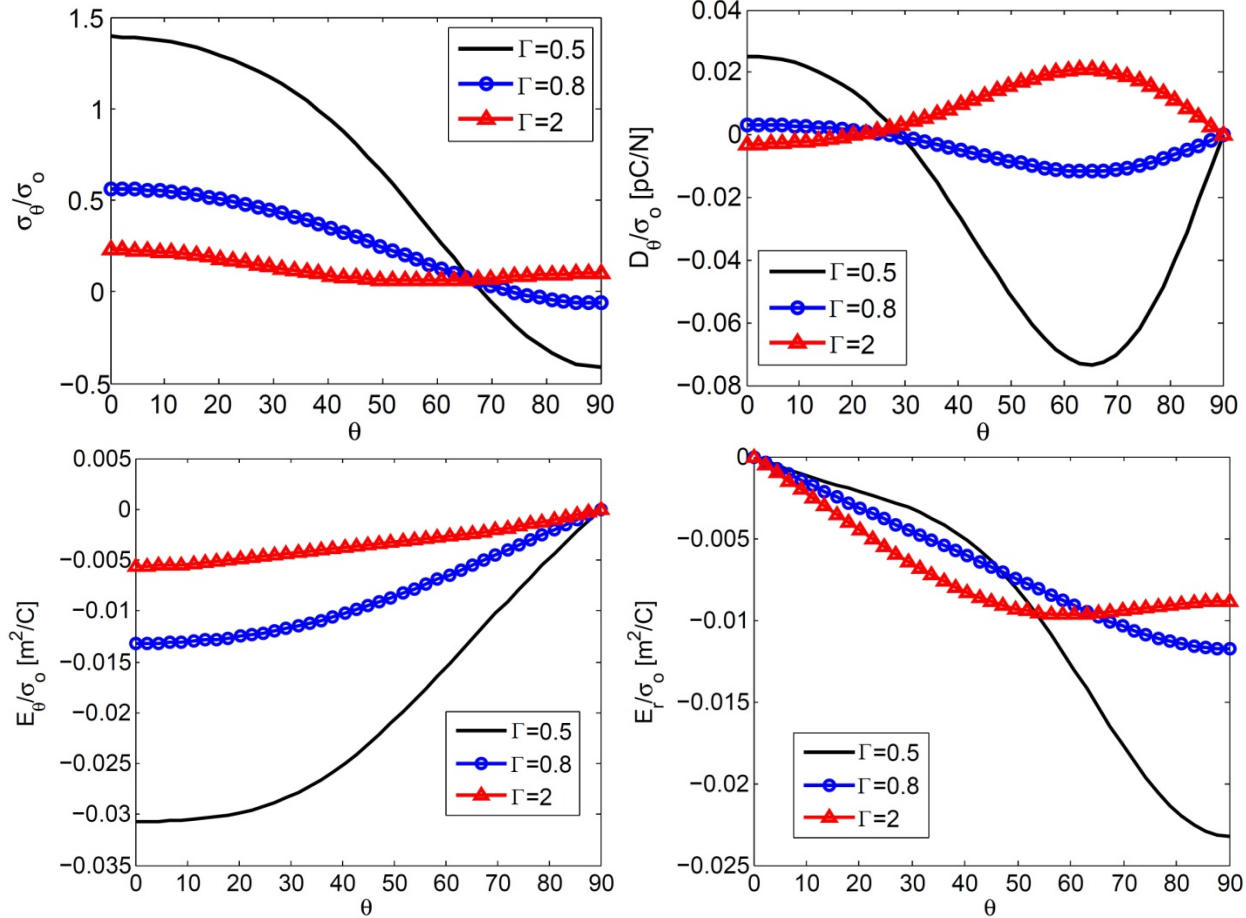


Figure 5.6: The effect of Γ on σ_θ / σ_0 , D_θ / σ_0 , E_θ / σ_0 and E_r / σ_0 along the inclusion periphery

5.4.3 Evaluation of the effective material properties of porous piezoelectric materials

In this subsection, we determine the material properties of a porous PZT-4 ceramic sample as functions of porosity volume fraction using different HDCG samples. The material properties of non-porous PZT-4 are listed in Table 1.1 (denoted PZT-4(2)).

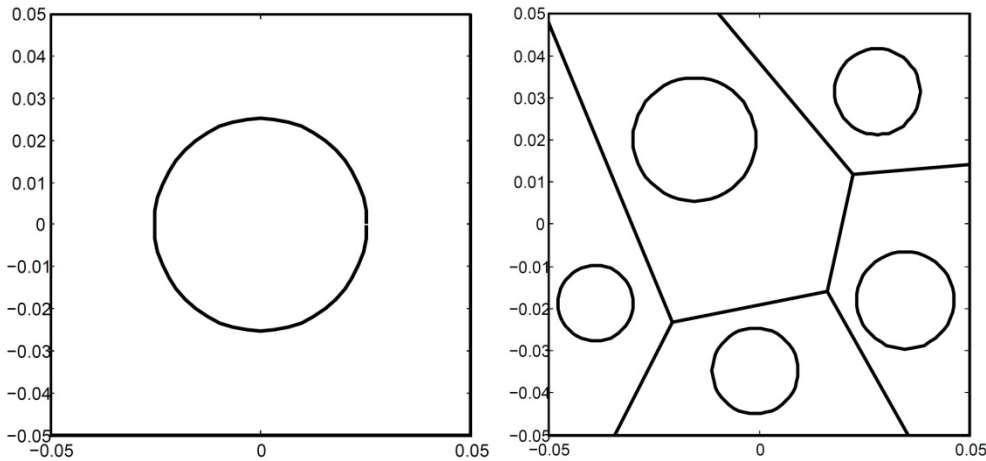


Figure 5.7: Two Representative volume elements (RVEs) used in the simulations

In order to calculate the effective material properties, the computational models presented in section 1.10 are used. Two types of representative volume element (RVE) are used here as shown in Figure 5.7 (the figure shows the case of VF=20%): (a) a unit cell grain with a circular void, (b) 5 HDCG grains with random circular voids. Plane strain assumption is used in this study and the direction of polarization is vertically upward in all grains. The results are compared with the predictions of Mori-Tanaka's model [4] presented in [5] for PZT-4.

Figure 5.8 shows the predictions of the effective properties of PZT-4 as functions of porosity volume fraction. A constraint was used in this mesh in order to prevent the radius of the void in any element from exceeding 80% of the distance between the center of the void and the closest point to it on the element's outer boundary. The figure shows very good agreement with the predictions of Mori-Tanaka's analytical model.

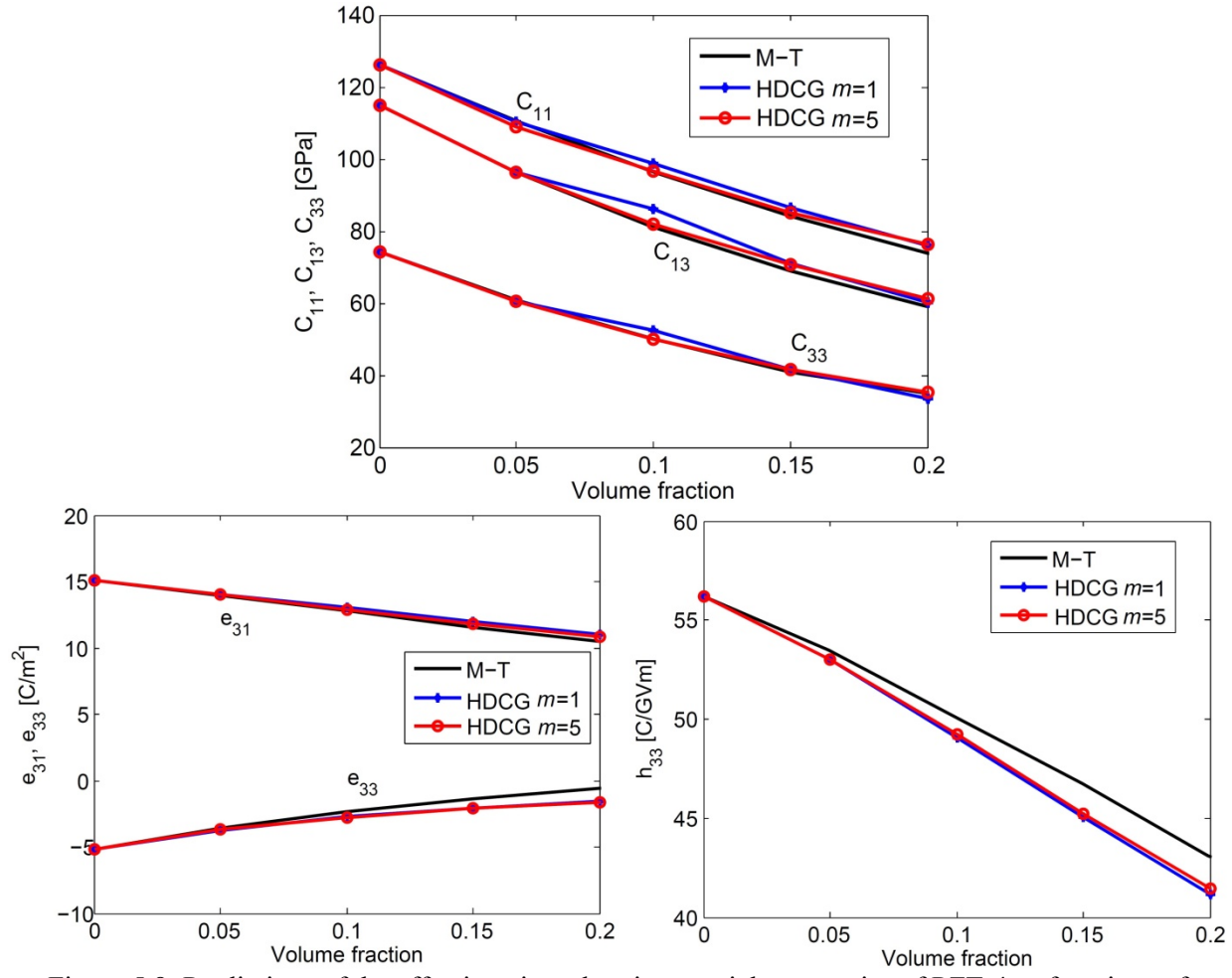


Figure 5.8: Predictions of the effective piezoelectric materials properties of PZT-4 as functions of porosity volume fraction (m is the number of grains used)

It should be noted that, with the same number of grains, the results slightly change as the irregular mesh changes because the stiffness matrices depends on the grain shape. Increasing the number of grains and the number of nodes per side in each grain (i.e., using more than two nodes per side) generally has the effect of decreasing this effect.

5.4.4 Evaluation of the effective material properties of piezoelectric composite material

The effective properties of SiC/PVDF particle composite is determined here and compared with other analytical and computational models. PVDF is an orthotropic, semi-crystalline polymer which exhibits piezoelectric effects if subjected to electric field along the 3-

axis. The PVDF polymer is reinforced with spherical SiC particles. Typical electromechanical properties of PVDF (supplied by NASA Langley Research Center) and SiC are given in Table 1.1. The numerical models used in section 1.10 are also used here to determine the effective material properties as functions of particle volume fraction. One HDCG grain is used in this simulation.

Since the particles are spherical, all the effective material properties can be determined using 2D models. Considering $x_1 - x_3$ plane, we can determine the properties: $C_{11}, C_{13}, C_{33}, e_{31}, e_{33}, h_{11}$, and h_{33} , considering $x_2 - x_3$ plane, we can determine the properties: $C_{22}, C_{23}, C_{33}, e_{32}, e_{33}, h_{22}$, and h_{33} , while considering $x_1 - x_2$ plane, only the properties: $C_{11}, C_{12}, C_{22}, h_{11}$, and h_{22} can be determined. Note that specifying the electric field in the horizontal direction, E_1 , is equivalent to specifying $\bar{\varphi}$ on the right side of the model instead of the upper side (see Figure 1.14). The three Young's moduli Y_1, Y_2 , and Y_3 can be obtained from the stiffness matrix constants C_{ij} .

Figure 5.9 presents the predictions of the different effective material constants as functions of particle volume fraction and compared with Mori-Tanaka (MT), Self Consistent (SC), Finite Element models using ANSYS (with large number of elements) and Odegard's proposed models, all presented in [6].

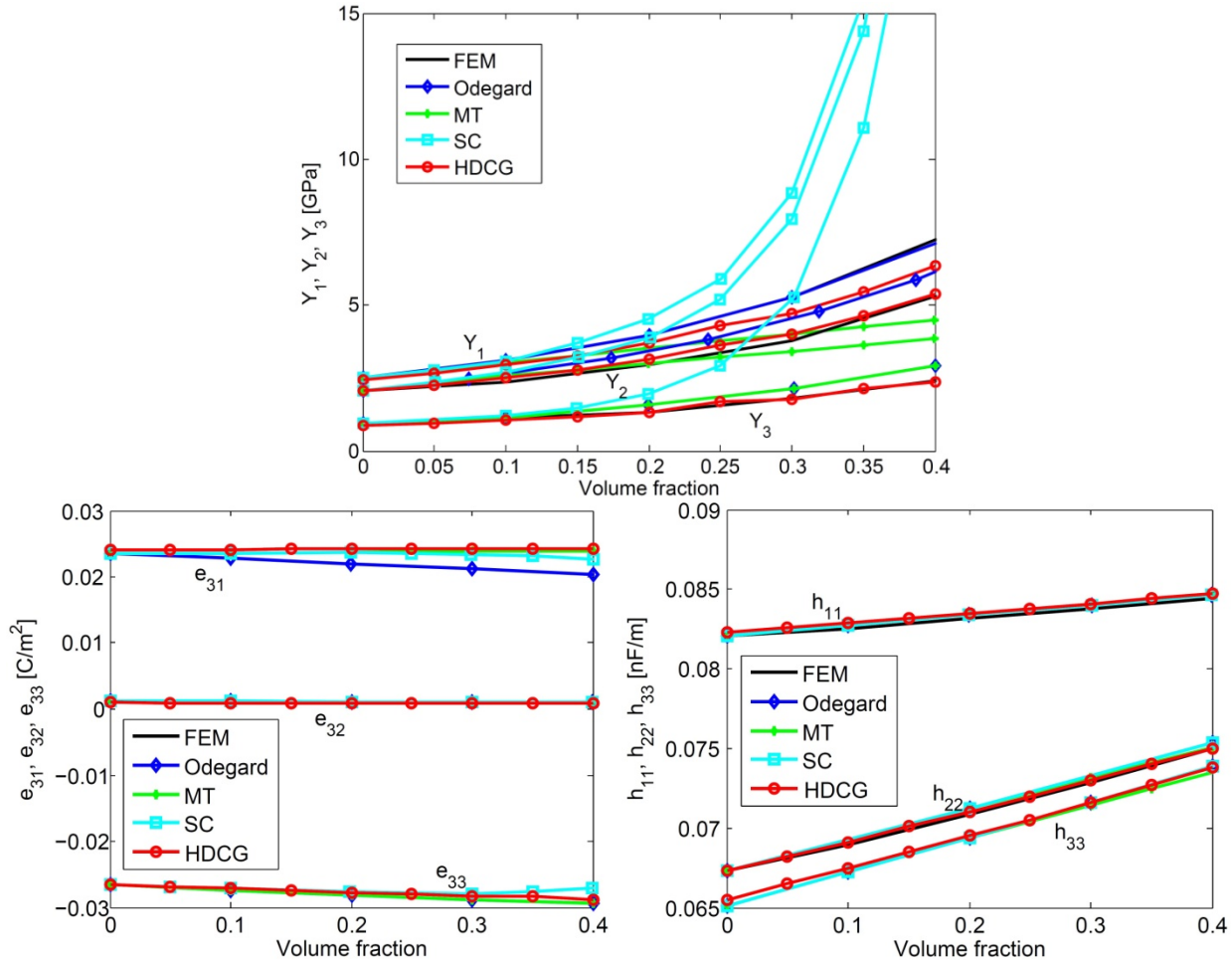


Figure 5.9: Predictions of the effective properties of SiC/PVDF piezoelectric composite as a function of particle volume fraction

It can be seen that the proposed model gives very accurate predictions using only one HDCG grain. The proposed grains are much more computationally efficient as well as numerically more accurate, than the simple finite element models using ANSYS, and can be used to model piezo-composites even if the arrangement of particles is not symmetrical which is the main assumption used with all the analytical models previously mentioned.

5.5 Summary and Conclusion

A new tool, which is not only mathematically highly accurate but also computationally very efficient, named “Hybrid Displacement Computational Grains” (HDCGs) is proposed to study

the micro-electro-mechanical behavior of composite piezoelectric materials. This method is based on a new hybrid variational principle, and independently assumed displacements and electric potentials in each HDCG. Each HDCG can efficiently model a single physical grain of the composite material, thus saving a significant time of generating a complex FEM meshes. HDCG can also model porous and composite piezoelectric materials even if the distribution of voids/inclusions is not symmetrical (which is assumption used with all analytical models). Because the trial solutions are complete but do not satisfy the governing differential equations a-priori, the formulation is very simple, and can accurately account for local field concentrations efficiently and accurately. Figure 5.10 illustrates the methods used in the formulation of HDCGs to satisfy the governing equations and enforce the various boundary conditions in a polycrystalline sample with voids/inclusions. The accuracy and efficiency of HDCGs was illustrated using different examples where the fields along the void/inclusion periphery were calculated, and the effective material properties of porous and composite materials were predicted, and compared with other analytical and computational models. The proposed HDCG is expected to become a very powerful tool of Direct Numerical Simulations (DNS) of the micro/meso mechanics of composite piezoelectric materials, and can possibly lead to efficient multi-scale modeling of piezoelectric devices.

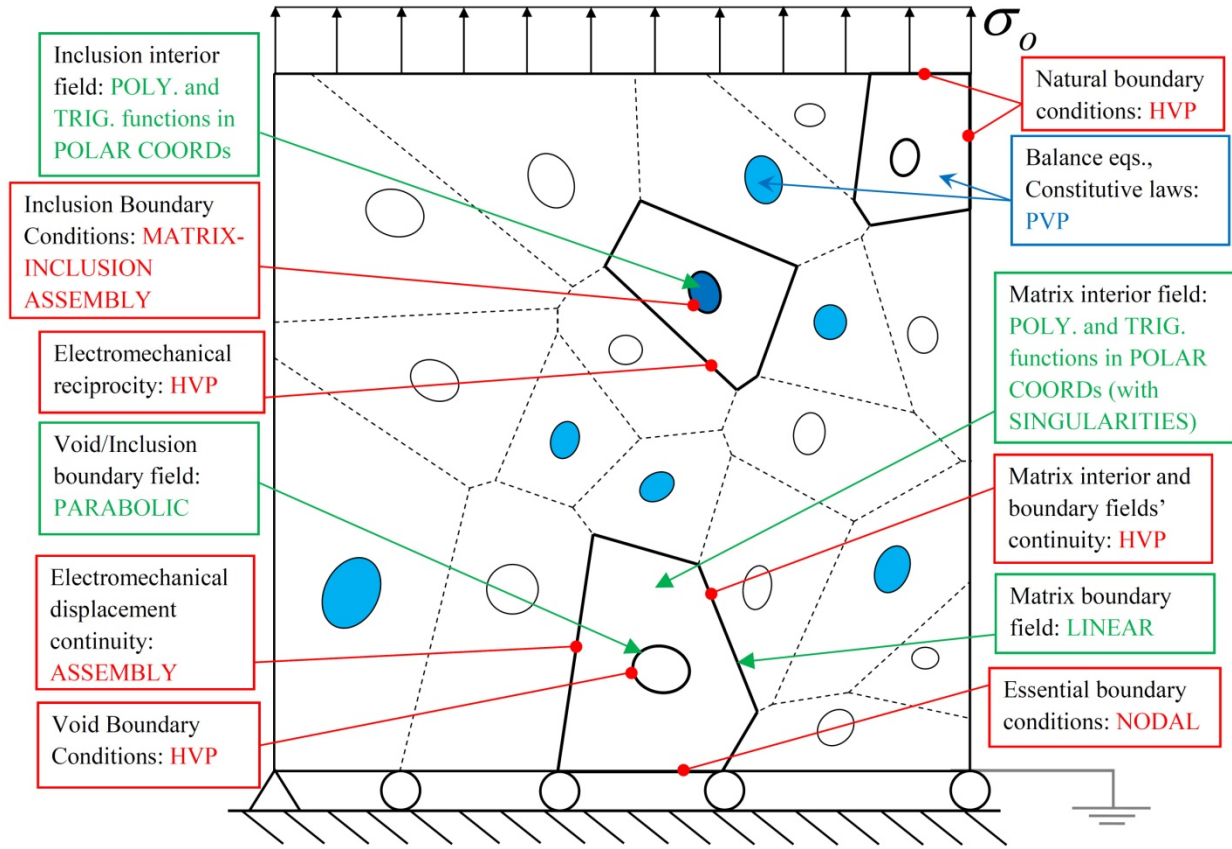


Figure 5.10: Illustration of the methods used in the formulation of HDCGs to satisfy the governing equations and enforce the various boundary conditions in a polycrystalline sample with voids/inclusions (HVP refers to Hybrid Variational Principle, EM: Electro-mechanical)

5.6 References of chapter 5

- [1] Atluri, S. N. (1975): On hybrid finite element models in solid mechanics. *Advances in Computer Methods for Partial Differential Equations*, R. Vichnevetsky (eds.), AICA, pp. 346-356.
- [2] Sosa, H. (1991): Plane problems in piezoelectric media with defects. *Int. J. Solids Struct.* vol. 28, no. 4, pp. 491–505.
- [3] Nelli Silva, E. C.; Ono Fonseca, J. S.; Kikuchi, N. (1997): Optimal design of piezoelectric microstructures. *Computational Mechanics*, vol. 19, pp. 397-410.

- [4] **Dunn, M. L.; Taya, M.** (1993). Micromechanics predictions of the effective electroelastic moduli of piezoelectric composites. *International Journal of Solids and Structures*, vol. 30, no. 2, pp. 161-175.
- [5] **Wang, H.; Tan, G.; Cen S.; Yao, Z.** (2005): Numerical determination of effective properties of voided piezoelectric materials using BNM, *Engineering Analysis with Boundary Elements*, vol. 29, pp. 636–646.
- [6] **Odegard, G.M.** (2004): Constitutive modeling of piezoelectric polymer composites. *Acta Materialia*, vol. 52, pp. 5315–5330.

Chapter 6 : Radial-Basis-Functions Computational Grains (RBFCGs) for modeling functionally-graded materials (FGM), magneto- electro-elastic (MEE) materials, and the switching phenomena in ferroelectric materials in 2D and 3D

6.1 Introduction

In this chapter, we present the Radial-Basis-Functions Computational Grains (RBFCGs) that is used to model functionally graded materials (FGM), general magneto-electro-elastic (MEE) materials (whose formulation can be simply reduced to piezoelectric or piezomagnetic materials), as well as the nonlinear behavior of ferroelectric materials.

In the early days of finite element research (1960-2000), the hybrid stress formulation of Pian [1], which uses interpolations for an equilibrated stress-field in the interior of a finite-element and inter-element compatible displacement fields only at the boundary of the element, was thought to be the only way of developing the stiffness matrices of arbitrary shaped finite elements in 2 and 3 dimensions (polygons with arbitrary number of sides in 2D, or polyhedra with arbitrary number of faces, each of which is an arbitrary polygon, in 3D); and that the primal formulations which use only element-displacement field were unable to achieve inter-element compatibility. Subsequent work, as for instance in the textbook by Atluri [2], has shown that there are many other, perhaps simpler and more numerically stable, methods (which avoid the troublesome LBB conditions [3]-[4]) for developing arbitrary shaped 2D and 3D Voronoi cell elements, by using methods such as multi-field collocation methods, Trefftz methods, Method of Fundamental Solutions, Radial-Basis-Function methods, Symmetric Galerkin Boundary Element Methods, etc. These ideas to develop stable, invariant, and simple Voronoi cells are pursued in

the present chapter, as well as in recent work by Bishay and Atluri [5]-[6], and by Dong and Atluri [7]-[10].

The Radial-Basis-Functions Computational Grains (RBFCGs) presented here are the extensions of VCFEM-RBF developed in [11] for 2D elasticity and VCFEM-RBF-W developed in [5] for 3D elasticity, by using Radial-Basis-Functions (RBF). The present RBFCGs are based on assuming internal as well as boundary fields separately for each of the primal variables (mechanical displacements, electric and magnetic potentials) and enforcing the compatibility between these fields. The compatibility between the interior and the boundary fields can be enforced using two methods. The first is done simply by collocating the interior and boundary primal fields at some boundary collocation-points, and the second is done by using the least squares method which is the limit of the collocation method as the number of collocation points increases to infinity. For both the 2D and the 3D RBFCGs, we assume the internal fields in terms of radial-basis-functions (RBF), while the boundary fields are assumed in terms of linear functions for the 2D case, and the linear Wachspress Barycentric functions for the 3D case. The present grains are much simpler and more efficient than Ghosh's hybrid-variational elements [12]. Also, the 3D RBFCGs avoid adding additional nodes inside the boundary-surfaces through the use of Wachspress functions as the boundary surface displacements and potentials. Ghosh's formulation, on the other hand, divides each surface of the 3D VCFEM into triangles, after adding a center node in each surface.

The rest of this chapter is organized as follows: section 6.2 discusses the computational methods used to model ferroelectric polycrystalline materials as compared to the proposed RBFCGs. Section 6.3 presents the formulation of the 2D and the 3D RBFCGs for modeling general magneto-electro-elastic materials, and the method used to better condition the system of

matrices to be solved. Section 6.4 is devoted for explaining the used switching criteria and kinetics used when modeling ferroelectric materials, while in section 6.5, the solution method used for the nonlinear behavior of ferroelectric materials is illustrated. Section 6.6 presents different 2D and 3D numerical examples for modeling functionally graded materials, magneto-electro-elastic materials as well as the ferroelectric and the ferroelastic switching phenomena. Summary and conclusions are given in section 6.7. Finally, references are listed in section 6.8.

6.2 Introduction to computational modeling of ferroelectric polycrystalline materials

Modeling ferroelectric polycrystalline material using the finite element method has been performed during the past 15 years, using different constitutive models (see [13]-[21] among others). Finite element modeling can deal with complex boundary value problems and explicitly takes the interaction between neighboring grains (inter-granular effects) into account. Randomly oriented crystal axes within elements, or rather grains, together with the corresponding material properties realize the locally anisotropic nature of the polycrystalline ferroelectric specimen. A macroscale finite element model for an electro-mechanically coupled material has been suggested by Ghandi and Hagwood ([22]-[23]). The phase/polarization state of materials is represented by internal variables in each element, which are updated in each simulation step based on a phenomenological model. Mesoscale finite element models has been developed by Hwang and McMeeking [13]-[14] and by Huo and Jiang [24]-[25]. The former modeled each crystallite as a cubic element with only one type of variant, with the tetragonal orientation for each element selected randomly. When an element satisfies a given switching criterion, switching occurs in the element and the tetragonal axis changes to a different permitted direction immediately. The latter modeled a crystallite as a body of mixture consisting of distinct types of constitutive variants, and characterized a grain by the values of volume fractions of variants. The

volume fractions are regarded as internal variables and updated at each simulation step by a switching criterion. Kim and Jiang [26] modeled the rate-dependent behavior of ferroelectric ceramics. They considered each crystal grain as a regular hexagon which was modeled by 12 triangular elements. Similar to [24]-[25], they regarded a finite element as a continuum body of mixture characterized by the volume fractions of the existing variants. Haug *et al.* [19] also modeled each grain using triangular or hexagonal elements. Kamlah *et al.* [16] modeled each crystal grain as a rectangular element.

Ferroelectric polycrystalline grains have random polyhedral shapes. Hence, to better model the polycrystalline microstructure, Voronoi cells which are based on Dirichlet tessellation of the considered body into irregular polygons in 2D, or irregular polyhedra in 3D, should be used. In this way, a grain in a representative ferroelectric microstructure is surrounded by a varying number of randomly shaped neighboring grains. This can also increase the computational efficiency since each grain is modeled by a single Voronoi cell and no further sub-discretization is required in one crystal grain structure. In consequence, Voronoi-based discretizations, together with randomly generated crystallographic axes for each grain, in general, represent the overall polycrystalline microstructure better. It is important to note that using regular elements (quadrilaterals in 2D or bricks in 3D) to model ferroelectric materials gives the same macroscopic response as that of the irregular Voronoi cell elements. However, the local distributions of stress, strain, electric field and electric displacement are different. This was shown in [27] for the 2D case, and is presented here for the 3D case as well. Local concentrations of stresses during switching, as a result of inter-granular effects, are thought to be the cause of micro-crack initiation along grain boundaries. For these reasons, a Direct Mesoscale

Numerical Simulation (DMNS) of ferroelectric materials, using 3D Radial-Basis-Functions Computational Grains (RBFCGs) is pursued in the present chapter.

Sze and Sheng [28] extended the Voronoi cell finite elements developed by Ghosh and his co-workers [12] based on Pian's hybrid stress finite element formulation [1] to model a ferroelectric polycrystalline. They used the Huo-Jiang single-crystal-multi-domain constitutive and switching model [24]-[26]. Using this same framework, Jayabal *et al.* [27] incorporated a micromechanical model based on well-established thermodynamic principles into the 2D Voronoi-cell finite elements. In their model, the switching process on the level of a single crystal of the overall ferroelectric polycrystalline is not continuous but faces a certain resistance or facilitation depending upon the changes in the combination of crystal variants.

The previously mentioned Voronoi cell formulations for modeling ferroelectric materials are based on a multi-field hybrid electromechanical variational principle (modified principle of complementary energy, or Hellinger–Reissner variational principle [29]) and have the same disadvantages of Pian's hybrid elements, namely: (1) Lagrangian multipliers are involved in the multi-field variational principle, and hence the derived elements suffer from LBB stability conditions [3]-[4], which are impossible to be satisfied a priori, (2) there are additional matrices (**H** and **G**) which need to be computed through numerical quadrature in each element, (3) **H** needs to be inverted in each element, thus raising the computational cost, and the rank of **G** (equals to the number of degrees of freedom in each element, less the number of rigid modes) in each element has to be assured a priori, (4) the use of "a priori equilibrated" stress field is difficult or even impossible for dynamical and geometrically nonlinear problems, (5) the assumed stress-field is often incomplete, and cannot account for the steep stress-gradients and

singularities often encountered in microstructures with inclusions or voids, in multifunctional materials, and (6) prohibitive computational costs.

Each 2D RBFCG is a random irregular polygon, while the 3D RBFCG has an arbitrary number of faces, and each face has an arbitrary number of edges. Considering only tetragonal unit cells composing the grains of a ferroelectric polycrystalline, each crystal grain (or RBFCG) in 2D analysis has a randomly generated crystallographic axes (axes 1 and 3) and 4 possible constitutive-variants (or domain types) parallel and perpendicular to the crystallographic axes. While in the 3D analysis, we have 6 possible variants parallel and perpendicular to the three randomly generated crystallographic axes (axes 1, 2 and 3). When dealing with 3D models, the amount of computation is increased, hence it is important to adopt efficient constitutive and switching models. The Huo-Jiang single-crystal-multi-domain constitutive and switching model, proposed in [24]-[25] and used in [26] and [28], requires solving the finite element system not only once in each simulation step. The system is solved n times in each simulation step, where n is the number of switching elements (the elements that have tendency to switch). The final configuration of volume fractions in each element at any time step is the one that yields the minimum Gibbs free energy of the whole body. This method is obviously inefficient and impractical especially for 3D simulations with large numbers of elements. For this reason, representative volume element (RVE) is used by Kim *et al.* [30] to incorporate this model in a 3D simulation. However, especially for ferroelectric polycrystalline samples, it is important to model the randomness of grain shapes in order to simulate the local interactions, and this cannot be done using RVE.

Any constitutive and switching model for ferroelectric materials can be incorporated with the developed RBFCGs to simulate the switching phenomenon. Here we use the switching model

in [27] which proved to be much more efficient than the previously mentioned models. It requires solving the FEM system of equations just once in each simulation step. In consequence, the proposed modeling approach includes the essential intergranular effects in ferroelectric polycrystals arising from individual grain geometries on the one hand, and the evolution of the underlying microstructures by switching effects on the other hand.

The readers are referred to sections 1.4 and 1.7 for an introduction to the governing equations, and the method used to generate the material matrices of each domain in each grain, or RBFCG, based on the orientation of the crystallographic axes of the grain. Section 1.6 also gives a description of ferroelectricity, which is important to be understood before reading the materials of this chapter.

6.3 Radial-Basis-Functions Computational Grains (RBFCGs) formulation for magneto-electro-elastic (MEE) materials

Discretizing the problem domain using the 2D or the 3D Voronoi cells (RBFCGs), so that each element has a unique shape, will allow us to study micromechanical problems of magneto-electro-elastic and ferroelectric materials, since the natural shapes and sizes of grains in the micro-scale are random and the Voronoi cells are the best approximation for this structure due to the randomness it provide to the element shapes and sizes. Each grain (or RBFCG) is surrounded by a varying number of randomly shaped neighboring grains, and possesses randomly generated crystallographic axes. The 2D grains, VC-RBF-1 and VC-RBF-2, based on radial-basis-functions presented in [11], and the 3D grain, VC-RBF-W, based on radial-basis-functions and Washspress functions presented in [5] for elasticity, and in [6] for modeling the switching phenomenon in ferroelectric materials, are extended here for the general case of magneto-electro-elastic materials.

6.3.1 Interior and boundary primal variables

Defining the mechanical displacement and the electric and magnetic potential fields using radial-basis-functions (RBF) in the interior of each grain, and as linear functions on the boundaries of each grain, we can write the internal fields as:

$$\begin{aligned} u_i(\mathbf{x}) &= \mathbf{R}^T(\mathbf{x})\mathbf{a}_{ui} + \mathbf{P}^T(\mathbf{x})\mathbf{b}_{ui}, \quad \text{in } \Omega^e \\ \varphi(\mathbf{x}) &= \mathbf{R}^T(\mathbf{x})\mathbf{a}_\varphi + \mathbf{P}^T(\mathbf{x})\mathbf{b}_\varphi, \quad \text{in } \Omega^e \\ \psi(\mathbf{x}) &= \mathbf{R}^T(\mathbf{x})\mathbf{a}_\psi + \mathbf{P}^T(\mathbf{x})\mathbf{b}_\psi, \quad \text{in } \Omega^e \end{aligned} \quad (6.1)$$

or,

$$u_i(\mathbf{x}) = \mathbf{M}(\mathbf{x})\mathbf{a}_{ui}, \quad \varphi(\mathbf{x}) = \mathbf{M}(\mathbf{x})\mathbf{a}_\varphi, \quad \psi(\mathbf{x}) = \mathbf{M}(\mathbf{x})\mathbf{a}_\psi \quad \text{in } \Omega^e \quad (6.2)$$

where $\mathbf{M}(\mathbf{x}) = \begin{bmatrix} \mathbf{R}^T(\mathbf{x}) & \mathbf{P}^T(\mathbf{x}) \end{bmatrix}$, $\mathbf{a}_{ui} = \begin{Bmatrix} \mathbf{a}_{ui} \\ \mathbf{b}_{ui} \end{Bmatrix}$, $\mathbf{a}_\varphi = \begin{Bmatrix} \mathbf{a}_\varphi \\ \mathbf{b}_\varphi \end{Bmatrix}$, $\mathbf{a}_\psi = \begin{Bmatrix} \mathbf{a}_\psi \\ \mathbf{b}_\psi \end{Bmatrix}$ and $i = 1, 3$ (for 2D

grains) or $i = 1-3$ (for 3D grains). $\mathbf{R}^T(\mathbf{x}) = [R^1(\mathbf{x}) \ R^2(\mathbf{x}) \dots R^L(\mathbf{x})]$ is a set of radial-basis-functions centered at L points $\mathbf{x}^{r1}, \mathbf{x}^{r2}, \dots, \mathbf{x}^{rl}, \dots, \mathbf{x}^{rL}$ on $\partial\Omega^e$; $\mathbf{P}^T(\mathbf{x}) = [P^1(\mathbf{x}) \ P^2(\mathbf{x}) \dots P^q(\mathbf{x})]$ is a set of q monomial functions which are complete to a certain order.

The radial-basis-functions to be used here have the form:

$$R^l(\mathbf{x}) = \begin{cases} \left(1 - \frac{d^l(\mathbf{x})}{r^l}\right)^3 \left(1 + 3\frac{d^l(\mathbf{x})}{r^l}\right) & d^l(\mathbf{x}) < r^l \\ 0 & d^l(\mathbf{x}) \geq r^l \end{cases} \quad (6.3)$$

where $d^l(\mathbf{x}) = |\mathbf{x} - \mathbf{x}^{rl}|$ is the Euclidean distance from point \mathbf{x} to point \mathbf{x}^{rl} , r^l is the support size of $R^l(\mathbf{x})$.

In this study, a first order complete polynomial basis is used:

$$\begin{aligned}\mathbf{P}^T(\mathbf{x}) &= [1 \quad x_1 \quad x_3] \quad \text{for 2D analysis} \\ \mathbf{P}^T(\mathbf{x}) &= [1 \quad x_1 \quad x_2 \quad x_3] \quad \text{for 3D analysis}\end{aligned}\tag{6.4}$$

The linear boundary fields along any boundary edge in a 2D grain or on any boundary surface in a 3D grain can be generally written in terms of the nodal values of mechanical displacements \mathbf{q}_{ui} , electric potential \mathbf{q}_φ , and magnetic potential \mathbf{q}_ψ as:

$$\tilde{u}_i(\mathbf{x}) = \tilde{\mathbf{N}}\mathbf{q}_{ui}, \quad \tilde{\varphi}(\mathbf{x}) = \tilde{\mathbf{N}}\mathbf{q}_\varphi, \quad \tilde{\psi}(\mathbf{x}) = \tilde{\mathbf{N}}\mathbf{q}_\psi \quad \text{on } \partial\Omega^e \tag{6.5}$$

In the 2D version of the RBFCG (see Figure 6.1), we use simple linear shape functions:

$$\tilde{\mathbf{N}} = [\tilde{N}_1 \quad \tilde{N}_2 \quad \dots \quad \tilde{N}_m] \tag{6.6}$$

where m is the number of nodes in the grain. If \mathbf{x} is on the edge connecting node a to node b , then: $\tilde{N}_a = \frac{1-\xi}{2}$, $\tilde{N}_b = \frac{1+\xi}{2}$, $\tilde{N}_{otherwise} = 0$, where $-1 \leq \xi \leq 1$ is the normalized running length from one corner to the other on each side of the boundary.

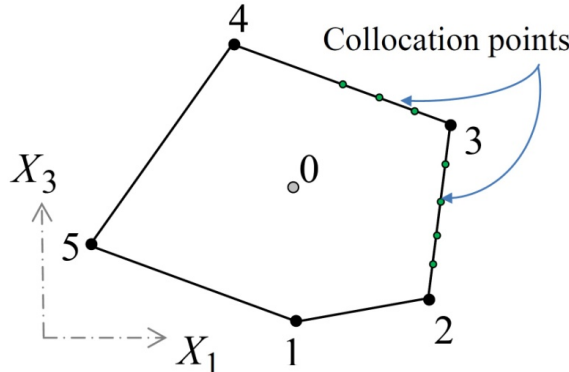


Figure 6.1: 2D irregular polygon (Voronoi cell) with 5 nodes ($m = 5$)

For the 3D version of RBFCG, the grain is an arbitrary polyhedron (3D Voronoi Cell) in the 3D space, as shown in Figure 6.2, with m -nodes $\mathbf{x}^1, \mathbf{x}^2, \dots, \mathbf{x}^m$, and corresponding nodal displacements $u_i^1, u_i^2, \dots, u_i^m$, nodal electric potential $\varphi^1, \varphi^2, \dots, \varphi^m$ and/or nodal magnetic

potential $\psi^1, \psi^2, \dots, \psi^m$. A smooth linear primal field assumption on each surface with n vertices can be used:

$$\tilde{\mathbf{N}} = [\lambda_1(\mathbf{x}) \quad \lambda_2(\mathbf{x}) \quad \dots \quad \lambda_m(\mathbf{x})] \quad (6.7)$$

If \mathbf{x} is on the boundary surface bounded by n nodes, then $\lambda_j(\mathbf{x}) \neq 0$, $\lambda_{otherwise}(\mathbf{x}) = 0$, where $j = \text{node numbers bounding this surface}$.

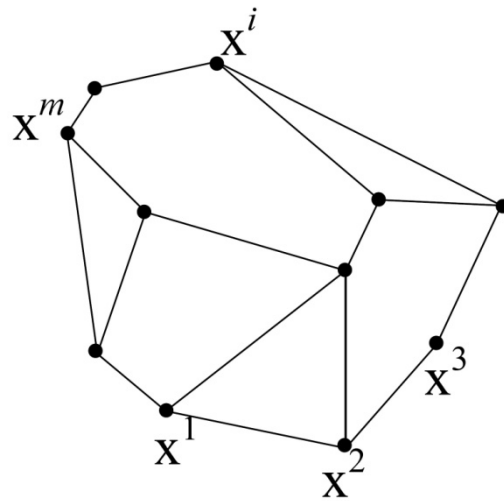


Figure 6.2: Polyhedron (3D Voronoi cell) element with arbitrary number of polygonal faces

Dealing with polygonal surfaces, Barycentric coordinates should be used to describe the mechanical displacement, and the electric and magnetic potential fields. The Barycentric coordinates, denoted as λ_i ($i = 1, 2, \dots, n$) where n is the number of vertices in the convex polygon, Ω_p , in general should satisfy two properties:

1. Non-negative: $\lambda_i \geq 0$ on Ω_p .
2. Linear completeness: For any linear function $f(\mathbf{x}): \Omega_p \rightarrow \mathbb{R}$, $f(\mathbf{x}) = \sum_{i=1}^n f(\mathbf{x}^i) \lambda_i$.

Any set of Barycentric coordinates under this definition also satisfies:

3. Partition of unity: $\sum_{i=1}^n \lambda_i \equiv 1$.

4. Linear precision: $\sum_{i=1}^n \mathbf{x}^i \lambda_i(\mathbf{x}) = \mathbf{x}$

5. Dirac delta: $\lambda_i(\mathbf{x}^j) = \delta_{ij}$.

In this work, we use the Wachspress coordinates [31], defined as follows: Let $\mathbf{x} \in \Omega_p$, where Ω_p here is the domain of a polygon as shown in Figure 6.3, and define the areas: B_i as the area of the triangle having $\mathbf{x}^{i-1}, \mathbf{x}^i$ and \mathbf{x}^{i+1} as its three vertices, and $A_i(\mathbf{x})$ as the area of the triangle having \mathbf{x}, \mathbf{x}^i and \mathbf{x}^{i+1} as its three vertices. This is illustrated in Figure 6.3.

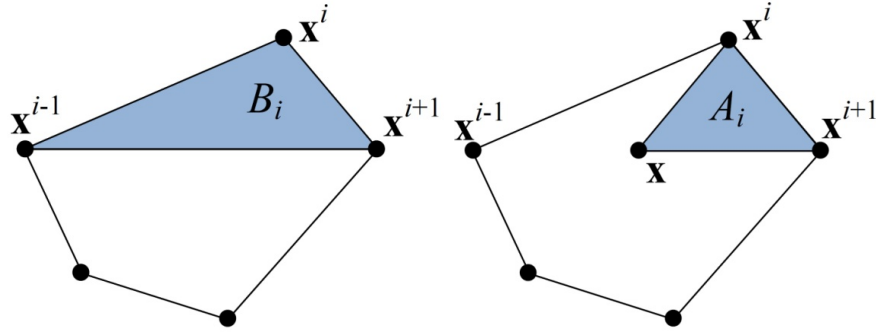


Figure 6.3: Definition of triangles B_i and $A_i(\mathbf{x})$

Define the Wachspress weight function as:

$$w_i(\mathbf{x}) = B_i \prod_{j \neq i, i-1} A_j(\mathbf{x}) \quad (6.8)$$

Then, the Wachspress coordinates are given by the rational functions:

$$\lambda_i(\mathbf{x}) = \frac{w_i(\mathbf{x})}{\sum_{j=1}^n w_j(\mathbf{x})} \quad (6.9)$$

Similar to the well-known triangular coordinates used in 2D triangular elements, where the shape functions associated with the three vertices are indeed the triangular coordinates themselves, the shape functions associated with the vertices of these polygonal surface mechanical displacements, electric and magnetic potential fields are the Barycentric coordinates

themselves. The triangular coordinates are actually a special case of the Barycentric coordinates when the polygon is just a triangle.

The compatibility between the interior fields in eq. (6.2) and the boundary fields in eq. (6.5) in each grain can be enforced in many ways, including:

- (a) Boundary collocation between (u_i, φ, ψ) and $(\tilde{u}_i, \tilde{\varphi}, \tilde{\psi})$ at selected points on $\partial\Omega^e$ or
- (b) The method of minimizing boundary-least-squares error between (u_i, φ, ψ) and $(\tilde{u}_i, \tilde{\varphi}, \tilde{\psi})$ on $\partial\Omega^e$.

Both methods are presented in the following:

Using the Collocation method:

The coefficients \mathbf{a}_{ui} , \mathbf{a}_φ and \mathbf{a}_ψ are obtained by enforcing the compatibility condition of the interior and the boundary fields at collocation points $\mathbf{x}^{r1}, \mathbf{x}^{r2}, \mathbf{x}^{rl}, \dots, \mathbf{x}^{rL}$ (see Figure 6.1 for the 2D case and Figure 6.4 (left) for the 3D case). This leads to:

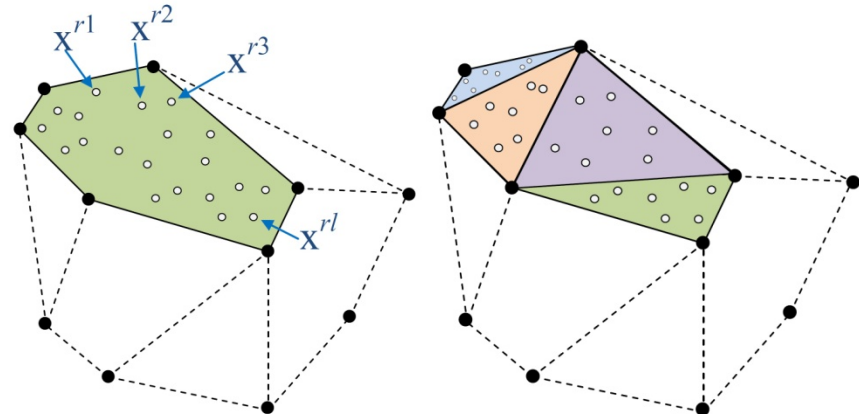


Figure 6.4: (left) collocation points on one boundary surface of the 3D RBFCG. (right) triangulating each boundary surface and taking the Gaussian points in each triangle to be the RBF centers and collocation points

$$\begin{bmatrix} \mathbf{R}_0 & \mathbf{P}_0 \\ \mathbf{P}_0^T & \mathbf{0} \end{bmatrix} \begin{Bmatrix} \mathbf{a}_{ui} \\ \mathbf{b}_{ui} \end{Bmatrix} = \begin{Bmatrix} \tilde{\mathbf{u}}_i^r \\ \mathbf{0} \end{Bmatrix}, \quad \begin{bmatrix} \mathbf{R}_0 & \mathbf{P}_0 \\ \mathbf{P}_0^T & \mathbf{0} \end{bmatrix} \begin{Bmatrix} \mathbf{a}_\varphi \\ \mathbf{b}_\varphi \end{Bmatrix} = \begin{Bmatrix} \tilde{\varphi}^r \\ \mathbf{0} \end{Bmatrix}, \quad \begin{bmatrix} \mathbf{R}_0 & \mathbf{P}_0 \\ \mathbf{P}_0^T & \mathbf{0} \end{bmatrix} \begin{Bmatrix} \mathbf{a}_\psi \\ \mathbf{b}_\psi \end{Bmatrix} = \begin{Bmatrix} \tilde{\psi}^r \\ \mathbf{0} \end{Bmatrix} \quad (6.10)$$

$$\mathbf{R}_0 = \begin{bmatrix} R^1(\mathbf{x}^{r1}) & R^2(\mathbf{x}^{r1}) & \dots & R^L(\mathbf{x}^{r1}) \\ R^1(\mathbf{x}^{r2}) & R^2(\mathbf{x}^{r2}) & \dots & R^L(\mathbf{x}^{r2}) \\ \vdots & \vdots & \vdots & \vdots \\ R^1(\mathbf{x}^{rL}) & R^2(\mathbf{x}^{rL}) & \dots & R^L(\mathbf{x}^{rL}) \end{bmatrix} \quad (6.11)$$

$$\mathbf{P}_0 = \begin{bmatrix} P^1(\mathbf{x}^{r1}) & P^2(\mathbf{x}^{r1}) & \dots & P^q(\mathbf{x}^{r1}) \\ P^1(\mathbf{x}^{r2}) & P^2(\mathbf{x}^{r2}) & \dots & P^q(\mathbf{x}^{r2}) \\ \vdots & \vdots & \vdots & \vdots \\ P^1(\mathbf{x}^{rL}) & P^2(\mathbf{x}^{rL}) & \dots & P^q(\mathbf{x}^{rL}) \end{bmatrix} \quad (6.12)$$

$$\begin{aligned} \left(\tilde{\mathbf{u}}_i^r \right)^T &= \left[\tilde{u}_i^{r1} \quad \tilde{u}_i^{r2} \quad \dots \quad \tilde{u}_i^{rL} \right] = \left[\sum_{k=1}^m \tilde{N}^k(\mathbf{x}^{r1}) u_i^k \quad \sum_{k=1}^m \tilde{N}^k(\mathbf{x}^{r2}) u_i^k \quad \dots \quad \sum_{k=1}^m \tilde{N}^k(\mathbf{x}^{rL}) u_i^k \right] \\ \left(\tilde{\Phi}^r \right)^T &= \left[\tilde{\phi}^{r1} \quad \tilde{\phi}^{r2} \quad \dots \quad \tilde{\phi}^{rL} \right] = \left[\sum_{k=1}^m \tilde{N}^k(\mathbf{x}^{r1}) \phi^k \quad \sum_{k=1}^m \tilde{N}^k(\mathbf{x}^{r2}) \phi^k \quad \dots \quad \sum_{k=1}^m \tilde{N}^k(\mathbf{x}^{rL}) \phi^k \right] \\ \left(\tilde{\Psi}^r \right)^T &= \left[\tilde{\psi}^{r1} \quad \tilde{\psi}^{r2} \quad \dots \quad \tilde{\psi}^{rL} \right] = \left[\sum_{k=1}^m \tilde{N}^k(\mathbf{x}^{r1}) \psi^k \quad \sum_{k=1}^m \tilde{N}^k(\mathbf{x}^{r2}) \psi^k \quad \dots \quad \sum_{k=1}^m \tilde{N}^k(\mathbf{x}^{rL}) \psi^k \right] \end{aligned} \quad (6.13)$$

Solving eq. (6.10) gives:

$$\begin{aligned} \mathbf{a}_{\mathbf{u}i} &= \mathbf{G_r} \tilde{\mathbf{u}}_i^r \quad \text{and} \quad \mathbf{b}_{\mathbf{u}i} = \mathbf{G_p} \tilde{\mathbf{u}}_i^r \\ \mathbf{a}_{\Phi} &= \mathbf{G_r} \tilde{\Phi}^r \quad \text{and} \quad \mathbf{b}_{\Phi} = \mathbf{G_p} \tilde{\Phi}^r \\ \mathbf{a}_{\Psi} &= \mathbf{G_r} \tilde{\Psi}^r \quad \text{and} \quad \mathbf{b}_{\Psi} = \mathbf{G_p} \tilde{\Psi}^r \end{aligned} \quad (6.14)$$

So the interior displacement, electric and magnetic potential fields have the form:

$$\begin{aligned} u_i(\mathbf{x}) &= \left[\mathbf{R}^T(\mathbf{x}) \mathbf{G_r} + \mathbf{P}^T(\mathbf{x}) \mathbf{G_p} \right] \tilde{\mathbf{u}}_i^r = \sum_{k=1}^m N_u^k(\mathbf{x}) u_i^k \quad \text{in } \Omega^e \\ \varphi(\mathbf{x}) &= \left[\mathbf{R}^T(\mathbf{x}) \mathbf{G_r} + \mathbf{P}^T(\mathbf{x}) \mathbf{G_p} \right] \tilde{\Phi}^r = \sum_{k=1}^m N_\varphi^k(\mathbf{x}) \phi^k \quad \text{in } \Omega^e \\ \psi(\mathbf{x}) &= \left[\mathbf{R}^T(\mathbf{x}) \mathbf{G_r} + \mathbf{P}^T(\mathbf{x}) \mathbf{G_p} \right] \tilde{\Psi}^r = \sum_{k=1}^m N_\psi^k(\mathbf{x}) \psi^k \quad \text{in } \Omega^e \end{aligned} \quad (6.15)$$

In terms of nodal displacements, electric and magnetic potential vectors, \mathbf{q}_u , \mathbf{q}_ϕ and \mathbf{q}_ψ , the interior displacement, electric and magnetic potential fields are expressed as:

$$\mathbf{u}(\mathbf{x}) = \mathbf{N}_u(\mathbf{x})\mathbf{q}_u, \quad \phi(\mathbf{x}) = \mathbf{N}_\phi(\mathbf{x})\mathbf{q}_\phi, \quad \psi(\mathbf{x}) = \mathbf{N}_\psi(\mathbf{x})\mathbf{q}_\psi \quad \text{in } \Omega^e \quad (6.16)$$

where $\mathbf{u} = \{u_1 \ u_3\}^T$ for the 2D case, and $\mathbf{u} = \{u_1 \ u_2 \ u_3\}^T$ for the 3D case.

Dong and Atluri [11] proved that for the RBFCG to pass the patch test with an error reduced to a satisfactory level, when the collocation method is used, the interior and boundary fields should be collocated at the quadrature points. Hence, the compatibility between the internal and the boundary fields is satisfied at least in a finite volume sense. For the 2D RBFCG, the collocation points are the Gaussian quadrature points along each boundary side (see Figure 6.1), and for the 3D RBFCG, the collocation points are the 2D triangular quadrature points on the triangles generated by triangulating each polygonal surface (see Figure 6.4 (right)). In this work, the collocation points used to enforce the compatibility between the interior and the boundary fields are six 1D Gaussian quadrature points on each side of the 2D RBFCG, and seven 2D triangular quadrature points, on each of the triangles generated by triangulating each polygonal surface for the 3D RBFCG.

In principle, as the number of quadrature points increases, error in patch test is decreased, provided that a sufficient quadrature order is used in the integration of the stiffness matrix. However, since the integrands in the stiffness matrix are not polynomials, the numerical quadrature is always approximate whatever the order of the quadrature. For the 2D RBFCG, each polygon is divided into triangles and seven triangular quadrature points in each triangle are used in the integration of the element stiffness matrix. For the 3D RBFCG, three-dimensional Delaunay triangulation is used to divide each grain into a number of tetrahedrons in order to use

the 3D tetrahedron numerical quadrature in calculating the stiffness matrix of each grain. In this work, we use eleven quadrature points in each tetrahedron for integrating the stiffness matrix in order to obtain sufficiently accurate results.

It should be mentioned here that the matrix that are being inverted in eq. (6.10), in order to obtain $\mathbf{a}_{\mathbf{u}_i}, \mathbf{b}_{\mathbf{u}_i}, \mathbf{a}_\phi, \mathbf{b}_\phi, \mathbf{a}_\psi$ and \mathbf{b}_ψ , has dimensions $n \times n$, where n is the number of RBF-basis functions plus the number of the P-basis functions. Here, the number of RBF-basis functions is taken to be exactly the number of collocation points, and the RBF centers are taken to be exactly the collocation points in the whole grain. Thus, $n = \text{number of collocation points} + \text{number of P-basis}$, which is $n = 6 \times \text{number of sides of the polygon} + 3$ for the 2D case, and $n = 7 \times \text{number of triangles on all boundaries} + 4$ for the 3D case.

Using the Least squares method:

When the number of collocation points is increased to a limit of infinity, it is equivalent to enforcing the compatibility between $\mathbf{u}, \varphi, \psi$ and $\tilde{\mathbf{u}}, \tilde{\varphi}, \tilde{\psi}$ using the least squares method, namely minimizing the following functional:

$$\Pi_1(u_i, \tilde{u}_i, \varphi, \tilde{\varphi}, \psi, \tilde{\psi}) = \int_{\partial\Omega^e} \{(u_i - \tilde{u}_i)(u_i - \tilde{u}_i) + (\varphi - \tilde{\varphi})(\varphi - \tilde{\varphi}) + (\psi - \tilde{\psi})(\psi - \tilde{\psi})\} dS \quad (6.17)$$

Using eqs. (6.2) and (6.5), the functional Π_1 can be written as:

$$\begin{aligned} \Pi_1(\mathbf{a}_{\mathbf{u}_i}, \mathbf{q}_{\mathbf{u}_i}, \mathbf{a}_\phi, \mathbf{q}_\phi, \mathbf{a}_\psi, \mathbf{q}_\psi) &= \int_{\partial\Omega^e} (\mathbf{a}_{\mathbf{u}_i}^T \mathbf{M}^T \mathbf{M} \mathbf{a}_{\mathbf{u}_i} - 2\mathbf{a}_{\mathbf{u}_i}^T \mathbf{M}^T \tilde{\mathbf{N}} \mathbf{q}_{\mathbf{u}_i} + \mathbf{q}_{\mathbf{u}_i}^T \tilde{\mathbf{N}}^T \tilde{\mathbf{N}} \mathbf{q}_{\mathbf{u}_i}) dS \\ &\quad + \int_{\partial\Omega^e} (\mathbf{a}_\phi^T \mathbf{M}^T \mathbf{M} \mathbf{a}_\phi - 2\mathbf{a}_\phi^T \mathbf{M}^T \tilde{\mathbf{N}} \mathbf{q}_\phi + \mathbf{q}_\phi^T \tilde{\mathbf{N}}^T \tilde{\mathbf{N}} \mathbf{q}_\phi) dS \\ &\quad + \int_{\partial\Omega^e} (\mathbf{a}_\psi^T \mathbf{M}^T \mathbf{M} \mathbf{a}_\psi - 2\mathbf{a}_\psi^T \mathbf{M}^T \tilde{\mathbf{N}} \mathbf{q}_\psi + \mathbf{q}_\psi^T \tilde{\mathbf{N}}^T \tilde{\mathbf{N}} \mathbf{q}_\psi) dS \quad (6.18) \\ &= (\mathbf{a}_\mathbf{u}^T \mathbf{U} \mathbf{a}_\mathbf{u} - 2\mathbf{a}_\mathbf{u}^T \mathbf{V} \mathbf{q}_\mathbf{u} + \mathbf{q}_\mathbf{u}^T \mathbf{W} \mathbf{q}_\mathbf{u}) + (\mathbf{a}_\phi^T \mathbf{U} \mathbf{a}_\phi - 2\mathbf{a}_\phi^T \mathbf{V} \mathbf{q}_\phi + \mathbf{q}_\phi^T \mathbf{W} \mathbf{q}_\phi) \\ &\quad + (\mathbf{a}_\psi^T \mathbf{U} \mathbf{a}_\psi - 2\mathbf{a}_\psi^T \mathbf{V} \mathbf{q}_\psi + \mathbf{q}_\psi^T \mathbf{W} \mathbf{q}_\psi) \end{aligned}$$

To minimize Π_1 for a fixed $\mathbf{q}_{\mathbf{u}i}$, \mathbf{q}_ϕ and \mathbf{q}_ψ we have,

$$\begin{aligned}\delta\Pi_1(\delta\mathbf{a}_{\mathbf{u}i}, \mathbf{q}_{\mathbf{u}i}, \delta\mathbf{a}_\phi, \mathbf{q}_\phi, \delta\mathbf{a}_\psi, \mathbf{q}_\psi) &= \left(2\delta\mathbf{a}_{\mathbf{u}i}^T \mathbf{U} \mathbf{a}_{\mathbf{u}i} - 2\delta\mathbf{a}_{\mathbf{u}i}^T \mathbf{V} \mathbf{q}_{\mathbf{u}i}\right) \\ &\quad + \left(2\delta\mathbf{a}_\phi^T \mathbf{U} \mathbf{a}_\phi - 2\delta\mathbf{a}_\phi^T \mathbf{V} \mathbf{q}_\phi\right) + \left(2\delta\mathbf{a}_\psi^T \mathbf{U} \mathbf{a}_\psi - 2\delta\mathbf{a}_\psi^T \mathbf{V} \mathbf{q}_\psi\right) = 0\end{aligned}\tag{6.19}$$

This should be true for any $\delta\mathbf{a}_{\mathbf{u}i}$, $\delta\mathbf{a}_\phi$ and $\delta\mathbf{a}_\psi$ hence;

$$\begin{aligned}\mathbf{U} \mathbf{a}_{\mathbf{u}i} &= \mathbf{V} \mathbf{q}_{\mathbf{u}i}, \quad \text{or} \quad \mathbf{a}_{\mathbf{u}i} = \mathbf{L} \mathbf{q}_{\mathbf{u}i} \\ \mathbf{U} \mathbf{a}_\phi &= \mathbf{V} \mathbf{q}_\phi, \quad \text{or} \quad \mathbf{a}_\phi = \mathbf{L} \mathbf{q}_\phi \\ \mathbf{U} \mathbf{a}_\psi &= \mathbf{V} \mathbf{q}_\psi, \quad \text{or} \quad \mathbf{a}_\psi = \mathbf{L} \mathbf{q}_\psi\end{aligned}\tag{6.20}$$

Substituting this into eq. (6.2) gives:

$$\begin{aligned}u_i(\mathbf{x}) &= \mathbf{M}(\mathbf{x}) \mathbf{a}_{\mathbf{u}i} = \mathbf{M}(\mathbf{x}) \mathbf{L} \mathbf{q}_{\mathbf{u}i} \quad \text{or} \quad \mathbf{u}(\mathbf{x}) = \mathbf{N}_\mathbf{u}(\mathbf{x}) \mathbf{q}_\mathbf{u} \quad \text{in } \Omega^e \\ \varphi(\mathbf{x}) &= \mathbf{M}(\mathbf{x}) \mathbf{a}_\phi = \mathbf{M}(\mathbf{x}) \mathbf{L} \mathbf{q}_\phi = \mathbf{N}_\phi(\mathbf{x}) \mathbf{q}_\phi \quad \text{in } \Omega^e \\ \psi(\mathbf{x}) &= \mathbf{M}(\mathbf{x}) \mathbf{a}_\psi = \mathbf{M}(\mathbf{x}) \mathbf{L} \mathbf{q}_\psi = \mathbf{N}_\psi(\mathbf{x}) \mathbf{q}_\psi \quad \text{in } \Omega^e\end{aligned}\tag{6.21}$$

Only the square matrix $\mathbf{U} = \int_{\partial\Omega^e} \mathbf{M}^T \mathbf{M} dS$ is being inverted here. The dimensions of this

matrix is also $n \times n$ where n is the number of RBF-basis functions plus the number of the P-basis functions. If we take the number of RBF-basis to be exactly the same as that of the integration points in the whole grain as we did with the collocation method, the number of unknowns

$\mathbf{a}_{\mathbf{u}i} = \begin{Bmatrix} \mathbf{a}_{\mathbf{u}i} \\ \mathbf{b}_{\mathbf{u}i} \end{Bmatrix}$, $\mathbf{a}_\phi = \begin{Bmatrix} \mathbf{a}_\phi \\ \mathbf{b}_\phi \end{Bmatrix}$ or $\mathbf{a}_\psi = \begin{Bmatrix} \mathbf{a}_\psi \\ \mathbf{b}_\psi \end{Bmatrix}$ will be larger than that of the equations (in a collocation

sense) by the number of the P-basis functions (3 for 2D grain and 4 for 3D grain). So the number of integration points in the whole grain used in evaluating \mathbf{U} and \mathbf{V} matrices should be larger than that of the RBF-basis functions.

For the 3D RBFCG, we select the RBF centers to be at the three Gaussian points in each triangle of the triangulated boundary surfaces, while seven Gaussian points per triangle are used

in integration. Hence the number of RBF-basis functions is $3 \times$ number of triangles on all boundaries. This number of RBF-basis functions proved to be enough to give sufficient accuracy unlike the case of the collocation method where seven collocation points per triangle are required to give an acceptable accuracy. Thus, $n = 3 \times$ number of triangles on all boundaries + 4. This number n is much less than that used for the collocation method, and hence the least square method yields a much cheaper grain while also leading to better accuracy as was illustrated in [5].

6.3.2 Finite element equation

Having the interior fields in terms of the nodal values of mechanical displacements, electric and magnetic potentials (as in eq. (6.16) for the collocation method, and eq. (6.21) for the least squares method), the corresponding interior strain and electric field intensity are:

$$\begin{aligned}\boldsymbol{\varepsilon} &= \partial_{\mathbf{u}} \mathbf{u} = \partial_{\mathbf{u}} (\mathbf{N}_{\mathbf{u}} \mathbf{q}_{\mathbf{u}}) = \mathbf{B}_{\mathbf{u}}(\mathbf{x}) \mathbf{q}_{\mathbf{u}} \quad \text{in } \Omega^e \\ -\mathbf{E} &= \partial_{\mathbf{e}} \varphi = \partial_{\mathbf{e}} (\mathbf{N}_{\varphi} \mathbf{q}_{\varphi}) = \mathbf{B}_{\varphi}(\mathbf{x}) \mathbf{q}_{\varphi} \quad \text{in } \Omega^e \\ -\mathbf{H} &= \partial_{\mathbf{e}} \psi = \partial_{\mathbf{e}} (\mathbf{N}_{\psi} \mathbf{q}_{\psi}) = \mathbf{B}_{\psi}(\mathbf{x}) \mathbf{q}_{\psi} \quad \text{in } \Omega^e\end{aligned}\tag{6.22}$$

Now we can use $\Pi(\mathbf{u}, \varphi, \psi)$, a functional used to develop irreducible or primal finite elements [29], to obtain the finite element equation for any of the two mentioned methods:

$$\begin{aligned}\Pi(\mathbf{u}, \varphi, \psi) &= \int_{\Omega} \left[\frac{1}{2} \begin{Bmatrix} \partial_{\mathbf{u}} \mathbf{u} \\ \partial_{\mathbf{e}} \varphi \\ \partial_{\mathbf{e}} \psi \end{Bmatrix}^T \begin{bmatrix} \mathbf{C} & \mathbf{e}^T & \mathbf{d}^T \\ \mathbf{e} & -\mathbf{h} & -\mathbf{n}^T \\ \mathbf{d} & -\mathbf{n} & -\mathbf{m} \end{bmatrix} \begin{Bmatrix} \partial_{\mathbf{u}} \mathbf{u} \\ \partial_{\mathbf{e}} \varphi \\ \partial_{\mathbf{e}} \psi \end{Bmatrix} - \bar{\mathbf{b}}^T \mathbf{u} + \bar{\rho}_f \varphi \right] d\Omega \\ &\quad - \int_{S_t} \bar{\mathbf{t}}^T \mathbf{u} ds - \int_{S_Q} \bar{\mathbf{Q}} \varphi ds - \int_{S_B} \bar{\mathbf{Q}}_M \psi ds\end{aligned}\tag{6.23}$$

Substituting the finite element interpolation functions, eqs. (6.16) and (6.22), we get after considering that the body is composed of N grains ($\Omega = \sum_{k=1}^N \Omega^k$):

$$\Pi = \sum_{k=1}^N \left(\frac{1}{2} \begin{Bmatrix} \mathbf{q}_\mathbf{u}^k \\ \mathbf{q}_\phi^k \\ \mathbf{q}_\psi^k \end{Bmatrix} \right)^T \begin{bmatrix} \int_{\Omega^k} \mathbf{B}_\mathbf{u}^T \mathbf{C}^k \mathbf{B}_\mathbf{u} d\Omega & \int_{\Omega^k} \mathbf{B}_\mathbf{u}^T \mathbf{e}^{kT} \mathbf{B}_\phi d\Omega & \int_{\Omega^k} \mathbf{B}_\mathbf{u}^T \mathbf{d}^{kT} \mathbf{B}_\psi d\Omega \\ \int_{\Omega^k} \mathbf{B}_\phi^T \mathbf{e}^k \mathbf{B}_\mathbf{u} d\Omega & - \int_{\Omega^k} \mathbf{B}_\phi^T \mathbf{h}^k \mathbf{B}_\phi d\Omega & - \int_{\Omega^k} \mathbf{B}_\phi^T \mathbf{n}^{kT} \mathbf{B}_\psi d\Omega \\ \int_{\Omega^k} \mathbf{B}_\psi^T \mathbf{d}^k \mathbf{B}_\mathbf{u} d\Omega & - \int_{\Omega^k} \mathbf{B}_\psi^T \mathbf{n}^k \mathbf{B}_\phi d\Omega & - \int_{\Omega^k} \mathbf{B}_\psi^T \mathbf{m}^k \mathbf{B}_\psi d\Omega \end{bmatrix} \begin{Bmatrix} \mathbf{q}_\mathbf{u}^k \\ \mathbf{q}_\phi^k \\ \mathbf{q}_\psi^k \end{Bmatrix} \right. \\ \left. - \left(\int_{\Omega^k} \bar{\mathbf{b}}^{kT} \mathbf{N}_\mathbf{u} d\Omega \right) \mathbf{q}_\mathbf{u}^k + \left(\int_{\Omega^k} \bar{\rho}_f^k \mathbf{N}_\phi d\Omega \right) \mathbf{q}_\phi^k \right. \\ \left. - \left(\int_{S_t^k} \bar{\mathbf{t}}^{kT} \mathbf{N}_\mathbf{u} ds \right) \mathbf{q}_\mathbf{u}^k - \left(\int_{S_Q^k} \bar{\mathcal{Q}}^k \mathbf{N}_\phi ds \right) \mathbf{q}_\phi^k - \left(\int_{S_B^k} \bar{\mathcal{Q}}_M^k \mathbf{N}_\psi ds \right) \mathbf{q}_\psi^k \right) \quad (6.24)$$

Equating the first variation of this functional with respect to $\{\mathbf{q}_\mathbf{u}^k \quad \mathbf{q}_\phi^k \quad \mathbf{q}_\psi^k\}^T$ to zero,

leads to the global finite element equation that is solved for the global nodal primal variables

$$\mathbf{q} = \{\mathbf{q}_\mathbf{u} \quad \mathbf{q}_\phi \quad \mathbf{q}_\psi\}^T = \sum_{k=1}^N \{\mathbf{q}_\mathbf{u}^k \quad \mathbf{q}_\phi^k \quad \mathbf{q}_\psi^k\}^T : \quad (6.25)$$

with the stiffness matrix and load vector having, respectively, the forms:

$$\mathbf{K} = \sum_{k=1}^N \begin{bmatrix} \int_{\Omega^k} \mathbf{B}_\mathbf{u}^T \mathbf{C}^k \mathbf{B}_\mathbf{u} d\Omega & \int_{\Omega^k} \mathbf{B}_\mathbf{u}^T \mathbf{e}^{kT} \mathbf{B}_\phi d\Omega & \int_{\Omega^k} \mathbf{B}_\mathbf{u}^T \mathbf{d}^{kT} \mathbf{B}_\psi d\Omega \\ \int_{\Omega^k} \mathbf{B}_\phi^T \mathbf{e}^k \mathbf{B}_\mathbf{u} d\Omega & - \int_{\Omega^k} \mathbf{B}_\phi^T \mathbf{h}^k \mathbf{B}_\phi d\Omega & - \int_{\Omega^k} \mathbf{B}_\phi^T \mathbf{n}^{kT} \mathbf{B}_\psi d\Omega \\ \int_{\Omega^k} \mathbf{B}_\psi^T \mathbf{d}^k \mathbf{B}_\mathbf{u} d\Omega & - \int_{\Omega^k} \mathbf{B}_\psi^T \mathbf{n}^k \mathbf{B}_\phi d\Omega & - \int_{\Omega^k} \mathbf{B}_\psi^T \mathbf{m}^k \mathbf{B}_\psi d\Omega \end{bmatrix} \quad (6.26)$$

$$\mathbf{F} = \begin{pmatrix} \mathbf{F}_{\mathbf{u}} \\ \mathbf{F}_{\varphi} \\ \mathbf{F}_{\psi} \end{pmatrix} = \sum_{k=1}^N \begin{pmatrix} \int_{\Omega^k} \bar{\mathbf{b}}^{kT} \mathbf{N}_{\mathbf{u}} d\Omega + \int_{S_t^k} \bar{\mathbf{t}}^{kT} \mathbf{N}_{\mathbf{u}} ds \\ - \int_{\Omega^k} \bar{\rho}_f^k \mathbf{N}_{\varphi} d\Omega + \int_{S_Q^k} \bar{Q}^k \mathbf{N}_{\varphi} ds \\ \int_{S_B^k} \bar{Q}_M^k \mathbf{N}_{\psi} ds \end{pmatrix} \quad (6.27)$$

We denote this grain as “RBFCG-1”. By increasing the number of RBF center/collocation points, the residual error produced in patch test can be reduced to a satisfactory level. However, RBFCG-1 may suffer from locking because the assumed interior displacement field is only complete to the first order, and the derived strains are locked together. This not only affects the accuracy of the mechanical displacements but also affect that of the electric and magnetic potentials due to the piezoelectric and piezomagnetic couplings. To improve the performance of RBFCG-1, we can further independently assume an interior strain field $\varepsilon_{ij}^{In}(\mathbf{x}, \mathbf{a}_{\varepsilon})$ which eliminates the shear locking terms, and determine the undetermined parameters \mathbf{a}_{ε} by enforcing the compatibility between $\varepsilon_{ij}^{In}(\mathbf{x}, \mathbf{a}_{\varepsilon})$ and $u_{(i,j)}(\mathbf{x}, \mathbf{q}_{\mathbf{u}})$ at several preselected collocation points. Similarly we can assume independent electric and magnetic fields, $-E_i^{In}(\mathbf{x}, \boldsymbol{\beta})$, $-H_i^{In}(\mathbf{x}, \boldsymbol{\gamma})$ and collocate them with the electric and magnetic fields derived from the electric and magnetic potentials, $\varphi_i(\mathbf{x}, \mathbf{q}_{\varphi})$, $\psi_i(\mathbf{x}, \mathbf{q}_{\psi})$.

So for the 2D grain, we can write:

$$\begin{aligned} \varepsilon_1^{In} &= \varepsilon_{11}^{In} = \mathbf{A}_{\varepsilon 1}(\mathbf{x}) \mathbf{a}_{\mathbf{I}}, & \varepsilon_3^{In} &= \varepsilon_{33}^{In} = \mathbf{A}_{\varepsilon 3}(\mathbf{x}) \mathbf{a}_{\mathbf{II}}, & \varepsilon_5^{In} &= \varepsilon_{13}^{In} = \mathbf{A}_{\varepsilon 5}(\mathbf{x}) \mathbf{a}_{\mathbf{III}} \\ -E_1^{In} &= \mathbf{A}_{\mathbf{E}1}(\mathbf{x}) \boldsymbol{\beta}_{\mathbf{I}}, & -E_3^{In} &= \mathbf{A}_{\mathbf{E}3}(\mathbf{x}) \boldsymbol{\beta}_{\mathbf{II}} \\ -H_1^{In} &= \mathbf{A}_{\mathbf{H}1}(\mathbf{x}) \boldsymbol{\gamma}_{\mathbf{I}}, & -H_3^{In} &= \mathbf{A}_{\mathbf{H}3}(\mathbf{x}) \boldsymbol{\gamma}_{\mathbf{II}} \end{aligned} \quad (6.28)$$

and for the 3D grain:

$$\begin{aligned}
\varepsilon_1^{In} &= \varepsilon_{11}^{In} = \mathbf{A}_{\varepsilon 1}(\mathbf{x}) \mathbf{a}_{\mathbf{I}}, & \varepsilon_2^{In} &= \varepsilon_{22}^{In} = \mathbf{A}_{\varepsilon 2}(\mathbf{x}) \mathbf{a}_{\mathbf{II}}, & \varepsilon_3^{In} &= \varepsilon_{33}^{In} = \mathbf{A}_{\varepsilon 3}(\mathbf{x}) \mathbf{a}_{\mathbf{III}}, \\
\varepsilon_4^{In} &= \varepsilon_{23}^{In} = \mathbf{A}_{\varepsilon 4}(\mathbf{x}) \mathbf{a}_{\mathbf{IV}}, & \varepsilon_5^{In} &= \varepsilon_{13}^{In} = \mathbf{A}_{\varepsilon 5}(\mathbf{x}) \mathbf{a}_{\mathbf{V}}, & \varepsilon_6^{In} &= \varepsilon_{12}^{In} = \mathbf{A}_{\varepsilon 6}(\mathbf{x}) \mathbf{a}_{\mathbf{VI}}, \\
-E_1^{In} &= \mathbf{A}_{\mathbf{E}1}(\mathbf{x}) \mathbf{\beta}_{\mathbf{I}}, & -E_2^{In} &= \mathbf{A}_{\mathbf{E}2}(\mathbf{x}) \mathbf{\beta}_{\mathbf{II}}, & -E_3^{In} &= \mathbf{A}_{\mathbf{E}3}(\mathbf{x}) \mathbf{\beta}_{\mathbf{III}} \\
-H_1^{In} &= \mathbf{A}_{\mathbf{H}1}(\mathbf{x}) \gamma_{\mathbf{I}}, & -H_2^{In} &= \mathbf{A}_{\mathbf{H}2}(\mathbf{x}) \gamma_{\mathbf{II}}, & -H_3^{In} &= \mathbf{A}_{\mathbf{H}3}(\mathbf{x}) \gamma_{\mathbf{III}}
\end{aligned} \tag{6.29}$$

The functions $\mathbf{A}_{\varepsilon j}(\mathbf{x}), \mathbf{A}_{\mathbf{E}j}(\mathbf{x})$, and $\mathbf{A}_{\mathbf{H}j}(\mathbf{x})$ can be written in the same form as $\mathbf{M}(\mathbf{x})$.

Collocating the independent fields (the components of normal strains, electric and magnetic fields) in eq. (6.28) or (6.29) with those in eq. (6.22) at enough points inside the grain, and collocating the shear terms (ε_5^{In} for the 2D case and $\varepsilon_4^{In}, \varepsilon_5^{In}$ and ε_6^{In} for the 3D case) only at the center of the grain, we get:

$$\begin{aligned}
\boldsymbol{\varepsilon}^{In} &= \mathbf{A}_{\varepsilon}(\mathbf{x}) \mathbf{a}_{\varepsilon} = \mathbf{B}_{\varepsilon}(\mathbf{x}) \mathbf{q}_{\mathbf{u}}, \\
-\mathbf{E}^{In} &= \mathbf{A}_{\mathbf{E}}(\mathbf{x}) \mathbf{\beta} = \mathbf{B}_{\mathbf{E}}(\mathbf{x}) \mathbf{q}_{\varphi}, \\
-\mathbf{H}^{In} &= \mathbf{A}_{\mathbf{H}}(\mathbf{x}) \gamma = \mathbf{B}_{\mathbf{H}}(\mathbf{x}) \mathbf{q}_{\psi},
\end{aligned} \tag{6.30}$$

Then we substitute in the functional Π as was done in equation (6.24) to get the stiffness matrix and load vector similar to that in eqs. (6.26) and (6.27), respectively, after replacing $\mathbf{B}_{\mathbf{u}}(\mathbf{x}), \mathbf{B}_{\varphi}(\mathbf{x})$ and $\mathbf{B}_{\psi}(\mathbf{x})$ by $\mathbf{B}_{\varepsilon}(\mathbf{x}), \mathbf{B}_{\mathbf{E}}(\mathbf{x})$ and $\mathbf{B}_{\mathbf{H}}(\mathbf{x})$. We denote this grain by “RBFCG-2”.

Actually the stiffness matrix of RBFCG-2 can be derived using the same procedure of deriving RBFCG-1, but with substituting the center point at every quadrature point in integrating the shear strains.

6.3.3 Conditioning of the system matrices

The finite element global system of equations to be solved in any of the previously presented grains is ill-conditioned because the stiffness matrix contains the material elastic stiffness matrix \mathbf{C} in the $\mathbf{K}_{\mathbf{uu}}$ part and also contains the dielectric material matrix \mathbf{h} in the $\mathbf{K}_{\varphi\varphi}$

part. The numerical values of the components of \mathbf{C} are as large as 10^{10} , and that of \mathbf{h} are as small as 10^{-9} . Hence the ratio is as large as 10^{19} , and this makes the global stiffness matrix ill-conditioned. To improve the conditioning we can use the following matrix instead of that of eq. (1.5) (after dropping the superscripts for clarity):

$$\begin{Bmatrix} \hat{\mathbf{C}} \\ \hat{\mathbf{D}} \\ \hat{\mathbf{B}} \end{Bmatrix} = \begin{Bmatrix} \hat{\mathbf{C}} & \hat{\mathbf{e}}^T & \hat{\mathbf{d}}^T \\ \hat{\mathbf{e}} & -\hat{\mathbf{h}} & -\hat{\mathbf{n}}^T \\ \hat{\mathbf{d}} & -\hat{\mathbf{g}} & -\hat{\mathbf{m}}^T \end{Bmatrix} \begin{Bmatrix} \mathbf{\varepsilon} \\ -\hat{\mathbf{E}} \\ -\hat{\mathbf{H}} \end{Bmatrix} \quad (6.31)$$

where $\hat{\sigma}_i = \frac{\sigma_i}{\tilde{c}}$, $\hat{D}_i = \frac{D_i}{\tilde{e}}$, $\hat{B}_i = \frac{B_i}{\tilde{d}}$, $\hat{E}_i = \frac{E_i \tilde{e}}{\tilde{c}}$, $\hat{H}_i = \frac{H_i \tilde{d}}{\tilde{c}}$ and

$$\hat{C}_{ij} = \frac{C_{ij}}{\tilde{c}}, \quad \hat{e}_{ij} = \frac{e_{ij}}{\tilde{e}}, \quad \hat{h}_{ij} = \frac{h_{ij} \tilde{c}}{\tilde{e}^2}, \quad \hat{d}_{ij} = \frac{d_{ij}}{\tilde{d}}, \quad \hat{n}_{ij} = \frac{n_{ij} \tilde{c}}{\tilde{e} \tilde{d}}, \quad \hat{m}_{ij} = \frac{m_{ij} \tilde{c}}{\tilde{d}^2}.$$

and from eq. (1.4), we also have $\hat{\varphi} = \frac{\varphi \tilde{e}}{\tilde{c}}$, $\hat{\psi} = \frac{\psi \tilde{d}}{\tilde{c}}$. Here we can select $\tilde{c} = C_{11}$, $\tilde{e} = e_{33}$ and

$$\tilde{d} = d_{33}.$$

Hence, the stiffness matrix will have the form:

$$\hat{\mathbf{K}} = \begin{bmatrix} \hat{\mathbf{K}}_{\mathbf{u}\mathbf{u}} & \hat{\mathbf{K}}_{\mathbf{u}\varphi} & \hat{\mathbf{K}}_{\mathbf{u}\psi} \\ \hat{\mathbf{K}}_{\varphi\mathbf{u}}^T & -\hat{\mathbf{K}}_{\varphi\varphi} & -\hat{\mathbf{K}}_{\varphi\psi} \\ \hat{\mathbf{K}}_{\psi\mathbf{u}}^T & -\hat{\mathbf{K}}_{\psi\varphi}^T & -\hat{\mathbf{K}}_{\psi\psi} \end{bmatrix} = \sum_{k=1}^N \begin{bmatrix} \int_{\Omega^k} \mathbf{B}_{\mathbf{u}}^T \hat{\mathbf{C}}^k \mathbf{B}_{\mathbf{u}} d\Omega & \int_{\Omega^k} \mathbf{B}_{\mathbf{u}}^T \hat{\mathbf{e}}^{kT} \mathbf{B}_{\varphi} d\Omega & \int_{\Omega^k} \mathbf{B}_{\mathbf{u}}^T \hat{\mathbf{d}}^{kT} \mathbf{B}_{\psi} d\Omega \\ \int_{\Omega^k} \mathbf{B}_{\varphi}^T \hat{\mathbf{e}}^k \mathbf{B}_{\mathbf{u}} d\Omega & - \int_{\Omega^k} \mathbf{B}_{\varphi}^T \hat{\mathbf{h}}^k \mathbf{B}_{\varphi} d\Omega & - \int_{\Omega^k} \mathbf{B}_{\varphi}^T \hat{\mathbf{n}}^{kT} \mathbf{B}_{\psi} d\Omega \\ \int_{\Omega^k} \mathbf{B}_{\psi}^T \hat{\mathbf{d}}^k \mathbf{B}_{\mathbf{u}} d\Omega & - \int_{\Omega^k} \mathbf{B}_{\psi}^T \hat{\mathbf{n}}^k \mathbf{B}_{\varphi} d\Omega & - \int_{\Omega^k} \mathbf{B}_{\psi}^T \hat{\mathbf{m}}^k \mathbf{B}_{\psi} d\Omega \end{bmatrix} \quad (6.32)$$

and the system to be solved takes the form:

$$\hat{\mathbf{K}} \hat{\mathbf{q}} = \hat{\mathbf{F}} \quad (6.33)$$

where

$$\hat{\mathbf{F}}^T = \begin{Bmatrix} \hat{\mathbf{F}}_{\mathbf{u}}^T & \hat{\mathbf{F}}_{\boldsymbol{\varphi}}^T & \hat{\mathbf{F}}_{\boldsymbol{\psi}}^T \end{Bmatrix}, \quad \hat{\mathbf{F}}_{\mathbf{u}} = \frac{\mathbf{F}_{\mathbf{u}}}{\tilde{c}}, \quad \hat{\mathbf{F}}_{\boldsymbol{\varphi}} = \frac{\mathbf{F}_{\boldsymbol{\varphi}}}{\tilde{e}}, \quad \hat{\mathbf{F}}_{\boldsymbol{\psi}} = \frac{\mathbf{F}_{\boldsymbol{\psi}}}{\tilde{d}} \quad (6.34)$$

$$\hat{\mathbf{q}}^T = \begin{Bmatrix} \mathbf{q}_{\mathbf{u}}^T & \hat{\mathbf{q}}_{\boldsymbol{\varphi}}^T & \hat{\mathbf{q}}_{\boldsymbol{\psi}}^T \end{Bmatrix} \text{ and } \hat{\mathbf{q}}_{\boldsymbol{\varphi}} = \frac{\mathbf{q}_{\boldsymbol{\varphi}} \tilde{e}}{\tilde{c}}, \quad \hat{\mathbf{q}}_{\boldsymbol{\psi}} = \frac{\mathbf{q}_{\boldsymbol{\psi}} \tilde{d}}{\tilde{c}}.$$

So, we solve the system (6.33) for $\hat{\mathbf{q}}$ from which we get $\mathbf{q}_{\mathbf{u}}$, $\mathbf{q}_{\boldsymbol{\varphi}} = \frac{\hat{\mathbf{q}}_{\boldsymbol{\varphi}} \tilde{c}}{\tilde{e}}$ and $\mathbf{q}_{\boldsymbol{\psi}} = \frac{\hat{\mathbf{q}}_{\boldsymbol{\psi}} \tilde{c}}{\tilde{d}}$.

6.4 Switching criterion and kinetics for ferroelectric materials

Gibbs energy density g can be related to the internal energy density U via a Legendre transformation, which results in:

$$\rho g = \rho U - \boldsymbol{\sigma} : \boldsymbol{\varepsilon} - \mathbf{E} \cdot \mathbf{D} - \eta T \quad (6.35)$$

Gibbs energy is considered to be composed of two parts, a linear (or reversible) part, g^L , which reflects the linear or reversible responses of the material and primarily depends on $\boldsymbol{\sigma}, \mathbf{E}$ and T , and a remnant (or irreversible) part, g^R , arising from the changes in the remnant state of the crystal with respect to a reference state, and is assumed to be a function of the remnant polarization and strain.

$$g = g^L(\boldsymbol{\sigma}, \mathbf{E}, T) + g^R(\mathbf{P}^R, \boldsymbol{\varepsilon}^R) \quad (6.36)$$

Substituting eqs. (1.29), (1.34), (6.35) and (6.36) into eq. (1.35), we get the local dissipation inequality for the isothermal case considered:

$$\boldsymbol{\sigma} : \dot{\boldsymbol{\varepsilon}}^R + \mathbf{E} \cdot \dot{\mathbf{P}}^R - \rho \partial_{\boldsymbol{\varepsilon}^R} g^R \cdot \dot{\boldsymbol{\varepsilon}}^R - \rho \partial_{\mathbf{P}^R} g^R \cdot \dot{\mathbf{P}}^R \geq 0 \quad (6.37)$$

In the case of a reversible response, the microscopic state of the crystal, as well as the remnant values, remain unaltered—such that $\dot{\mathbf{P}}^R = \mathbf{0}$ and $\dot{\boldsymbol{\varepsilon}}^R = \mathbf{0}$, and eq. (6.37) turns into an

equality taking the value zero. In this work, rate-effects will not be accounted for and also changes in volume fractions are done at discrete time intervals $\Delta t > 0$.

Several representation forms of Gibbs energy associated with the remnant state of the crystal, $g^R(\mathbf{P}^R, \boldsymbol{\varepsilon}^R)$, have been investigated in the literature (see [32] and [33] for example). Here we restrict ourselves to a quadratic form in terms of remnant polarization and strains, namely:

$$\rho g^R(\mathbf{P}^R, \boldsymbol{\varepsilon}^R) = \frac{1}{2} \boldsymbol{\varepsilon}^R : \mathbf{H}_\varepsilon : \boldsymbol{\varepsilon}^R + \frac{1}{2} \mathbf{P}^R \cdot \mathbf{H}_P \cdot \mathbf{P}^R \quad (6.38)$$

where \mathbf{H}_ε and \mathbf{H}_P denote the hardening-type tensors pertaining to the crystal's remnant strain and polarization respectively. Here, we assume the simplest format, i.e. the hardening-type tensors are chosen to be proportional to the symmetric identity tensors of fourth and second order:

$$\mathbf{H}_\varepsilon = H_\varepsilon \mathbf{I}^{sym}, \quad \mathbf{H}_P = H_P \mathbf{I}^{sym} \quad (6.39)$$

where H_ε and H_P are positive scalars, being referred to as hardening parameters, \mathbf{I}^{sym} is a symmetric identity tensor of the fourth order for strain and second order for polarization. H_ε and H_P are set constant in this work. Based on eqs. (6.37) and (6.38), the local dissipation inequality now corresponds to:

$$[\boldsymbol{\sigma} - \boldsymbol{\sigma}^b] : \dot{\boldsymbol{\varepsilon}}^R + [\mathbf{E} - \mathbf{E}^b] \cdot \dot{\mathbf{P}}^R \geq 0 \quad (6.40)$$

with

$$\boldsymbol{\sigma}^b = \rho \partial_{\boldsymbol{\varepsilon}^R} g^R = \mathbf{H}_\varepsilon : \boldsymbol{\varepsilon}^R = H_\varepsilon \boldsymbol{\varepsilon}^R \quad (6.41)$$

$$\mathbf{E}^b = \rho \partial_{\mathbf{P}^R} g^R = \mathbf{H}_P \cdot \mathbf{P}^R = H_P \mathbf{P}^R \quad (6.42)$$

The contributions σ^b and E^b are referred to as *back stress* and *back electric field*, respectively. If the remnant polarization and strain of a grain vary from a reference state, the back fields will either resist or assist further domain switching processes depending upon whether the process will take the current state further away from the reference state or closer to it. Here, the reference state is defined as the state at which the remnant polarization and strain of the single grain are zero.

The rate of change of the remnant strain and polarization is calculated from eq. (1.30) as:

$$\dot{\epsilon}^R = \sum_{i=1}^{N_d} \dot{c}_i \epsilon_i^s, \quad \dot{P}^R = \sum_{i=1}^{N_d} \dot{c}_i P_i^s \quad (6.43)$$

Substitution of eq. (6.43) into eq. (6.40) yields the local dissipation inequality to get the form:

$$\sum_{i=1}^{N_d} \left[[\sigma - \sigma^b] : \epsilon_i^s + [E - E^b] \cdot P_i^s \right] \dot{c}_i \geq 0 \quad \text{or} \quad \sum_{i=1}^{N_d} f_i \dot{c}_i \geq 0 \quad (6.44)$$

At the level of a single crystal, f_i denotes the force driving domain switching processes by altering the crystal variant i in combination with one or more of the remaining variants.

The switching criterion specifies the conditions under which domain switching commences. Let a domain switching process—transforming one variant into another—be referred to as a transformation system. For a 2D ferroelectric body with four types of different phases per element or grain, 6 such transformation systems can be observed, while for the 3D case with six types of variants, we have 15 transformation systems. Concerning notation, a transformation system that increases the variant j at the expense of another variant, say i , is denoted as $i \rightarrow j$. The related driving force f_{ij} is obtained from eq. (6.44) as,

$$f_{ij} = f_j - f_i = [\sigma - \sigma^b] : \epsilon_{i \rightarrow j}^s + [E - E^b] \cdot P_{i \rightarrow j}^s \quad \text{for } i, j = 1..N_d \quad (6.45)$$

where $\boldsymbol{\varepsilon}_{i \rightarrow j}^s = \boldsymbol{\varepsilon}_j^s - \boldsymbol{\varepsilon}_i^s$, $\mathbf{P}_{i \rightarrow j}^s = \mathbf{P}_j^s - \mathbf{P}_i^s$.

For the 2D case, four of the six possible forward transformation systems are related to 90° domain switching, while the remaining two correspond to 180° domain switching. For the 3D case, 12 of the possible 15 forward transformation systems are related to 90° domain switching, while the remaining three correspond to 180° domain switching. As soon as the driving force reaches a certain critical threshold values k_{90} or k_{180} associated with 90° or 180° domain switching respectively, the modeling of the related switching process is initiated. In other words, the transformation system is activated based on:

$$\begin{aligned} |f_{ij}| \geq k_{90} &\Rightarrow 90^\circ \text{ switching} \\ |f_{ij}| \geq k_{180} &\Rightarrow 180^\circ \text{ switching} \end{aligned} \quad (6.46)$$

So, the ferroelectric crystal exhibits reversible responses without any change in its microscopic state because the underlying volume fractions of crystal variants are unaltered until the driving force reaches any of the critical values. Once a transformation system becomes active, the associated discrete changes in the volume fractions as referred to the time or rather load interval $\Delta t > 0$ can be determined using eqs. (6.45) and (6.46). The update of a crystal variant j according to the $i \rightarrow j$ transformation system is represented by

$$\Delta c_j = \begin{cases} -\min\{c_i, \Delta \tilde{c}_j\} & \text{for } f_{ij} \leq -f_{cr} \\ 0 & \text{for } -f_{cr} \leq f_{ij} \leq f_{cr} \\ \min\{c_i, \Delta \tilde{c}_j\} & \text{for } f_{ij} \geq f_{cr} \end{cases} \quad (6.47)$$

$$\text{where } f_{cr} = \begin{cases} k_{90} & \text{for } 90^\circ \text{ switching} \\ k_{180} & \text{for } 180^\circ \text{ switching} \end{cases} \quad \text{and}$$

$$\Delta \tilde{c}_j = \frac{\langle |f_{ij}| - f_{cr} \rangle}{\boldsymbol{\varepsilon}_{i \rightarrow j}^s : \mathbf{H}_\varepsilon : \boldsymbol{\varepsilon}_{i \rightarrow j}^s + \mathbf{P}_{i \rightarrow j}^s : \mathbf{H}_P : \mathbf{P}_{i \rightarrow j}^s} \quad (6.48)$$

where $\langle \bullet \rangle = \frac{1}{2} [|\bullet| + \bullet]$. Note that: $\boldsymbol{\varepsilon}_1^s = \boldsymbol{\varepsilon}_2^s$, $\boldsymbol{\varepsilon}_3^s = \boldsymbol{\varepsilon}_4^s$, $\boldsymbol{\varepsilon}_5^s = \boldsymbol{\varepsilon}_6^s$, $\mathbf{P}_1^s = -\mathbf{P}_2^s$, $\mathbf{P}_3^s = -\mathbf{P}_4^s$ and $\mathbf{P}_5^s = -\mathbf{P}_6^s$.

For 180° switching, there is no change in the remnant strain and eq. (6.48) reduces to:

$$\Delta \tilde{c}_j = \frac{\langle |f_{ij}| - k_{180} \rangle}{4 \mathbf{P}_j^s : \mathbf{H}_P : \mathbf{P}_j^s}$$

Note that the consistency constraints on the volume fractions (see eq. (1.28)) are inherently guaranteed within the proposed model as the relation $f_{ij} = -f_{ji}$ generally holds. So for the forward transformation system $i \rightarrow j$ the volume fraction c_j increases by the same amount as c_i decreases.

Once the incremental volume fractions are obtained, the volume fractions of each grain should be updated:

$$c_{j(new)} = c_{j(old)} + \sum_{i=1, i \neq j}^{N_d} \Delta c_{ij} \quad \text{for } j = 1..N_d \quad (6.49)$$

Then, the material matrices as well as the remnant strain and polarization can be updated using eq. (1.30), while the back fields of the current crystal state can be determined via eqs. (6.41) and (6.42). As the back fields resist subsequent switching process in the same transformation system, increasing loading levels are required to continue the transformation of the respective phase. If the loading direction is reversed, however, the back fields additionally support the transformation process until the crystal reaches the reference state. Hardening or softening effects within the crystal—stemming from changing remnant states—are accounted for in the model by means of these back fields. In order to realize the crystal-to-crystal

interactions in a ferroelectric polycrystal, i.e. the so-called inter-granular effects, as well as to simulate general boundary value problems, the single crystal model proposed is embedded into an iterative finite element framework as will be discussed in the next section.

Note that the switching criterion used here is local in nature, unlike the switching criterion of Kim and Jiang [26] and others which is based on the overall energy release of the whole body. Using this local switching criterion prevents searching for the configuration that yields the minimum overall energy of the whole body in each simulation step. This search for the desired configuration requires solving the finite element system of equations as much as the number of the switching grains (the grains that tend to switch) in each simulation step. Hence it is computationally inefficient.

6.5 Solution method for simulating ferroelectric/ferroelastic switching

To calculate the response of a polycrystalline ferroelectric under electromechanical loading, the switching criterion and kinetic relations presented in the previous section should be implemented into a numerical algorithm to obtain the volume fractions of various domains in each grain at each time step.

First the body is discretized into randomly generated Voronoi cells (RBFCGs). Each RBFCG represents one crystal grain. Then randomly generated crystallographic axes are assigned to each RBFCG, modeling a crystal grain in a polycrystalline ferroelectric specimen. This is done by generating a random value for the angle θ -between the global X_1 axis and the local crystal axis 1 , x'_1 , in each grain for 2D analyses. x'_3 , or the crystal axis 3, is set by a 90° rotation of x'_1 in the $X_1 - X_3$ plane. For the 3D case, three Euler angles (θ, ϕ and ψ) are generated randomly for each polyhedron grain to define its crystallographic axes as was discussed in subsection 1.7.1. The crystallographic axes are mutually orthogonal.

Initially, each RBFCG modeling a crystal grain consists of N_d distinct types of domains, where N_d is the number of possible domain types in the grain ($N_d = 4$ in 2D analyses and $N_d = 6$ for the 3D case). The spontaneous polarization directions of the domains are parallel/opposite to the crystallographic axes in each grain. Hence for the system configuration which is defined by domain volume fractions, all domains in a grain are assigned with the same initial values of volume fraction, i.e. $1/N_d$. The net polarization and strain of the specimen are therefore zero at the initial instant of time. The back fields are also zero initially.

Suppose that the system configuration at time t is known. After an incremental time step Δt , the system configuration at time $t + \Delta t$ are determined as follows:

- (a) The load vector \mathbf{F} is updated to that at time $t + \Delta t$. By using the known values of volume fractions at time t and the known load vector at time $t + \Delta t$, the finite element system of equation is assembled and solved to obtain a new nodal electromechanical displacements $\mathbf{q} = \{\mathbf{q}_u \quad \mathbf{q}_\phi\}^T$. Based on the new grain electromechanical displacement vector \mathbf{q} , the grain area (volume) average linear strain and electric field are calculated as:

$$\bar{\boldsymbol{\epsilon}}^{Lk} = \frac{\int_{A^k} \boldsymbol{\epsilon}^L dA}{A^k} = \frac{\int_{A^k} \mathbf{B}_u dA}{A^k} \mathbf{q}_u \quad (6.50)$$

$$\bar{\mathbf{E}}^k = \frac{\int_{A^k} \mathbf{E} dA}{A^k} = \frac{-\int_{A^k} \mathbf{B}_\phi dA}{A^k} \mathbf{q}_\phi \quad (6.51)$$

where A and A^k are replaced by V and V^k respectively for the 3D case. A^k and V^k are the area and volume of grain k respectively.

Then the grain area (volume) average stress $\bar{\sigma}^k$ and linear electric displacement $\bar{\mathbf{D}}^{kL}$ are calculated from the linear constitutive relations (1.33) in which the material matrices are determined with the known values of volume fractions at time t .

$$\begin{Bmatrix} \bar{\sigma}^k \\ \bar{\mathbf{D}}^{Lk} \end{Bmatrix} = \begin{bmatrix} \mathbf{C}^k & \mathbf{e}^{kT} \\ \mathbf{e}^k & -\mathbf{h}^k \end{bmatrix} \begin{Bmatrix} \bar{\boldsymbol{\varepsilon}}^{Lk} \\ -\bar{\mathbf{E}}^k \end{Bmatrix} \quad (6.52)$$

- (b) All domains in a grain are assumed to be subjected to constant electric field and stress, $\bar{\mathbf{E}}$ and $\bar{\sigma}$. The driving force for all the transformation systems, f_{ij} , in each grain can then be computed using eq. (6.45), and compared with the critical values k_{90} and k_{180} . If the driving forces are less than the critical values, then no switching is done and loading is continued elastically.
 - (c) Once the driving force of any transformation system in a grain exceeds the corresponding critical value, then increments in volume fractions can be calculated using eq. (6.47) and the volume fractions of all domains in each grain can be updated using eq. (6.49). The average material matrices, remnant strain, $\mathbf{\epsilon}^{Rk}$, and polarization, \mathbf{P}^{Rk} , as well as the back fields in each grain should also be updated using eqs. (1.30), (6.41) and (6.42). Then the grain's macroscopic strain and polarization are calculated using equation (1.29).
 - (d) Using the new average material properties, the system of equations is assembled and solved. A new set of nodal electromechanical displacements can be obtained. For the same simulation step or load increment, the previous steps should be repeated with the new/updated volume fractions until some convergence criterion is met.
- By repeating the steps (a)–(d), the system configuration at the next time step can be found.

It was shown in [27], that for sufficiently small load increments, further iteration steps for the local volume fractions at fixed external loads (as described in (d)) are not necessary and do not significantly change the solution of the boundary value problems investigated. Moreover, by not allowing for additional iteration steps for a given load increment, the possible problem of back and forth switching, which depends in particular on the orientation of the local crystallographic axes with respect to the loading directions, is avoided. This algorithmic problem is due to the discrete nature of the switching criterion introduced.

6.6 Numerical Examples

In this section we present some numerical examples to show the performance and capabilities of the 2D and the 3D RBFCGs in modeling different Magneto-electro-elastic, functionally graded, and ferroelectric materials.

6.6.1 Patch test for Magneto-electro-elastic materials

Jiang and Ding [34] presented the analytical solutions of 2D magneto-electro-elastic beams with different loading and boundary conditions by expressing all variables in terms of four harmonic displacement functions. If the piezomagnetic and magneto-electric coefficients are set to zero, the solution reduces to that of piezoelectric materials. Here we consider a patch of a rectangular shape as shown in Figure 6.5. The body is fixed at its left edge and a uniformly distributed load of magnitude P is applied on its right edge. The lower left corner point is considered as the electric and magnetic ground. Here we select $L = 0.3$ m, $W = 0.15$ m, $P = 500$ Pa. The material used in this problem is the magneto-electro-elastic material used in [34]. The material properties are shown in Table 6.1 as MEE(1).

Table 6.1: Material properties used in the numerical examples [C'_{ij} in GPa, e'_{ij} in C/m², h'_{ii} in nC/(Vm), d'_{ij} in N/Am, n'_{ii} in pN/AV, and m'_{ii} in μ N/A²]

Property	$C'_{11} = C'_{22}$	C'_{12}	$C'_{13} = C'_{23}$	C'_{33}	$C'_{44} = C'_{55}$	C'_{33}
MEE(1)	166	77	78	162	43	44.5
Property	$e'_{31} = e'_{32}$	e'_{33}	$e'_{15} = e'_{24}$	$h'_{11} = h'_{22}$	h'_{33}	$d'_{31} = d'_{32}$
MEE(1)	-4.4	18.6	11.6	11.2	12.6	580.3
Property	d'_{33}	$d'_{15} = d'_{24}$	$n'_{11} = n'_{22}$	n'_{33}	$m'_{11} = m'_{22}$	m'_{33}
MEE(1)	699.7	550	5	3	5	10

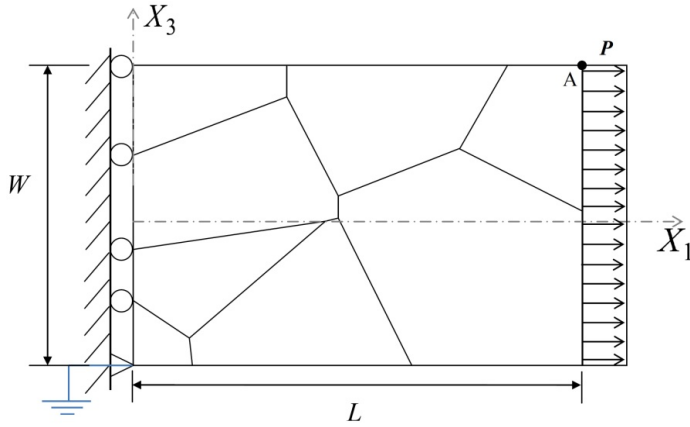


Figure 6.5: Patch test for 2D RBFCGs

We compare the results at point “A” (the upper right corner) with that of the analytical solution presented in [34]. The finite element mesh considered here consists of 8 RBFCGs as shown in the figure. The results to be compared are the vertical and horizontal displacements, the electric potential and the magnetic potential. The analytical and the finite element solutions at point “A” are presented in Table 6.2 with the percentage error in the different quantities.

Table 6.2: Analytical, RBFCG solutions and the error percent at point “A” in the patch test

	u_1	u_2	φ	ψ
Analytical	0.1205×10^{-7} m	-0.0227×10^{-7} m	-5.0163 V	0.1208 A
RBFCG-1	0.1203×10^{-7} m	-0.0226×10^{-7} m	-5.0162 V	0.1206 A
Absolute error %	0.1071	0.3025	0.0026	0.1589
RBFCG-2	0.1205×10^{-7} m	-0.0227×10^{-7} m	-5.0155 V	0.1204 A
Absolute error %	0.1290	0.4465	0.0159	0.3734

The error percent at point “A” in all variables does not exceed 1% .The error percent at all nodes defined by eq. (6.53) is: 0.027078 for RBFCG-1, and 0.048903 for RBFCG-2; hence both grain types pass the patch test with satisfactory accuracy.

$$Error \% = \frac{\|\mathbf{q} - \mathbf{q}^{exact}\|}{\|\mathbf{q}^{exact}\|} \times 100 \quad (6.53)$$

6.6.2 Effective material properties determination for functionally graded materials

One of the most important applications, that this new 3D RBFCGs can be used for, is the determination of the effective material properties of functionally graded materials (FGMs). These materials have microstructure and properties that vary in a continuous fashion, from one material to the other. The use of these materials reduces the service stresses of ceramic-coated metallic parts and the stresses developed during fabrication due to the differences in thermo-mechanical properties between metals and ceramics. Thus, replacing the sharp ceramic/metal interface with an intermediate graded layer of FGMs can stop problems like decohesion at the ceramic/metal interface, plastic deformation, void nucleation in the metal, and cracking within the ceramic. A schematic of a FGM is shown in Figure 6.6 to illustrate how the microstructure varies in a complex fashion from one pure material to the other.

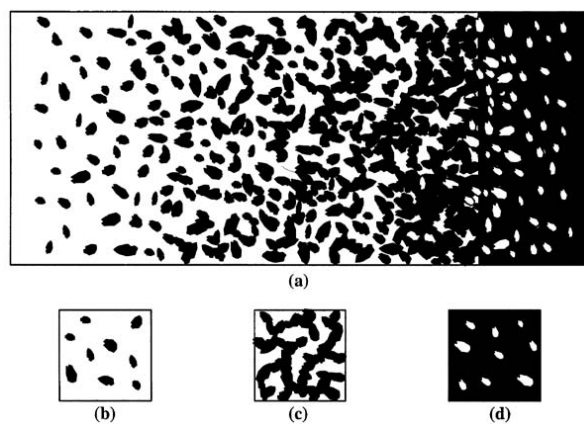


Figure 6.6: (a) A schematic representation of the variation in a FGM microstructure: (b) and (d) typical microstructure at small volume fractions of the two materials; (c) typical microstructure at comparable volume fractions of the two materials

It is important to study the distribution of stresses and the stress reduction mechanisms in these functionally graded materials, as well as determining the effective material properties of these heterogeneous materials as a function of volume fractions of the constituent materials. Several models have been developed to predict the effective elastic properties of heterogeneous materials and their dependence on material microstructure.

Based on the Eshelby's equivalent inclusion method [35], a number of self-consistent models were proposed [36]-[38]. These models are generally successful in predicting the effective material properties only for relatively simple microstructures and low volume fractions of the inclusions.

Based on the finite element analysis, a number of models that overcome the limitation of the low volume fraction of the inclusions were proposed [39]-[41]. These models assume that the heterogeneous material can be represented as a periodic repetition of a representative material element (RME). However, the real microstructures are rarely periodic. Consequently, non-homogeneity and nonlinearity in deformation at the structure length scale, which may occur under complex loading conditions, may not be predicted, if this local periodicity constraint is imposed.

Grujicic and Zhang [42] used two dimensional Voronoi cell finite elements to determine the effective elastic properties of FGMs. They used the 2D VCFEM developed by Ghosh and co-workers [12]. Following [42], the microstructure of the FGM can be modeled as 3D RBFCGs with embedded inclusions if the volume fraction (VF) of any of the two constituent materials ranges from 0 to 0.3, and as some intertwined clusters of the two phases if the VF of any of the materials ranges from 0.4 to 0.6. In the regions where the VF of one constituent ranges from 0.3

to 0.4, the microstructure is treated as consisting of the two basic microstructures mentioned above mixed in different proportions.

In order to obtain realistic predictions of a new material macroscopic behavior by computational means, three-dimensional numerical simulations of statistically representative micro-heterogeneous material samples are unavoidable.

Extending the 3D RBFCGs to include 3D inclusions and voids was done by Dong and Atluri [9]-[10] for elastic materials. Here, we examine our proposed RBFCGs in modeling FGMs when the volume fraction of any of the two constituent materials is in the range of 0.4 to 0.6.

Analysis of Ni₃Al/TiC system

Ni₃Al/TiC functionally graded material is considered here. The material properties of the constituent linear elastic materials are as follows: $E_{\text{Ni}_3\text{Al}} = 217 \text{ GPa}$, $\nu_{\text{Ni}_3\text{Al}} = 0.30$, $E_{\text{TiC}} = 440 \text{ GPa}$, and $\nu_{\text{TiC}} = 0.19$.

In order to account for the randomness of the microstructure, three samples of RVE are considered in this analysis. Each sample has a different mesh configuration composed of 50 3D RBFCGs. For each mesh configuration, six random distributions of the two materials are tested. Data points are calculated for the cases when the volume fraction of Ni₃Al ranges from 0.4 to 0.6.

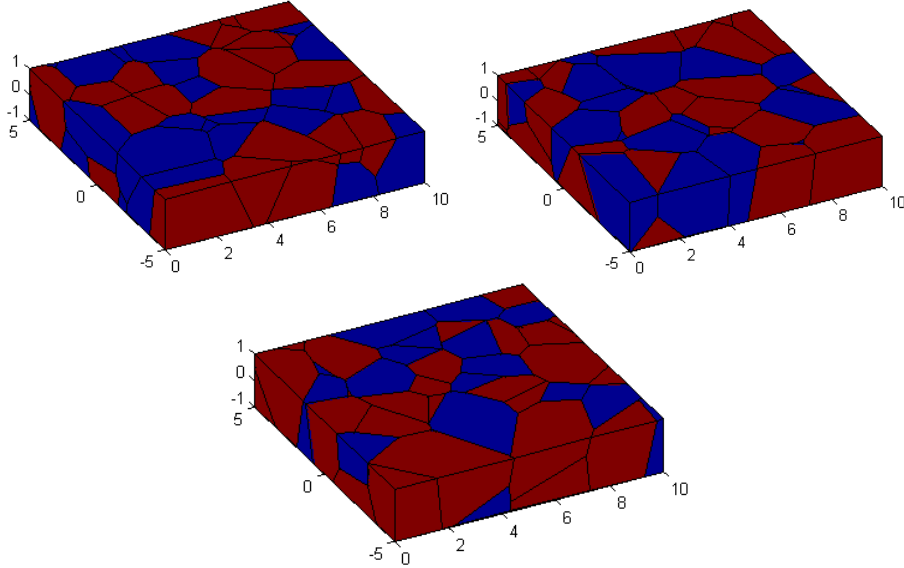


Figure 6.7: The three considered mesh configurations: the first with VF of $\text{Ni}_3\text{Al} \approx 0.6$, the second with VF of $\text{Ni}_3\text{Al} \approx 0.5$, the third with VF of $\text{Ni}_3\text{Al} \approx 0.4$ (The blue color denotes Ni_3Al and the red color denotes TiC)

Figure 6.7 shows the three considered mesh configurations for different random material distributions for three cases with Ni_3Al volume fraction $\approx 0.4, 0.5$ and 0.6 . In this figure the blue color denotes Ni_3Al while the red color denotes TiC .

The variations of the effective Elasticity modulus (Young's modulus) and the effective Poisson's ratio as the volume fraction of TiC is changed from 0.4 to 0.6 are shown in Figure 6.8 and compared with the experimental results [43] and other methods from the literature: the self-consistent method (SCM), the Equivalent inclusion method (EIM), and the VCFEM-2D (using 600 elements) [42].

It is clear from Figure 6.8 (left) that the current 3D model gives much better results for the effective Young's modulus than that of the 2D VCFEM based on hybrid stress formulation, even though the 3D model used only 50 elements while the 2D model used 600. As for the variation in the effective Poisson's ratio shown in Figure 6.8 (right), the results of the current model are comparable to the other models. Increasing the number of grains in the RVE is

expected to increase the resolution of the results. Including the effect of voids is expected to yield more realistic models, and considering the presence of inclusions is expected to aid in extending the results to the full range of volume fractions.

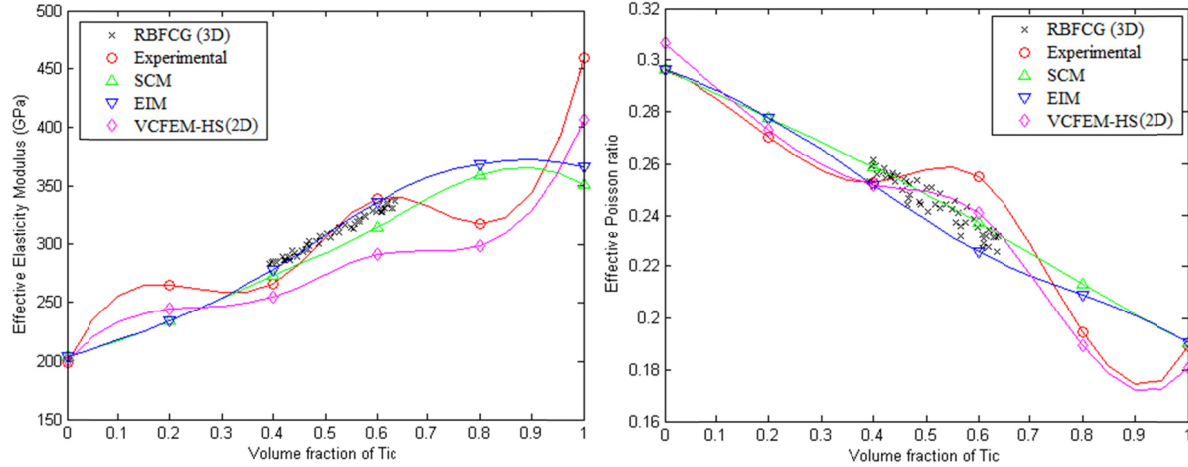


Figure 6.8: The results of the current model for the Effective Young's modulus (left) and effective Poisson's ratio (right) compared to the experimental and other models from the literature

6.6.3 Simulating ferroelectric materials

In this section, we present the results of the developed RBFCG models for ferroelectric switching (by applying cyclic electric loads that may be combined with constant mechanical loads) and ferroelastic switching (by applying only cyclic mechanical loads). The material used for the simulation is BaTiO₃. The properties of a BaTiO₃ crystal poled in x'_3 -crystallographic axis are:

$$\begin{aligned} C_{11} &= 166 \text{ GPa}, & C_{12} &= 77 \text{ GPa}, & C_{13} &= 77.5 \text{ GPa}, & C_{33} &= 162 \text{ GPa}, \\ C_{44} &= 42.9 \text{ GPa}; & e_{31} &= -4.4 \text{ C/m}^2, & e_{33} &= 18.6 \text{ C/m}^2, & e_{15} &= 11.6 \text{ C/m}^2; \\ h_{11} &= 11.151 \text{ pC/(Vm)}, & h_{33} &= 12.567 \text{ pC/(Vm)}; \\ \varepsilon_{33}^S &= 4.15 \times 10^{-3}, & p^S &= 0.23 \text{ C/m}^2. \end{aligned}$$

For 2D analysis, we take $\varepsilon_{11}^S = -\varepsilon_{33}^S$, while for 3D analysis, we use $\varepsilon_{11}^S = \varepsilon_{22}^S = -\varepsilon_{33}^S / 2$.

This will result in zero net spontaneous strain and polarization in the initial state before applying any loads.

The hardening parameters and the switching threshold values are taken to be:

$$H_\varepsilon = 3 \times 10^9 \text{ Pa}, \quad H_P = 10^6 \text{ Vm/C}, \quad k_{90} = 1.42 \times 10^5 \text{ Pa}, \quad k_{180} = 2k_{90}$$

The 2D specimen is a square with $L = W = 1 \text{ mm}$. The mesh used in the 2D simulation is composed of 200 RBFCGs (equivalent to 402 nodes), each having its own random shape as shown in Figure 6.9. The figure also shows the randomly generated direction of the x'_3 -crystallographic axis in each grain.

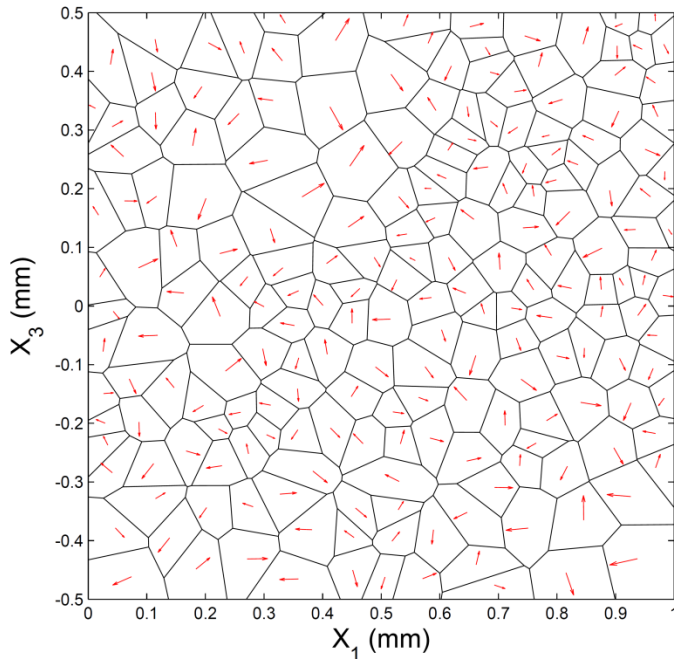


Figure 6.9: 2D mesh used in the simulation with the x'_3 -crystallographic axis of each grain shown

The lower surface of the specimen is constrained from motion in the X_3 direction, while the left surface is not allowed to move in the X_1 direction. Constraints were used to keep the

upper and right surfaces (edges in 2D analysis) straight. The lower surface is earthed, i.e. has electric potential $\varphi = 0$.

The 3D specimen is a cube with $L = W = D = 1$ mm. 100 RBFCGs only are composing the mesh which has 572 nodes as shown in Figure 6.10.

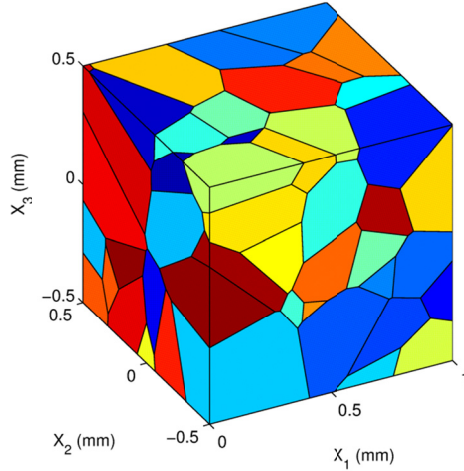


Figure 6.10: 3D mesh used in the simulation (100 3D Voronoi cells)

In addition to the boundary conditions considered in the 2D analysis, the back surface of the 3D specimen is prevented from motion in X_2 direction. The right, upper and front surfaces are constrained to be flat surfaces after deformation. Figure 6.11 shows a 3D representation of the considered ferroelectric material specimen and all the considered surfaces and dimensions with the global coordinate axes. In 2D analysis we only consider the projection of this model on $X_1 - X_3$ plane.

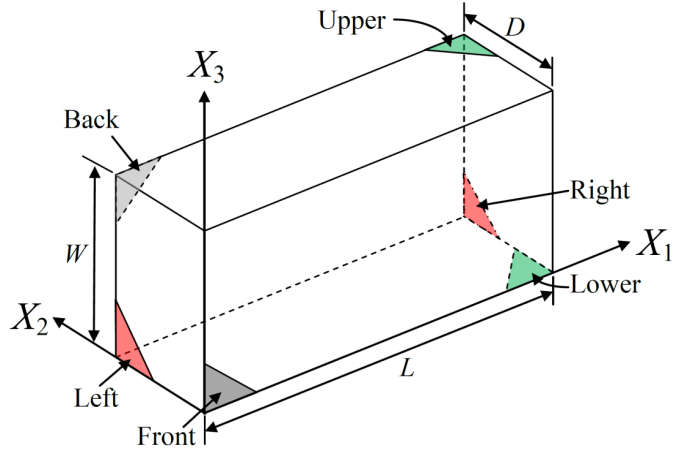


Figure 6.11: surfaces of the ferroelectric specimen

6.6.3.1 Ferroelectric switching

In this case switching is produced by cyclic external electric field applied to the ferroelectric polycrystalline. This results in the hysteresis and butterfly loops of macroscopic electric displacement and strain, respectively, versus electric field. Constant applied external compressive stresses cause these nonlinear loops to become flatter. Cyclic electric field is applied by specifying a constant value for the electric potential on the upper surface while the lower surface is earthed. The value of the electric potential on the upper surface is expressed as:

$$\bar{\varphi}(t) = W \times E \sin(2\pi ft) \quad (6.54)$$

where $E = 20 \times 10^5 \text{ V/m}$ is the amplitude of the applied electric field, and $f = 60 \text{ Hz}$ is the frequency of the applied electric load. t is the time in second. The time step used in the simulation is $\Delta t = 1/(624f) = 2.6709 \times 10^{-5} \text{ sec}$. In addition, constant compressive stress is applied on the upper surface of the specimen.

The experimentally observed material behavior for PZT-51 under the loading conditions considered is reported in [44] and is also shown in Figure 6.12. Corresponding simulation results, namely representative hysteresis loops of macroscopic electric displacement – electric

field and butterfly curves of macroscopic strain – electric field, are shown in Figure 6.13 for the 2D model. The simulation results match the experimental investigations, even though a two-dimensional formulation is considered and the material parameters adopted do not fully reflect the local properties of the material used for the experimental investigations (as these are not directly available in the literature).

The macroscopic electric displacement and strain are the area average electric displacement and strain calculated as:

$$D_3 = \frac{\sum_{k=1}^N \int_{A^k} D_3^k(\xi^\gamma) dA}{A} \quad (6.55)$$

$$\varepsilon_3 = \frac{\sum_{k=1}^N \int_{A^k} \varepsilon_3^k(\xi^\gamma) dA}{A} = \frac{\sum_{k=1}^N (\bar{\varepsilon}^L A^k + \bar{\varepsilon}^R A^k)}{A} \quad (6.56)$$

where A is the total surface area of the specimen $A=L \times W$. For the 3D analysis, we use volume average macroscopic strain which is calculated similarly but replacing the area integral by a volume integral in each grain and dividing by the total volume of the specimen instead of the total area.

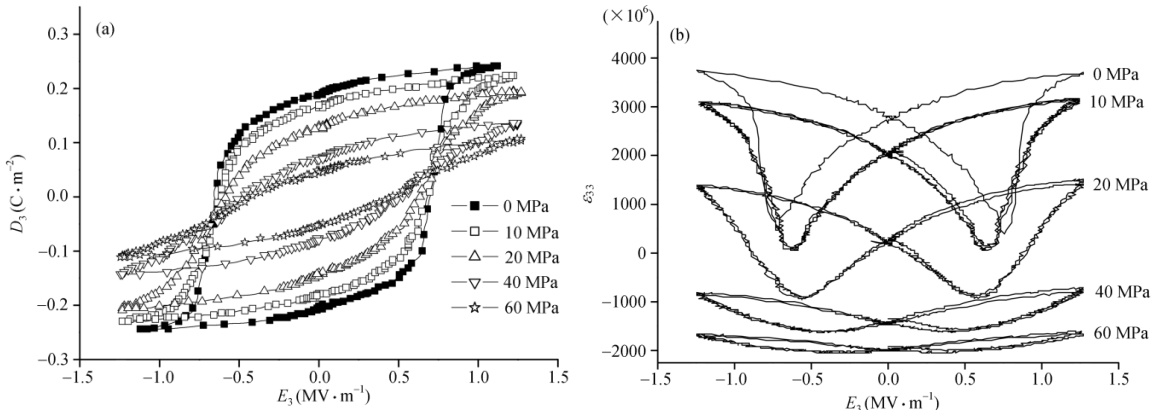


Figure 6.12: Experimental observation of a ferroelectric polycrystal (PZT-51) under electromechanical loading conditions with a cyclic external electric field and constant external compressive stresses, taken from [44]: (a) macroscopic electric displacement and (b) macroscopic strain

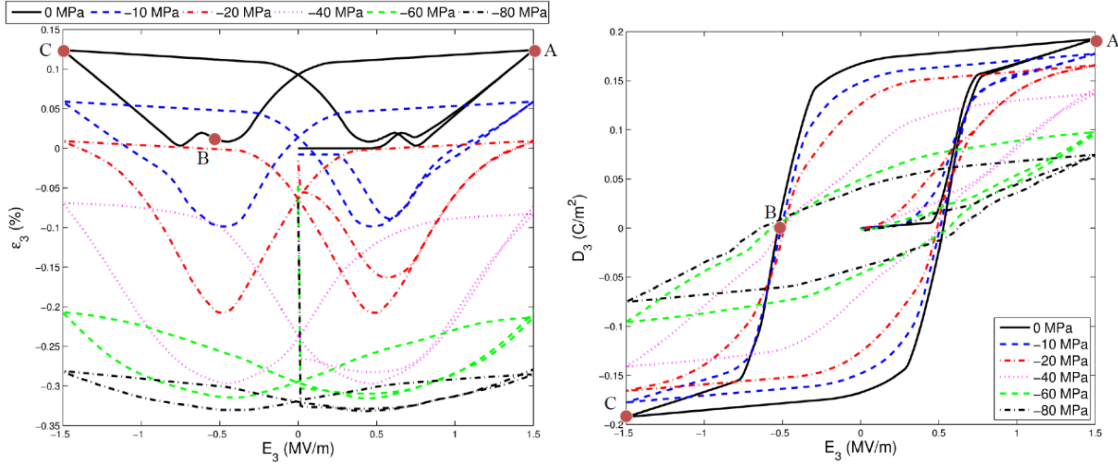


Figure 6.13: Simulated response of ferroelectric polycrystalline under electromechanical loading conditions with a cyclic external electric field and constant external compressive stresses (2D mesh: 200 RBFCGs)

Both Figure 6.12 and Figure 6.13 clearly show that increasing the magnitude of the constant uniaxial compressive stresses causes the hysteresis loop to contract. The microscopic or rather physical background for this macroscopically observed behavior lies in the fact that at larger external compressive stresses, domain switching processes locally experience higher resistance for switching. The butterfly curves show similar behavior, except that the curves are also shifted towards the compressive regime for increasing external compression levels. Moreover, the simulated response curves in Figure 6.13 are smooth, which is not the case for several FEM-based discrete switching models reported in the literature, but here stems from the incorporation of hardening contributions (back fields).

For the 3D case, Figure 6.14 shows the hysteresis and butterfly loops for different levels of externally applied compressive stresses on the upper surface.

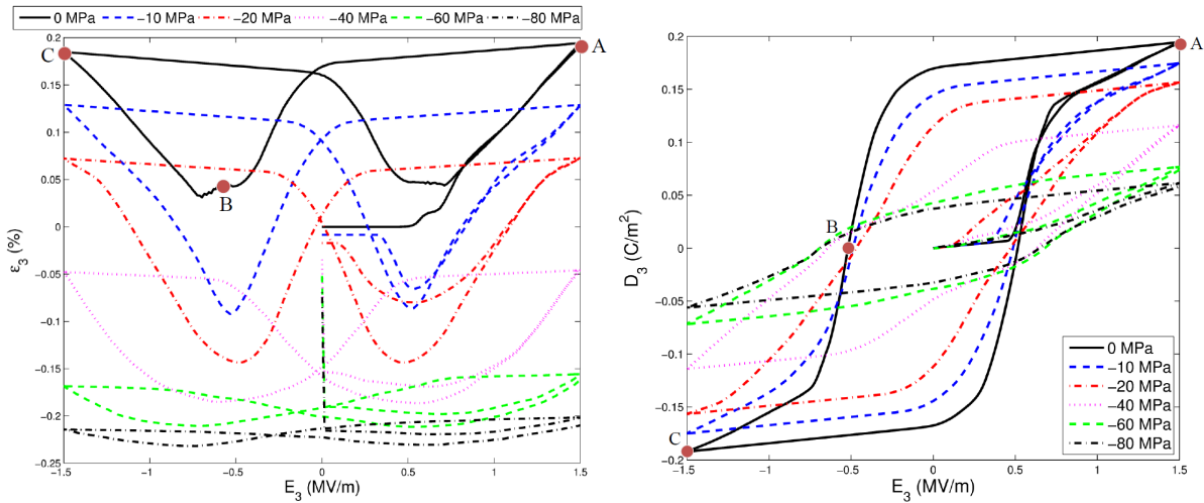


Figure 6.14: Simulated response of ferroelectric polycrystalline under electromechanical loading conditions with a cyclic external electric field and constant external compressive stresses (3D mesh: 100 RBFCGs)

Even though any regular mesh can also generate the same macroscopic response, the microstructure of the regular mesh will not be similar to that of the physical specimens because of the difference in grain geometries. The macroscopic response is just the average of the local response. So higher and lower values of stress and electric field can exist locally inside the specimen, but on average they are canceled out.

In order to show this, Figure 6.15 presents the distribution of the X_3 -component of strain, stress, electric field and electric displacement at three instants during the electric loading cycle in the absence of any applied compressive stress. These 3 particular points referred to as “A”, “B” and “C” are shown in the hysteresis and butterfly curves (A: fully poled along the positive X_3 -axis; B: electrically depoled; C: fully poled along the negative X_3 -axis). Figure 6.16 shows the same distributions for the 3D model. The plots are slightly transparent to show the distribution of the fields in the interior of the grains. Moreover, in Figure 6.17 some grains are removed from the model to clearly visualize the stress distribution, as an example, in the inner grains. (The model is also rotated in Figure 6.17 for better visualization).

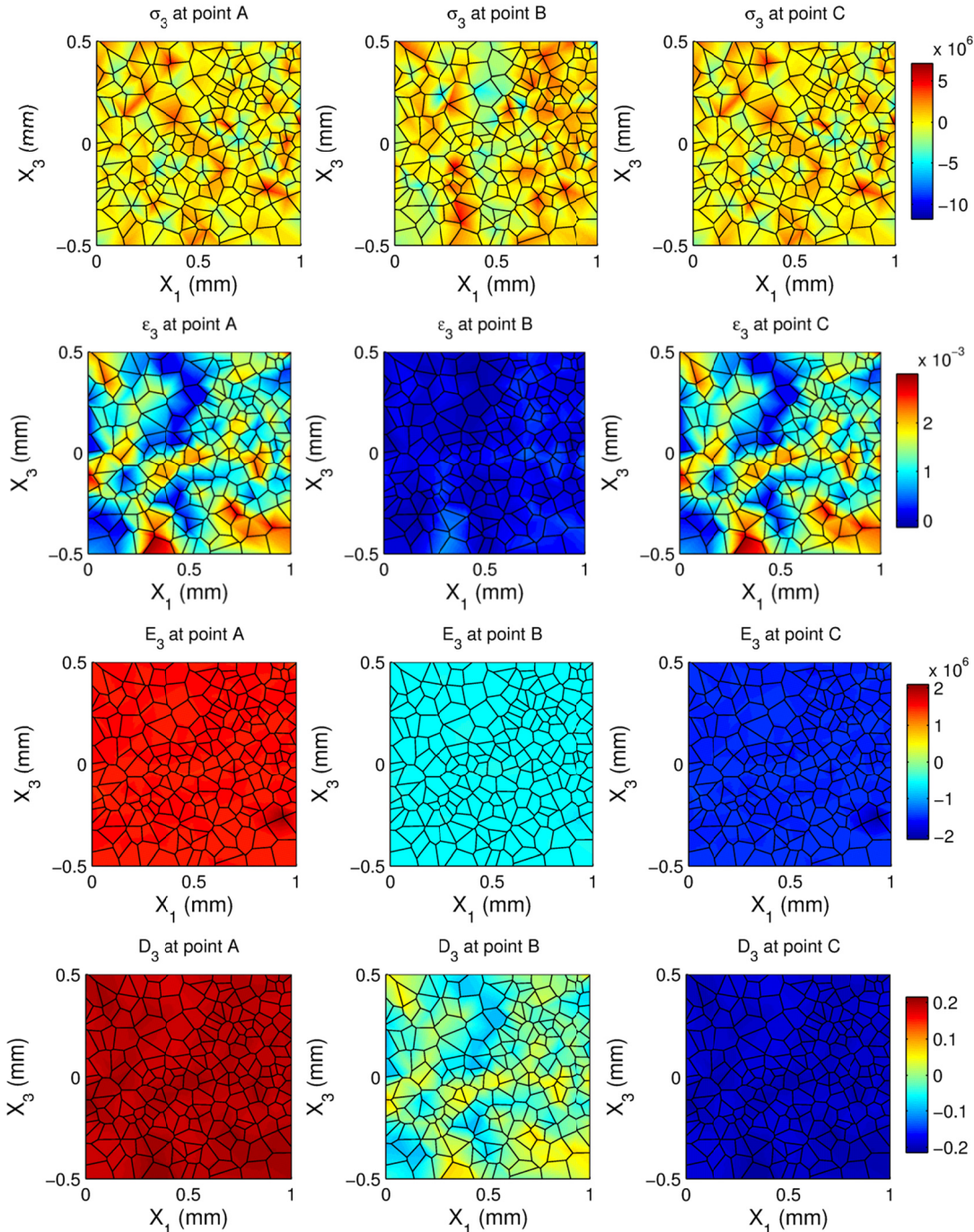
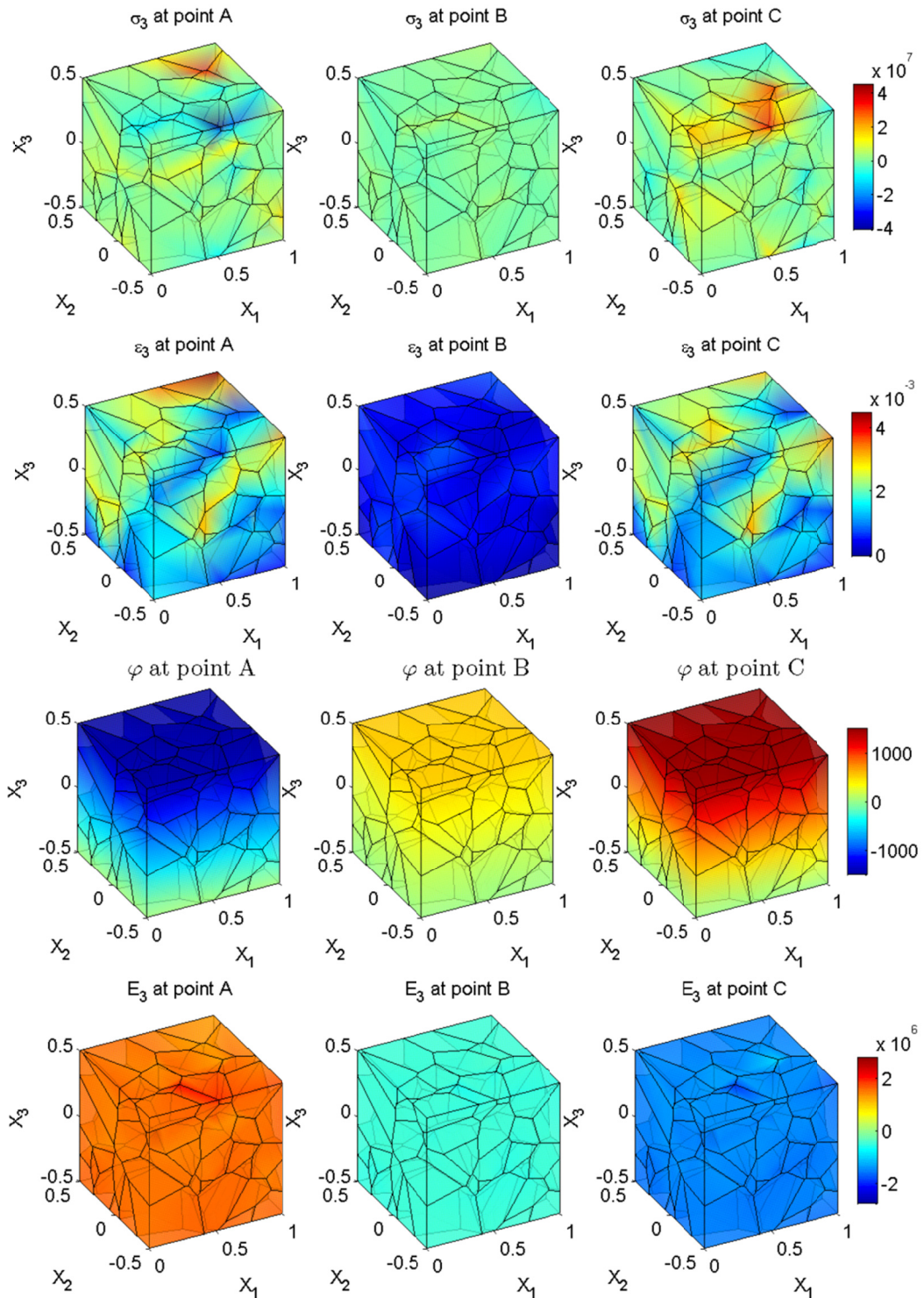


Figure 6.15: Simulation results representing the local distribution of strain, stress (Pa), electric field (V/m) and electric displacement (C/m^2) at points “A”, “B”, and “C”

The plots of the electric displacement in Figure 6.15 at loading points A and C display that the specimen is almost completely poled with respect to the macroscopic loading direction while at the macroscopically depoled state B, some individual crystals show zero net

contribution to the projected electric displacements. Other crystals, however, still show non-vanishing contributions either in positive or negative direction of the X_3 -axis. This can also be seen in Figure 6.16 for the 3D model. On the macroscopic level, however, these contributions in average cancel out each other so that the overall specimen possesses a negligible polarization as graphically displayed in the hysteresis loop in Figure 6.13 and Figure 6.14. The simulation results not only show the same macroscopic strain level at states A and C, but also similar internal strain field distribution as presented in Figure 6.15 for the 2D model. By analogy, similar stress contributions are observed at these two states as well. However for the 3D model in Figure 6.16, the strain and stress distributions are not exactly similar at points “A” and “C” because the sequence of switching occurred to reach point “A” is different from the switching sequence that occurred to achieve point “C”. Even though the level of macroscopic strain at these two instants may be similar, the local strain distribution is different. The locations of stress concentration are different because the switching sequence is the process that governs the inter-granular effects. For the depoled state B, the strains in most of the individual crystals are close to zero. The local stress distribution along the X_3 -axis turn out to take non-vanishing values within some grains in all the three states A, B and C even though their averaged values on the macroscopic scale are negligible. Similarly but not that pronounced, a non-homogeneous distribution of the electric field E_3 is observed.



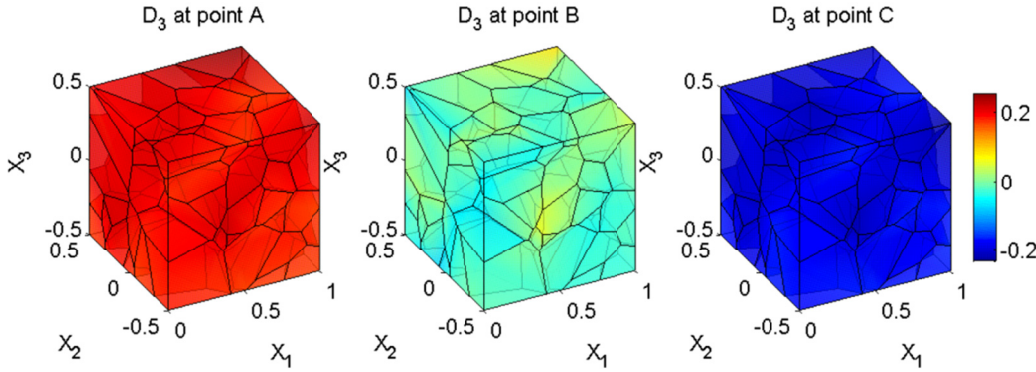


Figure 6.16: Simulation results representing the local distribution of strain, stress (Pa), electric potential (V), electric field (V/m) and electric displacement (C/m^2) at points “A”, “B”, and “C” (3D model: 100 RBFCGs)

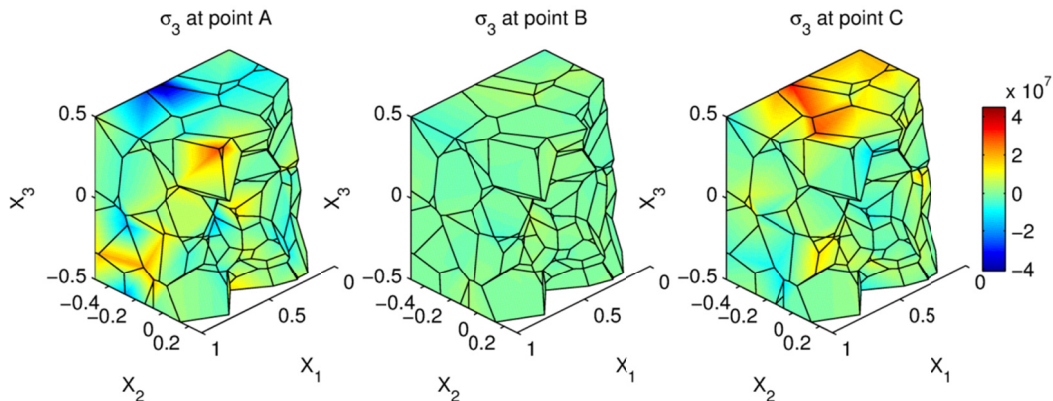


Figure 6.17: Some grains are removed from the ferroelectric specimen to show the stress distribution (Pa) in the inner grains

6.6.3.2 Ferroelastic switching

A uniformly cyclic stress is applied on the upper surface of a polycrystalline ferroelectric specimen. This case of loading causes only 90° switching. Since there is no applied electric field ($\bar{\mathbf{E}} = \mathbf{0}$), then the driving force, f_{ij} , in eq. (6.45) is only dependent on the applied stress, $\bar{\boldsymbol{\sigma}}$, the back stress, $\boldsymbol{\sigma}^b$, and the difference in the domains’ spontaneous strain vector, $\boldsymbol{\varepsilon}_{i \rightarrow j}^s$. Hence any 180° switching is prevented in all grains (i.e. $f_{12} = f_{34} = f_{56} = 0$), and we get the same value of volume fraction for domain types 1 and 2 and another value of volume fraction for domain types 3 and 4 (and a third value for domains of types 5 and 6 in 3D analysis) in each grain in each

simulation step. Consequently, the grain's piezoelectric matrix (\mathbf{e}^k or \mathbf{m}^k), and remnant polarization vector, $\mathbf{P}^{\mathbf{R}k}$, are always zero, and the grain's macroscopic electric displacement, \mathbf{D} will also be zero. So ferroelastic switching is easier than ferroelectric switching because the switching only affects the mechanical variables and the problem is reduced to a pure elastic problem with spontaneous strain that changes every time step as the domains switch in each grain by 90° .

For our simulations, the cyclic uniform stress that is applied on the upper surface of the specimen is expressed as:

$$\bar{\sigma}(t) = \sigma \sin(2\pi ft) \quad (6.57)$$

where $\sigma = 100 \text{ MPa}$ is the amplitude, and $f = 20 \text{ Hz}$ is the frequency of the applied mechanical load; t is the time in second. The time step used in the simulation is $\Delta t = 1 / (624f)$.

For the 2D model, Figure 6.18 (left) shows the hysteresis loop of the applied stress-macroscopic strain, while Figure 6.19 shows the hysteresis loop for the 3D model.

In each 2D grain there are two domain types or variants more aligned to X_3 -axis while the other two are more aligned to the X_1 -axis. The switching process changes the amount of the X_1 - and X_3 -aligned domains or volume fractions in the whole specimen as shown in Figure 6.18 (right). The results presented here together with the results in [26] and [28] are in qualitative agreement with the experimental observations.

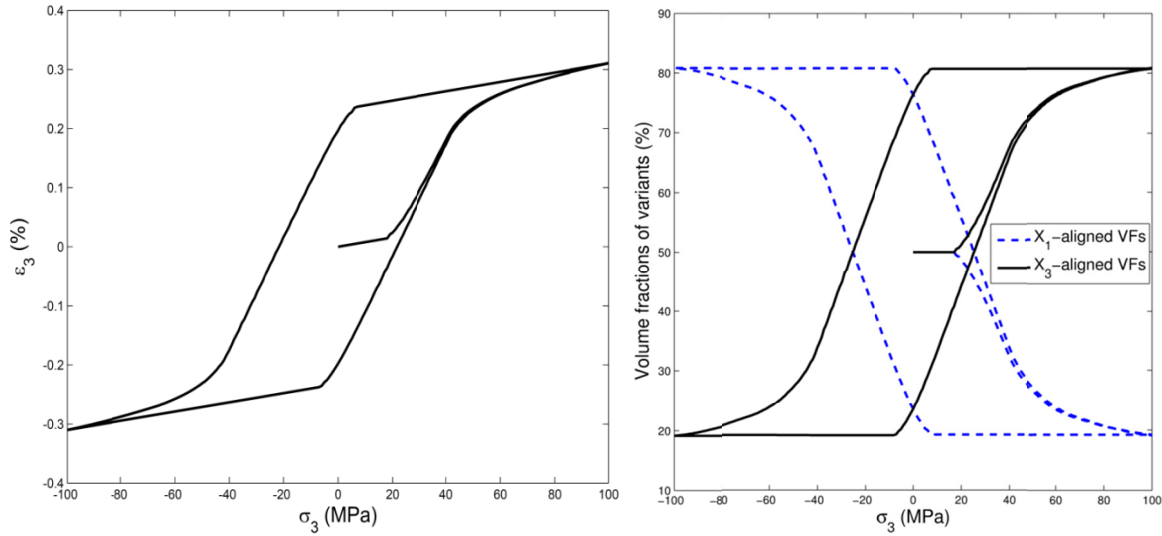


Figure 6.18: (Left): Stress-strain hysteresis loop in ferroelastic switching, (right): X_1 - and X_3 - aligned volume fractions in ferroelastic switching (2D model)

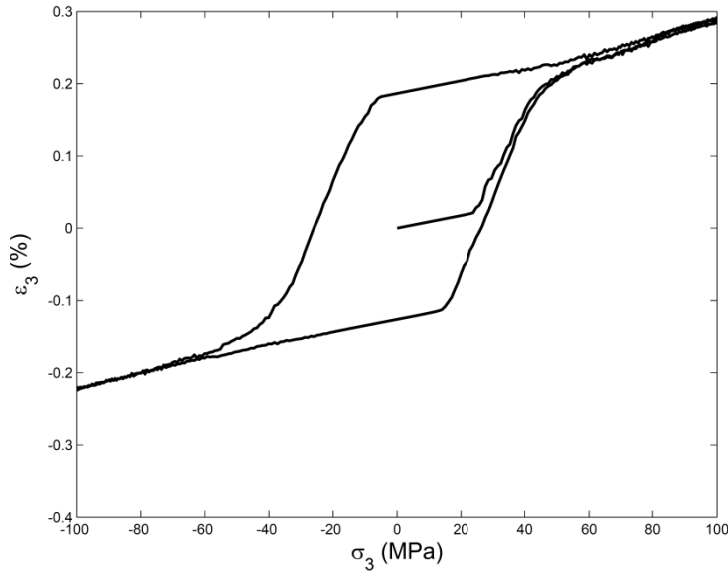


Figure 6.19: Stress-strain hysteresis loop in ferroelastic switching (3D model)

It should be noted that since the mesh is random and also the crystallographic axes in each grain is random, as the domain descritization and the random distribution of the crystallographic axes change, the resulting loop is slightly changed.

6.7 Summary and Conclusions

2D and 3D models of the Radial-Basis-Functions Computational Grains (RBFCGs), which are based on radial-basis-functions to describe the primal variables (mechanical displacements, electric and magnetic potentials) in the interior of each grain as well as linear functions to describe the primal variables on the grain boundaries, were developed to simulate magneto-electro-elastic (MEE) materials. The formulation can be reduced to model piezoelectric, piezomagnetic and elastic materials. Functionally graded materials that are composed of two constituents with spatially varying volume fractions can be directly modeled in 2D and 3D. Ferroelectric and ferroelastic switching in ferroelectric ceramic materials can be simulated when a switching criterion is introduced to govern the domain switching process in each grain in the polycrystalline ceramic. The linear functions used at the surfaces of the 3D grains are based on the Washpress functions. The compatibility between the assumed fields in the interior of a grain and those on the boundaries is met using either the collocation or the least squares methods. Independently assumed strain, electric and magnetic fields can also be used to avoid shear locking problem. The compatibility between these independently assumed secondary fields and those derived from the primary fields is also met using the same mentioned methods. Figure 6.20 illustrates the methods used in the formulation of RBFCGs to satisfy the governing equations and enforce the various boundary conditions in a polycrystalline sample.

The developed 2D and 3D RBFCGs were able to simulate ferroelectric and ferroelastic switching phenomena accurately, as compared to previous models in the literature and the experimental results. The complexity of geometry and domains orientation of the ferroelectric specimens as well as the distribution of the mechanical and electric fields during the cyclic electromechanical loadings can now be fully simulated using the 3D RBFCGs, and the randomly generated crystallographic axes in each grain. Each RBFCG represents a crystal grain having a

random shape and crystallographic coordinate system, and surrounded by a different number of neighboring grains.

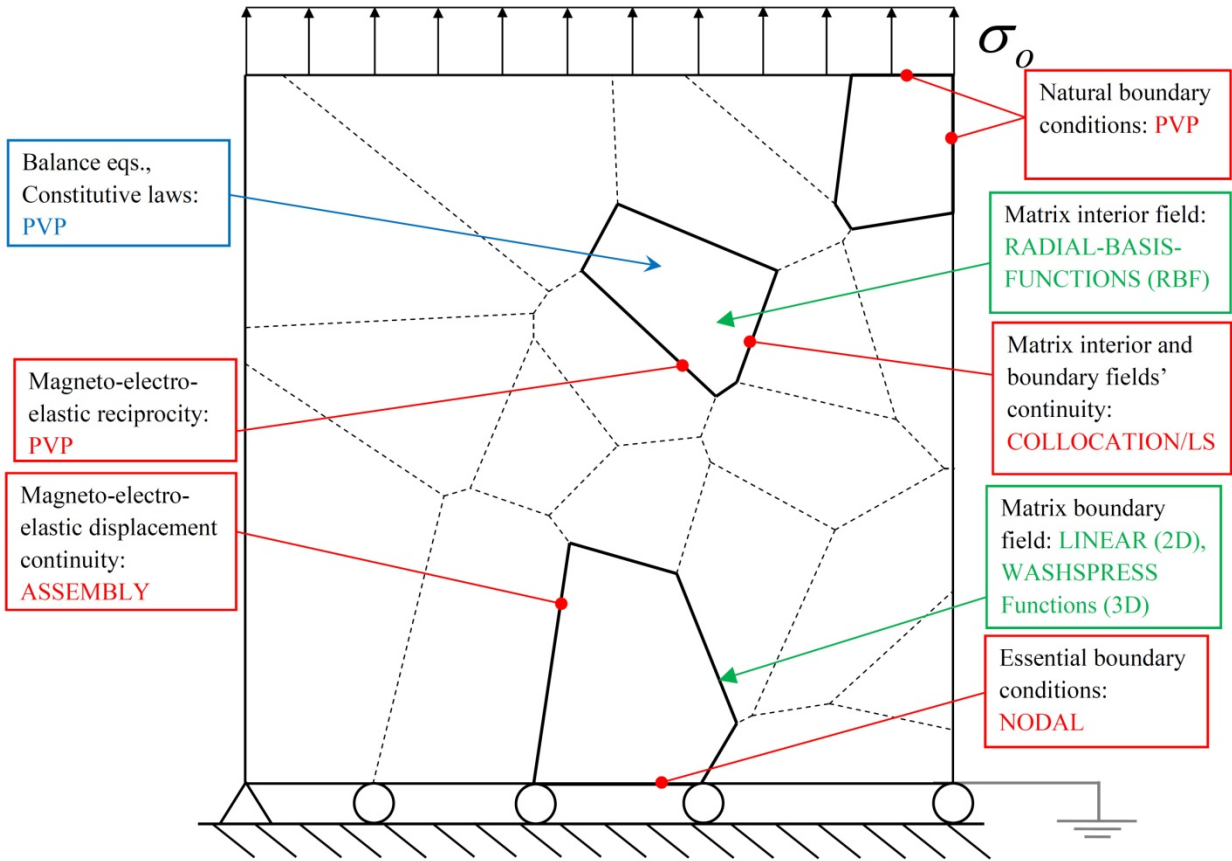


Figure 6.20: Illustration of the methods used in the formulation of RBFCGs to satisfy the governing equations and enforce the various boundary conditions in a polycrystalline sample (PVP refers to Primal Variational Principle)

This is the first time for 3D random computational grains to be implemented in a ferroelectric switching model. It was shown here that during the cyclic loading, domain switching can cause localized stresses inside the specimen and this is one of the causes of crack nucleation in ferroelectric materials. These localized stresses are not apparent in the macroscopic response which gives average values of the field distributions. However, the internal distributions are visualized here to show the localized concentrations of stresses and strains. In this work it was observed with the 3D model that points on the hysteresis and butterfly loops with similar

macroscopic stresses and strains may correspond to different stress and strain distributions in the microstructure. The cause of this is thought to lie in the fact that the sequence of switching is different as the body is being loaded to different points having the same level of macroscopic strain. The difference in this switching sequence causes the locations of the concentrated stresses and strains in the microstructure to change. Experimental testing is needed to verify this observation.

6.8 References of chapter 6

- [1] **Pian, T.H.H.** (1964): Derivation of element stiffness matrices by assumed stress distribution, *Am. Inst. Aeronaut. Astronaut. J.*, vol. 2, pp. 1333–1336.
- [2] **Atluri, S.N.** (2005): *Methods of Computer Modeling in Engineering & Sciences*, Volume I, Tech Science Press, USA.
- [3] **Babuska, I.** (1973): The finite element method with Lagrangian multipliers. *Numerische Mathematik*, vol. 20, no. 3, pp. 179–192.
- [4] **Brezzi, F.** (1974): On the existence, uniqueness and approximation of saddle-point problems arising from Lagrangian multipliers. *Revue Française D'automatique, Informatique, Recherche Opérationnelle, Analyse Numérique*, vol. 8, no. 2, pp. 129–151.
- [5] **Bishay, P. L.; Atluri, S. N.** (2012): High-performance 3D hybrid/mixed, and simple 3D Voronoi cell finite elements, for macro- & micro-mechanical modeling of solids, without using multi-field variational principles, *CMES: Computer Modeling in Engineering & Sciences*, vol. 84, no. 1, pp. 41-98.
- [6] **Bishay, P. L.; Atluri, S. N.** (2013): 2D and 3D Multiphysics Voronoi cells, based on radial-basis-functions, for direct mesoscale numerical simulation (DMNS) of the

switching phenomena in ferroelectric polycrystalline materials, *CMC: Computer Modeling in Engineering & Sciences*, vol. 33, no. 1, pp. 19-62.

- [7] **Dong, L.; Atluri, S. N.** (2012a): A simple multi-source-point Trefftz method for solving direct/inverse SHM problems of plane elasticity in arbitrary multiply-connected domains. *CMES: Computer Modeling in Engineering & Sciences*, vol. 85, no.1, pp.1–43.
- [8] **Dong, L.; Atluri, S. N.** (2012b): T-Trefftz Voronoi cell finite elements with elastic/rigid inclusions or voids for micromechanical analysis of composite and porous materials. *CMES: Computer Modeling in Engineering & Sciences*, vol.83, no.2, pp.183-219.
- [9] **Dong, L.; Atluri, S. N.** (2012c): Development of 3D T-Trefftz Voronoi cell finite elements with/without spherical voids &/or elastic/rigid inclusions for micromechanical modeling of heterogeneous materials. *CMC: Computers, Materials & Continua*, vol. 29, no. 2, pp. 169–211.
- [10] **Dong, L.; Atluri, S. N.** (2012d): Development of 3D Trefftz Voronoi cells with ellipsoidal voids &/or elastic/rigid inclusions for micromechanical modeling of heterogeneous materials. *CMC: Computers, Materials & Continua*, vol. 30, no. 1, pp. 39–82.
- [11] **Dong, L.; Atluri, S. N.** (2011): A simple procedure to develop efficient & stable hybrid/mixed elements, and Voronoi cell finite elements for macro- & micromechanics. *CMC: Computers, Materials & Continua*, vol. 24, no. 1, pp. 61–104.
- [12] **Ghosh, S.** (2011): *Micromechanical analysis and multi-scale modeling using the Voronoi cell finite element method*. CRC Press/Taylor & Francis.
- [13] **Hwang, S.C., McMeeking, R.M.** (1998): A finite element model of ferroelectric polycrystals. *Ferroelectrics*, vol. 211, pp. 177–194.

- [14] **Hwang, S.C., McMeeking, R.M.** (1999): A finite element model of ferroelastic polycrystals. *Int. J. Solids Struct.*, vol. 36, pp. 1541–1556.
- [15] **Steinkopff, T.** (1999): Finite-element modelling of ferroelectric domain switching in piezoelectric ceramics. *J Eur Ceram Soc*, vol. 19, pp. 1247–1249.
- [16] **Kamlah, M.; Liskowsky, A.C.; McMeeking, R.M.; Balke, H.** (2005): Finite element simulation of a polycrystalline ferroelectric based on a multi-domain single crystal switching model, *Int. J. Solids Struct.*, vol. 42, pp. 2949–2964.
- [17] **Arockiarajan, A.; Delibas, B.; Menzel, A.; Seemann, W.** (2006): Studies on rate-dependent switching effects of piezoelectric materials using a finite element model. *Comput Mater Sci*, vol. 37, pp. 306–317.
- [18] **Arockiarajan, A.; Menzel, A.; Delibas, B.; Seemann, W.** (2007): Micromechanical modeling of switching effects in piezoelectric materials—a robust coupled finite element approach. *J Intell Mater Syst Struct*, vol. 18, pp. 983–999.
- [19] **Haug, A.; Huber, J.E.; Onck, P. R.; Van derGiessen, E.** (2007): Multi-grain analysis versus self-consistent estimates of ferroelectric polycrystals. *J Mech Phys Solids*, vol. 55, pp. 648–665.
- [20] **Menzel, A.; Arockiarajan, A.; Sivakumar, S.M.** (2008): Two models to simulate rate-dependent domain switching effects—application to ferroelastic polycrystalline ceramics. *Smart Mater Struct*, vol. 17, pp. 015026–015038.
- [21] **Pathak, A.; McMeeking, R. M.** (2008): Three-dimensional finite element simulations of ferroelectric polycrystals under electrical and mechanical loading. *J Mech Phys Solids*, vol. 56, pp. 663–683.

- [22] **Ghandi, K., Hagwood, N.W.** (1996): Nonlinear finite element modeling of phase transitions in electro-mechanically coupled material, *96 SPIE Proc.* 2715, pp. 121–139.
- [23] **Ghandi, K., Hagwood, N.W.** (1997): A hybrid finite element for phase transitions in nonlinear electro-mechanically coupled material. *97 SPIE Proc.* 2339, 97–112.
- [24] **Huo, Y., Jiang, Q.** (1997): Modeling of domain switching in polycrystalline ferroelectric ceramics. *J. Smart Mat. Struct.* vol. 6, pp. 441–447.
- [25] **Huo, Y., Jiang, Q.** (1998): Modeling of domain switching in ferroelectric ceramics: an example. *Int. J. Solids Struct.*, vol. 35, pp. 1339–1353.
- [26] **Kim, S.J.; Jiang, Q.** (2002): A finite element model for rate-dependent behavior of ferroelectric ceramics. *Int J Solids Struct.*, vol. 39, pp. 1015–1030.
- [27] **Jayabal, K.; Menzel, A.; Arockiarajan, A.; Srinivasan, S. M.** (2011) Micromechanical modeling of switching phenomena in polycrystalline piezoceramics: application of a polygonal finite element approach. *Comput Mech*, vol. 48, pp. 421–435.
- [28] **Sze, K. Y.; Sheng, N.** (2005) Polygonal finite element method for nonlinear constitutive modeling of polycrystalline ferroelectrics. *Finite Elem Anal Des*, vol. 42, pp. 107–129.
- [29] **Sze, K.Y.; Pan, Y.S.** (1999): Hybrid finite element models for piezoelectric materials, *J. Sound Vib.*, vol. 226, pp. 519–547.
- [30] **Kim, S. J.; Choi, J.; Kwak, M.K.** (2003): A finite element prediction of ferroelectric switching behavior using a regular dodecahedron RVE. *Computational Mechanics*, vol. 31, pp. 469–478.
- [31] **Wachspress, E. L.** (1975): *A Rational Finite Element Basis*, Mathematics in Science and Engineering, vol. 114, Academic Press.

- [32] **Cocks, A.C.F; McMeeking, R.M.** (1999): A phenomenological constitutive law for the behavior of ferroelectric ceramics. *Ferroelectrics*, vol. 228, pp. 219–228.
- [33] **Kamlah, M.; Jiang, Q.** (1999): A constitutive model for ferroelectric PZT ceramics under uniaxial loading. *Smart Mater Struct*, vol. 8, pp. 441–459.
- [34] **Jiang A.; Ding H.** (2004): Analytical Solutions to Magneto-electro-elastic Beams, *Structural Engineering and Mechanics*, vol. 18, pp.195–209.
- [35] **Eshelby, J. D.** (1957): The determination of the elastic field of an ellipsoidal inclusion, and related problems. *Proc. R. Soc. Lond. A*, vol. 241, pp. 376–396.
- [36] **Hill, R.** (1965): A self-consistent mechanics of composite materials. *J. Mech. Phys. Solids*, vol. 13, pp. 213–222.
- [37] **Budiansky, B.** (1965): On the elastic moduli of some heterogeneous materials. *J. Mech. Phys. Solids*, vol. 13, pp. 223–227.
- [38] **Hori, M.; Nemat-Nasser, S.** (1993): Double-inclusion model and overall moduli of multi-phase composites. *Mechanics of Materials*, vol. 14, pp. 189–206.
- [39] **Christman, T.; Needleman, A.; Suresh, S.** (1989): An experimental and numerical study of deformation in metal-ceramic composites. *Acta Metallurgica*, vol. 37, no. 11, pp. 3029–3050.
- [40] **Tvergaard, V.** (1990): Analysis of tensile properties for a whisker-reinforced metal-matrix composite. *Acta Metallurgica et Materialia*, vol. 38, no. 2, pp. 185–194.
- [41] **Bao, G.; Hutchinson, J. W.; McMeeking, R. M.** (1991): Particle reinforcement of ductile matrices against plastic flow and creep. *Acta Metallurgica et Materialia*, vol. 39, no. 8, pp. 1871–1882.

- [42] **Grujicic, M.; Zhang, Y.** (1998): Determination of effective elastic properties of functionally graded materials using Voronoi cell finite element method. *Materials Science and Engineering* A251, pp. 64–76.
- [43] **Zhai, P.; Jiang, C.; Zhang, Q.** (1993): *Ceramic transactions: Functionally Gradient Materials*. The American Ceramic Society, Westerville, OH, p. 449.
- [44] **Li, F.; Fang, D.; Lee, J.; Kim, C.H.** (2006): Effects of compressive stress on the nonlinear electromechanical behavior of ferroelectric ceramics. *Sci China: Ser E Technol Sci*, vol. 49, pp. 29–37.

Chapter 7 : Dissertation Summary and Conclusions

In this dissertation, several numerical methods, composing the Multi-Physics Computational Grains (MPCGs) family, for solving different types of problems related to multifunctional materials are proposed. Each method has its own advantages in modeling specific types of materials and can be extended in several directions. Table 7.1 shows the four numerical methods we presented, the physics they are capable of handling, the microstructure configurations that can be simulated, and few suggested directions that can be taken to extend them. Alternative to Lekhnitskii formalism, Trefftz functions can be derived based on Stroh formalism. Defects of different shapes may be introduced to the formulations of some MPCGs. Dynamic, fracture and fatigue analyses can be performed when cracks are included in the grains to study the micro-crack propagation in micro-electro-mechanical systems (MEMS). Since many proposed computational grains have stiffness matrices similar to the regular finite elements, they can be implemented into commercially available FEM software, such as Abaqus, Ansys, MSC Patran & Nastran, or COMSOL Multiphysics, with a special Dirichlet tessellation mesher and a void/inclusion geometry-generator based on the specified volume fraction. This can also be combined with random crystallographic coordinate system generator for modeling grains in ferro-materials. This new family of numerical methods and finite elements are expected to grow, by introducing other novel methods, elements, or grain types, and to expand, by including more physics in the formulation. The numerical accuracy and efficiency these new techniques are bringing to the field of computational solid mechanics and the direct numerical simulation of the multiphysics of multifunctional materials will help increase the understanding of the material behavior, and predict the response of the different systems and structures used in modern engineering and sciences easily and efficiently.

Table 7.1: The proposed numerical methods and their capabilities

Numerical Method	Physics	2D/3D	Configurations	Can be extended to
Multi-Region Trefftz Collocation Grains (MTCGs)	- Linear Elasticity, - Electrostatics, - Magnetostatics, - Pizoelectricity, - Piezomagnetism	2D only	Porous/Composite Multi-grain (Direct and Inverse)	- Pyroelectricity, - Thermoelasticity, - Heat conduction, - Electric conduction, - Cracked composites, - Out of plane shear
Trefftz-Lekhnitskii Computational Grains (TLCG)	- Linear Elasticity, - Electrostatics, - Magnetostatics, - Pizoelectricity, - Piezomagnetism	2D only	Porous/Composite Multi-grain	- Pyroelectricity, - Thermoelasticity, - Heat conduction, - Electric conduction, - Cracked composites, - Out of plane shear
Hybrid Displacement Computational Grains (HDCG)	- Linear Elasticity, - Electrostatics, - Magnetostatics, - Pizoelectricity, - Piezomagnetism	2D and can be directly extended to 3D	Porous/Composite Multi-grain	- Pyroelectricity, - Thermoelasticity, - Heat conduction, - Electric conduction, - Cracked composites, - Out of plane shear
Radial-Basis-Functions Computational Grains (RBFCG)	- Linear Elasticity, - Electrostatics, - Magnetostatics, - Pizoelectricity, - Piezomagnetism - Ferroelectricity	2D and 3D	Multi-grain	- Pyroelectricity, - Thermoelasticity, - Heat conduction, - Electric conduction, - Ferromagnetism